Optimisation of the Acousto Optic Signal Detection for Biomedical Applications

Sonny Gunadi

A Thesis Submitted to the University College London
in Fulfilment of the Requirements for
the Degree of Doctor of Philosophy (Ph.D.)

Principal Supervisor
Dr Terence Leung

Secondary Supervisor
Prof Clare Elwell

Dept. Medical Physics & Bioengineering, UCL

September 2011

For my nephews, Xiang Rui,
Ryan, Dylan, Bennett and
niece, Beatrice.

Live Long and Prosper.

Declaration

I, Sonny Gunadi, confirm that the work presented in this thesis is my own. Where information has been derived from other sources, I confirm that this has been indicated in the thesis.

Acknowledgement

I would like to thank my supervisors Dr Terence Leung and Prof Clare Elwell for their constant support, guidance and encouragement in the course of this work.

It has been a fun and fruitful experience working with the fellow members of the AO group: Jack Honeysett, Sam Powell and Dr Shihong Jiang. I'm very grateful to Dr Jiang's support in using the CCD camera.

I am indebted to Prof Paul Beard, Dr Jan Laufer, Dr Thomas Allens, Dr Edward Zhang and Joanna Brunker of the Photoacoustics group, Dr Ilias Tachtsidis and Prof Jem Hebden for allowing me to use their equipment for extended period of time.

Dr Ben Price, who recently graduated, has been a great help in the phantom development. Many thanks to Dr Nick Everdell and Joe Evans (Implantable Device group) for their technical support.

I am grateful to the Worshipful Company of Scientific Instrument Makers and the UCL Graduate School for their financial support.

To my family, thank you for everything.

Abstract

Near infrared light has been widely used to probe human tissue oxygenation non-invasively. However the highly scattering nature of tissue limits light penetration depths and optical measurement is more sensitive to optical changes in the superficial region (SFR) of tissue. It is proposed that the penetration depth and the localisation of the optical measurement can be improved by the Acousto-Optic (AO) method. The AO method tags diffuse photons in an optically tissue mimicking medium by using focused ultrasound waves. Generally it is believed that the region probed by the AO method is decided by the position of the focused ultrasound region (FUR). Therefore the AO method can potentially improve the penetration depth and reduce the susceptibility in the SFR of the optical measurement by relocating the FUR to deeper region in tissue.

The spatial sensitivity of the AO measurement is mapped and compared to the spatial sensitivity of the optical measurement experimentally. The AO method can monitor absorption and scattering changes in deeper regions than the optical measurement. The AO method is less affected by the optical changes in the SFR. The most sensitive region probed by the AO method can be relocated by re-positioning the FUR. But it does not always coincide with the FUR. The AO spatial sensitivity depends on the overlap of the FUR and the photon path distribution. This overlap region affects the AO signal differently for absorption and scattering changes. Thus, concurrent monitoring of absorption and scattering changes require careful positioning of the FUR. Finally, it is also demonstrated that the pulsed-wave ultrasound can be used with the AO method in a cylindrical geometry. An optimal optodes' positions for the AO signal detection can be predicted experimentally for a given location of the FUR within a cylindrical geometry.

Publications

Gunadi, S., Powell, S., Elwell, C. E. and Leung, T. S. (2010). Optimization of the acousto-optic signal detection in cylindrical geometry. Proc. SPIE, 7564:756431.

Gunadi, S. and Leung, T. S. (2011). Regional sensitivity comparison between optical and acousto-optic sensing. Proc. SPIE, 7899:78992Q.

Gunadi, S. and Leung, T. S. (2011). "Spatial Sensitivity of Acousto-Optic and Optical Near-Infrared Spectroscopy Sensing Measurements." Journal of Biomedical Optics, 16(12): 127005.

Contents

List of Figures

List of Tables

Glossary

$\partial A_{SR}/\partial \rho$	Spatially Resolved Measurement using the CCD Camera
a.u.	Arbitrary Unit
AO	Acousto-Optic
CCD	Charge-Coupled Device
DCS	Diffuse Correlation Spectroscopy
FUR	Focused Ultrasound Region
HIFU	High Intensity Focused Ultrasound
I_{AC}	Ultrasound Modulated Intensity
I_{CCD}	Intensity Measurement by using the CCD Camera
I_{DC}	Un-modulated Intensity
I_{PC}	Intensity Measurement by using the Single Photon Counter
J_{AO}	Spatial Sensitivity of the AO Measurement
J_{CCD}	Spatial Sensitivity of the I_{CCD} Measurement
J_{PC}	Spatial Sensitivity of the I_{PC} Measurement
J_{SR}	Spatial Sensitivity of the $\partial A_{SR}/\partial \rho$ Measurement
MD	Modulation Depth
NIR	Near Infrared
NIRS	Near Infrared Spectroscopy
P_{peak}	Ultrasound Peak Pressure
PVA	Poly-vinyl Alcohol
ROI	Region of Interest
SA	Scanning Area
SFR	Superficial Region
μ_a	Absorption Coefficient
μ_s'	Transport Scattering Coefficient

1 Introduction

This chapter describes the basic background and the main motivations of the project, which is to improve the current usage of the near infrared (NIR) light in the monitoring of human tissue.

1.1 From Near Infrared Sensing to Acousto-Optic Sensing

The use of optical imaging or spectroscopic techniques in research, therapy and diagnosis in medicine is growing rapidly. Examples of optical techniques include: Laser Doppler Flowmetry [Bonner 1981], Laser Speckle Contrast Imaging [Boas 2010], Optical Coherence Tomography [Huang 1991], Photoacoustics imaging [Beard 2011], Acousto-Optic imaging [Wang 2004], Near Infrared (NIR) imaging [Gibson 2005] and Near Infrared Spectroscopy (NIRS) [Ferrari 2004, Wolf 2007]. NIRS is a widely adopted optical sensing technique in the measurement of concentrations of tissue chromophores such as oxy- and deoxy-haemoglobin, cytochrome-c-oxidase and water. This technique is non-invasive and safe because NIR light is non-ionising [Obrig 2003, Vo-Dinh 2003, Ferrari 2004, Niemz 2004, Wang 2004, Tuchin 2007, Wolf 2007, Durduran 2010]. A number of NIRS tissue monitoring devices are available commercially, for example: the Hamamatsu NIRO series [Suzuki 1999] and TRS (Time-Resolved System) [Ohmae 2006], the Somanetics INVOS Cerebral Oximeter [Yoshitani 2002], the CAS Medical Systems FORE-SIGHT Cerebral Oximeter [MacLeod 2006] and the ISS OxiplexTS Tissue Oximeter [Calderon-Arnulphi 2007].

The thesis started out as an investigation of the blood flow and total haemoglobin changes measurement using the single source and single detector Diffuse Correlation Spectroscopy (DCS) [Maret 1987, Boas 1997, Cheung 2001, Li 2005, Durduran 2010] technique, which is one of NIRS methods.

This technique can provide a measure of blood flow based on the fluctuations of the scattered intensity due to the Doppler Effect [Briers 1996], which is the result of collision between the photons and the moving red blood cells. The measure of blood flow can be estimated from the rate of decay of the autocorrelation function (which is detailed in section 3.2.3), which is an indicator of the rate of fluctuation. Higher fluctuation due to greater flow results in a faster decay in the correlation value. The total blood volume change can be estimated from the change of detected intensity. Higher blood volume absorbs more light, thus the detected intensity decreases. The DCS has been used clinically and validated with other blood flow measurements [Yu 2007, Zhou 2007, Li 2008, Buckley 2009, Durduran 2009, Kim 2009, Shang 2009, Zhou 2009, Carp 2010, Durduran 2010, Edlow 2010, Kim 2010, Mesquita 2010, Ninck 2010, Roche-Labarbe 2010, Carp 2011].

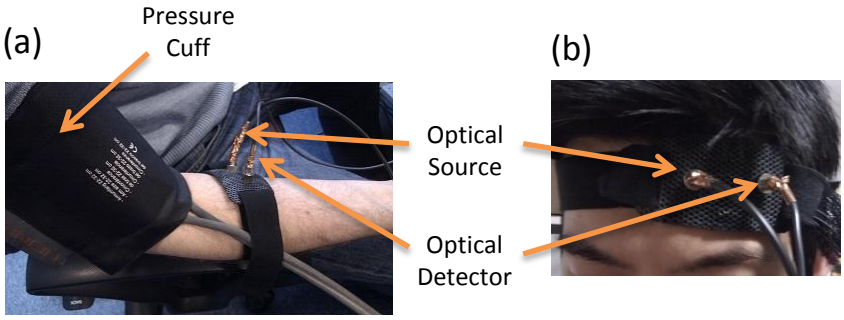

Figure 1-1 Optical measurements in: (a) a muscle cuff occlusion study and (b) a brain activation study.

The NIRS measurements using the single source and detector DCS system on the muscle and the brain of a healthy male human subject were conducted and the results are shown in Figure 1-1 (a) and (b) respectively. In the study of the muscle cuff occlusion, a pressure cuff was used to restrict the blood flow in the arm of a subject by applying different cuff pressures. The optical source and detector pair were placed on the arm and the detected intensity (number of photons per second) and the autocorrelation functions were measured at different cuff pressures.

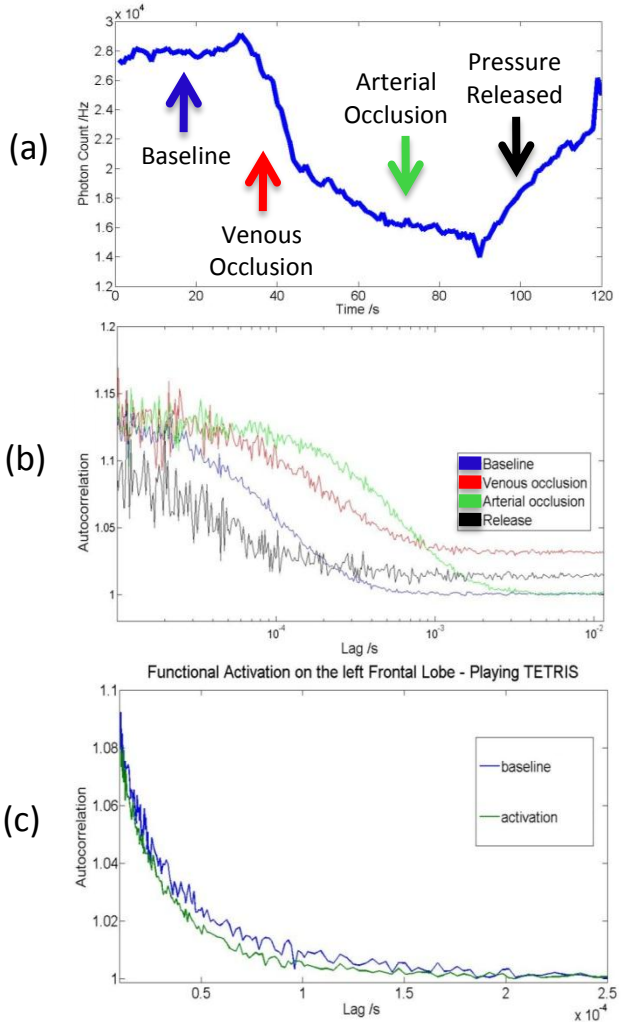

Figure 1-2 The results of the NIRS studies of a human subject using the DCS: (a) the detected light intensity profile when the blood volume in the subject's arm is normal (baseline), increasing (venous occlusion), approaching the maximum (arterial occlusion) and decreasing from the maximum (pressure released); (b) the relative measure of blood flow during the different stages of a cuff occlusion study that shows normal (baseline), slow (venous occlusion), slowest (arterial occlusion) and fast (release) flow rates; and (c) the increase in the relative blood flow measurement from minimal to increased brain activity.

The baseline measurements were the control measurements when no pressure was applied. The pressure was initially raised to 80 mmHg, which is higher than the typical venous blood pressure to stop the venous blood flow (venous occlusion). The pressure was subsequently raised to 200 mmHg, which is higher than the

typical arterial pressure to stop the arterial blood flow (arterial occlusion). Finally, the pressure was released. The change in the detected intensity and the measure of the blood flow during the different stages of occlusion are shown in Figure 1-2 (a) and (b) respectively.

When the venous blood flow was stopped and the blood began to pool in the venous system, the detected intensity dropped as shown in Figure 1-2 (a). The blood volume in the venous system continued to rise because the arterial blood flow was not stopped. This resulted in the continuous increase in light absorption, which is shown by the sharp decrease in the detected intensity in Figure 1-2 (a). The autocorrelation function in Figure 1-2 (b) during the venous occlusion showed a slower decay than that of the baseline because the net blood flow was slower. During the arterial occlusion, blood flow was stopped completely and the reduced intensity started to stabilise and the slowest decay of the autocorrelation function can be observed that shows the slowest relative blood flow. When pressure was released, the detected intensity was rising as the collected blood was released, which is also shown by the fastest decay of the autocorrelation function depicting the fastest relative blood flow.

Figure 1-2 (c) shows the result of another DCS study, whereby the optical probes of the DCS system was placed on the left forehead of a human subject to demonstrate the change in cerebral blood flow during the functional activation in the left frontal lobe, which is depicted in Figure 1-1 (a). The baseline autocorrelation function measurement (slow relative blood flow) was recorded when the subject was required to remain still and had his eyes closed. Subsequent measurement was carried out when the subject started playing a computer game. The result shows that during the period of increased brain activity, the rate of decay of the autocorrelation function was faster, which indicated an increase in blood flow to supply the additional nutrients needed by the activated frontal lobe.

Figure 1-3 The optical measurement of the tissue oxygenation and haemodynamics in: (a) the muscle[1] and (b) in the brain (from Okada et al. [Okada 2003]), that show the 'banana' shaped region that the light propagates from the optical source to the detector.

The NIRS measurements that are shown in Figure 1-2 can be simplified into the illustrations that are shown in Figure 1-3. In Figure 1-3 (a), it is obvious that if there are changes in the oxygenation and the blood flow in the skin, the optical measurement will be affected. The light propagates through the skin, the subcutaneous layers and through the tissue that consists of networks of different blood vessels and capillaries, and some of the light would eventually be measured. The blood in the arterioles and capillaries are rich in the oxygenated blood and the blood in the veins and venules contain a higher concentration of the deoxygenated

[1] Illustration of the capillary network: http://en.wikipedia.org/wiki/Capillary

blood from the organs in healthy tissue. It has been shown that the subcutaneous fat layer underneath the skin has significant effect on the optical measurement [Van Beekvelt 2001].

Figure 1-3 (b) shows the computer simulation of light propagation in a brain mimicking geometry by Okada et al. [Okada 2003]. It shows that the NIRS measurement is most sensitive to the regions in the superficial layer of the head. Similar to the situation that is shown in Figure 1-3 (a), the measurement is influenced by the optical property changes in the scalp [Villringer 1993] and the cerebral spinal fluid layer [Dehghani 2000]. Therefore the optical measurement accounts for the combination of all changes that occur in the whole volume tissue, which is covered the idealised 'banana' shaped light bundle. Often it is clinically more useful to measure the oxygenation and blood flow of a specific region of interest (ROI) within the tissue.

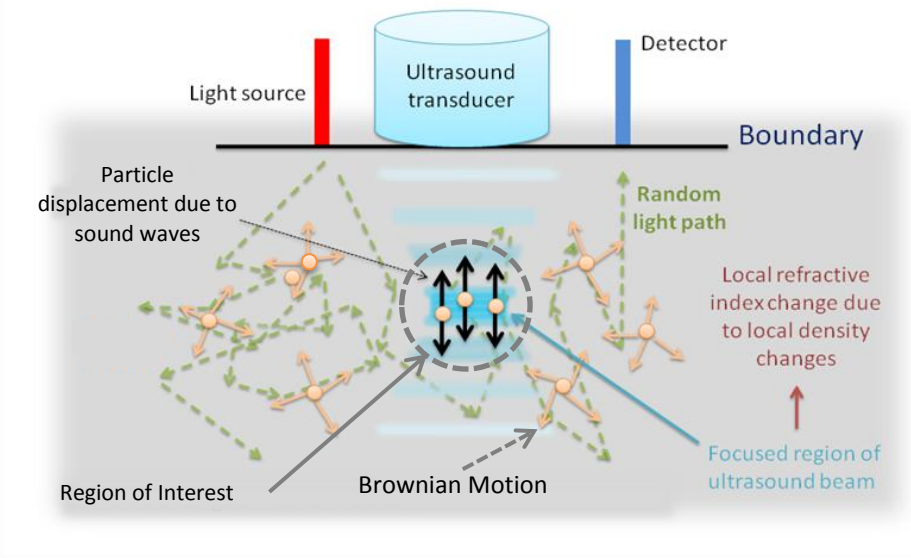

Figure 1-4 Focused ultrasound modulation of the multiple scattered light in a turbid medium

It has been suggested that the sensitivity of the current optical measurement in the ROI can be improved by incorporating a technique, which is known as the Ultrasound-modulated Optical Tomography (UOT) or Acousto-Optic

Tomography (AOT) [Wang 2004, Murray 2007]. This technique utilises focused ultrasonic waves in the ROI to label the photons that propagate into the ROI, which is also the location of the focused ultrasound region (FUR) as shown in Figure 1-4. The focused ultrasound waves modulate the density of scatterers and optical properties in the ROI according to the pressure waves. When the photons interact with the modulated medium, they are "tagged" [Leutz 1995, Wang 1995, Wang 1997, Sakadzic 2002].

The tagging process phase-shifts the photons due to the scattering by the displaced particles and the varying refractive index under the influence of ultrasound waves. The multiple scattered light form a temporally and spatially varying intensity pattern known as speckle at the point of observation. By examining the dynamics of the speckle pattern, the local information regarding the distribution (tissue structure) and dynamics of the scatterers can be extracted [Dainty 1975, Rabal 2009, Durduran 2010], whereby the emphasis in optical measurement is largely absorption monitoring [Wolf 2007]. However the major challenge in the AO measurement is the poor detection of the ultrasound modulated intensity, which has prevented this technique from clinical adoption [Wang 1995, Leveque 1999, Murray 2004, Sakadzic 2004, Li 2008, Xu 2010, Elson 2011].

The effects of the superficial region (SFR) in the AO measurement can be minimised. The most sensitive region of the AO measurement is generally believed to be re-locatable from the SFR to the deeper regions in tissue by repositioning the FUR in the ROI. Preliminary UOT studies have shown that the AO method has the potential to monitor chromophores' concentrations [Kim 2007, Bratchenia 2008, Bratchenia 2011] for tissue oxygenation mapping and monitoring. However, the AO method can also track optical scattering changes [Kothapalli 2007] and mechanical properties [Devi 2006, Devi 2008]. These capabilities allow the AO method to monitor localised tissue changes in High Intensity Focused Ultrasound (HIFU) therapy [Lai 2011], whereby cancerous tissue is ablated by intense focused ultrasound noninvasively. These lesions have

been shown to possess considerably higher optical absorption and scattering than normal tissue.

1.2 Thesis Aims

The overall aim of this thesis is to demonstrate that the AO measurement can improve upon the limitations of conventional optical measurement for potential tissue oxygenation and structural monitoring for clinical applications such as muscle and cerebral oxygenation measurement and HIFU therapy monitoring. To achieve this, the specific aims were as follows:

1. To map and compare the spatial sensitivity of the AO measurement and the optical measurements in response to a localised change in the optical absorption. The purpose of this comparison is to demonstrate that the region probed by the AO measurement can be relocated in a tissue mimicking phantom by repositioning the FUR in a predefined ROI. The spatial sensitivity maps can also provide information on the effects of the absorption changes occurring outside the ROI.
2. To map and compare the spatial sensitivity of the AO measurement and the optical measurements in response to a localised change in the optical scattering. This is important because HIFU lesions have been shown to have higher absorption and scattering than normal tissue. In conjunction with the results from the experiments carried out to achieve Aim 1, the scattering spatial sensitivity can provide information on the feasibility of the AO measurement to monitor these localised lesions, which are usually surrounded by normal healthy tissue.
3. To optimise the AO measurement method for a cylindrical geometry with pulsed-wave ultrasound. This is important because the majority of the AO studies in the literature have been conducted for a slab geometry in transmission mode, which is not representative of the real geometry of anatomical structures. Investigations in this area will be conducted to optimise the positioning of the optical probes and the parameters in the AO detection

method for a cylindrical geometry, which mimics the curvature of structures such as the limbs and head. In order to minimise the exposure of the laser light and the ultrasound waves, pulsed-wave ultrasound will be used. The feasibility of using a detection method based on the temporal intensity autocorrelation will also be investigated for the measurement of a pulsed-wave ultrasound generated AO signal.

1.3 Thesis Outline

The theoretical description of the optical and the AO principles are discussed in chapter 2 and 3 respectively. Chapter 2 introduces the basic principles of the optical measurement by using NIR light. It describes the mechanism of light propagation in tissue and the basic NIRS methods such as the differential and the spatially resolved methods. Descriptions of the NIRS spatial sensitivity and the maximum penetration depth studies are also presented. Chapter 3 starts by describing the propagation of ultrasound waves in tissue. It is followed by an introduction to laser speckle. Subsequently, the AO method is presented in detail and its biomedical applications are discussed.

The key components of the project are presented in chapters 4, 5, 6 and 7. Chapter 4 details the instrumentation and the development of phantoms for both optical and AO measurements. The basic AO measurements are also presented to demonstrate the effect of the acoustic magnitude and the basic parameters of the AO detection method, i.e. the measurement time and the operation mode.

Chapter 5 presents the comprehensive comparison between the spatial sensitivity of the optical and the AO measurements in response to a localised absorption change for potential tissue oxygenation monitoring. The chapter starts by presenting the control sensitivity measurement to assess the constraints of the optical and AO detections and the phantom design. It is followed by analysis of the optical and the AO spatial sensitivities in a pre-defined ROI and the SFR. Furthermore, multiple spatial sensitivity maps of the AO measurement are

presented for different locations of FUR. The strengths and the limitations of each method are discussed as well.

The analysis of the optical and AO spatial sensitivities when a localised change in the μ_s' is introduced in a tissue mimicking medium is described in chapter 6. The results are discussed in conjunctions with those from chapter 5 in order to verify the potential of the AO method for HIFU lesion monitoring.

Chapter 7 discusses that detection of AO signal in a cylindrical geometry using pulsed-wave focused ultrasound. The results of different optodes' positions are presented to demonstrate that the placement of the probes can be optimised for the AO measurement.

Finally, chapter 8 summarises the key contributions of this project. Proposals for further improvements to the work discussed in this thesis and future work are discussed as well.

2 Near Infrared Spectroscopy

It has been proposed that the AO method can potentially improve on conventional optical measurement techniques such as the Near Infrared Spectroscopy (NIRS). Furthermore, the performance of both methods will be compared by the investigation of their spatial sensitivities. The basic principles of NIRS and its limitations will be discussed in this chapter.

Figure 2-1 The absorption (μ_a) profiles of some tissue chromophores. [HbO_2: oxyhaemoglobin and Hb: deoxyhaemoglobin] [Durduran 2004]

Using NIRS to monitor human tissue oxygenation non-invasively was pioneered by Jobsis [Jobsis 1977]. NIRS exploits the low absorption of water and blood, which is the main constituent of human tissue, in the optical wavelength range of 650-950 nm. In this physiological window, which is shown in Figure 2-1, the NIR light can penetrate 1-2 cm into tissue [Wolf 2007]. Furthermore the absorption spectra of oxygenated and deoxygenated haemoglobins are distinct, which allow their concentrations to be measured. Figure 2-1 also shows that at wavelength 800 nm, the absorption coefficients (μ_a) of the oxy- and the deoxy-haemoglobins are the same, which is known as the isosbestic point.

However, light scattering is generally more dominant in human tissue than absorption. Thus light propagation in tissue is often modelled as a diffusive process, which forms the foundation of NIRS measurements. This enables the estimation of the concentration of tissue chromophores in the muscle and the brain in both adults and neonates. Furthermore, the blood flow can also be estimated by use of contrast agents or light fluctuation caused by the motion of red blood cells [Cheong 1990, Durduran 2004, Wolf 2007].

2.1 Light Propagation in Tissue

NIRS relies on the interaction of light with the tissue to provide spectroscopic information based on the optical properties of the medium. In this section, the mechanisms of light propagation in tissue are discussed.

2.1.1 Light Interaction with Tissue

2.1.1.1 Scattering

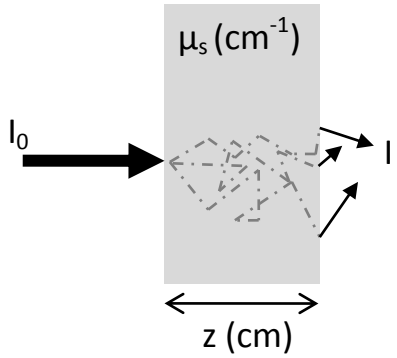

Figure 2-2 Light propagation through a homogeneous scattering medium

Light scattering is a phenomenon where the path of light propagation is no longer a straight path (of distance *z*) but the sum of random step sizes of each photon as shown in Figure 2-2. The random change in direction of propagation is caused by collision between photons and scattering particles in the medium. This change in propagation direction is caused by the refraction of light when the refractive index

of the scatterers is different from the medium. The process is elastic scattering when the energy of incident light is conserved or inelastic when some energy is lost or gained. The level of scattering depends on the optical wavelength and the size and geometry of the scattering particles.

The scattering property of a medium is described by the scattering coefficient μ_s (cm^{-1}), which is the probability of a photon will be scattered per unit propagation length. The reciprocal of the scattering coefficient is the scattering length, the average path length a photon travels between scattering events. If we consider only that each photon undergoes one scattering event for a collimated light source, I_0, is irradiated at a wholly scattering medium, the intensity $I(z)$ at the distance z is:

$$I(z) = I_0 e^{-\mu_s(\lambda)z} \tag{2-1}$$

And the attenuation due to the effect of scattering is:

$$A = ln\left(\frac{I_0}{I}\right) = \mu_s . z \tag{2-2}$$

The Mie theory is often used to explain the scattering of light by isotropic spherical particles within a homogeneous medium instead of Rayleigh's. This is because Rayleigh scattering is only applicable when the diameter of the scatterers is smaller than the wavelength of incident light. The Mie description does not have this limitation. Besides the stronger wavelength dependency, Rayleigh scattering tends to direct the scattered light more uniformly than Mie scattering, which tends to forward scatter. For a non-spherical scatterer, a combination of Rayleigh scatterers can be considered for particles of arbitrary geometry. Light propagation in turbid media such as biological tissue is typically anisotropic as they tend to forward scatter. This suggests that scattered light has directional preference depending on the incident angle.

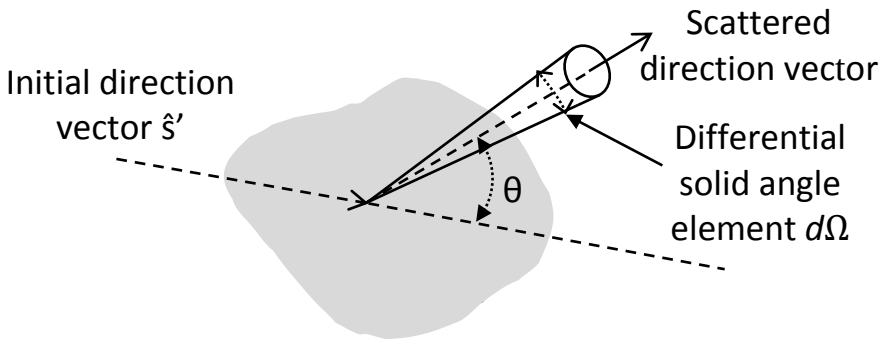

Figure 2-3 Phase function $p(\cos\theta)$ of the scattering angle

The measure of anisotropy of a highly scattering medium is defined by its anisotropy factor g (dimensionless). It is derived from mean cosine of the scattering angle θ [Wang 2007], which is shown in Figure 2-3:

$$g = \int_{4\pi} cos(\theta) \,.\, p\big(cos\,(\theta)\big).\, d\Omega$$

(2-3)

The phase function p is a probability density function of scattering from the initial direction ŝ is scattered into new direction ŝ. When g = 1, it means that the scattering is wholly forward; when g = -1, only backward scattering occurs. If g = 0, the light undergoes isotropic scattering. In biological tissue, the scattering is predominantly forward and g is between 0.7 and 0.9 [Niemz 2004, Tuchin 2007]. The scattering coefficient that is corrected by g is the reduced scattering coefficient μ_s', which is given by [Rabal 2009]:

$$\mu_s' = \mu_s(1 - g)$$

(2-4)

2.1.1.2 Absorption

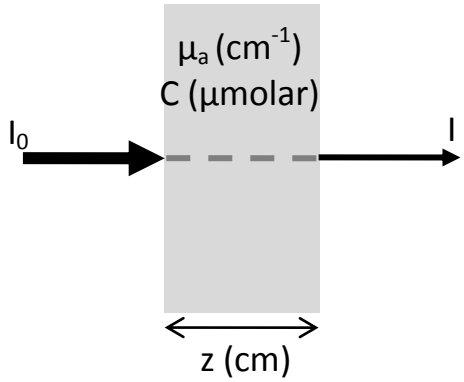

Figure 2-4 Light propagation through a homogeneous non-scattering medium, which contains an absorber of concentration C.

Figure 2-4 shows an idealized situation where a collimated beam of light, $I_{0,}$ of wavelength $\boldsymbol{\lambda}$ penetrates a homogeneous non-scattering medium of optical path-length z. From the Lambert's law:

$$I(z) = I_0 e^{-\mu_a(\lambda)z}$$

(2-5)

The reciprocal of the μ_a is the absorption length, which is defined as the mean distance a photon travels before absorption. Often it is very useful to express the μ_a in terms of the concentration of the absorber. According to the Beer-Lambert's law, the attenuation *A* (loss of light intensity due to absorption) measured in units of Optical Density (OD):

$$A = \log\left(\frac{I_0}{I}\right) = \varepsilon.C.z$$

(2-6)

$$A_{natural\ log} = \ln\left(\frac{I_0}{I}\right) = \mu_a.z$$

(2-7)

where ε is the specific extinction coefficient (cm^{-1} $\mu molar^{-1}$) and C is the concentration of absorber (μmolar). The same term can also be expressed as the specific absorption coefficient α (cm^{-1} $\mu molar^{-1}$), which is scaled by $\log_e$ (10). This is an issue of convention whereby the extinction coefficient is typically expressed in base 10 logarithm in equation (2-6) whilst the μ_a uses natural a logarithm in equation (2-5).

If the same slab geometry shown in Figure 2-4 is used but there is more than one type of absorber, the total absorption coefficient is the sum of product of each absorber's specific extinction coefficients and its corresponding concentrations.

When there are N chromophores, the attenuation is the linear sum of attenuation contribution of each type of chromophore, which is given by equation (2-8).

$$A = z \cdot \sum_{i}^{N} \varepsilon_i \cdot C_i$$

(2-8)

2.1.1.3 Total Attenuation Coefficient

In turbid media, such as biological tissue, both phenomena of absorption and scattering occur simultaneously. The combined light attenuation due to both absorption and scattering is defined by the total attenuation coefficient μ_t, which is the sum of μ_a and μ_s' as shown in equation (2-9). The total mean free optical path length is the reciprocal of the total attenuation coefficient.

$$\mu_t = \mu_a + \mu_s'$$

(2-9)

Another useful parameter is the *optical albedo* a, which is defined as:

$$a = \frac{\mu_s'}{\mu_s' + \mu_a}$$

(2-10)

When only scattering occurs, a = 1, and when the attenuation is wholly caused by absorption, a = 0.

2.1.2 Models of Light Transport

The interactions of light in a turbid medium can be explained mathematically by the Maxwell's equations [Hecht 2002, Chartier 2005]. But deriving an analytical solution from these equations is a complex problem. It is more practical to use the radiative transport theory, which is often described by the radiative transport equation (also known as the Boltzmann equation) [Wang 2007].

However, this radiative transport equation is difficult to solve due to the high number of unknowns. There are both analytical (such as Kubelka-Munk theory and the Diffusion Approximation) and stochastic (Monte Carlo method) solutions to the radiative transfer equations [Vo-Dinh 2003, Niemz 2004, Tuchin 2007, Wang 2007]. The diffusion approximation and the Monte Carlo method, which are widely adopted and verified, are briefly discussed here. The former is an approximation; therefore, it suffers from inaccuracy while the latter is an enormous computational task. The Hybrid Diffusion Theory and Monte Carlo Model [Wang 2007] attempts to fuse the benefits of the two techniques, namely accuracy and moderate computational load.

2.1.2.1 Diffusion Approximation

By assuming that the light propagation is isotropic in a medium where the light scattering greatly dominates the absorption ($\mu_s' >> \mu_a$), the radiative transport equation can be re-expressed into the diffusion equation, which is:

$$\frac{\partial \Phi(\vec{r},t)}{c\partial t} + \mu_a \Phi(\vec{r},t) - D\nabla^2 \Phi(\vec{r},t) = S(\vec{r},t) \tag{2-11}$$

where $\Phi(\vec{r},t)$: the fluence rate (W cm^{-2}); c: speed of light in medium (m/s); μ_a (cm^{-1}); $S(\vec{r},t)$: the flux of the light source (W.cm^{-2}); and D: the diffusion coefficient (cm^2/s), is given by:

$$D = \frac{1}{3(\mu_a + \mu_s')}$$

(2-12)

The diffusion approximation assumes that scattering strongly dominates the absorption. This is valid for most biological soft tissue in NIRS applications. For example: at optical wavelength 800 nm, the μ_s' and μ_a of healthy adult head are 9.4 and 0.16 cm^{-1} respectively. And the μ_s' and μ_a of healthy adult breast at 800 nm are 7.2-13.5 and 0.017-0.045 cm^{-1} respectively [Tuchin 2007]. Solutions to the diffusion equation can be derived analytically for simple geometry [Patterson 1989] or through computer simulations [Arridge 1993].

2.1.2.2 Monte Carlo Method

The Monte Carlo method is an iterative stochastic approach, used when solving a complex mathematical problem analytically, may be impractical. The general rules of the Monte Carlo simulation of light propagation in a turbid medium are detailed in the literature [Wang 1995, Wang 2007]. It is used to simulate each step of the photon random-walk path in a turbid medium. This method traces the optical path, *s*, of each photon within a predefined medium, which is defined by:

$$s = -\frac{\log_e \xi_0}{\mu_t}$$

(2-13)

Where ξ_0 is a pseudo-random number of uniform distribution.

After each path, *s*, the absorption reduces the weight of the photon and the photon is then scattered. The angle of scattering can be determined from the Henyey-Greenstein phase function [Wang 1995, Wang 2007]. The process is repeated until the criterion of photon termination is met i.e. its weight falls below certain threshold or escapes from the pre-defined boundaries of the medium. By capturing the escaped photons, the diffuse transmittance or reflectance of the medium can be estimated. However, the accuracy of this technique depends on the square root of the total number of simulated photons [Niemz 2004]. Therefore, it typically

requires hundreds of thousands to millions of photons to generate reasonably accurate simulation results depending on the nature of the application. This also means that it requires great amount of computational time.

The computation time can be reduced by distributed [Page 2006] or parallel computing approaches. Distributed computing splits the simulation between CPUs (central processing unit) of computers within a network. Parallel computing distributes the task among sub-processors of processor unit(s) of a computer. For example, by utilising the sub-processors of a three-dimensional graphic processing unit (GPU) [Alerstam 2008], the time required to simulate a million photons can be reduced from hours to minutes.

2.2 Near Infrared Spectroscopy Measurement

2.2.1 Differential Spectroscopy

The relationship of Beer-Lambert described by equation (2-6) or (2-7) assumes that the mean path length of a photon is *z*, which is shown in Figure 2-4. However, the actual mean path length is longer because of the scattering as shown in Figure 2-2. Furthermore, the additional attenuation due to scattering has not been taken in account. The modified Beer-Lambert equation attempts to reconcile the additional scattering effect and the complex geometry of human tissue by using the differential path length (DP), which is the mean path length *z* scaled by a differential path length factor (DPF) [Elwell 1995]. The modified Beer-Lambert equation is given by equation (2-14).

$$A = \ln\left(\frac{I_0}{I}\right) = \mu_a \cdot z \cdot B + G \tag{2-14}$$

where *B* is the DPF and *G* is the additional scattering and tissue geometry loss.

The DPF can be measured experimentally for different types of tissue [Delpy 1988, Van der Zee 1992, Arridge 1993] , but *G* is not known. Therefore equation (2-14) cannot be used directly to estimate the absolute concentration of

chromophores. But it can be used to estimate the change of concentration by considering the differential change of light attenuation ΔA, which is given by equation (2-15) whereby G is assumed to be constant throughout measurement and therefore can be cancelled.

$$\Delta A = \Delta \mu_a \cdot z \cdot B \tag{2-15}$$

And the change of concentration ΔC can be calculated from equation (2-16).

$$\Delta \mu_a = \varepsilon \cdot \Delta C \tag{2-16}$$

By employing M wavelengths, the concentration changes of N chromophores can be monitored by using equations (2-8), (2-15) and (2-16).

$$\begin{pmatrix} \Delta C_1 \\ \Delta C_2 \\ \vdots \\ \Delta C_N \end{pmatrix} = \frac{1}{z \cdot B} \begin{pmatrix} \varepsilon_{\lambda_1,1} & \cdots & \varepsilon_{\lambda_1,N} \\ \vdots & \ddots & \vdots \\ \varepsilon_{\lambda_M,1} & \cdots & \varepsilon_{\lambda_M,N} \end{pmatrix}^{-1} \cdot \begin{pmatrix} \Delta A(\lambda_1) \\ \Delta A(\lambda_2) \\ \vdots \\ \Delta A(\lambda_M) \end{pmatrix} \tag{2-17}$$

2.2.2 Spatial Sensitivity of Near Infrared Measurement

The main limitation of NIRS measurement is the complexity of human tissue, which is heterogeneous and multi-layered. NIRS measurement makes use of the diffusion approximation, which assumes that light propagation is isotropic in a homogeneous tissue, which is not always the case.

In cerebral monitoring, the diffusion approximation breaks down because of the cerebral spinal fluid (CSF) layer between the brain and the skull. This layer of clear fluid affects the light penetration depth across the brain. In this case, the Monte Carlo method [Firbank 1996] provides a better description of the light propagation in multi-layered model (including the CSF layer) than the diffusion approach. NIRS measures the optical property change in the sample volume where the light propagates from the optical source to the optical detector.

Simulation studies [Arridge 1995, Arridge 1995, Dehghani 2000, Okada 2003, Boas 2005] have shown that the NIR measurement is most sensitive to regions in the SFR of tissue in human heads, which is shown in Figure 2-5.

Figure 2-5 The spatial sensitivity (negative value depicts a drop in detected intensity): (a) an adult head by Monte Carlo simulation [Boas 2005]; (b) a neonatal head by finite-element method [Arridge 1995] (bright region denotes high sensitivity); (c) a multi-layered slab mimicking the adult head by Monte Carlo simulation [Okada 2003] (brigh region denotes high sensitivity); (d) adult head by finite element method [Dehghani 2000] (e) cross section of (d) with different optode separation distances.

2.2.2.1 Sensitivity Map

To investigate the NIR spatial sensitivity, Cui et al. [Cui 1991] experimentally measured the photon migration distribution of diffuse light and further study confirmed the 'banana' shape profile [Bruce 1994, Feng 1995] in simple homogenous reflectance geometry. This sensitivity profile [Boas 2005] or the photon measurement density function (PMDF) [Arridge 1995] can be mapped by introducing an optical defect within the tissue mimicking medium experimentally.

The spatial sensitivity at a specific position within a medium is defined as the change of detected measurement in response to a highly localised change in optical property in the same location when compared to reference measurement in the absence of the local perturbation. The sensitivity matrix $J_P(\boldsymbol{c}, \boldsymbol{s}, \boldsymbol{d})$ of mechanism P (e.g. absorption or scattering) at location $\boldsymbol{c}$ within the target medium, measured at location $\boldsymbol{d}$ with a light source at location $\boldsymbol{s}$; can be generalised into the following equation (2-18): [Arridge 1995, Firbank 1998, Ono 2000]

$$J_P(\boldsymbol{c}, \boldsymbol{s}, \boldsymbol{d}) = \frac{\Delta f_M(\boldsymbol{d})}{\Delta f_P(\boldsymbol{c})} \tag{2-18}$$

where Δf_M: the change in measured quantity e.g. the fluence and the intensity (in their respective units) and Δf_P: the difference between P value (e.g. the optical properties in their respective units) of the in-homogeneity and the background.

An example of absorption Jacobian for different optical source-detector separation is shown in Figure 2-6 [Arridge 1995, Boas 2005]. If J_P is known, Δf_P can be estimated from Δf_M (inverse Jacobian) [Arridge 1999, Boas 2005]. In tomographic image reconstruction, the Jacobian is iteratively updated in order to match Δf_M before Δf_P can be calculated.

Figure 2-6 The absorption sensitivity matrix of a homogeneous turbid medium (diameter 8 cm) of μ_s' and μ_a of 20 and 0.1 cm^{-1} respectively in: (a) reflection and (b) transmission modes (bright region denotes high sensitivity).

2.2.2.2 Photon Path Distribution

When the optical parameter is absorption and $\Delta f_{\mu_a}(\boldsymbol{c})$ in equation (2-18) is very large, $J_{\mu_a}(\boldsymbol{c}, \boldsymbol{s}, \boldsymbol{d})$ can be interpreted as the photon path distribution in a homogeneous semi-infinite medium and the diffusion approximation is valid [Fantini 1995]. Because of the very high absorption at position $\boldsymbol{c}$, photons that propagate through are absorbed. Thus the observed drop of measured intensity, $\Delta f_{\text{intensity}}(\boldsymbol{d})$, is proportional to the amount of photons that have similar path length [Del Bianco 2002]. By systematically relocating the local absorber throughout the medium, the photon path length distribution $J_P(\boldsymbol{s}, \boldsymbol{d})$ is generated.

2.2.2.3 Penetration Depth

The photon path distribution or the sensitivity map is often used in simulation studies (Figure 2-5) and reconstruction of optical images in imaging [Arridge 1999, Carraresi 2001, Gibson 2005, Ueda 2005]. Alternatively it can be used to assess the performance of the optical measurement system by experimentally mapping the spatial sensitivity map shown in Figure 2-6. One measure often used is the maximum penetration depth [Vaithianathan 2004, Correia 2009, Patil 2011] or the mean penetration [Del Bianco 2002] from the spatial sensitivity of the system. The maximum penetration depth is the deepest location within a medium whereby an optical change can still be measured.

Correia et al. [Correia 2010] used a predefined threshold value of penetration depth in order to identify the optimal optical wavelengths for optical topography. Patil et al. [Patil 2011] mapped the 3-D spatial sensitivity profile, which is shown in Figure 2-7. They also used the threshold approach to identify the maximum penetration depth of different source-detector separations. Vaithianathan et al. [Vaithianathan 2004] defined the penetration depth of their portable topography system when the sensitivity drops to the baseline level (or noise floor, whereby no change is detected). Alternatively, the mean penetration depth [Del Bianco 2002] can be calculated.

Figure 2-7 The 3-D spatial sensitivity map of the optical measurement when the source-detector spacing is 20 mm [Patil 2011].

2.2.3 **Spatially Resolved Spectroscopy**

The differential spectroscopy method can measure the changes in concentrations of the tissue oxy- and deoxy-haemoglobins. However, it cannot measure the absolute concentration or the tissue oxygen saturation (S_tO_2) or the tissue oxygenation index (TOI), which is the ratio of concentration of oxy-haemoglobin to the total concentration of oxy- and deoxy-haemoglobin. The Spatially Resolved Spectroscopy (SRS) [Matcher 1995, Delpy 1997] can be used to probe the absolute measurement of S_tO_2. This technique employs multiple detectors at

different separation distance ρ (mm) from the optical source. One example of such setup [Suzuki 1999] is shown in Figure 2-8 (a).

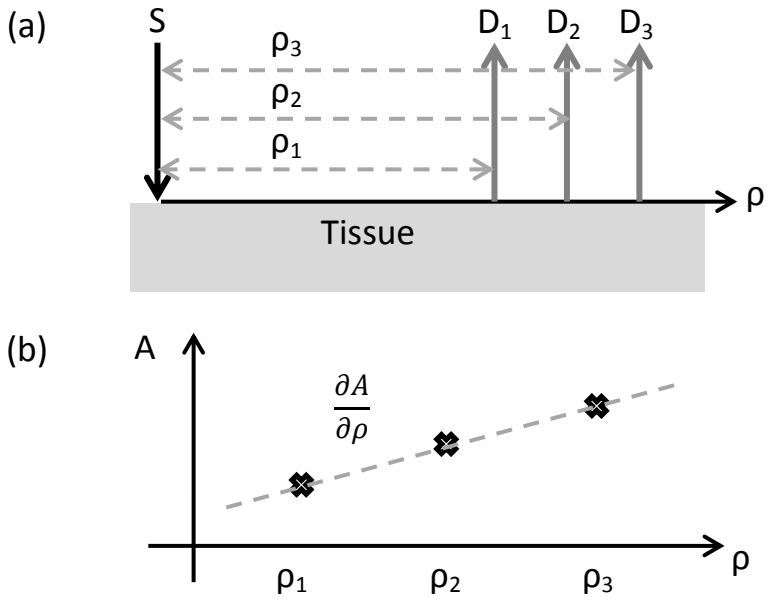

Figure 2-8 The basic optodes setup (a) of the spatial resolved spectroscopy and (b) the gradient of attenuation, $\frac{\partial A}{\partial \rho}$, which can be estimated by linear regression. [S: the optical source; D: the optical detectors; ρ: the optodes separation]

In SRS, the attenuations measured at the optical detectors are used to calculate an attenuation gradient shown in Figure 2-8 (b) by linear regression, which can be converted to the *scaled* μ_a, i.e. $k{\cdot}\mu_a$ (k is a constant). The relationship between $k{\cdot}\mu_a$ and the attenuation slope is described by equation (2-19) [Suzuki 1999], which is derived from a solution to the diffusion approximation for a semi-infinite medium [Patterson 1989].

$$k \cdot \mu_a = \frac{1}{3(1-h\lambda)}\left(\ln 10 \cdot \frac{\partial A}{\partial \rho} - \frac{2}{\rho}\right)^2 \tag{2-19}$$

where $\frac{\partial A}{\partial \rho}$ is the gradient of attenuation (O.D/mm) in logarithm base 10, λ is the optical wavelength (nm) and *h* is the constant of wavelength dependency of tissue scattering (6.3×10^{-4} mm^{-1}/nm) [Matcher 1997].

By employing equation (2-16) and multiple wavelengths, the *scaled* concentrations of oxy and deoxy-haemoglobins, $k \cdot O_2Hb$ and $k \cdot HHb$ respectively, can be calculated from equation (2-20) [Suzuki 1999].

$$\begin{bmatrix} k \cdot O_2Hb \\ k \cdot HHb \end{bmatrix} = [\boldsymbol{\varepsilon}_{i,j}]^{-1}[k \cdot \boldsymbol{\mu_a}(j)] \tag{2-20}$$

where $\boldsymbol{\varepsilon}_{i,j}$ is the extinction coefficient of chromophore *i* at wavelength *j*, $k \cdot \boldsymbol{\mu_a}(j)$ is the $k \cdot \mu_a$ at wavelength *j*, *i* = O_2Hb, HHb and *j* = λ_1, λ_2, λ_3. The TOI (%) can then be calculated from equation (2-21) [Suzuki 1999] where the unknown *k* is cancelled out.

$$TOI = \frac{k \cdot O_2Hb}{k \cdot O_2Hb + k \cdot HHb} \times 100\% \tag{2-21}$$

Examples of commercially available NIRS tissue oxygenation monitors that use this technique are the Hamamatsu NIRO series systems [Suzuki 1999] and the Artinis PortaMon system [Buchheit 2009].

3 Acousto-Optics: Ultrasound Modulation of Light

This chapter discusses the principles of the AO measurement. It starts by presenting a brief overview of ultrasound propagation in soft tissue, and is followed by a description of laser speckle and subsequently ultrasound modulated speckle with its biomedical applications.

3.1 Ultrasound Propagation in Tissue

3.1.1 Basic Principles of Ultrasound Propagation

Ultrasound is sound waves whose frequency exceeds the maximum frequency of audible sound, which is approximately 20 kHz in human. Ultrasound waves exhibit high (compression) and low (rarefaction) pressure due to the mechanical vibration of the particles within a medium in the longitudinal or transverse direction with respect to the direction of the propagation.

The speed of ultrasound propagation c_a (m/s) depends solely on the type of material meaning that it is always the same for a specific material [Hedrick 2005], which is given by equation (3-1):

$$c_a = \sqrt{\frac{K_m}{\rho_m}} \tag{3-1}$$

Where K_m is the bulk modulus of material (Pa) and ρ_m is the equilibrium density of material (g/m^3). The bulk modulus is a measure of stiffness of the medium. The basic acoustic properties of different materials are presented in Table 3-1. The acoustic impedance Z_a (rayls) is given by:

$$Z_a = \rho_m c_a$$

(3-2)

When ultrasound propagates from one layer of tissue to another, it may be transmitted, reflected or refracted depending on the difference of Z_a between the two layers. The higher degree of mismatch between the Z_a, the less ultrasound is transmitted. Thus ultrasound coupling gel is used to interface the ultrasound transducer and tissue in order to minimise the mismatch between the media.

Table 3-1 The ultrasound velocity and acoustic impedance of different materials [Hedrick 2005].

The magnitude of instantaneous ultrasound wave is given by its instantaneous sound intensity i_a, (W/m^2) which is given by equation (3-3).

$$i_a = \frac{{p_i}^2}{\rho_m c_a}$$

(3-3)

Where p_i is the instantaneous pressure (Pa), ρ_m is the density of material (g/m^3) and c_a is the acoustic velocity (m/s). Alternatively, the sound intensity can be expressed as time integrated intensity I_a (W/m^2), which is shown in equation (3-4).

$$I_a = \frac{{P_{peak}}^2}{2\rho_m c_a} \tag{3-4}$$

Where P_{peak} is the peak ultrasound pressure (Pa) and the sound power P_W (W) is given as the product of sound intensity I_a and the cross-sectional area A_s (m^2) of the irradiated region, which is shown in equation (3-5). Examples of the level of intensities used in some clinical situations are summarised in Table 3-2.

$$P_W = I_a \cdot A_s \tag{3-5}$$

Table 3-2 Ultrasound intensities in medicine [Ziskin 1993].

When ultrasound propagates in a medium, its peak pressure is attenuated because of absorption and scattering as shown in equation (3-6). The attenuation of a material depends on the irradiating ultrasound frequency. The higher the ultrasound frequency, the higher the attenuation,

$$P_{peak} = P_0 e^{-A_a z} \tag{3-6}$$

where P_0 is the initial peak pressure (Pa); A_a is the acoustic attenuation (Np/cm) at acoustic frequency, f_a, which is the sum of acoustic absorption and scattering coefficients; and z is the propagated distance. The attenuation of some human tissue at 1 MHz is shown in Table 3-3. The brain tissue has A_a of 0.098 Np/cm when f_a is 1 MHz. If f_a is 2 MHz, A_a of the brain is the product of 0.098 Np/cm/MHz and 2 MHz; which is 0.196 Np/cm. Similar conclusions can be drawn for other tissue types whereby their attenuations increase when f_a increases. This also means that a higher f_a ultrasound beam has a poorer penetration depth than that of lower f_a due to the higher A_a.

Table 3-3 The acoustic attenuation of some human tissue at the acoustic frequency f_a of 1 MHz [Hedrick 2005].

3.1.1.1 Particle Displacement Due to Ultrasound

As the ultrasound propagates within a medium, the particle within the medium is displaced by the pressure waves. In human tissue, the particles typically oscillate in the direction of propagation and the magnitude of the displacement velocity u_a (m/s) is given by equation (3-7) [Kinsler 1982].

$$u_a = \frac{\partial \xi}{\partial t} \tag{3-7}$$

where ξ is the particle displacement (m); t is time (s); equation (3-7) can be re-written into equation (3-8) [Humphrey 2007].

$$u_a = 2\pi f_a \xi_a$$

(3-8)

The relationship between the peak acoustic pressure and particle velocity is shown in equation (3-9):

$$u_a = \frac{P_{peak}}{\rho_m c_a}$$

(3-9)

So the maximum particle displacement ξ_a (m), which is also referred to as the acoustic amplitude, is given by equation (3-10):

$$\xi_a = \frac{P_{peak}}{2\pi f_a \rho_m c_a}$$

(3-10)

3.1.1.2 Change of Optical Refractive Index due to Ultrasound

When an illuminated homogeneous liquid or gaseous medium is irradiated by planar ultrasound waves, the medium behaves like an optical diffraction grating due to the change in local density. This effect was originally theorised by Brillouin [Chartier 2005]. In other words, the medium becomes parallel layers of different refractive indices according to the acoustic pressure waves, which is depicted in Figure 3-1. Optical grating by ultrasound is typically categorized into two regimes, the Raman-Nath [Raman 1935, Raman 1935] and Bragg effects [Klein 1967].

The Raman-Nath optical grating diffracts incident light into multiple observable beams from an arbitrary incident angle θ_a. On the other hand, the Bragg regime diffracts the incident light at a specific Bragg angle θ_B into a single diffracted beam besides the transmitted or refracted main beam. The defining characteristics for the two regimes are the thickness of the diffraction grating, which depends on the acoustic beam width; and the wavelength of the acoustic waves. The criteria for the Raman-Nath regime are large acoustic wavelength and thin grating. The

Bragg diffraction typically occurs at low acoustic wavelength and thick grating [Klein 1967, Moharam 1978, Kwiek 1996].

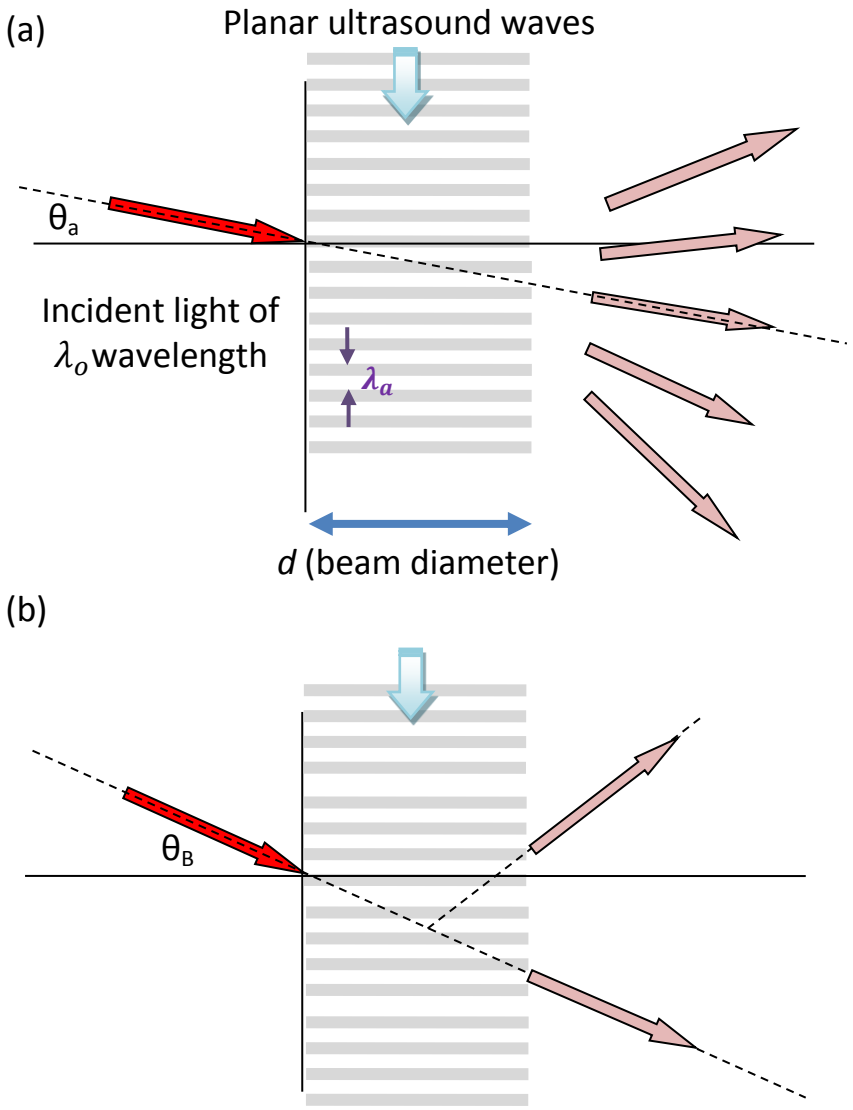

Figure 3-1 The Brillouin diffraction of light: (a) Raman-Nath effect and (b) the Bragg effect.

The optical diffraction regime is characterized by the Klein-Cook parameter Q [Klein 1967] as defined by equation (3-11). The parameter Q must be much smaller than 1 ($Q \ll 1$) for Raman-Nath regime, while the opposite means the

diffraction occurs in the Bragg regime ($Q \gg 1$) [Klein 1967, Moharam 1978, Kwiek 1996].

$$Q = \frac{2\pi\lambda_o d}{n_o {\lambda_a}^2}$$

(3-11)

where n_o: refractive index of medium; λ_o: optical wavelength (m); λ_a: acoustic wavelength (m); d: ultrasound beam diameter (FUR diameter) (m).

The relationship between the change of the refractive index Δn (dimensionless) and the ultrasound waves is given by equation (3-12),

$$\Delta n = \frac{T_{PE} \cdot n_0^3 \cdot \xi \cdot k_a}{2}$$

(3-12)

where T_{PE} is the material specific photoelectric tensor in arbitrary unit (a.u.); n_o: background refractive index; ξ: particle displacement (m); and k_a: the acoustic wave number (m^{-1}). Alternatively, the rate of change of refractive index by ultrasound pressure can be expressed directly as the adiabatic piezo-optic coefficient $\frac{\partial n}{\partial p}$ [Raman 1939], which can be directly to be determined from measurement.

3.1.1.3 Safety

Ultrasound waves are generally harmless (non-ionizing) when used for routine diagnostic purposes in adult. Therapeutic ultrasound, such as HIFU for example, exceeds the ultrasound dosage (the amount of acoustic energy is absorbed from the ultrasound exposure) [Duck 1987] that causes tissue damage. The ultrasound dosage depends on the type of tissue (absorption), the properties of the ultrasound beam (for example: size, frequency, intensity, continuous or pulsed), and the exposure time. In diagnostic ultrasound, the intensity exposure limits for different tissue types are summarised in Table 3-4 [Barnett 2000].

Table 3-4 The application specific maximum allowable I_{SPTA} (spatial-peak and time-averaged intensity [Hedrick 2005]) in diagnostic ultrasound by the Food and Drug Administration (FDA) and Output Display Standard (ODS), which is a voluntary scheme adopted by the American Institute of Ultrasound in Medicine and the National Electrical Manufacturers' Association. [Barnett 2000]

Alternatively, the unit-less mechanical index (MI) [Hedrick 2005] can be used and it is described by equation (3-3).

$$MI = \frac{C_{MI} p_{r\cdot 3}}{\sqrt{f_a}} \tag{3-13}$$

where C_{MI} is a constant and is equal to (1 MHz)$^{0.5}$/(1 MPA); $p_{r\cdot 3}$ is the derated peak negative pressure (MPa) in water, which can be calculated by equation (3-14); and f_a is the centre frequency of the ultrasound transducer (MHz).

$$p_{r\cdot 3} = p_r \mathrm{e}^{-A_a f_a z_a} \tag{3-14}$$

where p_r is the peak negative (rarefaction) pressure (MPa); A_a is the acoustic attenuation of water (0.035 Np/cm/MHz) and z_a is the distance between the point of interest and the ultrasound source (cm).

The maximum MI limit set by the FDA is 1.9 [Hedrick 2005]. This means that for f_a = 1 MHz and a focal distance 6.35 cm, the maximum allowed peak negative

pressure is 2.37 MPa. And for f_a = 0.66 MHz and a focal distance 7.26 cm, the maximum allowed negative peak negative pressure is 1.79 MPa.

3.2 Laser Speckle

3.2.1 Static and Dynamic Speckle

The speckle pattern featured in Figure 3-2 is the result of constructive and destructive interference of scattered light at the optical detector when a rough static surface is irradiated by a coherent light source. Such speckle pattern is stationary (non-time varying) and its granular pattern consists of spatially varying intensity from dark to bright spots. The bright spots are often referred to as speckle grains.

Figure 3-2 An image of the laser speckle pattern [Rabal 2009]

The dynamic speckle pattern is formed at the detector when the coherent light is reflected off a moving rough surface or when it is multiple scattered within a diffusive medium, which contains particles in motion. This temporally and spatially varying speckle pattern can be analysed spatially or temporally for an ergodic system. The spatial variation has been used to image capillary blood flow in superficial layer of human tissue such as Laser Doppler flowmetry [Bonner 1981, Briers 2001] and Laser Speckle Contrast imaging [Boas 2010]. Diffuse Correlation Spectroscopy (DCS) [Pine 1988, Yodh 1992, Boas 1997, Li 2005, Carp 2011] records the temporal fluctuations to provide a measure of change in

volumetric blood flow in deeper tissue regions. The speckle pattern can also be used in structural imaging, i.e. Optical Coherence Tomography [Huang 1991].

3.2.2 **Speckle Dimension**

The size of speckle is defined as the average distance between the maximum intensity and the adjacent minimum on the speckle pattern [Dainty 1975]. By using the same principle of Airy pattern formation [Hecht 2002], the transverse size [Li 1992] of the speckle D_s from the specular reflection of coherent light from a circular diffusing surface in the Fraunhofer region (far-field) [Dainty 1975, Hecht 2002], which is shown in Figure 3-3, is given by equation (3-15):

$$D_s \approx \frac{1.2\lambda_o L}{D} \tag{3-15}$$

where λ_o: Optical wavelength (m); L: Distance between detection plane and diffuser (m); D: Detection aperture diameter (m).

For an optical fibre detector, the light detection depends on its numerical aperture (NA), which is shown in equation (3-16), in the absence of a physical aperture.

$$NA = n_o \sin\theta_s \tag{3-16}$$

where n_o: ambient refractive index (dimensionless); $\sin\theta_s \approx \frac{D/2}{2}$ when θ_s is small (small angle approximation). Equation (3-15) can then be written into [Dainty 1975]:

$$D_s \approx \frac{0.6\lambda_o}{NA} \tag{3-17}$$

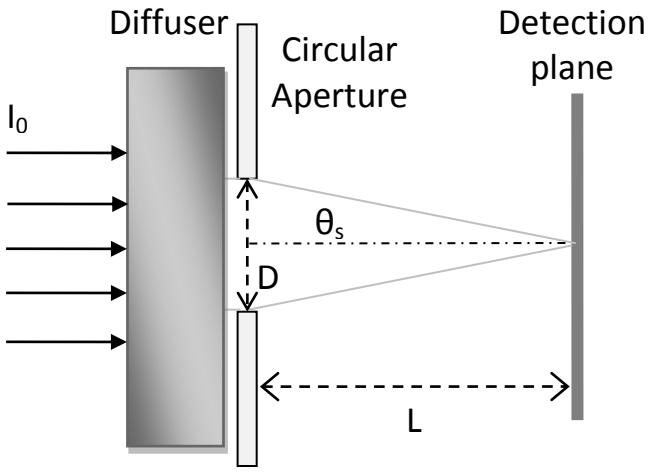

Figure 3-3 Formation of specular speckle pattern by a diffusing surface through a circular aperture

The speckle dimension in the near-field configuration (Fresnel regime) [Dainty 1975, Hecht 2002] can still be estimated using equation (3-15) [Chu 2007, Gatti 2008]. The Fresnel and Fraunhofer zone can be differentiated by the Fresnel number F_N, which is defined by: [Hecht 2002, Goodman 2005]

$$F_N = \frac{\left(\frac{D}{2}\right)^2}{L\lambda_0} \tag{3-18}$$

where $F_N \geq 1$: near-field and $F_N \ll 1$: far-field.

[For example: for the wavelengths 632.8 and 808 nm and a single mode fibre as detector (typical NA ≈ 0.11 [Sterling 2003]) and n_o = 1 (air), the estimated average speckle sizes are about 4 and 5 μm respectively by using equation (3-17); which are smaller than the fibre core diameter of 9 μm. Therefore the possibility of spatial averaging of the speckle intensity cannot be completely ruled out.

When the detection plane is in direct contact with the medium, the speckle are in the deep Fresnel zone (very close to or directly on the surface of the diffusing medium), which can be estimated by equation (3-19) [Gatti 2008]:

$$L_{DFZ} < \frac{\phi_0 D_s}{\lambda_0} \tag{3-19}$$

where L_{DFZ}: distance from sample to optical detector (m); D_s: speckle size (m); λ_0: optical wavelength (m); ϕ_0: speckle dimension in the speckle source plane (surface of the diffuser) (m).

The source plane speckle (speckle formed at the surface of the medium when L = 0 in Figure 3-3) dimension ϕ_0 depends on the size of the scatterers, the roughness of the source plane and D_s [Gatti 2008]. And the average speckle dimension D_s is approximately equal to ϕ_0 [Giglio 2001, Gatti 2008] in the deep Fresnel zone, which can only be accurately estimated from measurements [Magatti 2009]. And assuming that ϕ_0 depends greatly on the diameter of the scatterers [Giglio 2001], $D_s \approx \phi_0$.

3.2.3 Temporal Intensity Autocorrelation Function of Dynamic Speckle

When a monochromatic coherent light source illuminates a slab of scattering medium as shown in Figure 3-4, the temporal autocorrelation of the electric field of multiple scattered light at one detection point is given by [Leutz 1995]:

$$G_1(\tau) = \langle E_s(t) E_s^*(t+\tau) \rangle \tag{3-20}$$

where G_1: electric field autocorrelation function; $E_s(t)$: electric field of scattered photon propagated through path length *s*.(V.m^{-1}); τ: lag time (s); *t*: time (s).

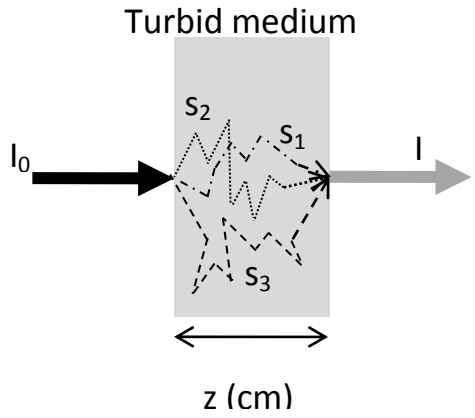

Figure 3-4 Multiple scattered photons propagate through different path length *s* in a turbid medium.

According to the weak scattering approximation [Leutz 1995], photons that propagate through the same path length strongly correlate with each other when the optical wavelength is very small compared to the mean free path, so equation (3-20) can be re-written into equation (3-21) [Leutz 1995]:

$$G_1(\tau) = \int_z^{\infty} p(s)\langle E_s(t)E_s{}^*(t+\tau)\rangle ds \tag{3-21}$$

where $p(s)$ is the probability density function of light propagating through the path length s and E_S^*: complex conjugate of E_s.

By using the Siegert relation (Li 2005), the electric field autocorrelation function can then be calculated from the normalised temporal intensity autocorrelation computed by using equation (3-22).

$$g_2(\tau) = 1 + \beta|g_1(\tau)|^2 \tag{3-22}$$

where β: dimensionless coherent factor depending on experimental setup; g_1: the normalised electric field autocorrelation function; g_2: the normalised intensity

autocorrelation function measured by DCS, which can be described by the following equation (3-23):

$$g_2(\tau) = \frac{\langle I(t)I(t+\tau)\rangle_{t_\int}}{\langle I(t)\rangle_{t_\int}^2} \tag{3-23}$$

where $\langle I(t)\rangle_{t_\int}$ is the time averaged intensity over the integration time of the autocorrelation function, $t_\int$, which is also the measurement time. The coherent factor is a weighting factor, which depends on the experimental configuration. It can be assumed to the unity when the detection aperture is smaller than the dimension of the speckle [Tuchin 2007].

The dynamism of the speckle can be derived from the rate of the exponential decay of the autocorrelation curve whereby faster scatterers produces faster decay rate [Bonner 1981]. The decay is often referred to as the decorrelation of the speckle and it can be quantified as the decorrelation time [Rajan 2008]. The decorrelation time is the lag time when the speckle intensity loses its correlation (when $g^{(2)}$ drops from 1 to $\frac{1}{e}$). A fluid medium that consists of fast moving scatterers possesses fast decorrelation time and a diffusive solid medium has a very slow decorrelation time.

3.2.4 Spatial Measurement of Dynamic Speckle: Speckle Contrast

The speckle contrast K_s is the measure of the spatial 'blurriness' [Boas 2010] of the speckle pattern captured by a detector such as the CCD camera. The blurring is observed when the intensity of the captured light is integrated over the recoding time (exposure time [Yuan 2005]) of the CCD camera. The blurring is caused by the average of the intensity variation due to the Doppler Effect on the multiple-scattered light from the moving scatterers. The faster the motion of scatterers, the more blurring is induced. K_s is defined as the ratio of the spatial standard deviation

σ_s (counts) of the speckle intensity to the mean speckle intensity $\langle I_s \rangle$ (counts), which is shown in equation (3-24).

$$K_S = \frac{\sigma_s}{\langle I_s \rangle} \tag{3-24}$$

This means that the smaller the speckle contrast, the faster the scatterers are moving. When $K_S = 1$, the scatterers are not moving.

3.3 Ultrasound Modulated Speckle

The mechanism of ultrasound modulation of multiple scattered light was first provided by Leutz and Maret [Leutz 1995], which provides both analytical and experimental solutions of the AO effect. However, this early model only considers the displacement of particle under the influence of ultrasonic waves in a slab geometry in transmission mode. Kempe et al. [Kempe 1997] subsequently demonstrated the AO effect by using a quasi-continuous- ultrasound waves and suggested that the dominant factor was the phase accumulation due to the scatterers' displacements. Alternatively, this effect can also be considered as the minute change in the photon frequency due to the collision with the ultrasound displaced scatterers (Doppler Effect) [Briers 1996]. Mahan et al. [Mahan 1998] described the coherent AO effect as a function of light intensity changes due to optical diffraction where the mean free path is smaller than the acoustic wavelength. A more comprehensive description of the coherent AO effect of both particle displacement *and* refractive index variation was provided by Wang [Wang 2001, Wang 2001].

There are three established mechanisms that govern the ultrasound modulation of multiple scattered coherent light in the literature:

1. Optical property (μ_a, μ_s' and index of refraction) variation due to change in a local medium density under the influence of ultrasonic perturbations [Mahan

1998]. Coherent light is not needed theoretically but it is too weak to be detected experimentally [Wang 1997].

2. Optical phase changes due to the displacement of local scatterers as a result of the ultrasonic wave propagation [Leutz 1995]. The motion of the scatterers is assumed to follow the acoustic pressure wave, which in turn modulates the light physical path length when the photon collides with the displaced scatterers. This means that the fluctuation of speckle intensity is modulated by the ultrasound wave. This mechanism requires coherent light.

3. Optical phase changes due to ultrasound modulation of index of refraction [Wang 2001]. This results in modulation of phase of light between consecutive scattering events, which is then observable in the fluctuation of speckle intensity. This too requires coherent light.

3.3.1 Incoherent Effects

The first mechanism is the variation of optical properties of a medium under the perturbation of ultrasonic waves has been modelled analytically by Mahan et al. [Mahan 1998]. This effect is often known as the *non-phase* or *incoherent* mechanism because it does not require a coherent light source. This model assumes Brillouin scattering [Hecht 2002, Chartier 2005], which is the optical diffraction of light by ultrasonic waves that induces phase shifts in the propagating light waves. However, this model only considers the effect of density variations of medium on light scattering when the scattering length of the turbid medium is small compared with the wavelength of the acoustic waves.

However, attempts to detect the AO signal due to this mechanism by using incoherent light source have not been successful [Wang 1997], which suggests that this effect might be too minute to be detected in comparison to the coherent mechanisms.

In recent developments of AO theory, Liu et al. [Liu 2008] and Bal et al. [Bal 2010] propose new theories on *non-phase* mechanisms. The modulation of the refractive index under ultrasonic perturbation, as described by Wang, assumes straight-line path lengths between scattering events within a turbid medium. Liu et al. [Liu 2008] suggest that the optical grating effect would cause curvature of the scattering paths, which in turn would result in a variation in the modulated signal as a function of amplitude and photon exit location. Bal et al. [Bal 2010] further suggest that it is possible to extract the optical properties of the medium by considering the incoherent AO effect as an inverse problem.

3.3.2 **Coherent Effects**

The second and third mechanisms described above have been fairly well described in the literature [Leutz 1995, Lev 2000, Granot 2001, Wang 2001, Wang 2001, Sakadzic 2002, Blonigen 2005, Sakadzic 2005, Sakadzic 2006] and are generally referred to as the *phase* or *coherent* mechanisms of the AO effect. These two mechanisms are also known as the coherent mechanisms because the coherent light is required to observe them experimentally. Granot et al. [Granot 2001] also analytically modelled the modulated light intensity as a function of the geometric arrangement between the ultrasound transducer and the optical detector. Devi et al. [Devi 2006] followed by suggesting that besides the variation in optical properties, the mechanical properties of the medium should not be neglected.

Elazar et al. [Elazar 2008] suggested that the minute deviation in the optical wavelength of the photons (Doppler effect) due to the collision with ultrasound mediated particle motion is not analogous to the phase change due to the scatterer displacement, which is contradictory to Briers' description [Briers 1996]. According to Briers, the effects of the photon collision with a moving scatterer measured in two different domains, the Fourier domain (the Doppler effect) and the temporal domain (time-varying speckle intensity), are equivalent and therefore must not be superimposed in Laser Doppler Flowmetry.

This section describes AO phase modulation of coherent light due to the ultrasonic displacement of scattering particles and variations in the refractive index, based on the models of Wang and Sakadzic. It starts with a simple model based on purely isotropic scattering medium without optical absorption before moving on to a more realistic model, which incorporates anisotropic scattering, absorption and Brownian motion of scatterers.

3.3.2.1 Isotropic Medium

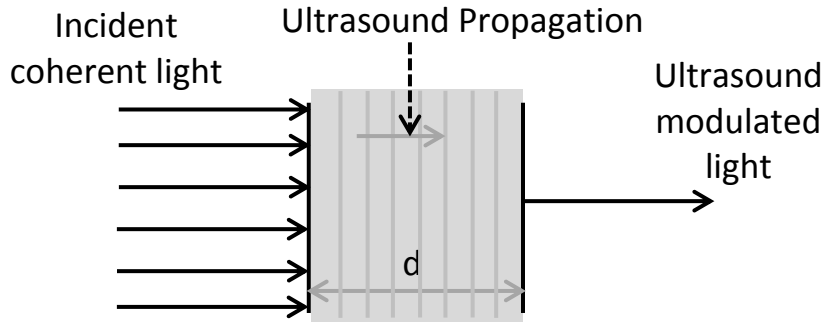

Figure 3-5 A semi-infinite slab medium, which is wholly irradiated by uniform plane ultrasound wave.

If the effect of the Brownian motion is ignored, the phase variation of the photons under ultrasound modulation is the sum of the phase variation due to refractive index changes and scatterers' displacements. So, equation (3-21) can be rewritten into for *j*-path:

$$G_1(\tau) = \int_0^\infty p(s)\left\langle \mathrm{e}^{-\mathrm{i}\Delta\phi(t,\tau)}\right\rangle ds \tag{3-25}$$

$$\Delta\phi(t,\tau) = \Sigma_j^N \Delta\phi_{n_j}(t,\tau) + \Sigma_j^{N-1}\Delta\phi_{\mathrm{d}j}(t,\tau) \tag{3-26}$$

where $\Delta\phi$: total phase variation due to ultrasound modulation

$\Delta\phi_{n_j}$: phase variation due to refractive index changes

$$\Delta\phi_{n_j}(t,\tau) = \phi_{n_j}(t+\tau) - \phi_{nj}(t)$$

(3-27)

$\Delta\phi_{dj}$: phase variation due to scatterers' displacement

$$\Delta\phi_{d_j}(t,\tau) = \phi_{d_j}(t+\tau) - \phi_{dj}(t)$$

(3-28)

N: total number of free paths.

According to Wang [Wang 2001], ϕ_{n_j} and ϕ_{dj} can be defined by the following equation (3-29) and equation (3-30):

$$\phi_{nj}(t) = 2n_0k_0\eta A \sin\left(\boldsymbol{k}_a \cdot \boldsymbol{r}_{j-1} + \frac{k_a l_j \cos\theta_j}{2} - \omega_a t\right) \times \frac{1}{\cos\theta_j} \sin\left(\frac{k_a l_j \cos\theta_j}{2}\right)$$

(3-29)

$$\phi_{\mathrm{d}j}(t) = -n_0k_0\left(\hat{\boldsymbol{k}}_{j+1} - \hat{\boldsymbol{k}}_j\right) \cdot \boldsymbol{A} \sin\left(\boldsymbol{k}_a \cdot \boldsymbol{r}_j - \omega_a t\right)$$

(3-30)

where n_0: refractive index of medium

k_0: optical wave number (rad/m)

η: elasto-optical coefficient of the medium, which is given by:

$$\eta = \frac{\partial n}{\partial p}\rho {c_s}^2$$

(3-31)

$\frac{\partial n}{\partial p}$: adiabatic piezo-optical coefficient of the medium (m^2/N)

ρ: density of medium (kg m^{-3})

c_s: speed of sound in the medium (m/s)

A: acoustic amplitude (m)

$\boldsymbol{k}_a$: acoustic wave vector

$\boldsymbol{r}_j$: position of the j-th scatterer

k_a: acoustic wave number (rad/m)

l_j: length of *j*-th free-path

θ_j: angle between the j-th free path optical and acoustic wave vectors (rad)

ω_a: angular acoustic frequency (rad/s)

$\hat{\boldsymbol{k}}_j$: unit optical wave vector of j-th free path

$\boldsymbol{A}$: acoustic amplitude vector

The probability density function $p(s)$ can be derived from the diffusion approximation [Wang 2001] by assuming zero-boundary conditions [Patterson 1989] for the geometry shown in Figure 3-4. Subsequently, by completing the integration of equation (3-25), the electric field autocorrelation function is given by:

$$G_1(\tau) = \frac{d\mu_s \sinh\left(\sqrt{\varepsilon\{1-\cos\omega_a\,\tau\}}\right)}{\sinh\left(d\mu_s\sqrt{\varepsilon\{1-\cos\omega_a\,\tau\}}\right)} \tag{3-32}$$

where ε: a function of light modulation contribution from the particle displacement and the variation of refractive index; μ_s: scattering coefficient (m^{-1}); *d*: slab thickness (m); ω_a: angular acoustic frequency (rad/s); and τ: lag time (s).

Figure 3-6 shows the examples of the electric field autocorrelation functions calculated using equation (3-32). The parameters are: $\frac{\partial n}{\partial p}$ = 1.466×10^{-10} m^2/N, ρ = 1000 kg/m^3, c_s = 1480 m/s, n_0 = 1.33, λ_o (optical wavelength) = 500 nm, *d* = 5 cm and *A* = 0.1 nm.

By using the Wiener-Khinchin theorem [Wang 2001], the intensity of the ultrasound modulated light can be calculated from equation (3-33):

$$I_n = \frac{1}{T_a}\int_0^{T_a} \cos(2\pi n f_a)\cdot G_1(\tau)\,\mathrm{d}\tau \tag{3-33}$$

where I_0: un-modulated intensity (W m^{-2}); I_1: modulated intensity (W m^{-2}); f_a: acoustic frequency (Hz); and T_a: acoustic period (s).

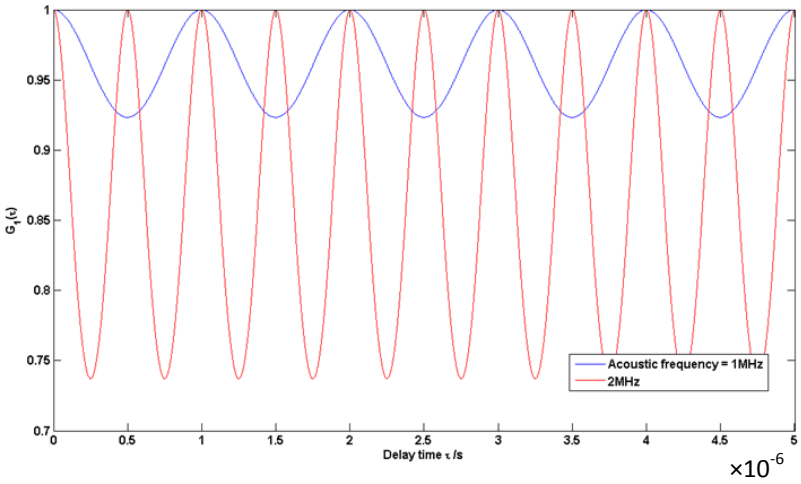

Figure 3-6 The electric field autocorrelation functions of acoustic frequency f_a 1 and 2 MHz when the effect of speckle decorrelation due to the Brownian motion of particles is ignored. The AC intensity is the magnitude of sinusoidal modulation and the DC is the baseline of the G_1.

By the definition of the model, the modulation depth (MD) is proportional to the ratio of the ultrasound modulated intensity to the un-modulated intensity:

$$M = \frac{I_1}{I_0} \tag{3-34}$$

Figure 3-6 shows that the level of modulation increases with acoustic frequency. It is because the contribution from the modulated refractive index increases with the acoustic frequency, even though the contribution of the modulated scatterers'

displacement remains constant [Wang 2001]. By using the same method and parameters to generate Figure 3-6 (unless stated otherwise), Figure 3-7 and Figure 3-8 show the effects of different acoustic amplitude and scattering length on the MD. The MD also increases with acoustic amplitude (Figure 3-7) because it leads to greater modulation of scatterers' displacement and refractive index. Figure 3-8 implies that when the scattering coefficient increases, the light undergoes more scattering events along the ultrasound perturbed paths resulting in higher MD. The validity of this analytical model had been verified using Monte Carlo simulations by Wang [Wang 2001].

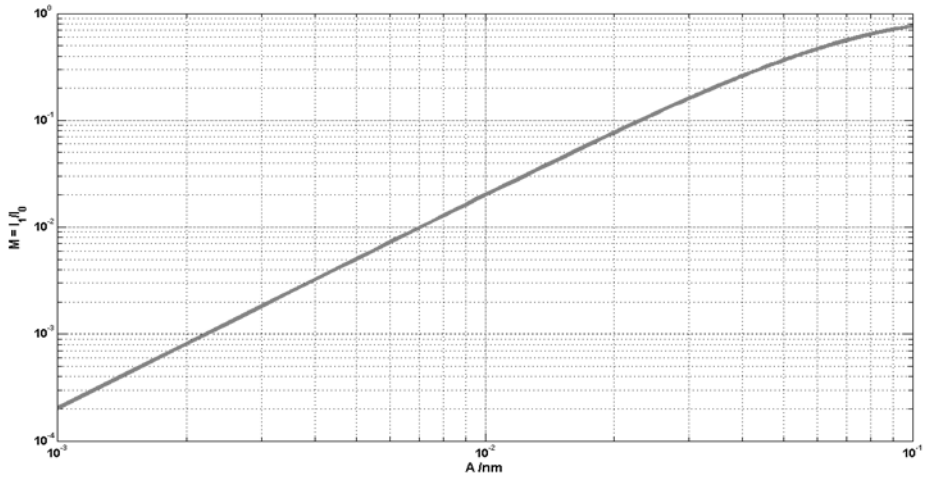

Figure 3-7 The effect of changing the acoustic amplitude on the MD when f_a = 1 MHz

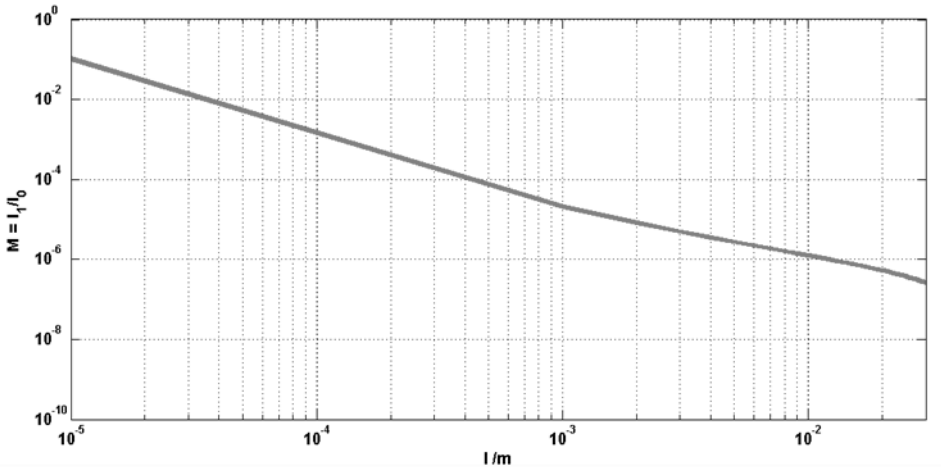

Figure 3-8 The effect of changing the mean free path length on the MD when f_a = 1 MHz

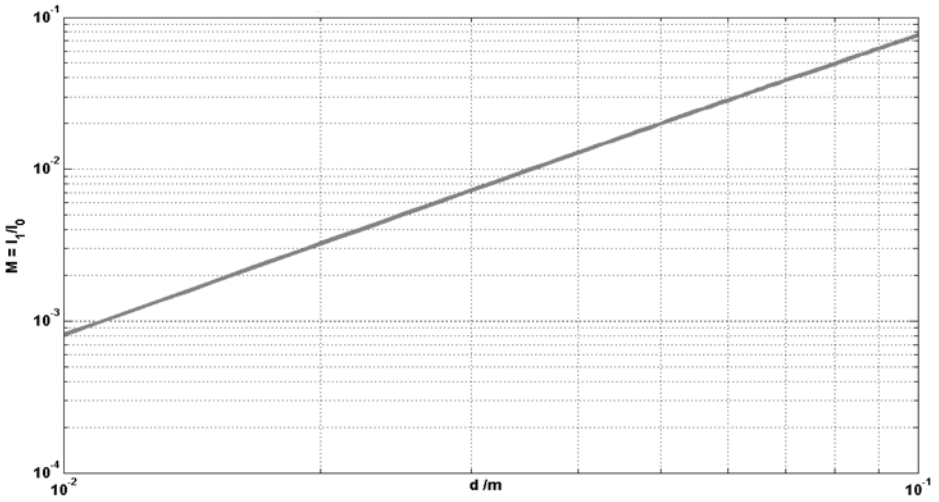

Figure 3-9 The effect of changing the slab thickness d on the MD when f_a = 1 MHz

3.3.2.2 Anisotropic Medium

The model describing the modulation of optical phases in 3.3.2.1 is not realistic as it has only considered isotropic scattering medium and the effect of absorption is ignored. Sakadzic et al. [Sakadzic 2002] improve on this analytical model by incorporating the Brownian motion, anisotropic scattering and absorption of the medium.

Assuming that the phase variation is very small (<<1) [Sakadzic 2002], equation (3-25) can be simplified to the following equations:

$$G_1(\tau) = \int_0^\infty p(s)\mathrm{e}^{-\frac{\langle \Delta\phi(t,\tau)^2 \rangle}{2}} ds \tag{3-35}$$

where $\langle \Delta\phi(t,\tau)^2 \rangle$ is a function of contributions from the change of refractive index δ_n and particle displacement δ_d parameters [Sakadzic 2002].

The probability density function of path length s can be derived by solving the diffusion equation for the semi-infinite slab geometry (Figure 3-5) by assuming extrapolated-boundary conditions [Sakadzic 2002]. By completing the integration of equation (3-35) and implementing the effects of Brownian motion of the scatterers [Pine 1988, Leutz 1995, Sakadzic 2002], the field autocorrelation function is given by:

$$G_1(\tau) = C\frac{\sinh\left(z_0\sqrt{(s_U + s_B + \mu_a)D^{-1}}\right)}{\sinh\left(L_0\sqrt{(s_U + s_B + \mu_a)D^{-1}}\right)} \tag{3-36}$$

$$C = \frac{\sinh\left(L_0\sqrt{\mu_a D^{-1}}\right)}{\sinh\left(z_0\sqrt{\mu_a D^{-1}}\right)} \tag{3-37}$$

$$S_U = \frac{1}{2}(2n_0 k_0 A)^2 \cdot \sin^2\left(\frac{\omega_a \tau}{2}\right) \cdot (\delta_n + \delta_d)$$

(3-38)

$$s_B = \frac{2\tau}{\tau_0}\mu_s'$$

(3-39)

$$D = \frac{1}{3\mu s'}$$

(3-40)

$$L_0 = d + \frac{1.4208}{\mu_s'}$$

(3-41)

$$z_o = \frac{1.7104}{\mu_s'}$$

(3-42)

where C: a constant; S_U: ultrasound modulation contribution to $G_1(\tau)$; S_B: Brownian motion contribution to $G_1(\tau)$; τ_0: single Brownian particle relaxation time (s); L_0: the distance between the extrapolated boundaries of the slab geometry (cm); z_0: initial scattering depth (cm); D: diffusion coefficient (cm^2/s).

Figure 3-10 shows the resulting electric field autocorrelation functions of the analytical model when it is implemented in Matlab by using the following parameters: $\frac{\partial n}{\partial p}$ = 1.466×10^{-10} m^2/N, ρ = 1000 kg/m^3, c_s = 1480 m/s, n_0 = 1.33, λ_o (optical wavelength) = 500 nm, d = 2 cm and A = 0.1 nm. It also shows that increasing the Brownian motion of the scatterers by reducing its single particle relaxation time, causes the autocorrelation function to decay exponentially (Figure 3-11) at a greater rate. In order to quantify the modulation of depth, Sakadzic et al. [Sakadzic 2002] suggests that it is equal to the variation of the electric field autocorrelation from τ = 0 to $\tau = \frac{T_a}{2}$ or the maximum observable variation due to ultrasonic modulation. By using this approach, Figure 3-12, Figure 3-13, Figure

3-14, Figure 3-15,Figure 3-16 and Figure 3-17 were produced by ignoring the effect of Brownian motion. They show the effect of varying the properties of the medium on the modulation of depth.

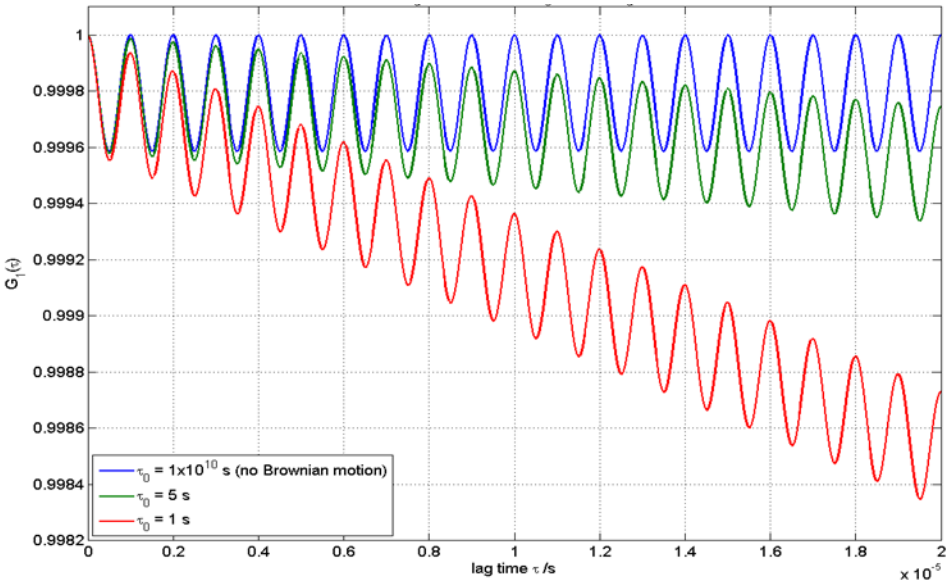

Figure 3-10 The effect of Brownian motion on the electric field autocorrelation functions for d = 2cm, g = 0.7, A = 0.1 nm, f_a = 1MHz, μ_s = 12 cm^{-1} & μ_a = 0.03 cm^{-1}

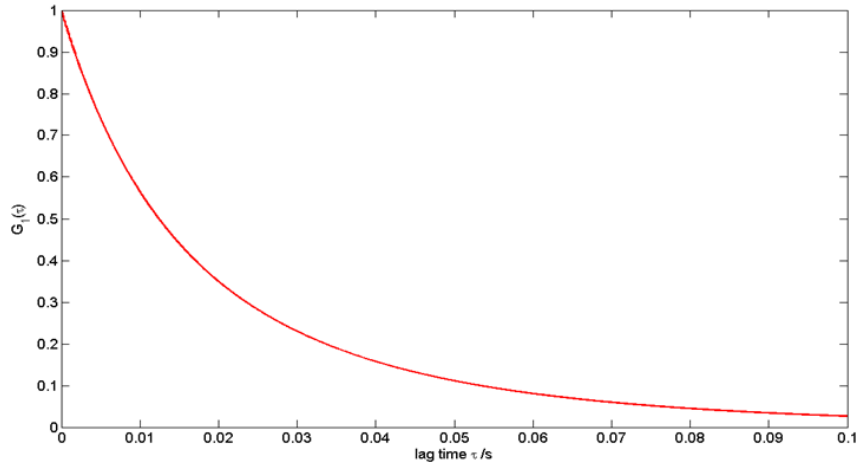

Figure 3-11 Exponential decay of the electric field autocorrelation function due to the Brownian motion of scatterers when τ_0 = 1s, d = 2cm, g = 0.7, A = 0.1 nm, f_a = 1MHz, μ_s = 12 cm^{-1} & μ_a = 0.03 cm^{-1}

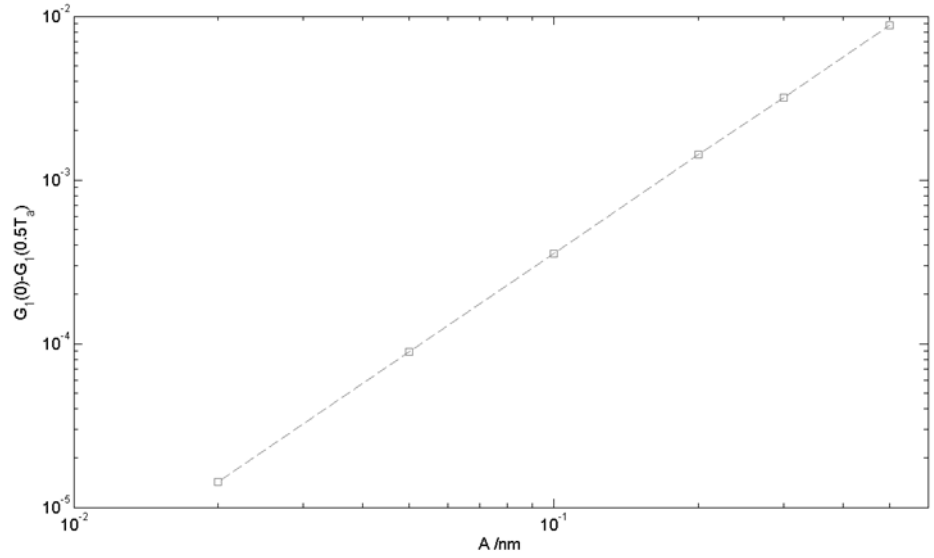

Figure 3-12 The influence of different acoustic amplitude on the MD when τ_0 = 10^{10} s, d = 2cm, g = 0.7, f_a = 1MHz, μ_s = 10 cm^{-1} & μ_a = 0.03 cm^{-1}

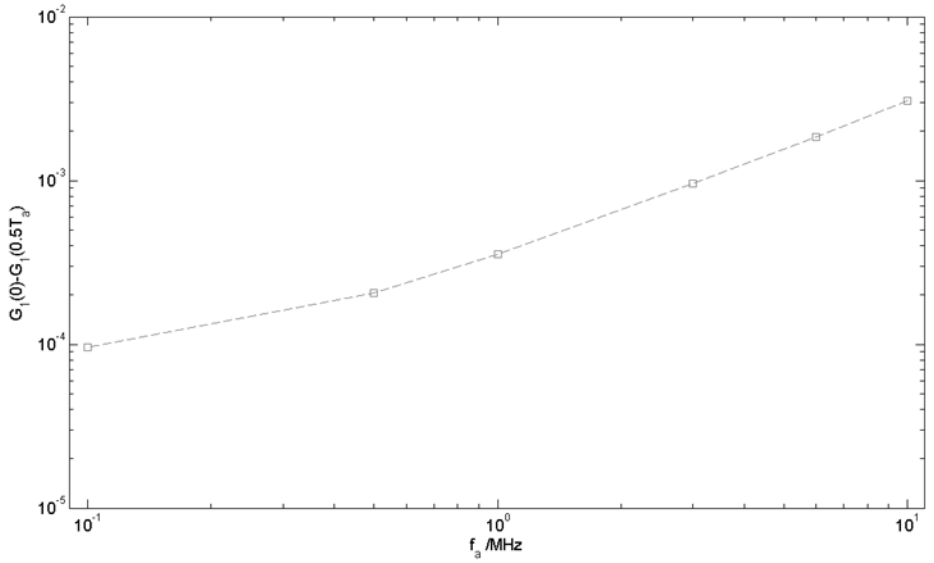

Figure 3-13 The influence of variation in acoustic frequency on the MD for τ_0 = 10^{10} s, d = 2cm, A = 0.1 nm, g = 0.7, μ_s = 10 cm^{-1} & μ_a = 0.03 cm^{-1}

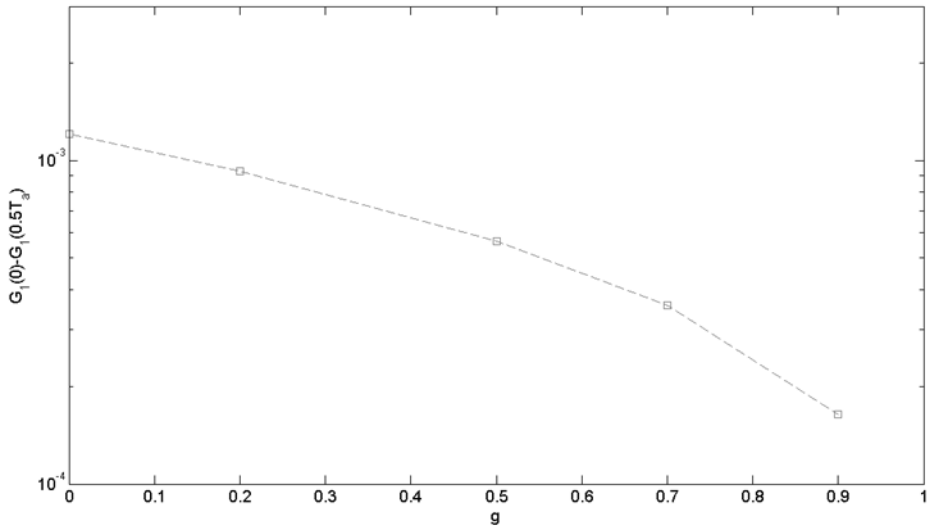

Figure 3-14 The effect of variation in anisotropy factor on the MD when τ_0 = 10^{10}s, d = 2cm, A = 0.1 nm, f_a = 1MHz, μ_s = 12 cm^{-1} & μ_a = 0.03 cm^{-1}

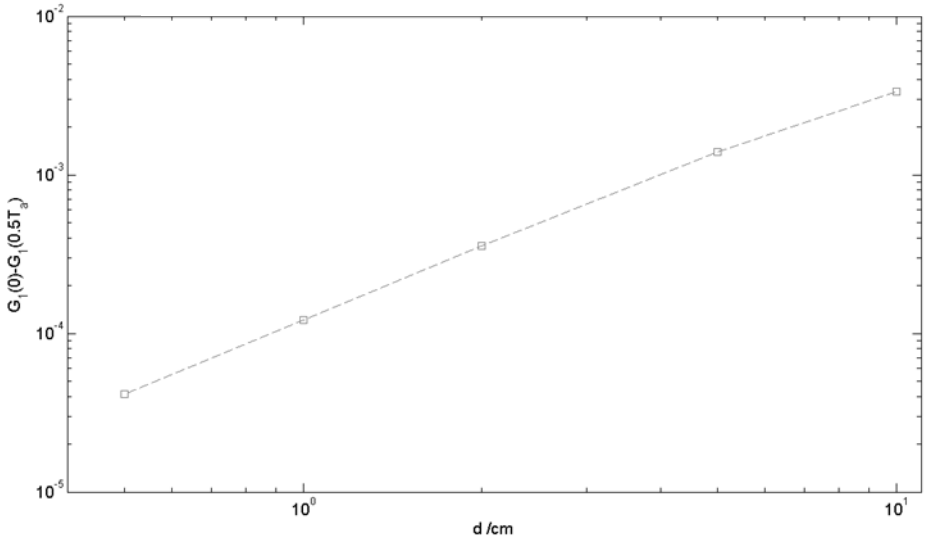

Figure 3-15 The influence of variation in slab thickness on the MD when τ_0 = 10^{10}s, g = 0.7, A = 0.1 nm, f_a = 1MHz, μ_s = 12 cm^{-1} & μ_a = 0.03 cm^{-1}

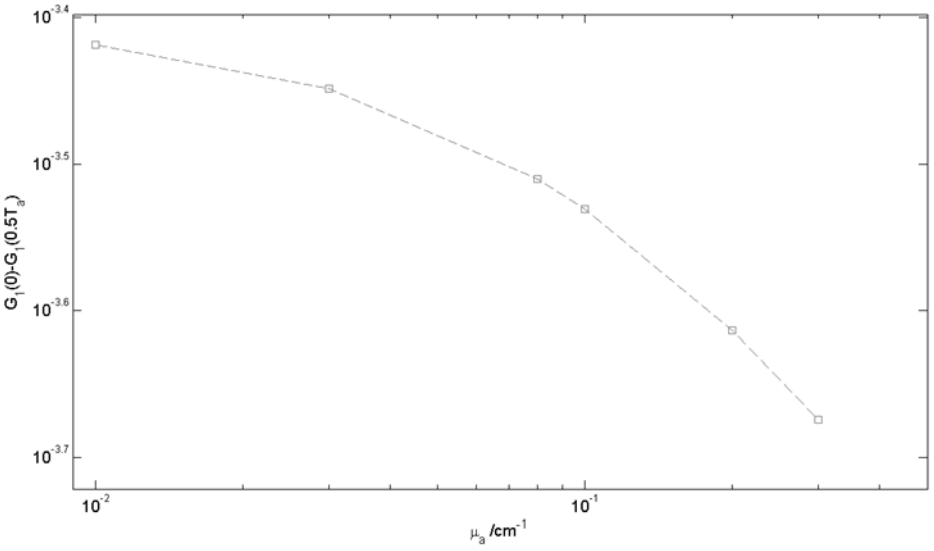

Figure 3-16 The influence of variation in the μ_a on the MD when $\tau_0 = 10^{10}$s, d = 2cm, g = 0.7, A = 0.1 nm, f_a = 1MHz & μ_s = 12 cm^{-1}

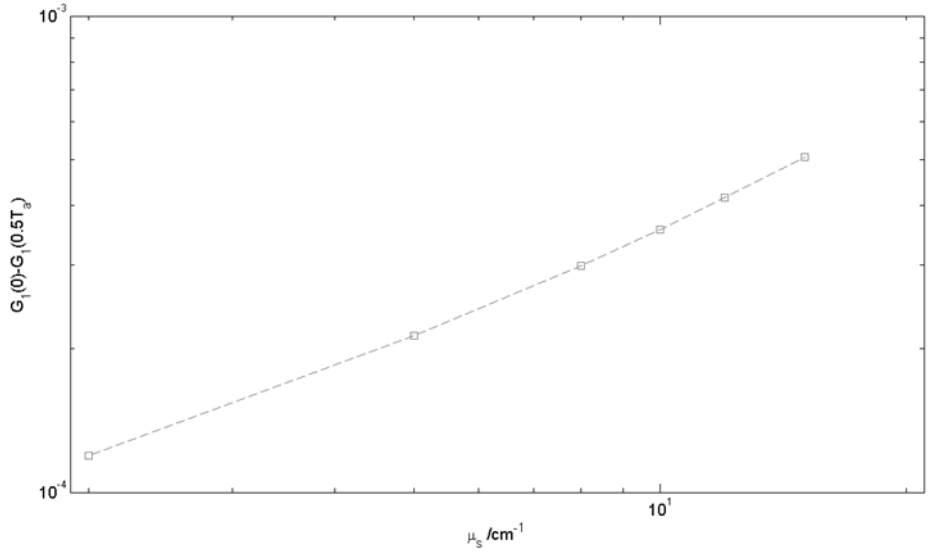

Figure 3-17 The influence of variation in scattering coefficient on the MD when τ_0 = 10^{10}s, d = 2cm, g = 0.7, A = 0.1 nm, f_a = 1MHz, & μ_a = 0.03 cm^{-1}

The results demonstrate similar conclusions to the isotropic analytical model discussed in section 3.3.2.1 on the effect of increasing the scattering coefficient,

acoustic amplitude, slab thickness and acoustic frequency. Figure 3-14 shows that increasing the anisotropy factor results in decreasing the MD. This is because of the decrease in the contribution of scatterers' displacement depends on solely the μ_s' [Sakadzic 2007], which means that there are less scattering events. The result also shows that decreasing the absorption length of the medium decreases the MD, because higher absorption increases the probability of the ultrasound modulated light being absorbed before detection. This model had been verified by Monte Carlo simulations by Sakadzic [Sakadzic 2002].

Sakadzic et al. extended the current model for the use of ultrasonic pulses [Sakadzic 2005] and into a more generalised *temporal correlation transfer equation* (CTE) [Sakadzic 2006, Sakadzic 2007] for the AO effect, so that heterogeneous mediums and continuous-wave and pulsed ultrasound beam can be analytically studied and simulated.

3.3.2.3 Anti-Correlation Effect

According to the theory described in section 3.3.2.1 and 3.3.2.2, increasing the μ_s' of the phantom should result in the increase in the AO MD. It is because light that propagates through the FUR will undergo more scattering events resulting in higher phase accumulation. However such models are typically only applicable in semi-infinite slab geometry with uniform planar ultrasound waves. Sakadzic et al. [Sakadzic 2005] suggested that there is correlation between the phase contribution between the particle displacement and refractive index variation, which is shown in equation (3-43).

$$\langle \Delta\phi^2 \rangle = \langle \Delta\phi_n^2 \rangle + \langle \Delta\phi_d^2 \rangle + \langle 2 \cdot \Delta\phi_n \cdot \Delta\phi_d \rangle \tag{3-43}$$

Figure 3-18 The relationship between the acoustic frequency on the magnitudes of $\langle \Delta\phi_n^2 \rangle$, $\langle \Delta\phi_d^2 \rangle$ and $-\langle 2 \cdot \Delta\phi_n \cdot \Delta\phi_d \rangle$, which are denoted by C_n, C_d and $-C_{n,d}$ (multipled by -1) respectively. (*l*: mean path length and *s*: path length) [Sakadzic 2005]

The averaged phase contribution of each mechanism may be negative, thus the cross term of equation (3-43) may be negative. This *anti-correlation* contribution will counteract the combined contribution from particle displacement and refractive index variation, which is shown in Figure 3-18. The results show that the cross term will cancel out the phase contribution from the particle displacement and the variation of refractive index depending on the acoustic frequency. This result has been observed experimentally and by computer simulation by Kothapalli et al.[Kothapalli 2007].

The model [Sakadzic 2005] described was implemented in Matlab and the result is presented in Figure 3-19 using parameters described in the literature. This result also shows that an increase in μ_s' will increase the MD and the MD will peak at a particular value of μ_s' depending on the acoustic wavelength.

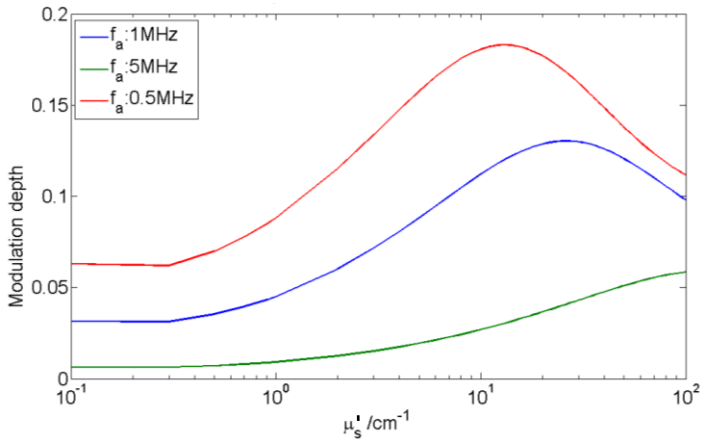

Figure 3-19 The effect of acoustic wavelength variation on the MD when the anti-correlation contribution is factored in.

3.4 Biomedical Application of Acousto-Optics

3.4.1 Imaging

The use of AO techniques in biomedical applications has been primarily targeted for breast cancer imaging purposes [Marks 1993, Wang 1995, Kempe 1997, Zhu 1999, DiMarzio 2003, Sakadzic 2004, Wang 2004, Elson 2011]. This is because imaging techniques that exploit NIR light can provide useful information e.g. oxygenation for the detection of the tumours in soft tissue, which supplements the more established diagnostic imaging modalities such as x-ray computer tomography (x-ray CT), medical ultrasonography and magnetic resonance imaging (MRI). In certain cases, the vasculature of the lesions provides better optical contrast [DiMarzio 2003, Wang 2004].

However, purely optical imaging techniques such as Diffuse Optical Tomography (DOT) suffer from poor resolution. The AO method on the other hand retains the good tissue contrast of purely optical methods while providing good spatial resolution of ultrasonography [DiMarzio 2003, Wang 2004, Tuchin 2007, Wang 2007]. Therefore, by combining the advantages of both optical and ultrasound

methods, the AO imaging has the potential to provide imaging and spectroscopic measurement at the same time.

One of the first AO images of a highly absorbing object within a turbid medium was produced by Wang and Zhao [Wang 1995] and the technique was then termed Acousto-Optical Tomography (AOT) [Kempe 1997] or Ultrasound Modulated Optical Tomography (UOT) [Wang 1997]. The approach of using highly absorbing target(s) within homogenous turbid medium has been widely adopted in most AO tomography studies [Kempe 1997, Wang 1997, Wang 1998, Leveque 1999, Murray 2004, Kothapalli 2007, Li 2008]. However Devi et al. [Devi 2006, Devi 2008] suggested that the MD was not only a function of optical properties but also the mechanical properties of medium. The key challenge in the AO imaging is the detection of the weak AO signal. The most recent developments in the use of the AO method to focus light in a turbid medium [Xu 2011] and AO coherence tomography [Lesaffre 2011].

3.4.1.1 Detection of Acousto-Optic Signal in Imaging

The focus of AO imaging research has been to improve the detection of AO signal [Elson 2011]. Early studies [Leutz 1995, Wang 1995, Wang 1997, Wang 1998] used a photo-multiplier-tube (PMT) as the optical detector. However Leveque et al. found that the signal to noise ratio of the ultrasound modulated signal could be improved by a parallel detection scheme using a charge-coupled device (CCD) [Leveque 1999, Leveque-Fort 2001]. The pixel size of the CCD was matched to the average dimension of the speckle grain so that each pixel only monitored the intensity fluctuation of one speckle. The improvement in signal to noise ratio (by a factor of the square-root of total number of CCD pixels) was achieved by averaging all the simultaneously detected signals over a four phase detection scheme [Leveque-Fort 2001]. Another variation of the parallel detection scheme was proposed by Li et al.[Li 2002] to measure the ultrasound modulated speckle contrast. The MD in this case is proportional to the difference of the recorded speckle contrast between the on and off stages of the ultrasound [Zemp 2006].

They also rotate the CCD camera [Li 2004] as in CT imaging to image buried objects.

However the PMT or the CCD based detection schemes suffer from the speckle decorrelation due to the Brownian motion of scatterers. Murray et al. [Murray 2004] suggested the use of photorefractive crystal (PRC) interferometer to adaptively compensate the low frequency shift of speckle decorrelation. A newer development is the use of the spectral-hole burning method [Li 2008, Xu 2010] to improve detection.

Rousseau et al. [Rousseau 2008] developed a system that used a powerful and long laser pulse to increase the photon density within the ultrasonic focal region in an attempt to improve the AO detection besides the intense acoustic bursts.

Another development in the detection of the AO signal is the use of the non-linear second order response of the ultrasound modulated speckle intensity [Selb 2002] to improve the spatial resolution of the AO images. Devi et al. [Devi 2006, Devi 2008] and Leutz et al. [Leutz 1995] combined modules of a single photon counting PMT and digital correlator that could compute the intensity autocorrelation function in real time.

Bossy et al. [Bossy 2005] attempted a hybrid implementation of the AO method by combining the AO imaging and the conventional medical ultrasound scanner. This demonstrated the potential of co-registering images using both imaging modalities.

3.4.1.2 Ultrasound Excitation in Acousto-Optic Imaging

Early demonstration of the AO effect used continuous-wave ultrasound excitation as shown by Leutz et al. [Leutz 1995] and Wang et al. [Wang 1995]. Wang et al. [Wang 1998] suggested that the image acquisition time of AO tomography could be improved by using frequency-swept ultrasonic waves [Wang 1998, Forget 2003]. Each location of a scan-line in the ultrasound axis within the medium is

frequency-encoded, thus the scan can be acquired in a single measurement. The resolution of images can be also controlled by the corresponding sweep rate.

However the contrast and resolution of AO images could be also improved by using ultrasonic pulses [Kempe 1997, Selb 2002] instead of continuous wave. Unfortunately the use of short ultrasound pulses increases the shot noise [Lev 2003]. Lev at al. also suggested that the shot noise could be reduced by using pulsed-waves of ultrasound, where the phase transition between the acoustic cycles was matched. Furthermore, this approach also lowered the average power dissipation by the ultrasound transducer, which in turn minimised the risk of damage due to overheating.

Another possible strategy is to increase the acoustic power because the MD increases with increasing acoustic amplitude according to the described analytical models. This approach was taken further by Kim et al. [Kim 2006] and Li et al. [Li 2010, Li 2011] to use the radiation force [Calle 2005] to induce greater particle displacement in order to generate higher AO modulation.

The output power of the ultrasound transducer could be further improved by using a HIFU transducer [Draudt 2009]. Full power HIFU pressure waves are highly non-linear and are typically used for ultrasound ablation or surgery [Hill 1995, Kennedy 2003], obviously not suitable for diagnostic AO imaging. Alternatively, AO imaging has been suggested as a possible method to monitor HIFU treatment [Lai 2011].

3.4.2 Multi-wavelength Spectroscopic Mapping

The first quantitative AO measurement of turbid media using two optical wavelengths was demonstrated by Lev et al. [Lev 2002] whereby they mapped the photon density within a diffusive medium using the AO method and derived an expression for the blood concentration. They subsequently demonstrated the AO effects in a rat model and human arm [Lev 2003]. They further showed the feasibility of AO physiological measurement in osteoporosis assessment of the adult hand [Lev 2005].

Kim et al. [Kim 2007] combined intense ultrasound bursts and multi-wavelengths laser sources to estimate the absorption of buried dye in a tissue mimicking phantom. Bratchenia et al. [Bratchenia 2008, Bratchenia 2009, Bratchenia 2011] subsequently mapped the estimated total absorbance in blood vessel phantom studies by using a model based on the Beer-Lambert law. But the presented model required the estimation of parameter values through Monte Carlo simulation and assumed uniform scattering throughout the medium.

Lai et al. [Lai 2009] proposed the pressure contrast AO imaging whereby the μ_s' at the location of the FUR can be quantified by using two different acoustic pressures. The ratio of two AO signal when two pressures are used is dubbed the pressure contrast signal (PCS), which is found to depend on only the ratio of the pressures used and the local optical property in the FUR. The measured PCS of the localised scattering inclusions are found to be very similar to the measured PCS of the homogeneous phantoms that have the same μ_s'. Therefore this method requires calibration the PCS and the pressures used to particular optical property for quantification measurement, instead of the inversion method [Bratchenia 2009, Bratchenia 2011].

In conclusion, the use of AO techniques for localised quantitative measurement is a relatively new approach and very much in its infancy.

4 Instrumentation and Phantom Development for Acousto-Optic Measurement

This chapter details the major instruments and tissue mimicking phantoms used in this work. It is then followed by a section on the basic detection of the AO signal.

4.1 Instrumentation

4.1.1 Laser Source

Figure 4-1 The fibre-coupled continuous wave 808nm laser source.

The laser source is an 808 nm continuous wave diode laser system (CrystaLaser IRCL-100-808-S) as shown in Figure 4-1. It is powered by the DC-12 power supply to provide a laser output power of 100 mW. Since the laser system is fibre-coupled by a one metre long 62.5 μm multi-mode fibre, which introduces some power loss, only 45 mW is delivered at the end of the fibre due to the poor fibre coupling. The coherence length of the laser system exceeds 10 metres.

4.1.2 Single Photon Counter

The light detector is a single photon counter (Perkin Elmer SPCM-AQR-14), which is based on an avalanche photodiode that detect photons of wavelength range from 400 to 1060 nm. The module, which is shown in Figure 4-2, is

thermoelectrically cooled to ensure stability for ambient room temperature changes between 5° and 40° C. The photon counter produces a 35 ns TTL pulse when a photon is detected. However it has a dead time of 50 ns between each detected photon. The dark photon count of the module is under 100 counts per second (Hz). The photon-counting can be turned on and off by supplying a corresponding TTL high and low to the gating input. Its quantum efficiency performance is shown in Figure 4-3, which shows 54% efficiency in detecting 808 nm light.

Figure 4-2 Image of the photon counter[2]: the actual photon counter is fibre-coupled at the light detection area instead of the avalanche photodiode.

Figure 4-3 The typical quantum efficiency of the SPCM-AQR-1x series photon counter[2] (unit specific performance data is not available): the *Pd* at 808 nm ≈ 54%.

[2] http://www.htds.fr/doc/optronique/militaireAerospace/SPCM-AQR.pdf

However, the photon detection is linear when the count rate is less than 1 MHz, which is shown in Figure 4-4. At higher photon counts, the true count rate has to be corrected by a correction factor that increases non-linearly with increasing count rate. Therefore, it is generally a good idea to ensure that the range of intensity measurement should lie around the 1 MHz mark.

Figure 4-4 The linearity of the SPCM-AQR-1x series photon counter[3] (unit specific performance data is not available) at different photon count rates; the correction factors are 1.01, 1.08 and 1.4 when the mean count rates are 200 kHz, 1MHz and 5 MHz respectively.

4.1.3 **Digital Correlator**

4.1.3.1 Basic Operation

The digital correlator (Correlator.com Flex02-01D) is depicted in Figure 4-5. It draws power from the USB connection, which also serves as the data link between the unit and computer. The two channels A and B allow operations of single channel autocorrelation, dual channel autocorrelation and cross-correlation. The strength of this correlator is its 640 MHz system clock speed, which translates to a shortest sampling time of 1.56 ns for the estimated correlation functions (depending on the operation mode).

[3] http://www.htds.fr/doc/optronique/militaireAerospace/SPCM-AQR.pdf

Depending on the requirements, the digital correlator can compute the correlation function in multi-tau and linear-tau sampling mode. The multi-tau mode [Schätzel 1988, Schätzel 1990] can compute the correlation function from lag time 1.56 ns to 36.7 minutes, which makes it the ideal operation mode for large lag time study. However, the lag time is sampled in a non-linear fashion in the multi-tau mode. The first 32 correlation samples are sampled at 1.56 ns, and the following 16 samples are sampled at 2×1.56 ns. The sampling time is doubled for every batch of 16 samples until 36.7 min.

Figure 4-5 An image[4] of the Flex02-01D digital correlator unit.

In the linear mode operation, the sampling time of the correlation function is fixed depending on the setting of the correlator, which in turn also affects the maximum lag time of the measured autocorrelation function. For this work, we only consider the real time operation (fastest), which is the 1-bit operation with sampling periods of 1.56 to 6.25 ns (512 autocorrelation samples) and 6.25 to 30 ns (768 autocorrelation samples). The total measurement time is the integration time $t_{\int}$. The signal-to-noise ratio of the measurement can be improved by using a longer integration time [Schätzel 1990].

The photon counter and digital correlator are housed in a metal casing, which is shown in Figure 4-6.

[4] http://www.correlator.com/flex01d15.htm

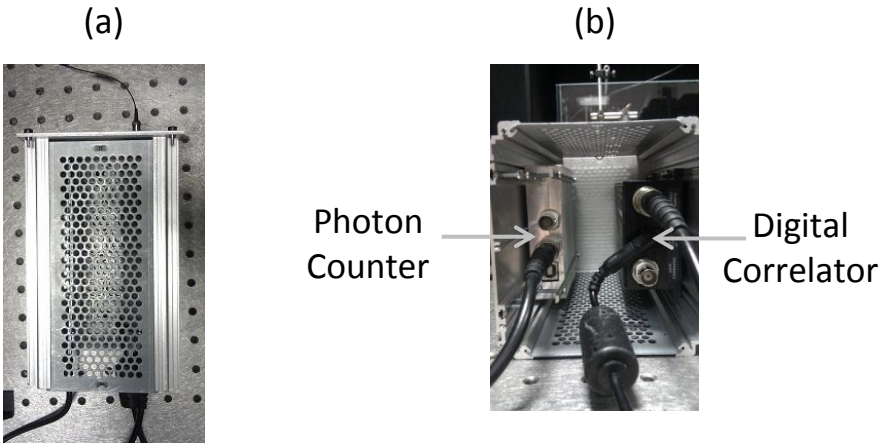

Figure 4-6 (a) The combined unit of the photon counter and the digital correlator, which is housed in a metallic casing that also functions as heat sink. (b) the inner view of the metallic casing.

4.1.3.2 Autocorrelation Function

The conventional un-normalised autocorrelation function [Schätzel 1990] is shown in equation (4-1) for a sequence of photon counts *n*.

$$G_n^{(2)}(k) = \frac{1}{M}\sum_{i=1}^{M} n_i n_{i+k} \tag{4-1}$$

For i = 1, 2, 3, …, M samples of the photon count sequence and k = 1, 2, 3, … correlation samples at different lag time. Typically, the autocorrelation function is normalised by the square of its mean photon count S_0, which is depicted by equation (4-3); as shown in equation (4-2).

$$g_n^{(2)}(k) = \frac{G_n^{(2)}(k)}{{S_0}^2} \tag{4-2}$$

$$S_0 = \frac{1}{M}\sum_{i=1}^{M} n_i$$

(4-3)

However, such asymmetrical normalisation will result in poorer signal-to-noise ratio especially at large lag time [Schätzel 1988, Schätzel 1990]. To compensate, the asymmetrical normalisation scheme is used. This method uses a second photon count monitor S_k for different lag time element k in equation (4-4). The resulting symmetrical autocorrelation function is shown in equation (4-5).

$$S_k = \frac{1}{M}\sum_{i=1}^{M} n_{i+k}$$

(4-4)

$$g_n^{(2)}(k) = \frac{G_n^{(2)}(k)}{S_0 \cdot S_k}$$

(4-5)

4.1.4 **Ultrasound Transducer**

The continuous wave and pulsed ultrasound transducers are shown in Figure 4-7 and Figure 4-8 respectively. These two transducers are driven by a signal generator (Agilent Technologies, 33210A) through a 75 W RF amplifier (Electronics & Innovation Ltd, A075).

Figure 4-7 An image of the continuous wave ultrasound transducer PA 304 with a centre frequency of 0.66 MHz.

Figure 4-8 An image of the pulsed-wave ultrasound transducer of 1 MHz centre frequency.

The 0.66 MHz (Precision Acoustics PA304) transducer is designed for HIFU therapy research and has a focal distance of 72.6 mm. Its focal region is 4.2 by 4.4 mm (focal zone widths) by 29.36 mm (focal zone length). It is capable of outputting maximum acoustic power of 99.45 W when excitation peak-to-peak voltage of 243.8 is used, which translates to sound intensity of 683 Wcm^{-2}. It can operate in this level up to 30 seconds continuously without overheating. However, it will require 5 minutes of cooling afterwards. Depending on the situation, this transducer can produce continuous ultrasound waves for an extended period of time (< 10 minutes), so long as the excitation voltage is not higher than 100 V peak-to-peak.

The 1 MHz (Olympus Panametrics V392SU) transducer has a focal distance of 63.5 mm and focal region of 2.56 mm (focal zone width) by 29.36 mm (focal zone length). It is designed to produce pulses of ultrasound waves when it is powered by a large negative spike potential. However, it can still be used for pulsed-wave operation providing that its output power limit of 25 mW is not exceeded.

4.1.5 **Needle Hydrophone**

A needle hydrophone system (Precision Acoustics HP1 SN:121 1mm diameter), which is shown in Figure 4-9, was used in part to measure the peak pressure of the ultrasound wave produced by the transducers described in section 4.1.4. The hydrophone system can be connected to a digital oscilloscope, which can measure

the peak voltage of the captured ultrasonic wave. The voltage can be converted to the peak pressure by the following equation:

$$P_{peak} = \frac{V_{peak}}{S_{nh}} \tag{4-6}$$

Where V_{peak}: peak voltage measured (mV); P_{peak}: peak acoustic pressure (MPa); and S_{nh}: sensitivity of the needle hydrophone for a particular acoustic frequency i.e. $S_{nh:0.66MHz}$ = 1659 mV/MPa and $S_{nh:1MHz}$ = 2303 mV/MPa.

Figure 4-9 An image of the needle hydrophone system.

4.2 Phantom Development

4.2.1 Intralipid Solution

One of the most widely used dynamic phantoms for optical studies in the literature is diluted solutions of fat emulsion such as Intralipid. It is cheap and readily available. However, it is not a product which is produced to a certain optical property specification. It is also perishable and its optical properties can change over time due to sedimentation [Cubeddu 1997].

4.2.1.1 Transport Scattering Coefficient

The scattering properties of fat emulsion solution such as Intralipid can be estimated from the average size and the refractive index of the micelles by using the Mie theory [van Staveren 1991], which yields the following relationship for a concentration of 10% Intralipid solution:

$$\mu_s^C(\lambda) = C_1 \lambda_O^{-2.4} \; (mL^{-1}L\, mm^{-1}) \tag{4-7}$$

$$g^C(\lambda) = 1.1 - C_2 \lambda_O \tag{4-8}$$

where λ_O is the optical wavelength (μm); C_1: dimensionless constant (0.016); C_2: dimensionless constant (0.58); and μ_s^C: scattering coefficient in 10% Intralipid concentration ($mL^{-1}L\, mm^{-1}$).

The μ_s' of the solution can be calculated using equation (4-9).

$$\mu_s^{CP} = \mu_s^C (1 - g^C) \tag{4-9}$$

The volume V_I (mL) of the 10% Intralipid solution required to achieve the μ_s' (mm^{-1}) for the final diluted solution of total volume V_T (L) can be calculated by using [van Staveren 1991]:

$$V_I = \frac{V_T \cdot \mu_s'}{\mu_s^{CP}} \tag{4-10}$$

Equations (4-7) and (4-8) are only valid when 0.4 μm < λ <1.1 μm for Intralipid concentration from 0.4% to 1.7%. However comparison to published results of measured 10% Intralipid scattering coefficients yielded about 8% variation (128.3 cm^{-1} and ± 140 cm^{-1}) [van Staveren 1991, Flock 1992, Michels 2008]. Examples of the μ_s' (cm^{-1}) of different concentrations in percentage (V_I/V_T × 10%) of the

Intralipid solution is shown in Table 4-1, which is calculated by using equation (4-10).

Intralipid concentration (%)	μ_s' (cm^{-1}) at 632.8 nm
0.25	3.20
0.5	6.41
0.75	9.62
1	12.8
2	25.6
5	64.1

Table 4-1 Scattering coefficients of different Intralipid concentrations (from 0.25% to 5%).

4.2.1.2 Absorption Coefficient

The absorption of the Intralipid solution can be set by adding a NIR dye (ICI S109564), which has been characterised by using a spectrometer and the result is shown in Figure 4-10.

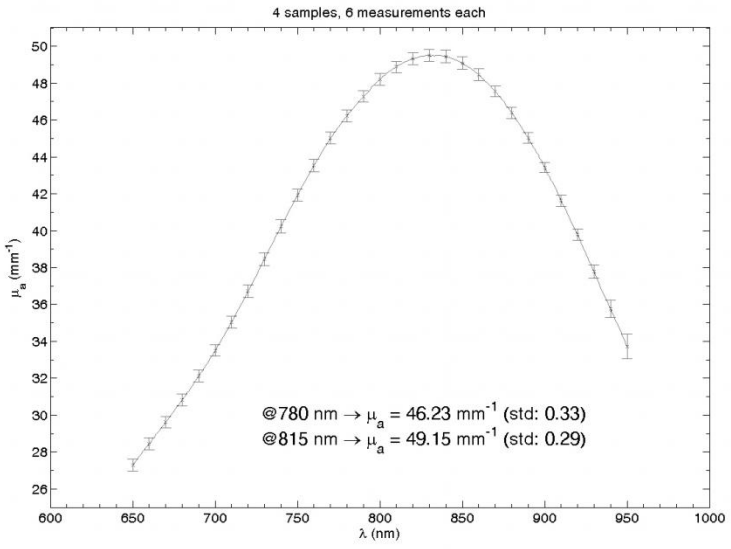

Figure 4-10 The measured μ_a of the NIR dye (ICI S109564) for a range of wavelength from 650 to 950 nm.

The μ_a of the Intralipid solution can be adjusted by the following:

$$V_{dye} = \frac{\mu_a \cdot V_T}{\mu_a'} \tag{4-11}$$

where V_{dye} is the volume of the dye (mL) needed to achieve a target μ_a of a total volume of mixture V_T (mL). μ_a' is the characterised absorption, which can be read from Figure 4-10 for an optical wavelength.

4.2.2 Polyvinyl Alcohol Gel Phantom

This section discusses the preparation of the elastic PVA gel phantom, whose optical and mechanical properties can be readily adjusted to that of healthy human soft tissue. Greater detail of this phantom can be found to chapter 4 of Price's thesis [Price 2010].

4.2.2.1 Transport Scattering Coefficient

Figure 4-11 The relationship between the concentration of TiO_2 and μ_s' of PVA gel phantom [Price 2010].

Price et al.[Price 2010] shows the linear relationship between the amount of titanium dioxide (TiO_2) in PVA gel phantom and its μ_s', which is reproduced in Figure 4-11. The linear relationship depicted in Figure 4-11 can be expressed by:

$$\mu_s' = C_C \cdot C_{TiO_2} \tag{4-12}$$

where μ_s' is the transport scattering coefficient of the PVA gel (mm^{-1}), C_{TiO_2} is the concentration of the TiO_2 grains (g/L) and C_C is a calibration constant of 0.7572.

4.2.2.2 Absorption Coefficient

The absorption of the PVA gel phantom can be adjusted by adding the appropriate amount of NIR dye, which is described in section 4.2.1.2. In the absence of other absorber, μ_a of the gel is 0.0235 cm^{-1} at 780 nm.

Alternatively, the black polyurethane pigment (Tiranti 410-520) can be used. However, this pigment is harder to control as it is in gel form and it requires a 'warm' solvent of diluted ethanol. The μ_a of this pigment for a concentration of 6.67 g/L has been characterised and the result is shown in Figure 4-12.

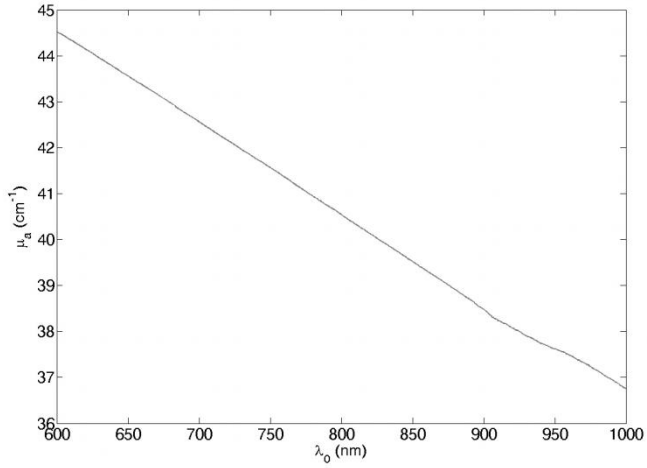

Figure 4-12 The resulting μ_a of mixing 2 g of the black pigment in a 300 mL solvent (50% water and 50% ethanol by volume).

4.2.2.3 PVA Gel Preparation

The basic setup of PVA gel preparation is shown in Figure 4-13. The PVA gel phantoms used in this thesis are 10% by the total weight of solvent mixture, and have similar mechanical properties to that of soft tissue. For example, a 10% mixture of 500 mL solvent requires 50 g of PVA grains.

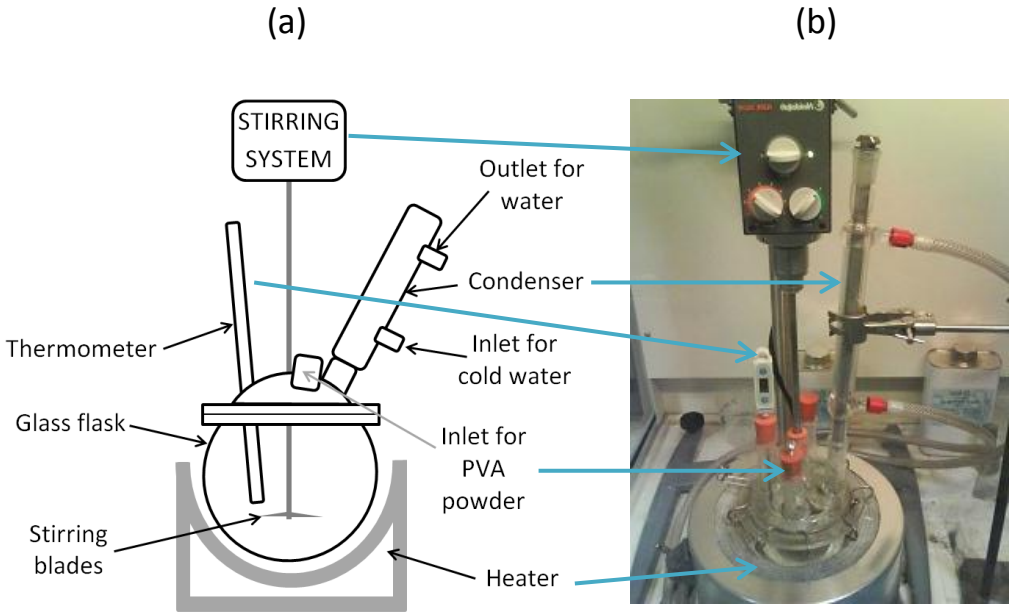

Figure 4-13 The basic setup of the preparation of the PVA gel phantom (a) and an image of the apparatus (b).

A solvent mixture of 50% deionised water and 50% ethanol by volume is held within an air-tight glass vessel, which is being heated and stirred continuously. Both the scatterer and absorber are added in the first instance to ensure that the mixture is homogenous. When the temperature of the mixture reaches 80°C, the PVA grain is very slowly added into the glass vessel through one of the inlets. The PVA will dissolve after two hours of continuous stirring and heating at 80°C.

When the PVA grains are completed dissolved, the resulting mixture can then be poured it into a prepared mould. The mould is left standing for an hour before put into the freezer (-13°C) for 22 hours. After the freeze-cycle, the gel can then be

transferred into a mixture of 50% ethanol and 50% water for thawing and storage. Examples of the PVA gel phantoms can be found in Figure 4-14 and Figure 4-15.

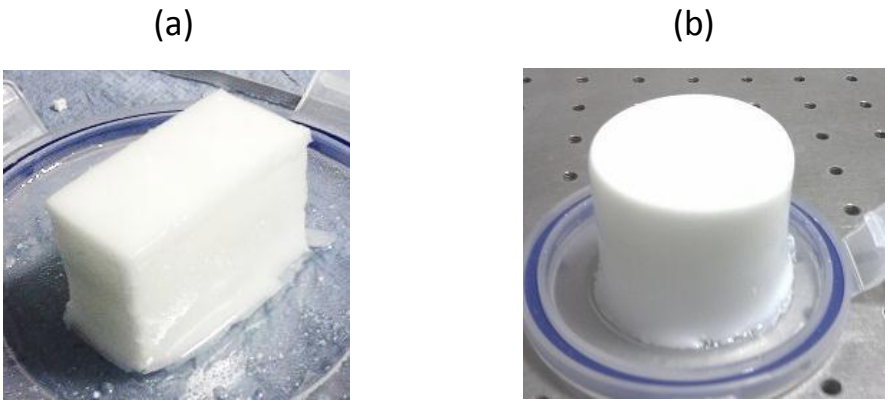

Figure 4-14 Samples of PVA gel phantoms of different shapes: (a) cuboid and (b) cylinder, which can be easily built by using appropriate moulds.

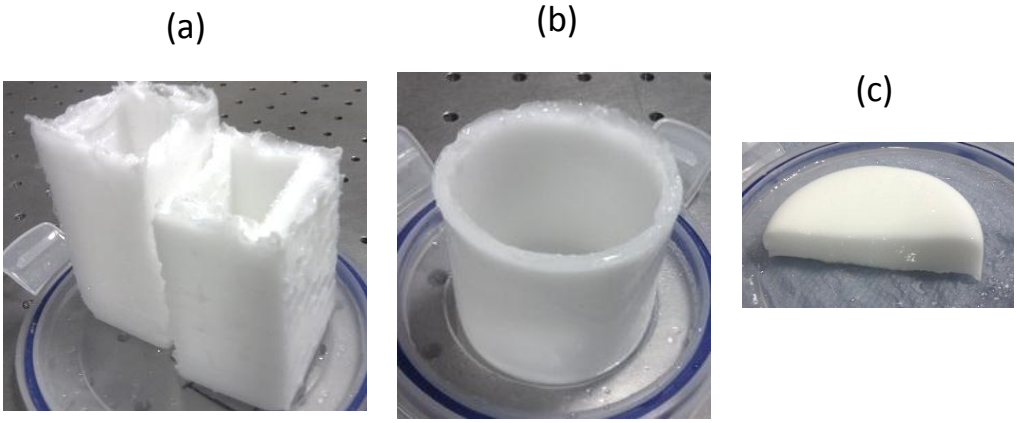

Figure 4-15 The PVA gel phantom can be made into different shapes i.e. (a) cuboid containers, (b) cylindrical container (c) arbitrary shape. This can be achieved by using the appropriate moulds and the gels can be sliced.

The PVA gel phantoms have several limitations. They require continuous storage in a mixture of the same solvent. Furthermore, over time their mechanical properties will change (becoming stiffer) as their weight will very slowly decrease. This also means that the speed of sound propagation in the phantom will

change and it will affect AO measurement. The NIR dye in the PVA gel will also diffuse out of the phantom after more than 12 hours of continuous immersion as shown in Figure 4-16.

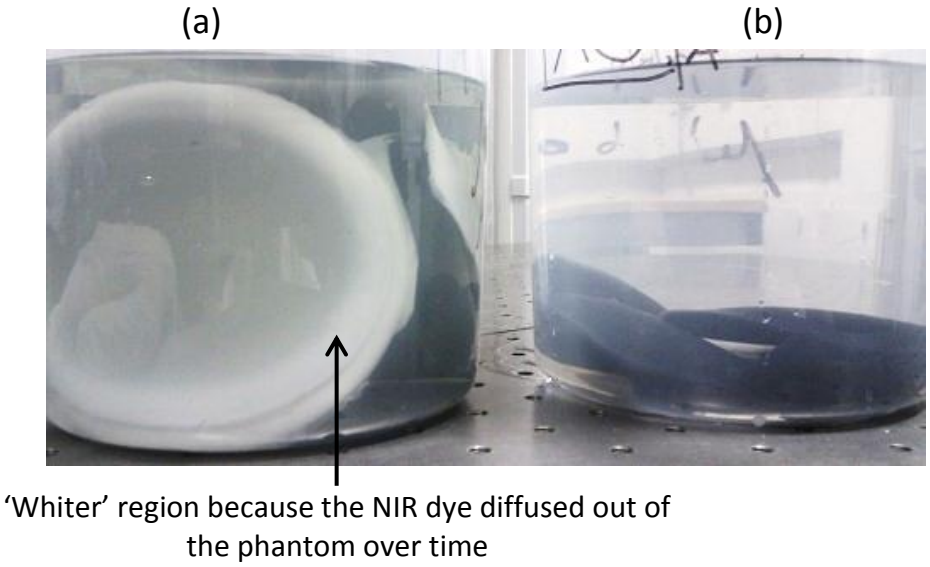

Figure 4-16 (a) The NIR dye diffuses out of the slab PVA gel phantoms in the water and ethanol solution over time. (b) The problem is not observed when the black polyurethane pigment is added instead of the NIR dye.

4.3 Basic Detection of Acousto-Optic Signal

The aim of this section is to detect the AO signal in transmission mode using a PVA gel phantom and an Intralipid phantom. The parameters of the digital correlator and the ultrasonic excitation are also investigated, e.g. the ultrasound excitation voltage and the integration time of the digital correlator, so that the optimal configuration can be found.

4.3.1 Materials and Methods

The basic diagram of the experimental setup is shown in Figure 4-17 (a) by using the equipment, which is described in section 4.1. A cuboid PVA gel phantom shown in Figure 4-17 (a) and an Intralipid phantom shown in Figure 4-17 (c) were

built according to section 4.2 to achieve μ_s' of 12 cm^{-1} and μ_a of 0.0235 cm^{-1} at 780 nm. The dimension of the PVA gel phantom is 60 by 30 by 45 mm. The 0.66 MHz transducer was used to generate continuous ultrasound waves. The FUR is placed at the centre of the phantom, in the axis of the optical source and detector.

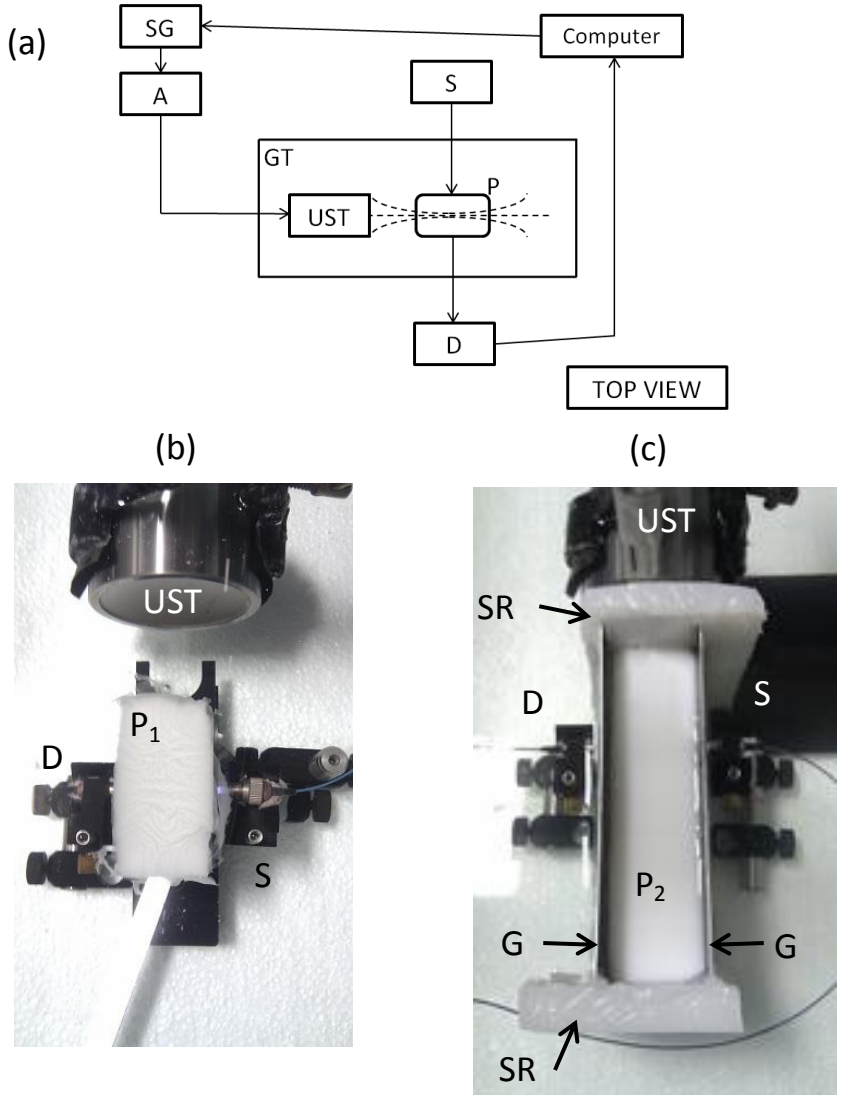

Figure 4-17 The basic schematic of the experimental setup (a); the image of the setup for: (b) PVA gel and (c) Intralipid phantoms. [SG: signal generator; A: RF amplifier; S: optical source; D: optical detector; UST: ultrasound transducer (0.66 MHz); P_1: PVA gel phantom; P_2: Intralipid phantom in a clear glass tank (GT); G: clear glass; SR: silicon rubber]

The diluted Intralipid solution was contained in a container (inner dimension of 130 by 35 by 120 mm) shown in Figure 4-17 (c), which consisted of clear glass (thickness 3 mm) for light transmission, silicone rubber for acoustic propagation and aluminium sheet covered by a layer of black plastic to prevent light reflection. The silicone rubber (ACC silicone MM228, thickness = 11 mm) has a Young's modulus of 0.62 MPa and was used as the interface due to its high stiffness to ensure that its shape would not change when the phantom was partially submerged in water and contained Intralipid solution. But it has fairly high acoustic attenuation, which is approximately 2.8 dB cm^{-1} (at acoustic frequency of 1 MHz) for general type of silicone rubber [Zell 2007] as compared to that of water of 0.0022 dB cm^{-1} or soft tissue of 0.5-1 dB cm^{-1} [Hedrick 2005]) at acoustic frequency of 1 MHz.

Preliminary study showed that there was adequate ultrasound propagated through these interfaces even when relatively low ultrasound excitation voltage was used. Furthermore the loss due to acoustic attenuation could be compensated by using higher excitation voltage. The same silicone rubber interface was also used to allow ultrasonic waves to propagate out of the phantom. It was assumed the mismatch of acoustic impedance between the Intralipid suspension and silicone would result in minimal reflection of the ultrasound.

The normal (ultrasound off) and the AO (ultrasound on) autocorrelation functions of the two types of phantom were measured at different integration times $t_{\int}$ and ultrasound excitation voltages V_{pp}. Measurements were also conducted in both multi-tau and linear-tau modes for comparison. The multi- and linear-tau modes of the digital correlation are discussed in section 4.1.3.1.

Unless otherwise stated, the basic settings for these measurements are $t_{\int}$ = 10 s, V_{pp} = 20 V for both multi- and linear-tau operation. Additional setting for the linear mode: 1-bit operation at sampling time of 20 ns, which results in a lag time τ from 20 ns to 1.54 ms for 768 correlation samples.

4.3.2 **Results and Discussions**

4.3.2.1 Multi-Tau versus Linear Tau Modes

The comparisons of multi-tau and linear-tau autocorrelation functions are presented in Figure 4-18 and Figure 4-19 for the PVA gel and the Intralipid phantoms respectively. Multi-tau autocorrelation function is sampled at non-linear sampling rate and linear-tau autocorrelation function is sampled at fixed sampling rate. These measurements were recorded when the ultrasound transducer was switched off.

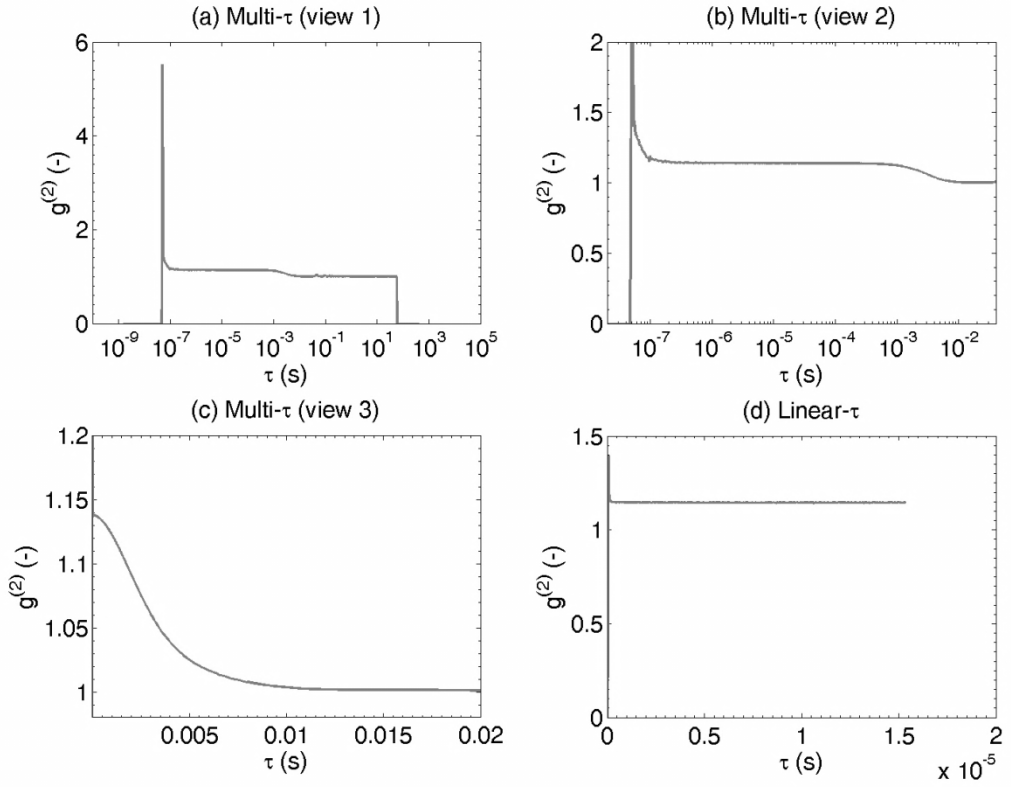

Figure 4-18 The autocorrelation functions of the PVA gel phantom measurement: (a) the full-view multi-tau autocorrelation, (b) the zoomed-in view of the multi-tau autocorrelation, (c) the linear τ-axis view of the multi-tau autocorrelation, (d) the linear-tau autocorrelation function, which only shows portion of the multi-tau measurement due to the limited number of correlation samples.

Figure 4-18 (a) shows the full multi-tau autocorrelation function, where the autocorrelation function starts at $\tau \approx 50$ ns because of the dead time of the photon counter. At this point, there is also a large distortion from the digital correlator, which extends to $\tau \approx 0.2$ μs in Figure 4-18 (b). The autocorrelation function stays linear until $\tau \approx 1$ ms, at which it starts to 'decorrelate'. This is caused by the speckle decorrelation after $\tau \approx 0.01$ s in Figure 4-18 (c). The linear-tau autocorrelation in Figure 4-18 (d) exhibit similar artefact at very low τ and it stays at constant level throughout because its largest τ only extends to 1.54 ms.

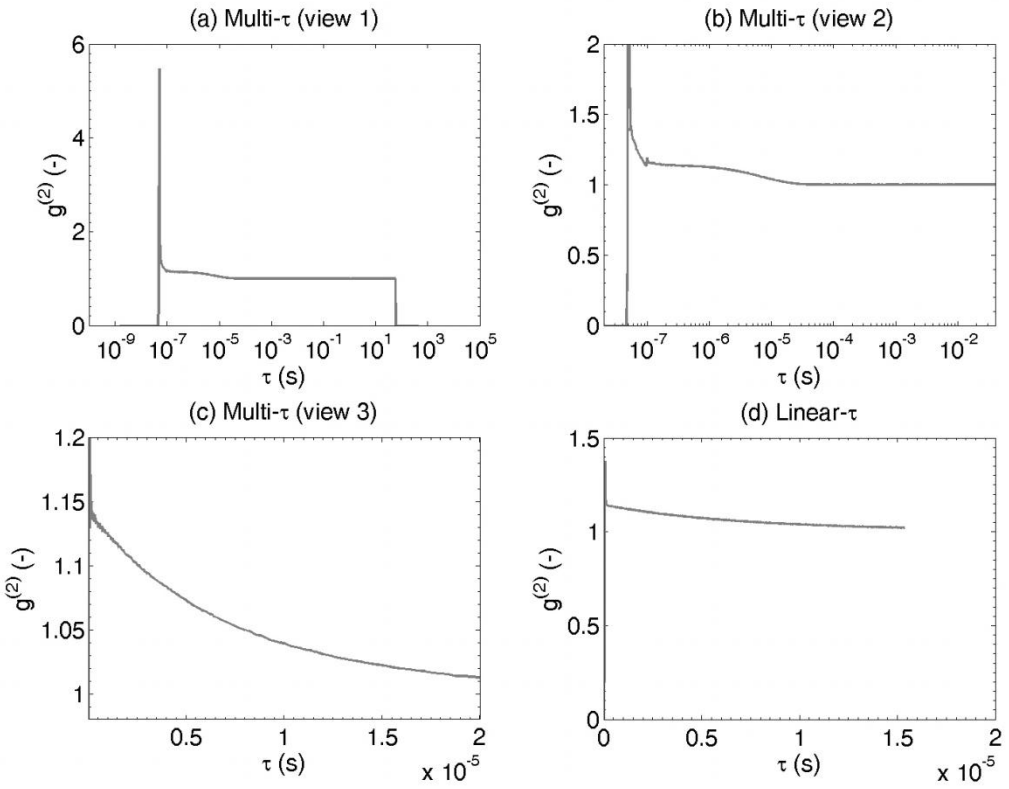

Figure 4-19 (a)-(c) The multi-tau autocorrelation functions of the Intralipid solution phantom measurement and (d) the linear tau autocorrelation function. They show the faster decorrelation of the speckle due to the Brownian motion of lipid particles.

The $g^{(2)}$ of the Intralipid phantom shows similar distortion at $\tau \approx 0$. However, the obvious difference is that the speckle starts to decorrelate at 1 μs and becomes

completely de-correlated at 30 μs. The linear-tau $g^{(2)}$ in Figure 4-19 (d) also shows faster exponential decay due to the Brownian motion of the scatterers in the fluid phantom.

These results imply that the multi-tau mode is more suitable for study that probes the decorrelation rate of diffuse medium where a large τ is needed to show the full dynamism of speckle. The linear tau operation can only show partial or no decorrelation effect depending on the type of medium.

4.3.2.2 Speckle Decorrelation Time

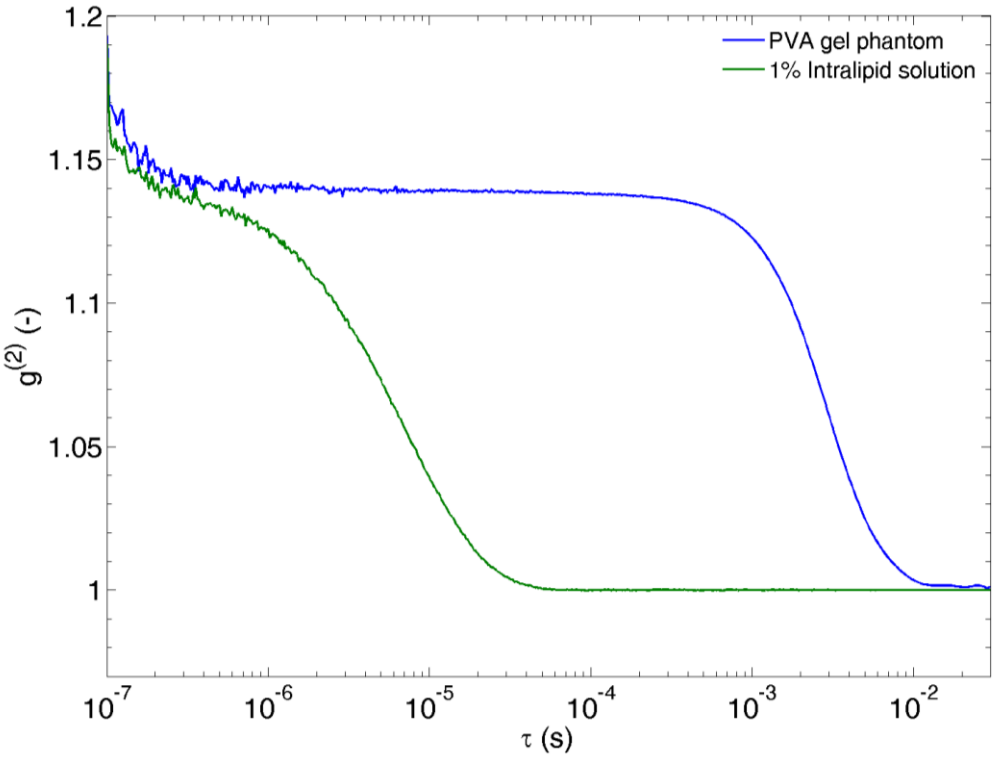

Figure 4-20 The speckle decorrelation rates of the PVA gel and Intralipid phantoms. Their optical properties are the same, which are μ_s' = 12 cm^{-1} and μ_a = 0.0235 cm^{-1} at 780 nm. The faster decorrelation rate of the Intralipid phantom is caused by the Brownian motion of scatterers.

The multi-tau $g^{(2)}$ of the PVA gel and Intralipid phantoms are plotted in Figure 4-20, and show the obvious difference in decorrelation rate. The decorrelation

time of the two media can be estimated from the $g^{(2)}$, which is the lag time when the correlation value drops from the unity (full correlation) to e^{-1} [Rajan 2008].

However, the unity correlation value is not shown in Figure 4-20. The $g^{(2)}$ is often normalised so that $g^{(2)}(0) = 1$ and $g^{(2)}(\infty) = 0$ [Bonner 1981, Boas 1997, Li 2005]; which means that at $\tau \approx 0$ s, the speckles are correlated and as τ increases, the speckles will slowly decorrelate and eventually become de-correlated at large τ when $g^{(2)}$ drops to zero. The $g^{(2)}$ in Figure 4-20 are converted to the reduced intensity autocorrelations, which are used by Li et al. [Li 2005]. The reduced $g^{(2)}$ is equal to $(g^{(2)}-1)/\beta$ and β can be estimated from the following process.

The normalised electric field autocorrelation function, $g^{(1)}$, is given by [Li 2005]:

$$g^{(1)}(\tau) = \frac{\langle E(t)E^*(t+\tau)\rangle}{\langle |E(t)|^2\rangle} = \frac{G^{(1)}(\tau)}{G^{(1)}(0)} \tag{4-13}$$

where $G^{(1)}(\tau)$ is the electric field autocorrelation function and $G^{(1)}(0) = \langle I(t)\rangle$, which is the time averaged intensity.

By rearranging the Siegert relationship, which is described in section 3.2.3, the following expression can be derived:

$$\left|G^{(1)}(\tau)\right| = \frac{\langle I(t)\rangle}{\sqrt{\beta}}\sqrt{g^{(2)}(\tau) - 1} \tag{4-14}$$

By combining equations (4-13) and (4-14), an expression for $g_{x,y}^{(1)}$ is given by:

$$g^{(1)}(\tau) = \sqrt{\frac{g^{(2)}(\tau) - 1}{\beta}} \tag{4-15}$$

When τ = 0 s and $g^{(1)}(0) = 1$, equation (4-15) can be rearranged so that β can be estimated from the following expression:

$$\beta = g^{(2)}(0) - 1$$

(4-16)

However, the digital correlator does not estimate the correlation value at $\tau = 0$, the 'zero' lag time, because of the dead time of the photon counter and the digital correlator. Instead of using $\tau = 0$, an alternative τ_0 is chosen when τ is very close to the zero lag time and when the autocorrelation values of $g^{(2)}(\tau_0)$ are nearly equal when ultrasound is switched on and off. Thus, β can be estimated by using equation (4-16). The results show the decorrelation times of the PVA gel and Intralipid phantoms in Figure 4-21.

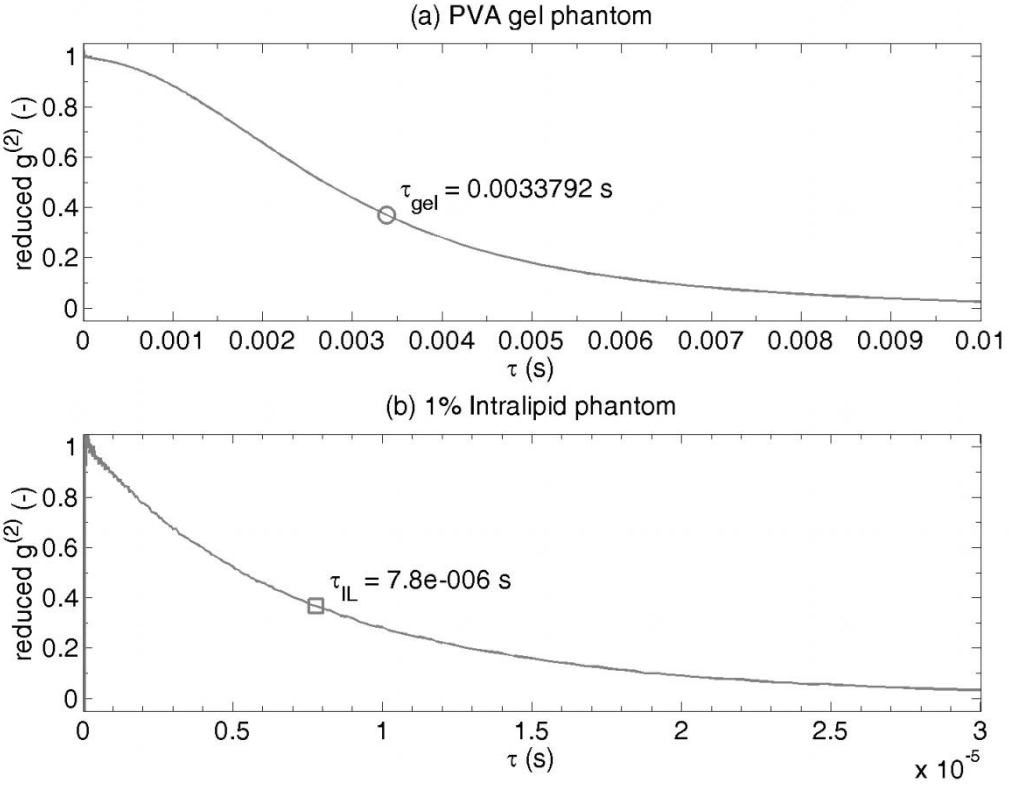

Figure 4-21 The speckle decorrelation times of (a) the PVA gel phantom and (b) 1% Intralipid phantom are 3.4 ms and 7.8 μs respectively. The decorrelation time is the lag time when the normalised autocorrelation function drops from the unity to e^{-1} (0.368).

4.3.2.3 Multi-Tau versus Linear Tau Modes of AO Measurements

This section describes the distinction between the AO and normal (optical) autocorrelation functions of using the PVA gel and Intralipid phantoms. The ultrasound transducer was activated for the AO measurements.

4.3.2.3.1 PVA Gel Phantom Measurement

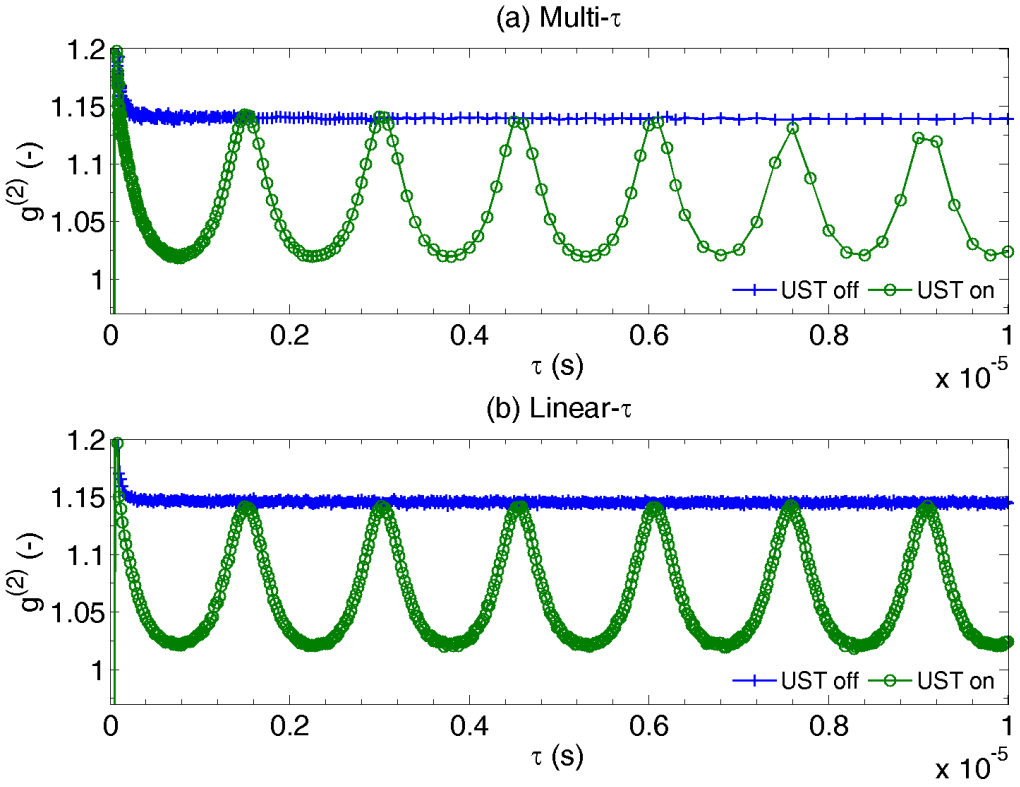

Figure 4-22 The comparison the normal and the AO autocorrelation functions of the PVA gel phantom in transmission mode when: (a) the multi-tau and (b) linear-tau modes are used. The multi-tau mode exhibits under-sampling at larger lag time while the linear mode shows the consistent AO modulation.

The comparison of the normal and AO autocorrelation function $g^{(2)}$ of the PVA gel phantom is presented in Figure 4-22. The AO modulation is obvious in both multi- and linear-tau $g^{(2)}$. The constant level of sinusoidal modulation agrees with the theory that is depicted in Figure 3-6. However, the multi-tau $g^{(2)}$ is under-sampled at large τ in Figure 4-22 (a). This implies that linear-tau operation is

more convenient for the AO measurement if the Fourier transform method is used in post-processing as discussed in section 3.3.2.1, which requires regular sampling.

4.3.2.3.2 Intralipid Phantom Measurement

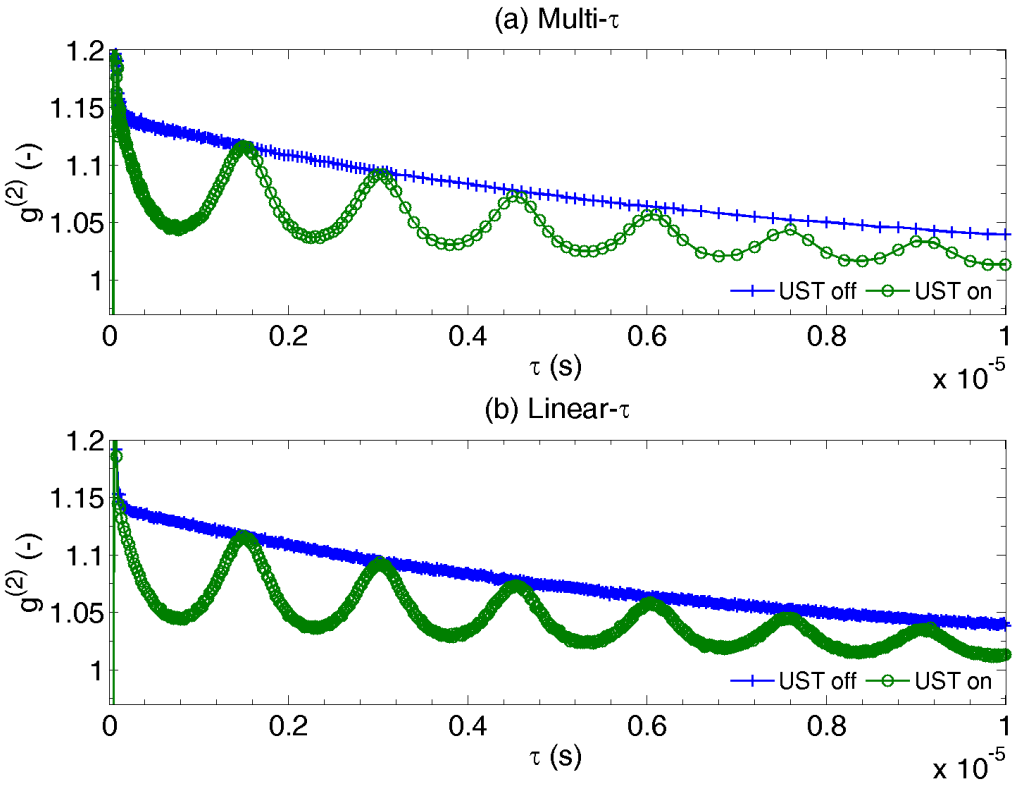

Figure 4-23 The comparison the normal and AO autocorrelation functions of the Intralipid phantom in transmission mode when: (a) the multi-tau and (b) linear-tau modes are used.

The multi- and linear-tau $g^{(2)}$ of the AO measurements using the Intralipid phantom are presented in Figure 4-23. This phantom has a faster decorrelation time, which is also evident in the exponential decay of the autocorrelation functions, which is also demonstrated in the literature [Leutz 1995]. In this case, the under-sampling effect observed in Figure 4-22 (a) is not obvious in Figure 4-23 (a).

The AO modulation in the PVA gel phantom measurement (Figure 4-22) is higher than that of the Intralipid measurement because the ultrasound waves is attenuated by the silicone rubber wall of the Intralipid phantom, which is shown in Figure 4-17 (c).

4.3.2.4 Effects of Varying Ultrasound Magnitude

In this study, the ultrasonic excitation voltage was gradually increased from 5 to 100 V peak-to-peak. The AO measurement results are presented in Figure 4-24 and Figure 4-25 for the PVA gel and Intralipid phantoms respectively. Only linear-tau $g^{(2)}$ was measured for this study.

4.3.2.4.1 PVA Gel Phantom Measurement

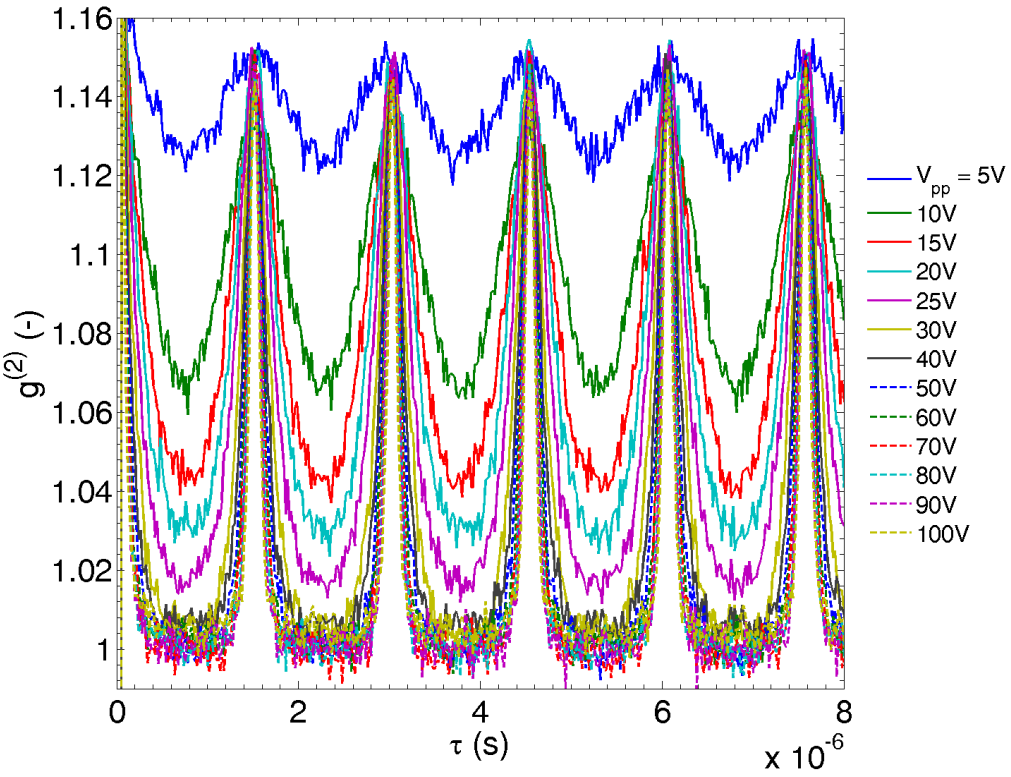

Figure 4-24 The comparison of the normal and AO autocorrelation functions of the PVA gel phantoms in transmission mode when a varying ultrasonic excitation voltage V_{pp} is used. The autocorrelation starts to saturate when $V_{pp} \geq 30$ V.

Figure 4-24 shows that increasing the excitation voltage increases the AO modulation, which agrees with AO theory [Sakadzic 2002]. Higher excitation voltage produces higher peak acoustic pressure that translates into greater particle displacement and variation of the refractive index, which causes greater AO modulation. However, increasing the peak pressure will cause the AO modulation to become non-linear. This is possibly caused by the ultrasound wave that becomes non-linear at higher pressure or the interaction between light and ultrasound is non-linear. Eventually, the AO modulation saturates when the excitation voltage is higher than 30 V.

This suggests that a low or moderate acoustic power should be used in AO measurement to prevent saturation of $g^{(2)}$. This is important because MD of the AO signal is extracted from the $g^{(2)}$ by the Fourier transform method that is discussed in section 3.3.2.1.

4.3.2.4.2 Intralipid Phantom Measurement

The result of ultrasound excitation study using the Intralipid phantom is presented in Figure 4-25. The obvious observation is that the AO modulation saturates at higher excitation voltage (> 50 V) when compared to the result of the PVA gel measurement (Figure 4-24). For the same excitation voltage, the AO modulation of the Intralipid phantom measurement is smaller when compared with that of the PVA gel phantom. This is because the silicone rubber wall of the phantom attenuates the ultrasound beam.

Increasing the excitation voltage also causes a faster exponential decay of the $g^{(2)}$. This could be caused by acoustic streaming and small bubbles, which produced at high acoustic pressure. A preliminary study showed that the presence of small bubbles in deionised and degassed water when peak acoustic pressure exceeds 250 kPa.

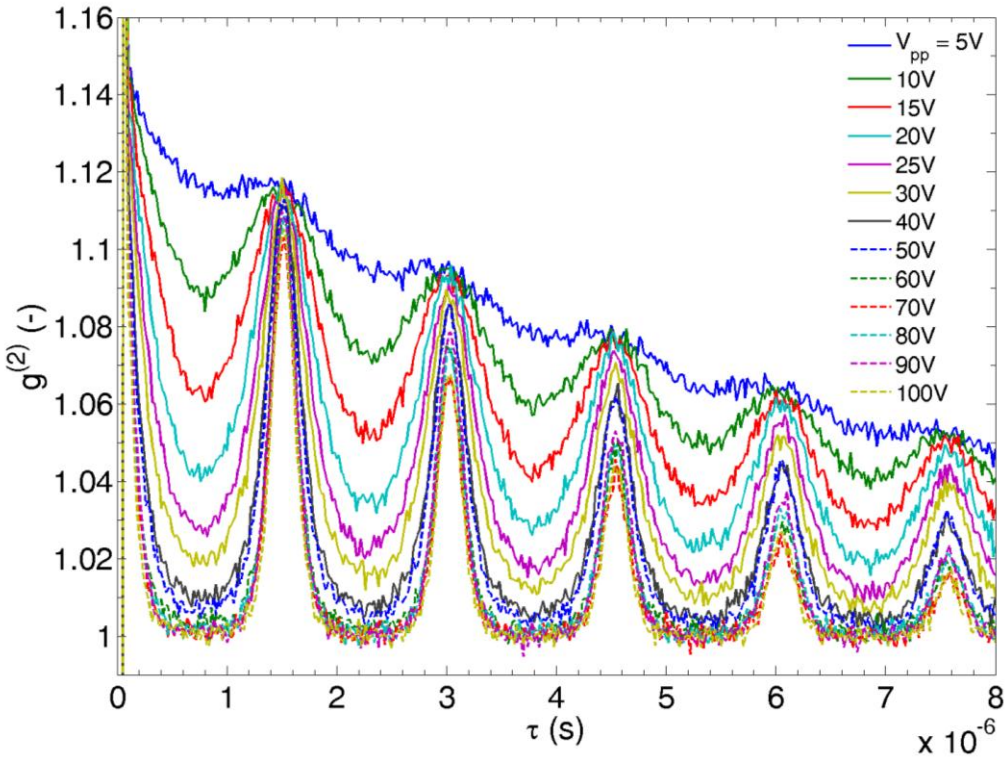

Figure 4-25 The comparison the normal and the AO autocorrelation functions of the Intralipid phantom in transmission mode when varying level of ultrasonic excitation voltage V_{pp} is used. Larger V_{pp} increases the degree of AO modulation and increasing V_{pp} further (> 50 V) causes the autocorrelation function to saturate.

4.3.2.5 Integration Time of Digital Correlator

This section explores the effect of varying integration time $t_{\int}$ on the normal and AO autocorrelation functions for the PVA gel and Intralipid phantoms. In addition, more measurements were carried out when the amount of light injected into the phantoms was attenuated by a neutral density filter, which was introduced in between the optical source and phantom.

4.3.2.5.1 PVA Gel Phantom Measurement

The results of the PVA gel phantom measurements are presented in Figure 4-26 and Figure 4-27 for high and low input light intensities respectively. The use of high input light intensity resulted in an average photon count rate of

approximately 1 MHz and low input light intensity resulted in an average intensity of approximately 200 kHz. The general observation is that the statistical noise of the measurements can be minimised by increasing the integration time and the detected intensity [Schätzel 1990]. When the high input light intensity is used, an integration time of 10 s is generally adequate. When the low input light intensity is used, 30 s or longer is required.

When low $t_{\int}$ and low input light intensity are used, Figure 4-26 (a)-(c) show higher noise level, and the peak value of the sinusoidal autocorrelation function and the baseline value of the un-modulated autocorrelation function is not the same. This suggests that there is a slight normalisation error caused by the higher noise level shown in Figure 4-26 (b). This error can be minimised when a longer $t_{\int}$ is used as shown in Figure 4-26 (d)-(f). Low photon count and short $t_{\int}$ result in very noisy autocorrelation function in Figure 4-27. Increasing $t_{\int}$ generally improve the signal to noise ratio. However, $t_{\int}$ will have to be longer than 60 s in order to achieve the same fidelity as that of when high input light intensity is used, which is shown in Figure 4-26 (f).

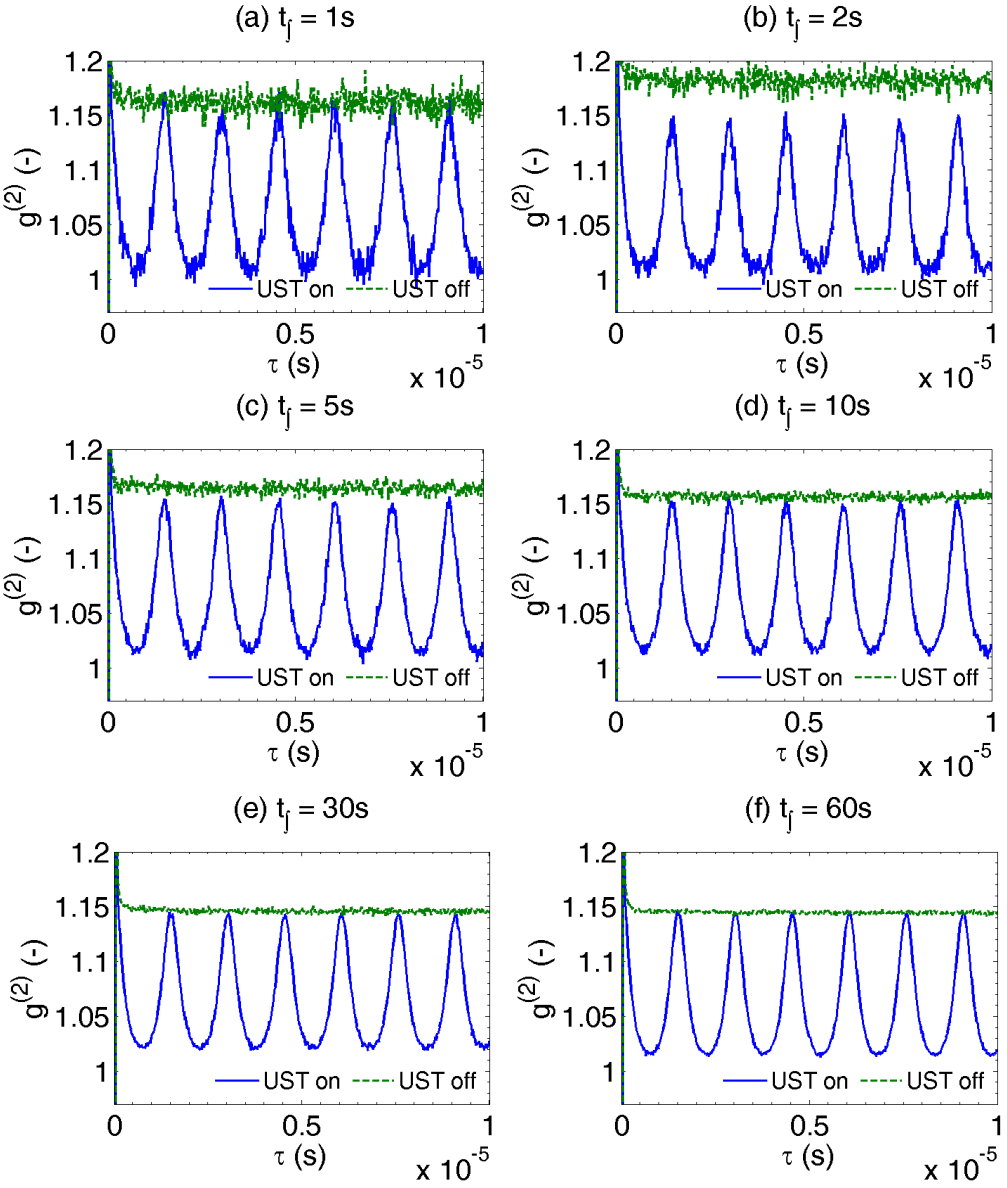

Figure 4-26 The comparison between the normal and AO autocorrelation functions when different integration time $t_\int$ and high input light intensity are used for the PVA gel phantom measurements in transmission mode.

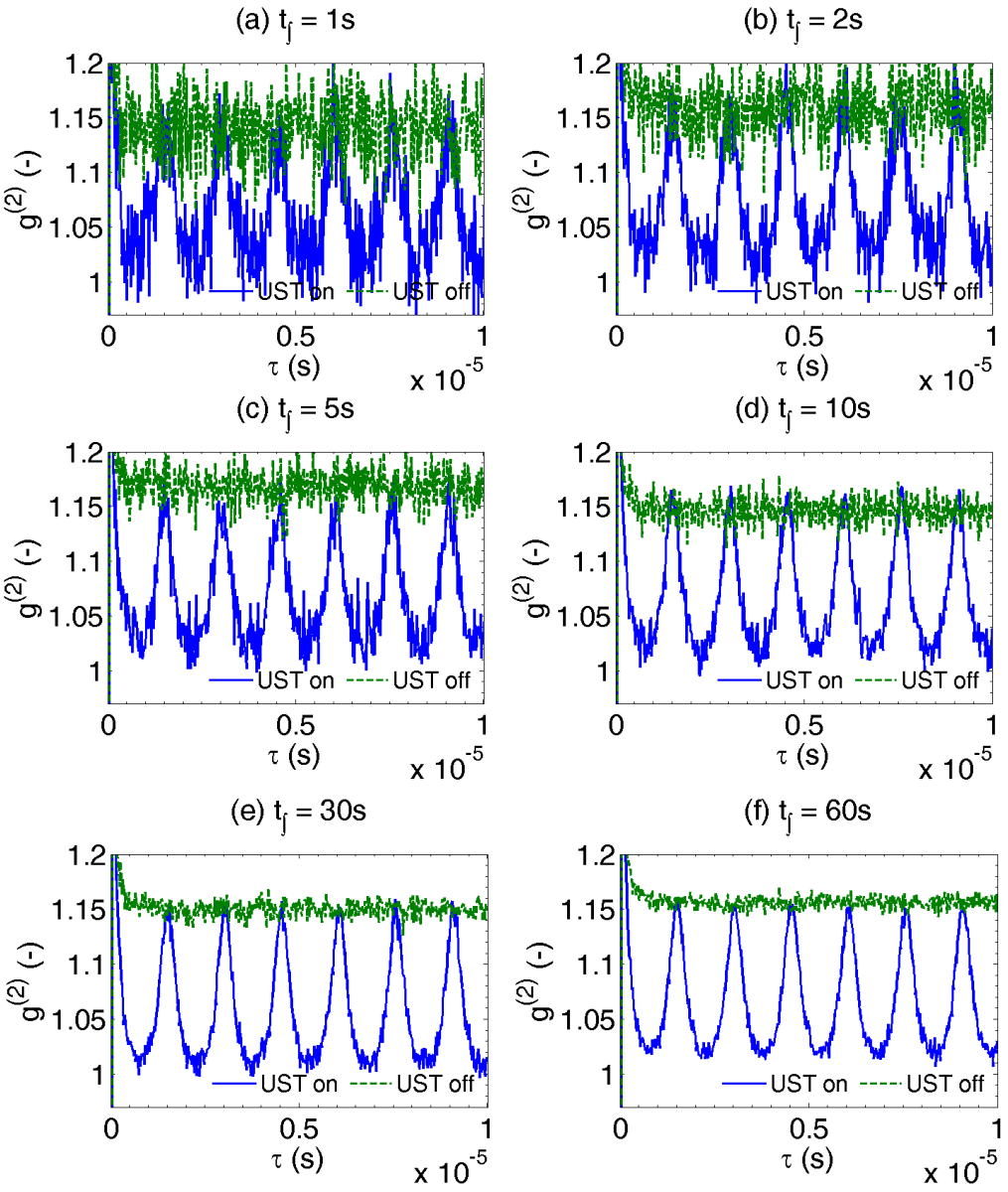

Figure 4-27 The comparison between the normal and AO autocorrelation functions when different integration time $t_\int$ and low input light intensity are used for the PVA gel phantom measurements in transmission mode.

4.3.2.5.2 Intralipid Phantom Measurement

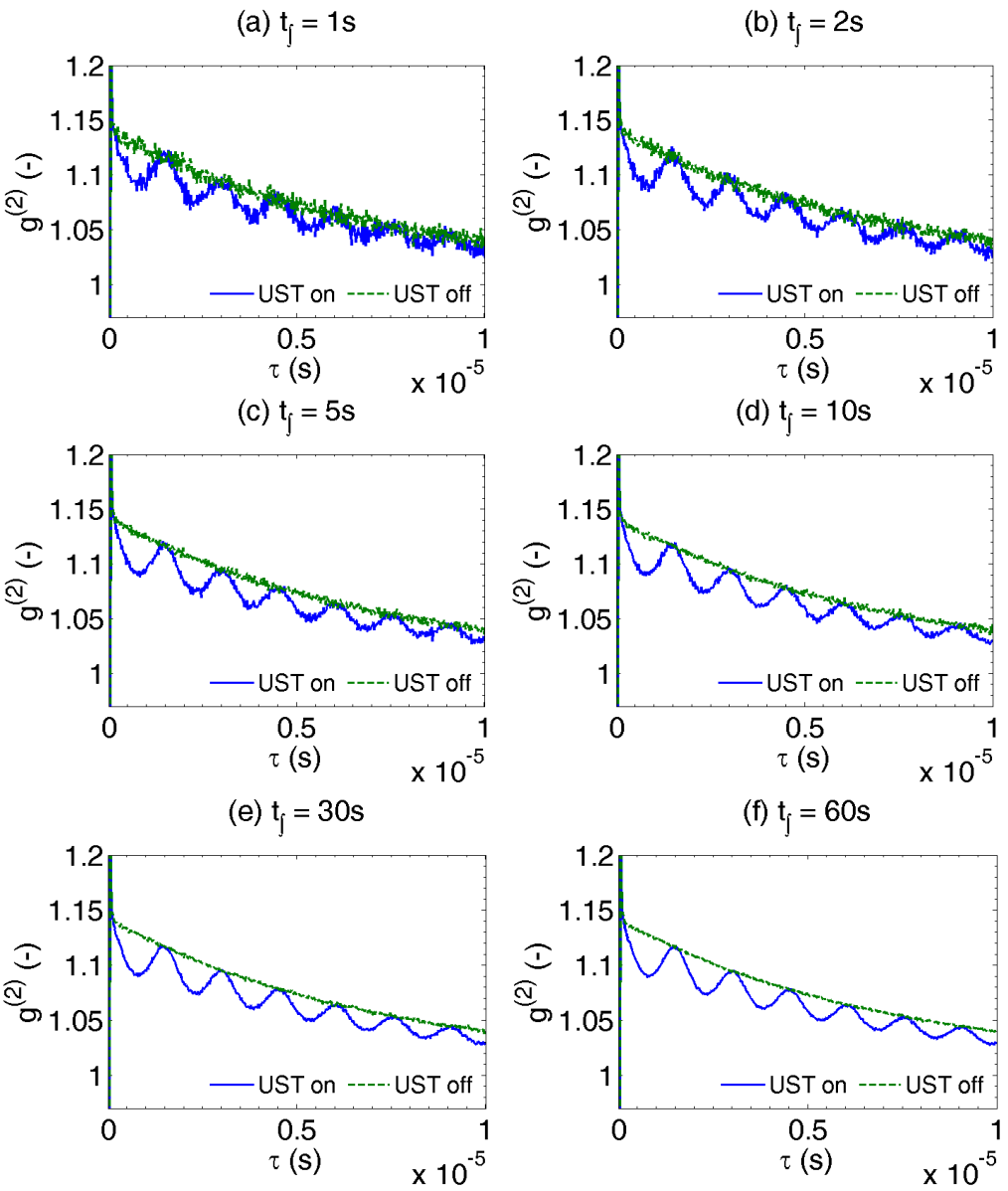

Figure 4-28 The comparison between the normal and AO autocorrelation functions when different integration time $t_{\int}$ and high input light intensity are used in the Intralipid phantom measurements in transmission mode.

The integration time study results for the Intralipid phantom are summarised in Figure 4-28 and Figure 4-29 for high and low input light situation respectively.

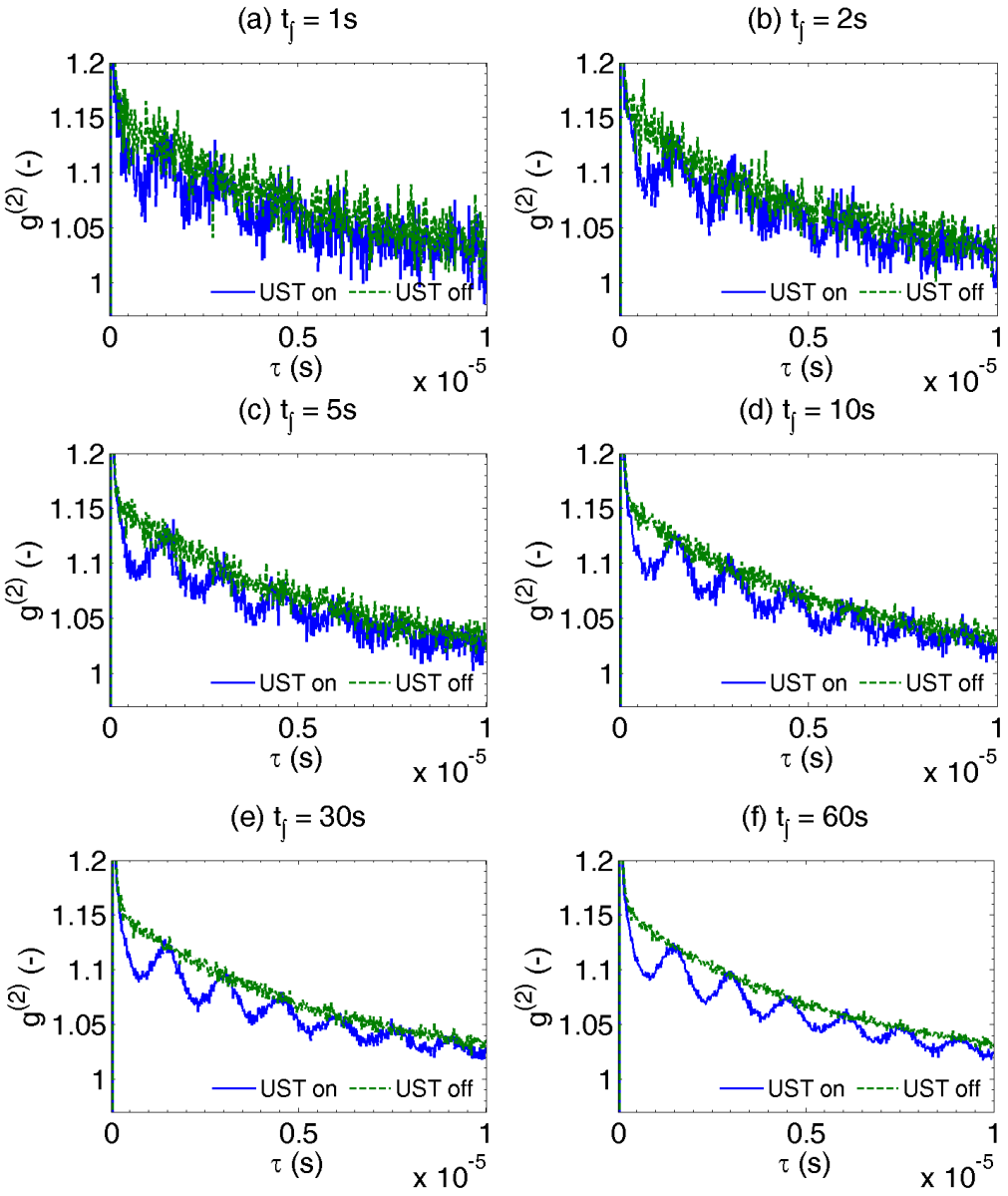

Figure 4-29 The comparison between the normal and AO autocorrelation functions when different integration time $t_\int$ and low input light intensity are used for Intralipid phantom in transmission mode.

When compared with the results shown in section 4.3.2.5.1, the drift of the autocorrelation function baseline in Intralipid phantom is less. Secondly, the AO modulation is smaller in Intralipid phantom measurement because of reduced peak ultrasound pressure caused by the silicone rubber wall. These observations are

similar to other results presented in the previous section. Generally, longer $t_{\int}$ and higher input light intensity improve the signal to noise ratio of measurement.

4.3.3 Summary

In summary, the key findings of section 4.3 are:

1. The multi-tau autocorrelation is suitable for study where the decorrelation rate of speckles because of the large range of lag time. The decorrelation time of a medium can be estimated from the temporal intensity autocorrelation function.
2. Linear-tau operation suits AO measurements because the fixed sampling rate simplifies the post signal processing of AO measurement.
3. Increasing the integration time (measurement time) and the input light intensity generally reduces the statistical noise of the autocorrelation function.
4. A continuous-wave ultrasound peak pressure higher than 250 kPa for a fluid based phantom such the Intralipid phantom should be avoided because the autocorrelation function becomes non-linear and saturated.

5 Spatial Sensitivity to a Localised Change in Absorption

The limitations of conventional NIRS systems for non-invasive tissue oxygenation monitoring are discussed in section 2.2.2. Experimental and simulation studies of NIRS spatial sensitivity have demonstrated that NIRS measurement suffers from poor sensitivity when the ROI is in the deeper region and it is highly susceptible to significant absorption changes in the SFR of tissue. It is proposed that the AO method, which is discussed in section 3.3, can potentially improve the sensitivity in the ROI.

The spatial sensitivity of an optical system can be defined as the amount of change detected by the AO or optical system in response to a localised absorption change in a particular location within a medium [Cui 1991]. It has been shown in optical measurement that the observed drop in recorded intensity is proportional to the amount of light that has similar path lengths for a given location of the local absorber [Fantini 1995]. The effect of a small absorbing defect on the light propagation is summarised in Figure 5-1 [Ostermeyer 1997]. For a single light source and an absorbing sphere in an infinite diffusive medium, the total fluence rate at a particular location is reduced because the propagating photons are being absorbed by the sphere. The change of the fluence from the steady state (when light is isotropic) is shown in Figure 5-1. The closer the location is to the absorbing sphere, the greater amount of the light is absorbed and the highest absorption occurs within the sphere.

Therefore, by systematically relocating the local absorber throughout a predefined scanning area within the medium and recording the change in detected intensity accordingly; a map of the photon path distribution can be formed [Fantini 1995]. This photon path distribution can also be interpreted as the photon density measurement function [Arridge 1995] or the spatial sensitivity [Vaithianathan 2004, Patil 2011] of the optical system.

Figure 5-1 The change in the total fluence rate ϕ^{Pert} (solid line) from the steady state (ϕ^{Pert} = 0) due to an absorbing (μ_a is twice of background) sphere is the sum of the changes, which is caused by the surface (dotted line) and the volume (dashed) of the absorbing sphere [Ostermeyer 1997].

Another method uses the similar principle but instead of a highly absorbing local absorber, a highly absorbing plate with an opening [Del Bianco 2002] is used. The small opening allows diffuse photons to propagate through. By relocating the opening, the photon path distribution can also be obtained.

The aim of the experimental study described in this chapter is to demonstrate that the sensitivity of optical measurements in the ROI can be improved by using the AO method. To do so, the spatial sensitivity to local absorption change of AO and optical measurements were mapped and compared in both transmission and reflection modes. The AO detection system is discussed in section 4.3, whereby it records the normalised temporal intensity autocorrelation of the ultrasound modulated speckle. Three optical measurements were investigated and they are:

1. The intensity measurement using the single photon counter I_{PC} that is described in section 4.1.1, 4.1.2 and 4.1.3.
2. The intensity measurement using the CCD camera I_{CCD}.

3. Spatially resolved measurement using the CCD camera $\frac{\partial A_{SR}}{\partial \rho}$. This technique is discussed in section 2.2.3 and employed in a commercially available clinical NIRS monitor Hamamatsu NIRO 300 [Suzuki 1999].

AO and optical compatible phantoms for the background medium and a local absorber were developed for the spatial sensitivity measurements in transmission and reflection modes. A ROI was defined in the medium and the FUR was placed there. The local absorber, that had very high μ_a to ensure maximal light absorption, was introduced within the phantoms and both AO and optical measurements were made. The local absorber was then systematically relocated within a predefined scanning area and measurements were repeated. Reference measurements were also made when the local absorber was removed from the medium so that the change in detected signal could be calculated to form the sensitivity map.

To inform about the performance of the detection methods, the superficial and the ROI sensitivities are compared and discussed. Additional comparisons were made based on the mean penetration depth [Del Bianco 2002] and penetration depth [Vaithianathan 2004, Correia 2010, Patil 2011].

5.1 Materials and Methods

5.1.1 Experimental Setup

The schematic of the experimental setup is shown in Figure 5-2 for a reflection mode configuration. The same setup is applicable to transmission mode measurement except the positions of the optical source-detector pair and a different phantom is used. The geometric illustrations and images of the phantoms for transmission and reflection mode measurement are shown in Figure 5-3 and Figure 5-4 respectively. The phantom is partially submerged in a clear glass tank, which is filled with deionised water for acoustic coupling between the focused ultrasound waves and the phantom. The setup was contained in a black enclosure to block out external light.

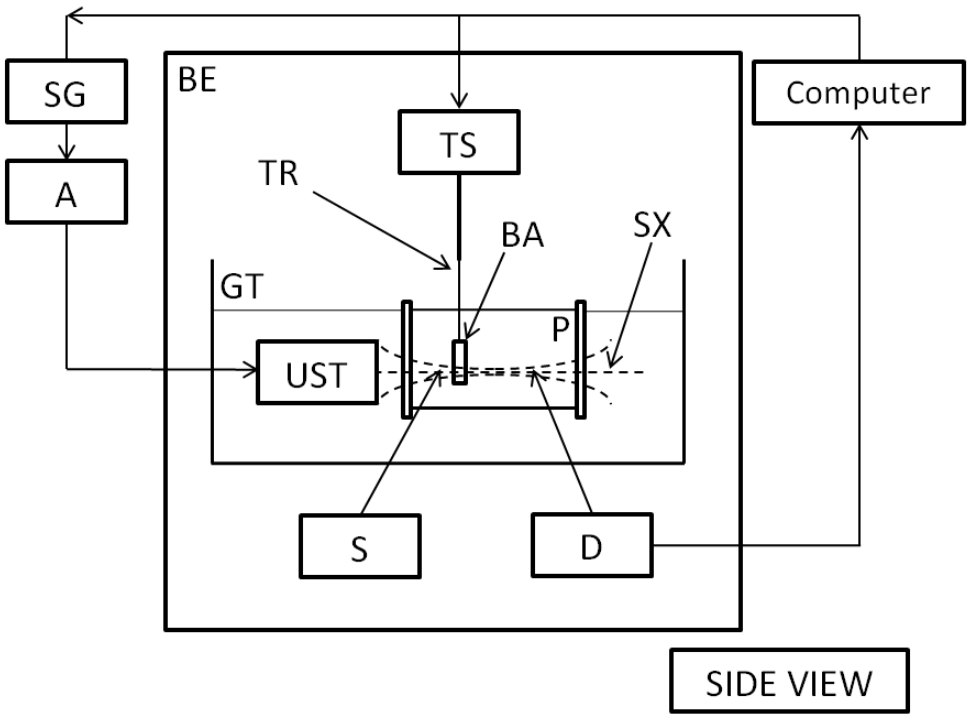

Figure 5-2 The top view of the experimental setup: UST: ultrasound transducer, GT: clear glass tank (6 mm thickness), P: phantom, S: optical source, D: optical detector, BA: black local absorber, TR: thin metallic rod, TS: translation stages, BE: black enclosure, SG: signal generator and A: RF amplifier.

5.1.2 **Phantoms**

Conventional tissue mimicking phantoms [Firbank 1995, Cubeddu 1997, Hebden 2006, Pogue 2006, Price 2010] used in optical measurement studies have to be adapted for spatial sensitivity mapping. This is because the localised change in optical properties needs to be relocated throughout the phantom. Typically the local change in optical property is achieved by a solid absorber, which can be spherical [Fantini 1995, Patil 2011] or cylindrical [Bruce 1994, Vaithianathan 2004]. The position of the local absorber within a fluid phantom is mechanically controlled. More advanced design is based on photochromic material (electrical charge [Barbour 2006] or heat [Hebden 2008]) that allows dynamic control of the location of the localised change in absorption.

However solid phantoms are not suitable for AO studies because they would strongly attenuate and reflect the ultrasonic waves. Typical phantoms used in AO studies are gel [Devi 2006] or fluid [Wang 1995] based in order to allow ultrasonic propagation. A summary of phantoms used in AO studies can be found in section 9.2. Elastic gels and rubber [Rickey 1995, Chu 1997, Zell 2007] are often used in ultrasound imaging studies because of their compliance and stability respectively.

The size of the phantom has to be able to contain the predefined scanning area (SA) for sensitivity mapping. A small SA might result in potential loss of information from the sensitivity maps and a large SA would result in inadequate detected light intensity. The transmission mode SA, its size was set to 24 by 24 mm to allow the optical detector to capture adequate photons. For reflection mode, SA was 30 (typical S-D separation in optical measurement) by 20 mm. These dimensions had been verified and optimised from our preliminary study [Gunadi 2011]. They are also similar to those that are used in the literature (transmission [Fantini 1995] and reflection [Bruce 1994] modes) so that the resulting sensitivity map would contain useful information. For simplicity, the *x*-axis of SA is the horizontal distance from the optical detector for transmission mode and from the optical source for reflection mode. The *y*-axis is the perpendicular distance from the detection plane for both modes. They are shown in Figure 5-3 (a) and Figure 5-4 (a) for transmission and reflection modes respectively.

The focal distance of the ultrasound transducer was also taken in to consideration when defining the dimension of the SA and the phantom. The centre of the FUR is the point where maximum peak acoustic pressure is observed. The ultrasound transducer has a focal distance of 73 mm. This implies that the space available between the centre of SA (also the centre of FUR) in the FUR horizontal axis is less than half of the focal distance i.e. 36.5 mm because of the gap between transducer and phantom and thickness of the interface between them.

In summary, the requirements for the phantom and the local absorber, which are suitable for both AO and optical measurements, are:

1. Minimal acoustic attenuation.
2. Minimal mismatch in acoustic impedance of the phantom, local absorber and UST.
3. Optical properties can be controlled.
4. Local absorber can be readily re-positioned.
5. Optically and acoustically stable during the process of mapping.

5.1.2.1 Tissue Mimicking Phantom

The tissue mimicking phantom (P) is the background diffusing medium whose optical property is similar to that of the healthy soft tissue. To allow ease of acoustic propagation and relocation of the local absorber, a fluid phantom was used. The fluid phantom consisted of Intralipid solution that was diluted to achieve the desired optical properties. Its acoustic properties were similar to water [Kinnunen 2005, Laufer 2010] at room temperature. In the beginning, the absorption was set low (μ_a of water is 0.0235 cm^{-1} at wavelength 633 nm) and the μ_s' was set to 12 cm^{-1} at wavelength 633 nm by diluting 10% Intralipid to 9.35% [van Staveren 1991, Flock 1992], which are typical of human tissue level. The details of the determination of optical properties of Intralipid solution can be found in section 4.2.1. However, the disadvantage of using Intralipid solution is that its optical properties may vary slightly over an extended period of time as the fat globules may set at the bottom of the phantom. However, its effect can be averted by reference measurements, which were carried out over the course of mapping. It is discussed in more detail in later section of this chapter. The Intralipid phantom development is described in section 4.3.1. The resulting Intralipid phantoms for the transmission and the reflection mode measurements are depicted in Figure 5-3 (b) and Figure 5-4 (b) respectively.

The silicone rubber was milky in colour; therefore the SA was positioned so that the distance between the rubber and SA was significantly more than the scattering

length of the background medium. This was carried out to ensure that the silicone rubber would have minimal effect on the measurement.

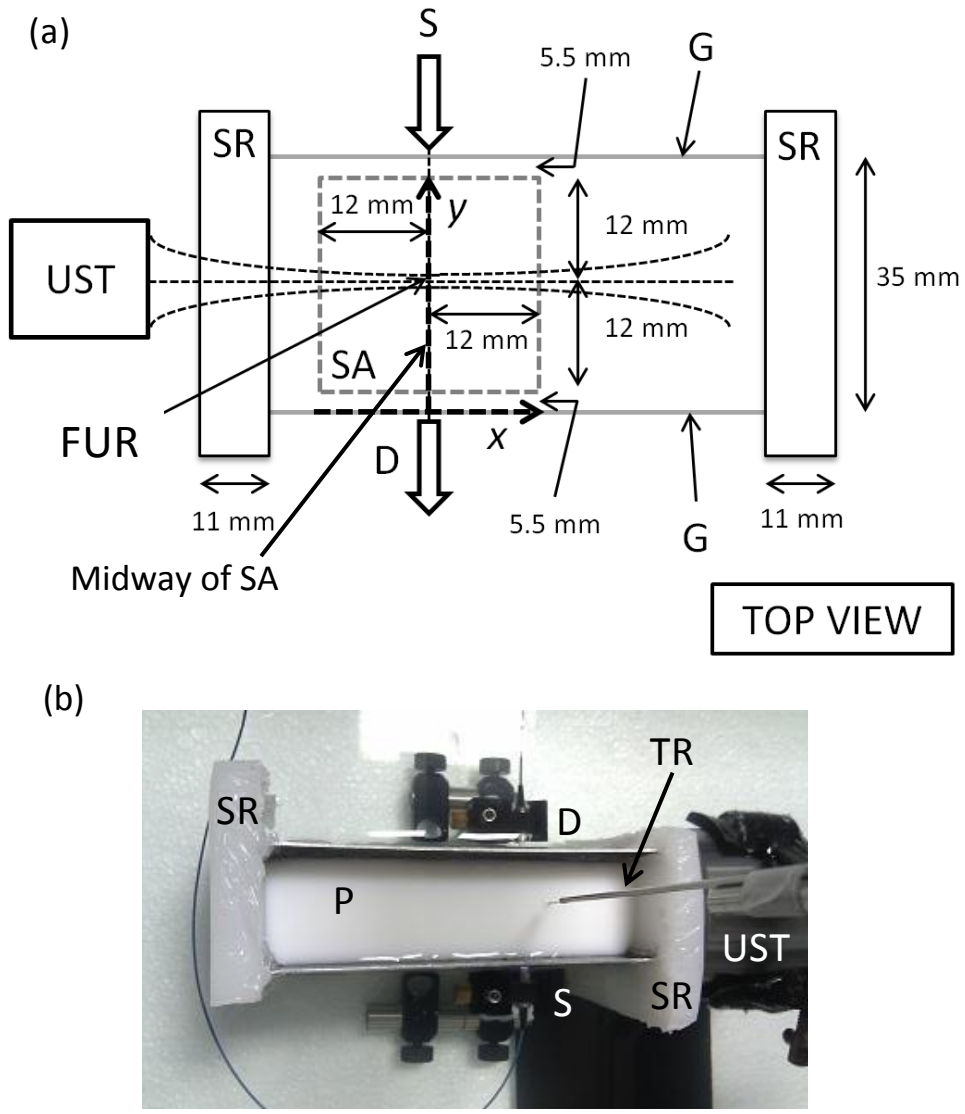

Figure 5-3 (a) Geometry of the transmission mode phantom and the corresponding scanning area (SA) with the maximum peak pressure of the FUR at the centre of SA; the distance between D and SA is 5.5 mm; x-axis: horizontal distance from D, y-axis: perpendicular distance from D, G: clear glass, SR: silicone rubber; (b) picture of the phantom.

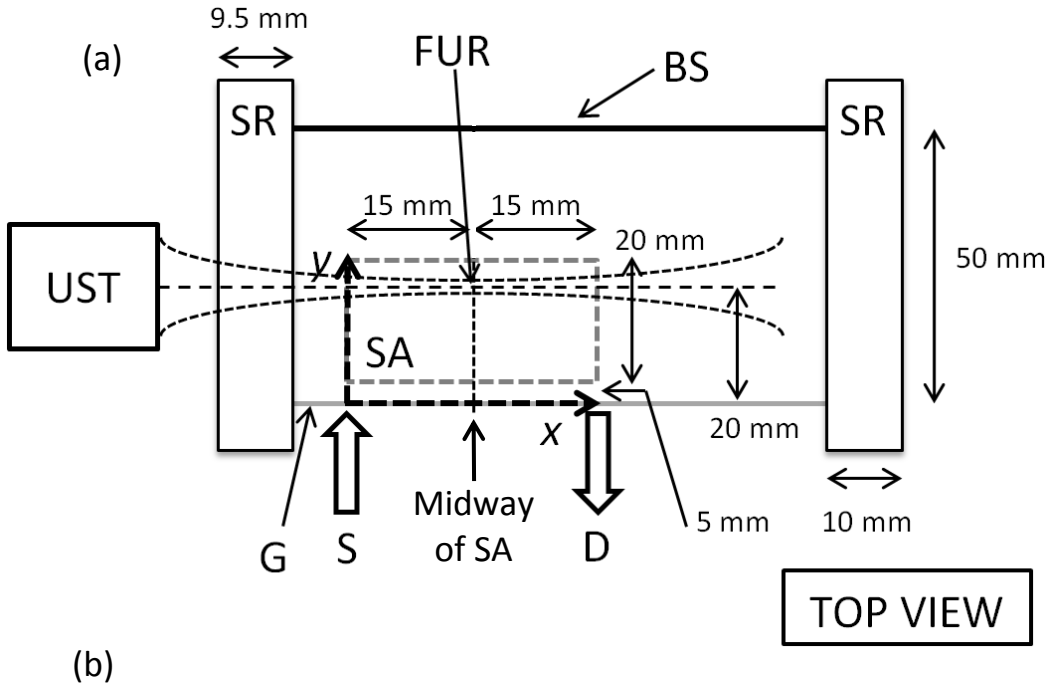

Figure 5-4 (a) Geometry of the reflection mode phantom and the corresponding scanning area (SA) with maximum peak pressure of FUR 20 mm from the S-D plane (y-axis); x-axis: perpendicular distance from S; BS: black surface

5.1.2.2 Local Absorber

The local absorber of 5 × 5 × 12 mm is made of 10% poly-vinyl alcohol (PVA) soft gel [Price 2010], which is shown in Figure 5-5 (a). Its optical properties are: μ_s' = 12 cm^{-1} and μ_a = 40.3 cm^{-1} at 780 nm, which were achieved by doping the

PVA with titanium dioxide and black polyurethane pigment (Tiranti 410-520) for scattering and absorption respectively. The black pigment is used instead of the NIR dye because the pigment does not diffuse out of the PVA gel when submerged in water. Preparation of the PVA gel is detailed in section 4.2.2. The local absorber was held by a thin metallic rod within P, which is shown in Figure 5-4 (b).

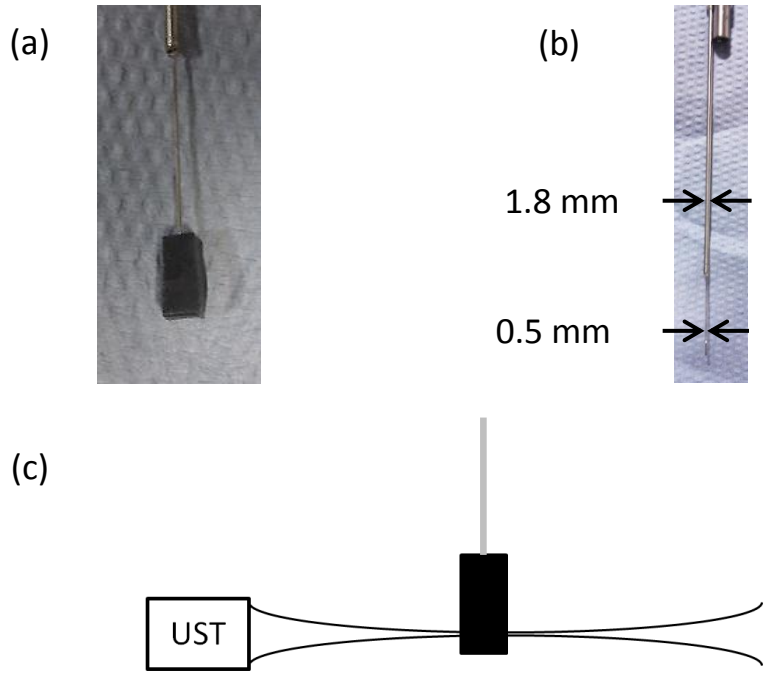

Figure 5-5 (a) An image of the local absorber held by a thin metallic rod (TR) (b) and only the lower portion of the absober (c) will coincide with the FUR during scanning to minimise the effect on the ultrasound propagation by TR.

The acoustic property of the PVA gel has to be taken into account when it is in the FUR. Another important point is that the PVA gel used in this study is different from those in the literature because it is made of a solvent of 50% water and 50% ethanol by volume, instead of just water. However, according to Price et al. [Price 2010] the Young's modulus of the PVA gel made in this way is 20kPa at 20% strain, which is highly similar to healthy breast tissue. Therefore, it is assumed

that the acoustic properties of the ethanol-water based PVA gel is similar to those of the healthy breast tissue.

Assuming that the acoustic impedance of water at room temperature Z_{water} is 1.48 MRayls [Hedrick 2005] and the PVA, Z_{breast} is averaged to 1.54 MRayls (1.42-1.66 MRayls) [Zell 2007], the percentage of reflection $\%R$ is 0.40% by using equation (5-1). Therefore, there is no significant acoustic reflection due to the impedance mismatch.

$$\%R = \left(\frac{Z_{breast} - Z_{\omega ater}}{Z_{breast} + Z_{\omega ater}}\right)^2 \times 100\% \tag{5-1}$$

Furthermore, the speed of sound in healthy breast tissue at room temperature is 1500 m/s (average of 1430-1570 m/s) [Zell 2007], which is also similar to the speed of sound in water of 1480 m/s [Hedrick 2005].

A control sensitivity map study was carried out to verify these assumptions, whereas the local perturbation, which was made of the PVA gel, possessed the same optical properties as the background medium. So, any significant change in its spatial sensitivity can be attributed to changes in ultrasound propagation due to the slight difference in the mechanical properties between the local absorber and the background medium.

5.1.3 Measurement Systems

This section details the instrumentation and methods that measure the optical and AO signals.

5.1.3.1 Acousto-Optic Measurement

The acoustic generation was provided by an immersion focused ultrasound transducer (Precision Acoustics, PA304), whose centre frequency f_a is 0.66 MHz. Its focal distance is 72.6 mm and its focal region is 4.2 by 4.4 mm (focal zone widths) by 29.36 mm (focal zone length). The transducer was operated in the

continuous wave mode to achieve peak acoustic pressure of 180.8 kPa at its peak focal region in the phantoms. The low acoustic pressure was used to minimize the possibility of cavitation and excessive heating. The transducer was driven by a signal generator (Agilent Technologies, 33210A) through a RF amplifier (Electronics & Innovation Ltd, A075).

The AO detection system is based on the detection of temporal variation of laser speckle intensity due to the AO effect, which is detailed in section 3.3. The laser source is a multi-mode 62.5 μm fibre-coupled continuous 808 nm laser source (CrystaLaser, IRCL-100-808-S) of a coherent length more than 10m. The detector is a single mode 9 μm fibre-coupled single photon counter (PC) (Perkin Elmer, SPCM-AQR-14) and a digital correlator (Correlator.com, Flex02-01D), which is connected to the computer. More details about the instrumentation can be found in section 4.1.

The digital correlator was operated in linear mode to record the normalised temporal intensity autocorrelation function $g_{x,y}^{(2)}(\tau)$ when the ultrasound was activated, where τ is the lag time in seconds and (x,y) denotes the position of the local absorber in the phantom. An additional reference measurement of the autocorrelation function $refg_{x}^{(2)}(\tau)$ was recorded when the local absorber was relocated out of the phantom for every x position. The autocorrelation function was sampled at a period of 20 ns from the lag time of 20 ns to 15.36 μs. The integration time (measurement time) was set to 20 seconds. The MD is then computed from $g_{x,y}^{(2)}(\tau)$.

5.1.3.2 Intensity Measurement using the Single Photon Counter, I_{PC}

The first optical system uses the same optical component as the AO detection system discussed in section 5.1.3.1 when the ultrasound is deactivated. The measurement is the mean intensity $I_{PC}(x,y)$ in photon count per second (Hz), which is the average of the intensity time series $I_{x,y}(t)$ over the course of the 20

seconds measurement period for every position of the local absorber. Similarly, a reference intensity measurement $refI_x(t)$ was also recorded.

5.1.3.3 Intensity Measurement using the CCD camera, I_{CCD}

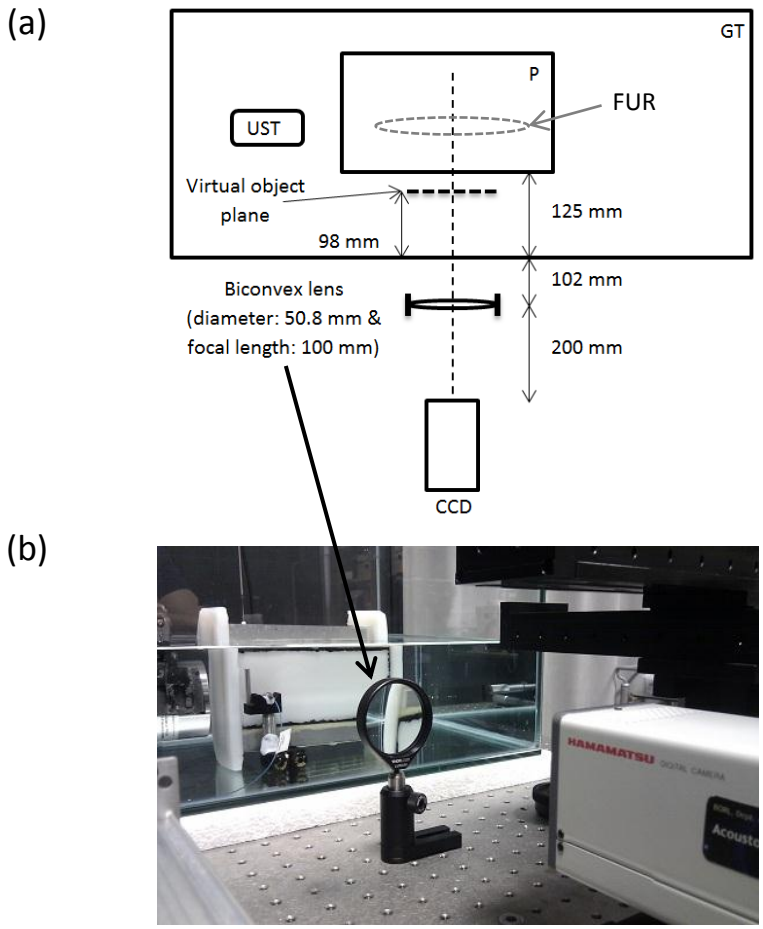

Figure 5-6 (a) The CCD incorporates a lens setup to maximise light detection (with unity magnification) and the speckle size is matched to the CCD pixel size. (b) An image of the CCD setup for a reflection mode measurement.

The second optical system uses the 12-bit 1344 x 1024 (8.67 x 6.60 mm) CCD camera (Hamamatsu Orca 03G02), which is shown in Figure 5-6. The CCD setup incorporated a lens to maximise light detection (magnification factor is unity) and was adjusted to match the speckle size to the pixel size, which is 6.45 μm. The exposure time was set to 5 ms to ensure adequate detection of light.

The CCD camera captured five images for every location of local absorber. The median value of spatial mean intensities of the five images was chosen as the CCD intensity $I_{CCD}(x, y)$. This was carried out to reject potential outlier measurements, which might be affected by presence of reflective dust particles in GT that might come into the view of the camera. Likewise, reference CCD intensity $refI_{CCD}(x)$ was recorded for every *x* position.

5.1.3.4 Spatially Resolved Measurement using the CCD camera, $\partial A_{SR}/\partial \rho$

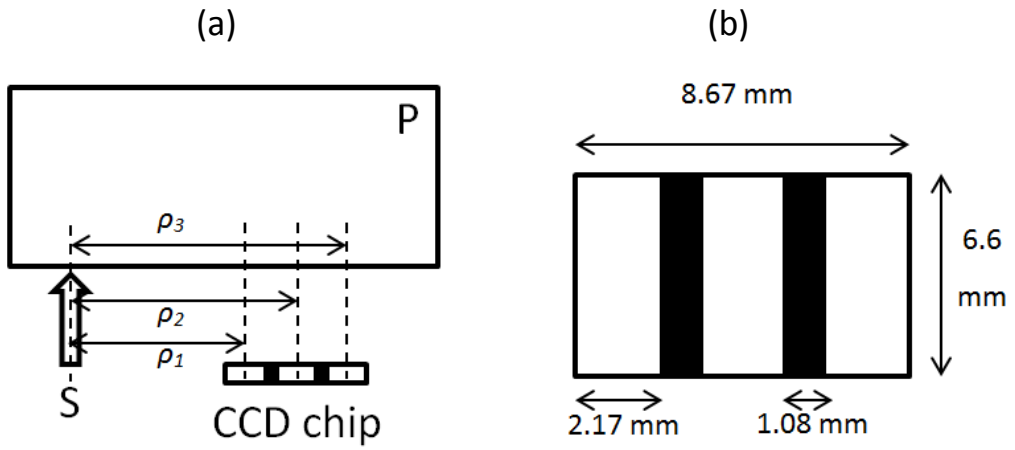

Figure 5-7 (a) The schematic diagram depicts the segmentation of the CCD image area into three independent optical detectors where ρ_1 is distance from S to the first segment of the CCD chip and similarly for ρ_2 and ρ_3. (b) Dimension of the segmented CCD image area.

The CCD camera can also be used for the spatially resolved measurement, which is the third optical measurement for this study. The spatially resolved mode is achieved by additional post-processing the same images captured for $I_{CCD}(x, y)$ in section 5.1.3.3. Each image is segmented into three parts to simulate three optical detectors separated by a predefined distance ρ as shown in Figure 5-7 (a). The segmentation strategy shown in Figure 5-7 (b) is the same method used by Suzuki et al. [Suzuki 1999]. Instead of using intensity, the spatially resolved method uses the attenuation gradient $\frac{\partial A_{SR}}{\partial \rho}$ (O.D mm^{-1}) detected across the three detectors over

distance ρ (mm). The attenuation at n-th segment of the CCD, $A_n(x,y)$ (O.D) is defined as:

$$A_n(x,y) = -\log_e\big(I_n(x,y)\big) \tag{5-2}$$

where $I_n(x,y)$ is the average intensity of the n-th CCD segment the mean intensities of the five captured CCD images.

In the absence of the local absorber, it can be readily predicted that $A_1 < A_2 < A_3$ simply because the intensities detected at ρ_1 < intensity at ρ_2 < intensity at ρ_3; which will result in a positive attenuation gradient. The gradient of the first order polynomial from the least-square fit of $A_n(x,y)$ over ρ_n is the attenuation gradient, $\frac{\partial A_{SR}(x,y)}{\partial \rho}$. The reference attenuation gradient $\frac{\partial A_{SR}^{ref}(x)}{\partial \rho}$ is estimated by the same process when the local absorber is removed from the phantom.

5.1.4 Mapping Systems

Three linear translation stages (Zaber LSR150A) were combined to form a three-dimensional stage to position the local absorber and the needle hydrophone for mapping of the spatial sensitivity and the ultrasound field respectively. The ultrasound generation, instrument control and data acquisition of each measurement technique was automated by a LABVIEW program, which was developed specifically for sensitivity and ultrasound field mapping.

5.1.4.1 Sensitivity Mapping

The local absorber was positioned throughout the SA by 1 mm for both transmission and reflection mapping. In addition, the mapping system also re-positioned the local absorber to a pre-set position outside the phantom for the reference measurements. The reference measurement was taken for every column of the SA.

Figure 5-3 shows the transmission mode SA, which was 24 by 24 mm inclusive of position 0 mm; resulting in 625 measurements and 25 reference measurements. Similarly, reflection mode mapping produced 651 measurements and 31 reference values for each method from a given SA of 30 mm by 20 mm, which is illustrated in Figure 5-4.

With 20 seconds of integration time, there are a total of 650 (625+25) measurements in transmission mode, which will require about 3.5 hours to complete using the photon counter setup. The AO measurement requires data acquisition when ultrasound is activated and deactivated, thus it requires 7 hours. The exposure time of the CCD is very short compared to the integration time of the digital correlator. However, the large image size will require about 1 s gap between subsequent images for data transfer from the camera and the computer. Therefore, the experimental time for the CCD is approximately equal to 650 × 10 s × 2 (for ultrasound on-off), which equals to 3.6 hours. However, these are under-estimates of the mapping time because the time required for relocating the local absorber and instrument switching are not considered. The scanning direction is from positive x position to zero or negative and from $y = 0$ to positive y position.

5.1.4.2 Ultrasound Field Mapping

On top of the sensitivity measurement, another LABVIEW program was developed to map the acoustic field within the SAs at the same resolution of 1 mm by using a needle hydrophone (Precision Acoustics HP1, 1mm diameter) and a digital oscilloscope (Tektronix TDS2014B). The size of the phantoms cannot accommodate the needle hydrophone; therefore the ultrasound field of peak pressure P_{peak} (kPa) was mapped by tilting the needle hydrophone at 15°, which is shown in Figure 5-8 (a). Detail of peak pressure measurement has been described in section 4.1.5. The recorded pressure field was then normalised by its maximum value.

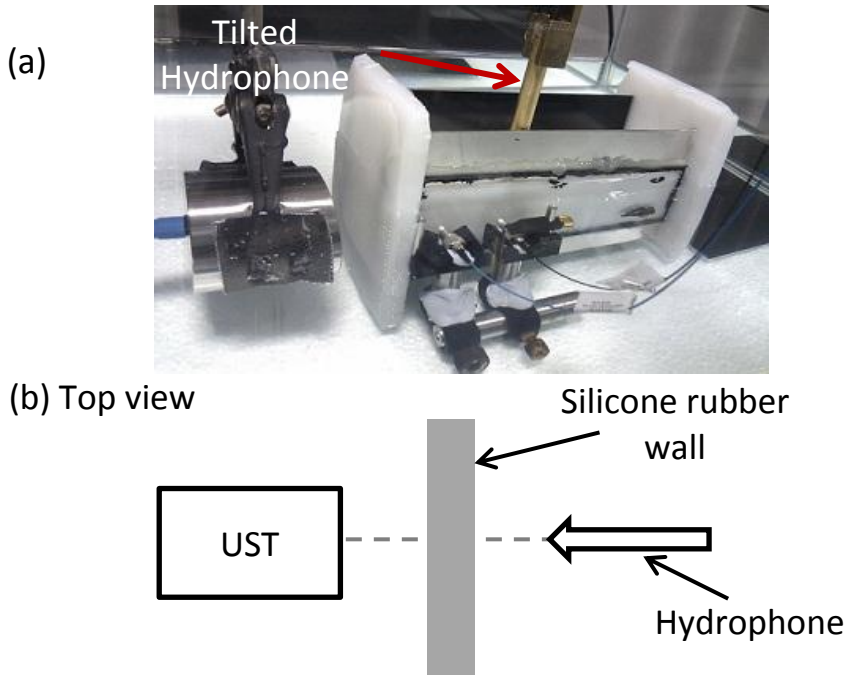

Figure 5-8 (a) The mapping of scaled peak pressure of the acoustic field in the reflection mode phantom and (b) the schematic diagram of the un-scaled P_{peak} measurement.

An un-scaled measurement of maximum P_{peak} of the FUR was acquired by using the same set of instruments but the phantom was removed from the glass tank. The silicone rubber wall was detached from the phantom and it was then placed in between the ultrasound transducer and the needle hydrophone that is depicted in Figure 5-8 (b). The maximum P_{peak} was then measured using the needle hydrophone, which was 180.8 kPa. The ultrasound field was then computed by re-scaling the normalised field by 180.8 kPa.

5.1.5 **Sensitivity Maps**

This section discusses how the spatial sensitivity map of each measurement method is computed. For ease of comparison, the sensitivity scale is set from 0 to 100%.

5.1.5.1 AO Measurement

The AO signal is quantified by the MD, which is proportional to the ratio of ultrasound modulated intensity I_{AC} to the un-modulated intensity I_{DC}. The following details the procedure to extract the MD from the normalised intensity autocorrelation function, $g_{x,y}^{(2)}(\tau)$.

It has been shown that MD can be computed from the normalised electric field autocorrelation function $g_{x,y}^{(1)}$ [Wang 2001], which can be calculated by using equation (4-16). According to Wang [Wang 2001], the I_{AC} and I_{DC} of the AO signal are the magnitudes of the Fourier transform of the $g_{x,y}^{(1)}(\tau)$ at the ultrasound frequency f_a and zero frequency f_0 respectively. Thus MD can be computed from the following equation:

$$MD_{x,y} = \frac{FT_{f_a}\left\{g_{x,y}^{(1)}(\tau)\right\}}{FT_{f_0}\left\{g_{x,y}^{(1)}(\tau)\right\}} \tag{5-3}$$

where FT is the Fourier transform, f_a is the centre frequency of the ultrasound transducer (0.66 MHz) and f_0 = 0 Hz.

The reference MD for a given y position, $MD^{ref}(x)$, can be calculated by using equation (5-3). Therefore the AO sensitivity $J_{AO}(x,y)$ (%) can be derived from:

$$J_{AO}(x,y) = \frac{MD^{ref}(x) - MD(x,y)}{MD^{ref}(x)} \times 100\% \tag{5-4}$$

5.1.5.2 Intensity Measurement using the Single Photon Counter, I_{PC}

The sensitivity of the I_{PC} measurement, J_{PC} can be calculated using the similar approach of equation (5-4) from the time-averaged intensity $I_{PC}(x,y)$:

$$J_{PC}(x,y) = \frac{I_{PC}^{ref}(x) - I_{PC}(x,y)}{I_{PC}^{ref}(x)} \times 100\%$$

(5-5)

5.1.5.3 Intensity Measurement using a CCD camera, I_{CCD}

Similar to the J_{PC}, the spatial sensitivity of the I_{CCD} measurement is given by:

$$J_{CCD}(x,y) = \frac{I_{CCD}^{ref}(x) - I_{CCD}(y)}{I_{CCD}^{ref}(x)} \times 100\%$$

(5-6)

5.1.5.4 Spatially Resolved Measurement using a CCD camera, $\partial A_{SR}/\partial \rho$

From the attenuation gradient, which is described in section 5.1.5.4, the spatial sensitivity of the $\frac{\partial A_{SR}}{\partial \rho}$ measurement, $J_{SR}(x,y)$:

$$J_{SR}(x,y) = \frac{\frac{\partial A_{SR}^{ref}(x)}{\partial \rho} - \frac{\partial A_{SR}(x,y)}{\partial \rho}}{\frac{\partial A_{SR}^{ref}(x)}{\partial \rho}} \times 100\%$$

(5-7)

5.1.6 Mean and Midway Sensitivity in the Superficial Region and Region of Interest

The mean sensitivity $\langle J \rangle$ at different depths y (mm) is the mean sensitivity for a *layer* (across x-axis) for each y (mm). From this mean sensitivity at different depths, the mean penetration depth of the reflection mode measurement [Del Bianco 2002] can be calculated from:

$$\langle y \rangle = \frac{\sum J(y) \cdot y}{\sum J(y)}$$

(5-8)

Alternatively, another way to view the penetration depth is by only consider a single *x* position, which is the midway of the SA. The *midway sensitivity* is defined as the sensitivity of y mm when *x* = 0 mm for transmission mode SA and *x* = 15 mm for reflection mode SA. The maximum penetration depth can be estimated when the midway sensitivity reaches the background noise level [Vaithianathan 2004] when the local absorber is so deep in the phantom that there is no detectable change. This background noise method cannot be considered here because the *y*-axis of the reflection mode SA is not deep enough to reach that level. The maximum penetration depth can also defined as be the *y* position whereby the midway sensitivity equals or exceeds pre-defined sensitivity value (threshold) [Correia 2010, Patil 2011].

Instead of using a pre-set value of sensitivity, the maximum sensitivity recorded in the ROI is used in this study for comparison between different detection techniques. The location of the ROI is the same as that of the FUR and its width is the 3 dB drop from the maximum peak pressure of the FUR. Further comparison will be made for the sensitivities in ROI and in the SFR, which is defined as the sensitivity at *y* when *y* is closest to the optical detector i.e. at 5.5 mm. In the context of mean or maximum penetration depth, the *y*-axis can be considered as depths in mm.

5.2 Transmission Mode

The interpretation of the sensitivity map is quite straightforward. For example, a zero sensitivity value at (x, y) suggests that there is no change in the measurement when the local absorber was located at position (x, y). A 10% value would mean a 10% signal reduction when the local absorber or the local perturbation was introduced. On the other hand, a negative sensitivity implies that there is an increase in the detected signal.

This section presents the measurement results and sensitivity maps of the transmission mode.

5.2.1 **Control Sensitivity Maps**

As discussed in section 5.1.2, the optical properties of the local perturbation and the background diffusive medium can be adjusted so that they are the same. However, the same assumption cannot be made about their acoustic properties. Therefore there is a need to conduct a control spatial sensitivity measurement to verify whether the difference in the acoustic properties would result in significant change in the spatial sensitivity.

By using the same experimental setup and post-processing procedures, the spatial sensitivity maps J_{AO} and J_{PC} were mapped. The optical properties of the local perturbation and the diluted Intralipid solution were both set to the following: μ_s' = 12 cm^{-1} and μ_a = 0.00235 cm^{-1} at wavelength 780 nm.

5.2.1.1 Results

The AO and I_{PC} measurement results are shown in Figure 5-9 and their reference measurements' results are presented in Figure 5-10.

The I_{DC} of the AO measurement in Figure 5-9 (b) and its reference in Figure 5-10b shows no significant effect of the local perturbation. However, Figure 5-9 (a) and (c) show there are a small increase of the I_{AC} and the MD in the FUR. Their respective reference measurements show a trend of slight increase in signal when x is near 0 mm even though the local perturbation was absence. The I_{PC} in Figure 5-9 (d) shows there was a drop in intensity when the local perturbation is near x = 0 mm. However, I_{PC}^{ref} in Figure 5-10d shows similar intensity pattern.

Based on the observation of the results, the drop in I_{PC} can be attributed to the instability of the Intralipid solution because the trend of intensity observed is similar between the I_{PC} and I_{PC}^{ref}. The control spatial sensitivities of J_{AO} and J_{AC} and the location of the FUR are shown in Figure 5-11 (a), (c) and (b) respectively. The sensitivity maps show no significant change in the detected signal for both AO and I_{PC} measurement.

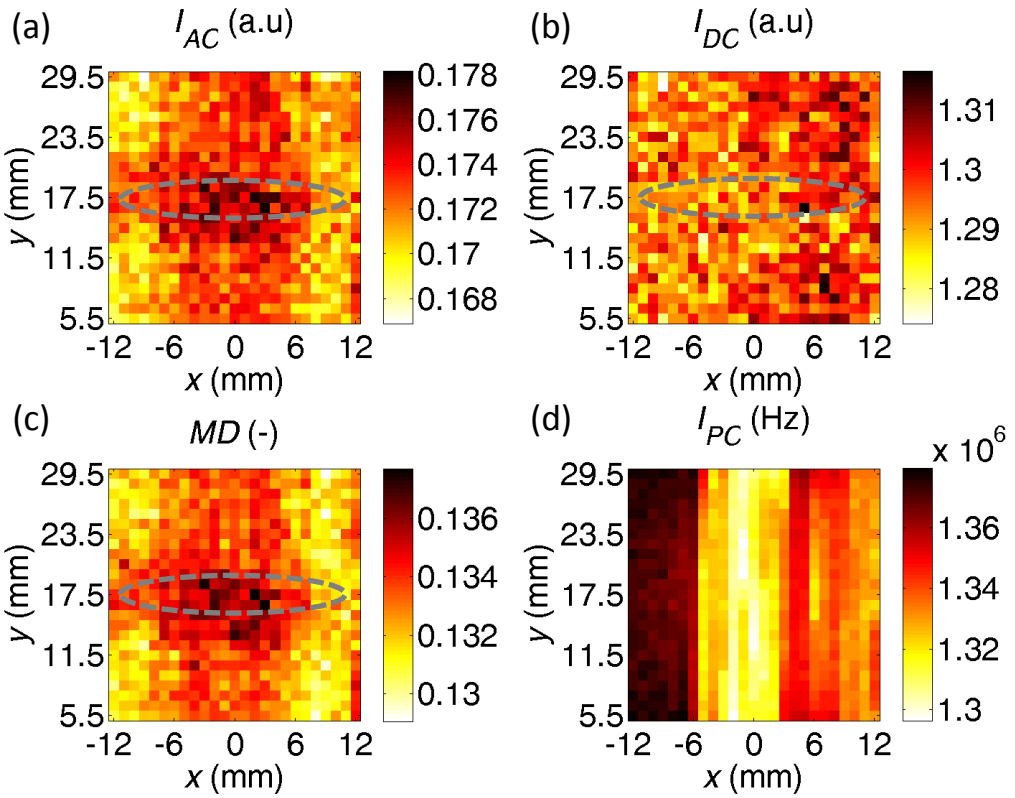

Figure 5-9 The control measurement results of AO: (a) I_{AC}, (b) I_{DC}, (c) MD; and (d) I_{PC} for transmission mode when the background μ_a = 0.0235 cm^{-1}. (dashed line: FUR)

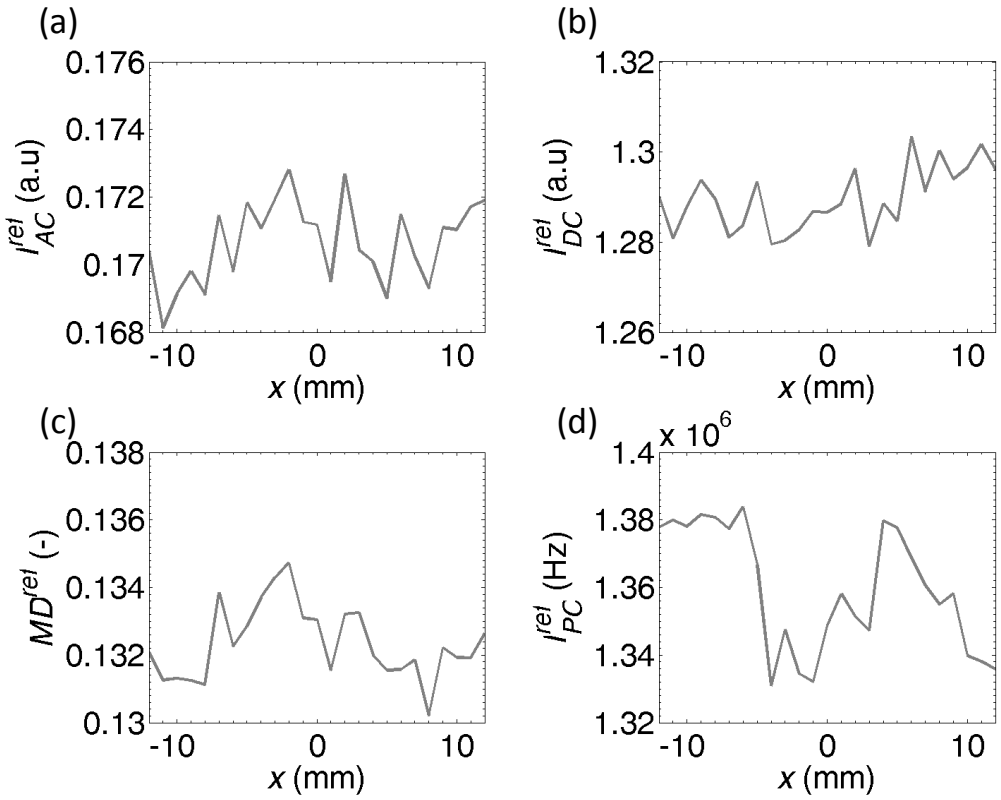

Figure 5-10 The reference control measurement results of AO: (a) I_{AC}, (b) I_{DC}, (c) MD; and (d) I_{PC} for transmission mode when the background μ_a = 0.0235 cm^{-1}. (dashed line: FUR)

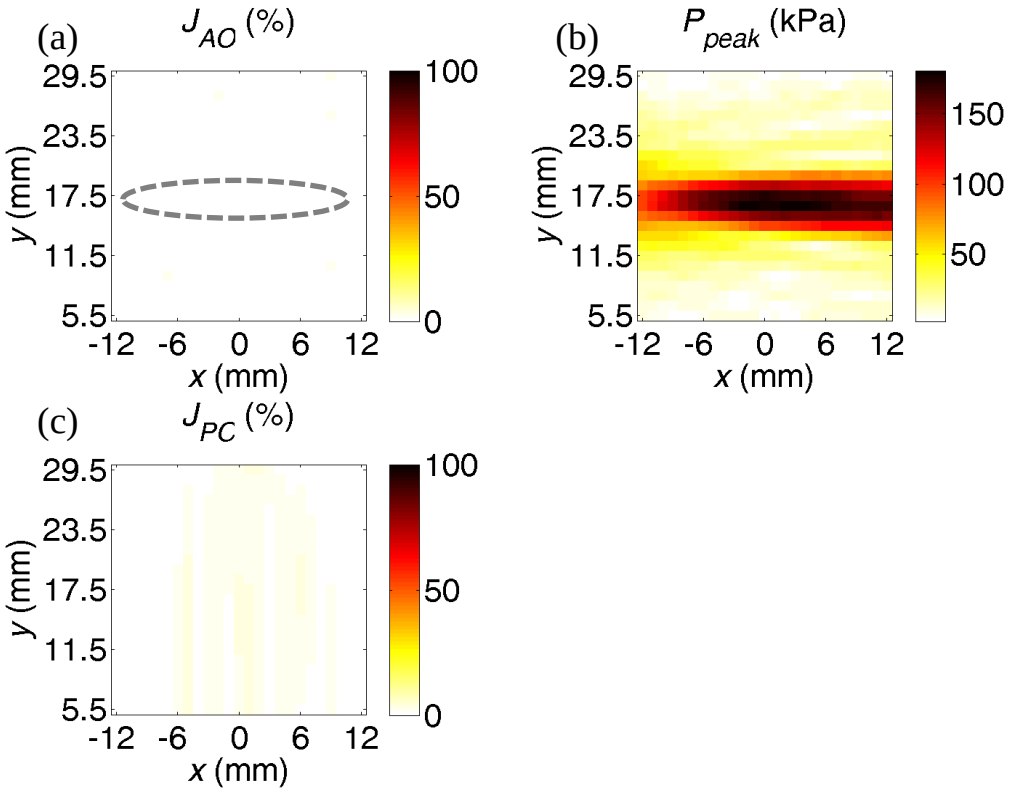

Figure 5-11 The control spatial sensitivity maps of (a) AO and (c) I_{PC} with (b) the FUR for transmission mode when the background μ_a = 0.0235 cm^{-1}: no significant change in both the AO and the I_{PC} measurements. (dashed line: FUR)

5.2.1.2 Mean and Midway Sensitivity in the Superficial Region and Region of Interest

The mean sensitivities $\langle J(y) \rangle$ as a function of depths in the y-axis for both methods are shown in Figure 5-12. The localised increase in the MD observed in Figure 5-9 (c) is also observable in the $\langle J_{AO} \rangle$. This phenomenon is caused by the slight increase in the speed of sound within the PVA-based local perturbation as mentioned in section 5.1.2.2. In the mechanism that modulates the phase due to the varying refractive index [Wang 2001], which is shown in equations (3-29) and (3-31), the speed of sound is squared in the phase accumulation. Therefore a small increase in the speed of sound will result in a significant increase in accumulated phase. However, the maximum detectable mean sensitivity change is under 2%,

which is fairly small as shown in Table 5-1. It is also interesting to note that the AO measurement detects very small to no change when the local perturbation is very close to optical source and detector. The $<J_{PC}>$ shows that the phantom and the local perturbation are assumed to be optically homogeneous. The change is under 1% in Table 5-1.

Alternatively, the midway sensitivities at different depths y when x = 0 mm are plotted in Figure 5-13, which illustrates similar conclusions to Figure 5-12 and Table 5-1. The same behaviour is also observed in Table 5-2

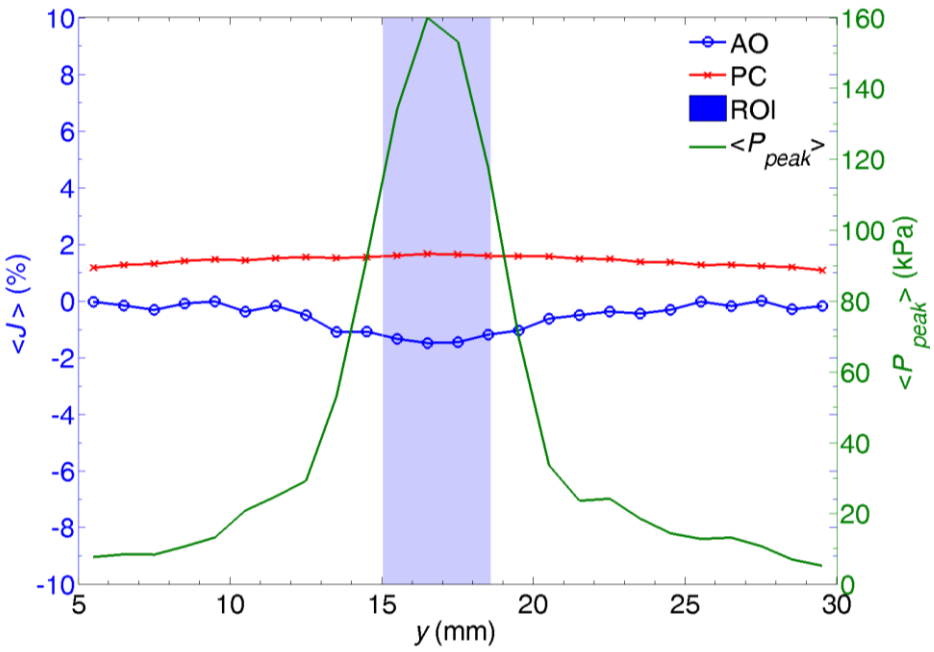

Figure 5-12 The control mean sensitivity of AO and I_{PC} at different depth y for transmission mode when the background μ_a = 0.0235 cm^{-1}: the phantom and the local perturbation are optically homogeneous and the slight increase in the AO sensitivity in the FUR is the result of mismatch of their acoustic properties.

Detection Method	<J(SFR)> (%)	<J(ROI)> (%)
I_{PC}	1.2	1.7
AO	-0.03	-1.5

Table 5-1 Comparison between the control mean sensitivity of AO and I_{PC} in the SFR and the ROI for transmission mode when the background μ_a = 0.0235 cm^{-1}: the absolute maximum detected change is under +/- 2%.

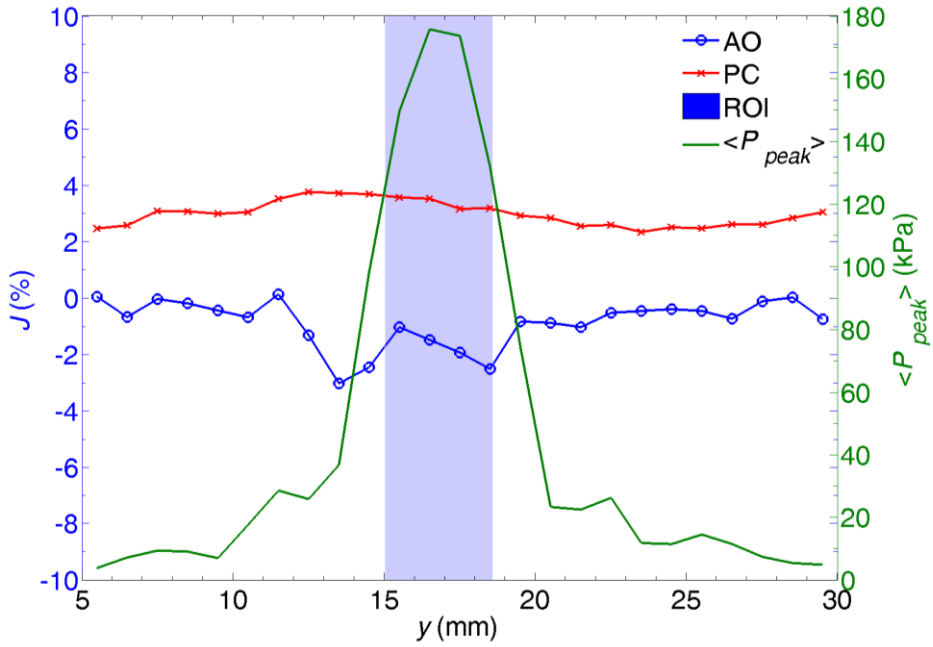

Figure 5-13 The control midway sensitivity of AO and I_{PC} at different depth y for transmission mode when the background μ_a = 0.0235 cm^{-1}.

Detection Method	J(SFR) (%)	J(ROI) (%)
I_{PC}	2.5	3.2
AO	0.04	-2.5

Table 5-2 Comparison of the control midway sensitivity of AO and I_{PC} in the SFR and the ROI for transmission mode when the background μ_a = 0.0235 cm^{-1}.

5.2.2 **Sensitivity Maps**

This section presents the mapping results of the spatial sensitivity in transmission mode for the AO and optical measurements with the local absorber. The measurement results are shown in Figure 5-14 (a)-(c) for AO system and (d)-(e) for optical measurements. The reference measurement results are shown in Figure 5-15 (a)-(c) and (d)-(e) for AO and optical measurements respectively.

Figure 5-14 (a) shows that there is a localised drop in the I_{AC} at the centre of the SA, which coincides with the FUR. However, an even the larger drop is observed when the local absorber is very close to the optical source whereby the local absorber blocks most of the light. This causes the large reduction in the I_{AC} and it is also observable in the I_{DC}, which is shown in Figure 5-14 (b). But the amount of change observed in the I_{AC} in the ROI is much larger than the I_{DC}, which results in the highly localised drop in the MD observed in Figure 5-14 (c). Recall that the MD is proportional to the ratio of the I_{AC} and the I_{DC}. When the local absorber is in FUR, it absorbs more I_{AC} than the I_{DC} that results in the large decrease in the MD. This result was also observed in the literature [Bratchenia 2011]. Furthermore, the MD increases when the local absorber is very close to the optical source and detector. At these positions, the local absorber absorbs more I_{DC} than the I_{AC}. These results demonstrate the light tagging ability of the AO method.

The general pattern of the detected intensities by the optical systems shown in Figure 5-14 (d)-(e) agree with the literature [Fantini 1995], which is shown in Figure 5-14 (f); whereby the largest changes are observed at locations very close to the optical source and detector. The slight differences are because of the different geometry and optical properties of phantoms. The I_{PC} demonstrates greater degree of observable change due to its superior quantum efficiency (55%) as compared to the I_{CCD}'s (30%) at the optical wavelength 808 nm.

The spatial sensitivity map of the AO, I_{PC} and I_{CCD} transmission measurements are shown in Figure 5-16 (a), (c) and (d) respectively with the corresponding the FUR in Figure 5-16b. The AO spatial sensitivity shows that the most sensitive region coincides with the FUR in the centre of the SA between the optical probes, which agrees with our previous result [Gunadi 2011]. In fact, the sensitivities are negative when the local absorber is very close to the optical source and detector. In these regions, the local absorber blocks more I_{DC} than I_{AC} resulting in increase in the MD.

Once again, the optical measurements are most sensitive in regions very close to optical source and detector because the local absorber blocks the most amount of the light. This pattern is typical behaviour of conventional optical system. But the I_{PC} detection is the most sensitive in the ROI when compared to both the AO and I_{CCD} methods.

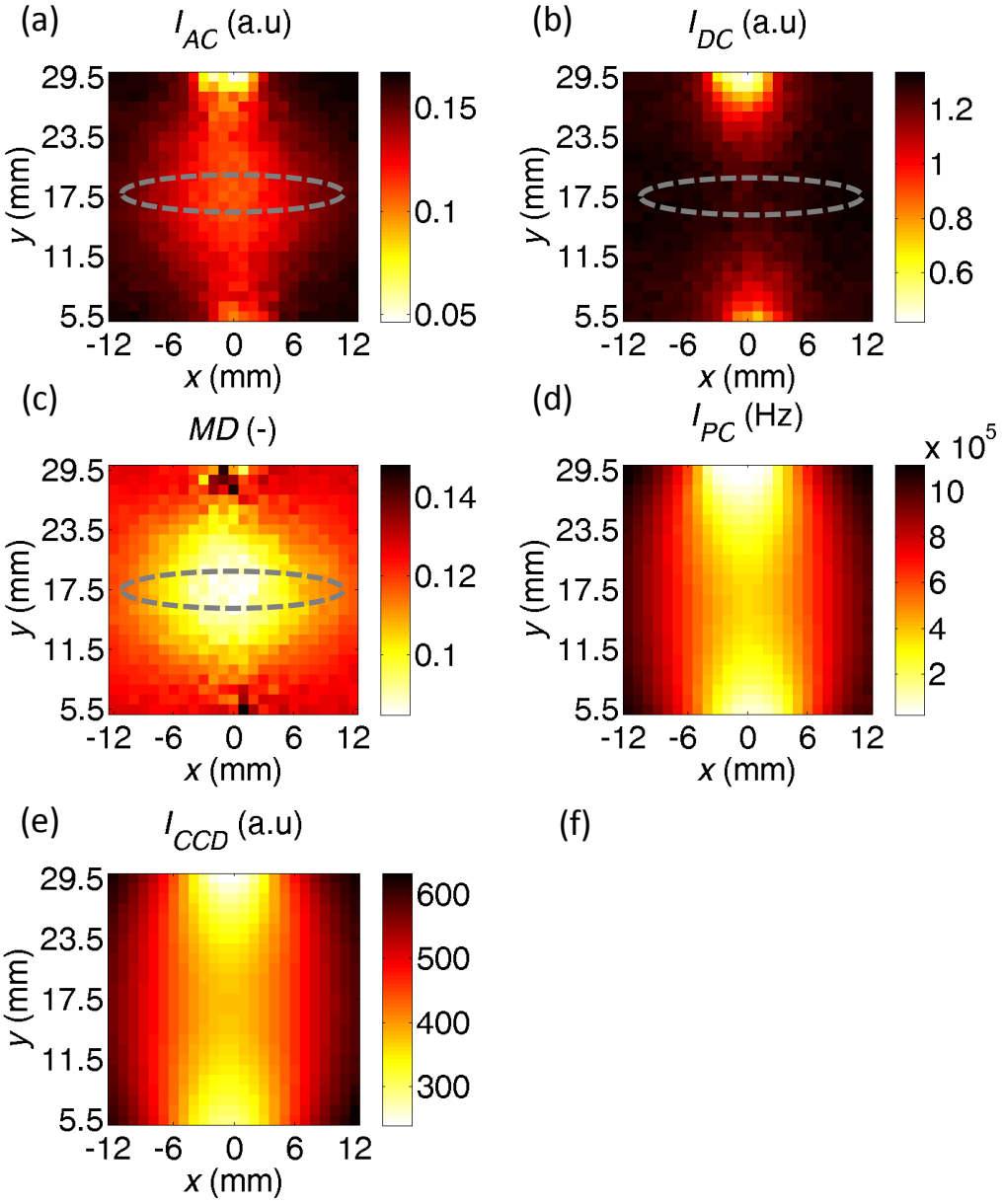

Figure 5-14 The measurement results of AO: (a) I_{AC}, (b) I_{DC}, (c) MD ; (d) I_{PC}; (e) I_{CCD}; and (f) the literature [Fantini 1995] for transmission mode when the background μ_a = 0.0235 cm^{-1}: there is very localised MD reduction in the FUR and good agreement between the optical results and the literature can be observed. (dashed line: FUR)

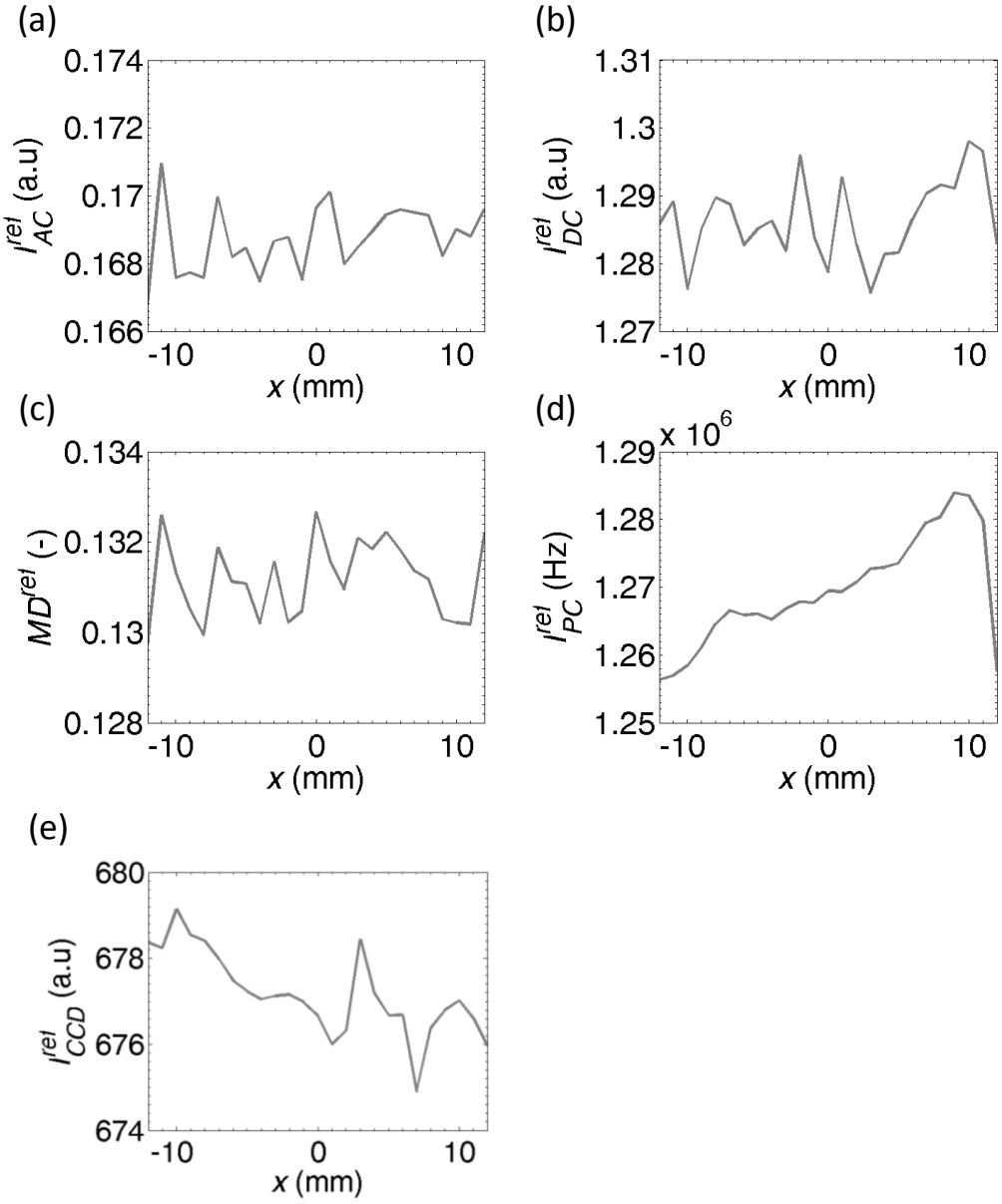

Figure 5-15 The reference measurement results of: AO (a) I_{AC}, (b) I_{DC}, (c) MD; (d) I_{PC}; and I_{CCD} for transmission mode when the background μ_a = 0.0235 cm^{-1}: they show the variation and drift of detected signal over the course of the scanning period. (dashed line: FUR)

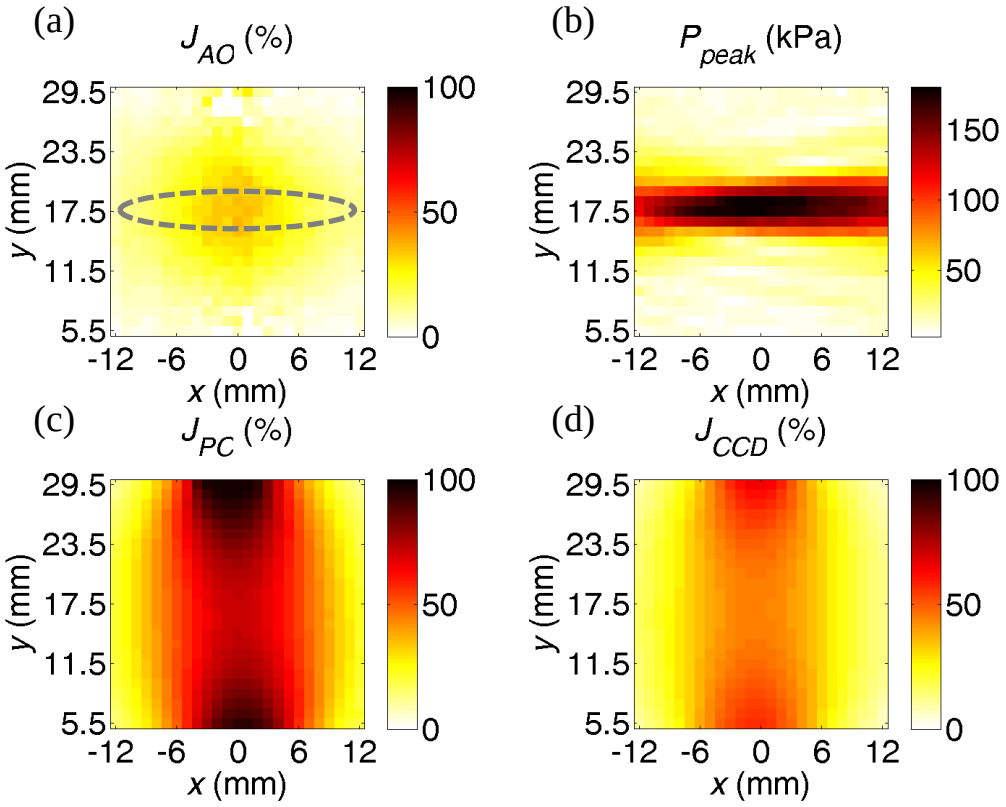

Figure 5-16 The spatial sensititivity maps of: (a) AO; (b); (c) I_{PC} and (d) I_{CCD} for transmission mode when the background μ_a = 0.0235 cm^{-1}: there is a highly localised AO sensitivity in the FUR.

5.2.3 Mean and Midway Sensitivity in the Superficial Region and the Region of Interest

The summaries of the mean sensitivity observed in the ROI are depicted in Figure 5-17 and Table 5-7. In the context of depth, AO is most sensitive in the ROI in transmission mode measurement when compared to its mean sensitivity near the SFR of the phantom. However, the absolute mean sensitivities $<J_{PC}>$ and $<J_{CCD}>$ are high than the maximum AO sensitivity. But the optical measurements are less sensitive in the ROI when compared to the SFR. Table 5-3 shows that the $<J_{AO}>$ in ROI is twenty times the value at the SFR. In SFR, little change is observed as

the $<J_{AO}>$ approaches zero. On the other hand, $<J_{PC}>$ and $<J_{CCD}>$ at SFR are slightly higher when compared to the ROI.

Similar conclusions mentioned above can be drawn from the plots of midway sensitivities as shown in Figure 5-18 and Table 5-4. However, the presence of the local absorber near the optical source causes the MD to increase in Figure 5-18. The local absorber blocks more I_{DC} but little or no I_{AC}, thus the MD increases.

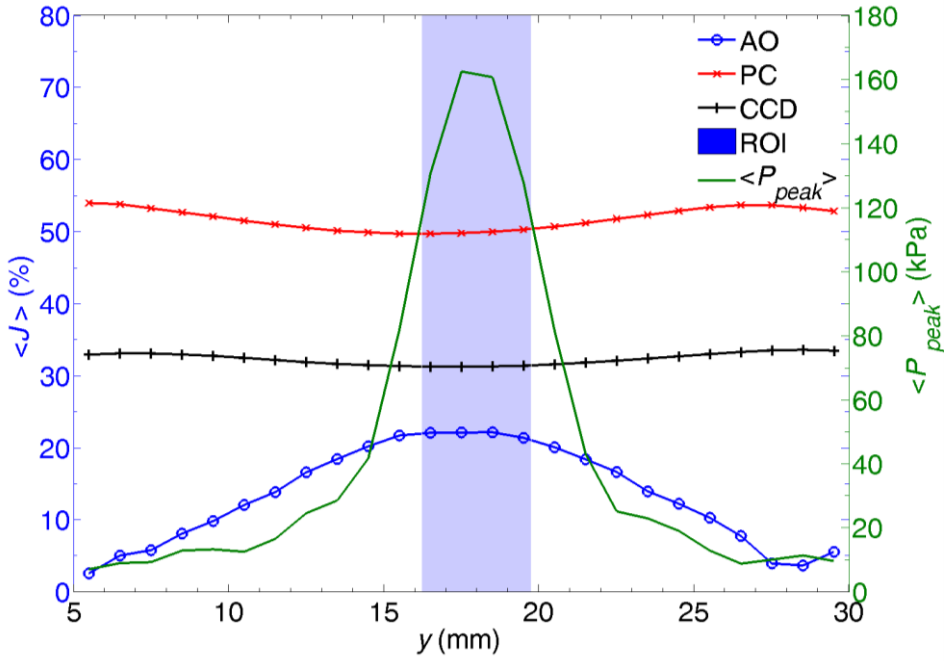

Figure 5-17 The mean sensitivity of AO, I_{PC} and I_{CCD} at different depth y for transmission mode when the background μ_a = 0.0235 cm^{-1}: the AO has the least absolute mean sensitivity in the ROI but higher than its $<J(y=5.5)>$ (SFR) and the opposite phenomena are observed for the optical measurements in spite of their higher absolute $<J(\text{ROI})>$.

Detection Method	<J(SFR)> (%)	<J(ROI)> (%)	Is <J(ROI)> higher than <J(SFR)>?
I_{CCD}	32.9	31.3	No
I_{PC}	53.9	49.8	No
AO	2.6	22.1	Yes

Table 5-3 Comparison of the mean sensitivity of AO, I_{PC} and I_{CCD} in the SFR and the ROI for transmission mode when the background μ_a = 0.0235 cm^{-1}: only the AO method achieved higher sensitivity in the ROI.

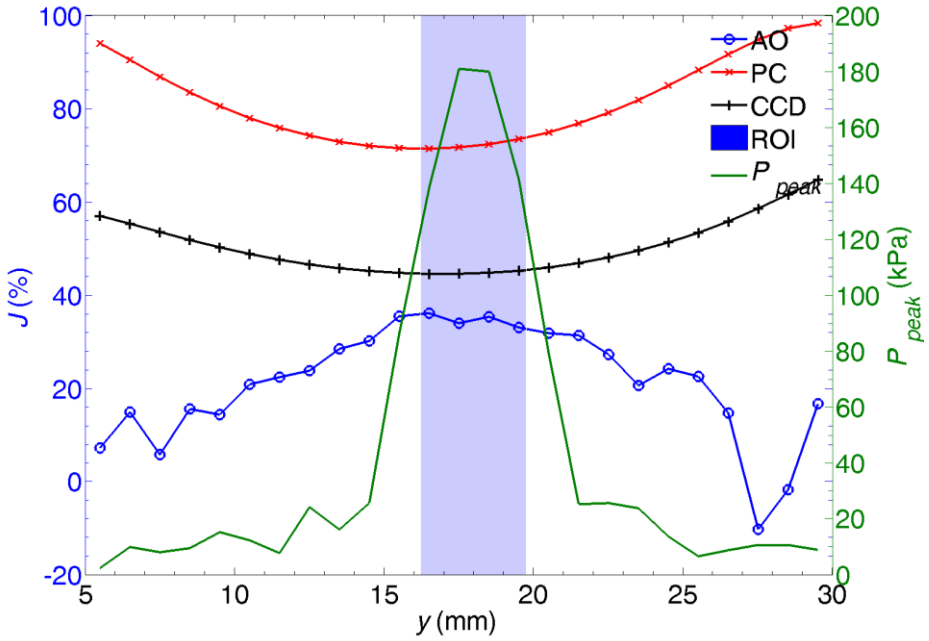

Figure 5-18 The midway sensitivities of AO, I_{PC} and I_{CCD} at different depth y for transmission mode when the background μ_a = 0.0235 cm^{-1}: the AO method is more sensitive in the ROI than in the SFR even though the midway J_{AO} is lowest when compared to the midway J_{PC} and J_{CCD}. The negative J_{AO} (0, 27.5) implies that the presence of local absorber near the optical source causes an increase in MD because it blocks more I_{DC} than I_{AC}.

Detection Method	J(SFR) (%)	J(ROI) (%)	Is J(ROI) higher than J(SFR)?
I_{CCD}	57.0	44.6	No
I_{PC}	93.9	71.7	No
AO	7.3	34.0	Yes

Table 5-4 Comparison of the midway sensitivity of AO, I_{PC} and I_{CCD} in the SFR and the ROI for transmission mode when the background μ_a = 0.0235 cm^{-1}, which demonstrates that only the AO method is more sensitive in the ROI than in the SFR.

5.2.4 Effects of Background Absorption on the Spatial Sensitivity

The background μ_a of the phantom used to produce the results shown in section 5.2.2 and 5.2.3 is similar to that of water's μ_a (0.0235 cm^{-1}). This section describes the results of the experiment when the background μ_a was increased to the level of tissue, which is typically 0.1 cm^{-1}.

5.2.4.1 Materials and Methods

The higher background absorption was achieved by adding the appropriate amount of the NIR dye (ICI S109564), which is detailed in section 4.2.1.2. The experiments were repeated for AO and I_{PC} measurements using the same setup and procedures.

5.2.4.2 Sensitivity Maps

The AO and I_{PC} measurement results are shown in Figure 5-19 and their reference measurements are shown in Figure 5-20. In general, similar trends can be observed when these results are compared to the case of minimal background absorption. Because of the higher background absorption, there are more photons (both modulated and un-modulated) being absorbed. The same phenomenon can

be observed by comparing the reference measurements in Figure 5-20 to those depicted in Figure 5-15 (minimal background absorption); all measurements are lower in Figure 5-20 than in Figure 5-15. The amount of the MD difference (between the MD in Figure 5-19 and in Figure 5-14) in the centre of the FUR and away from the FUR (e.g. position x = 12 mm and y = 29.5 mm) is less prominent when compared to the result in Figure 5-14.

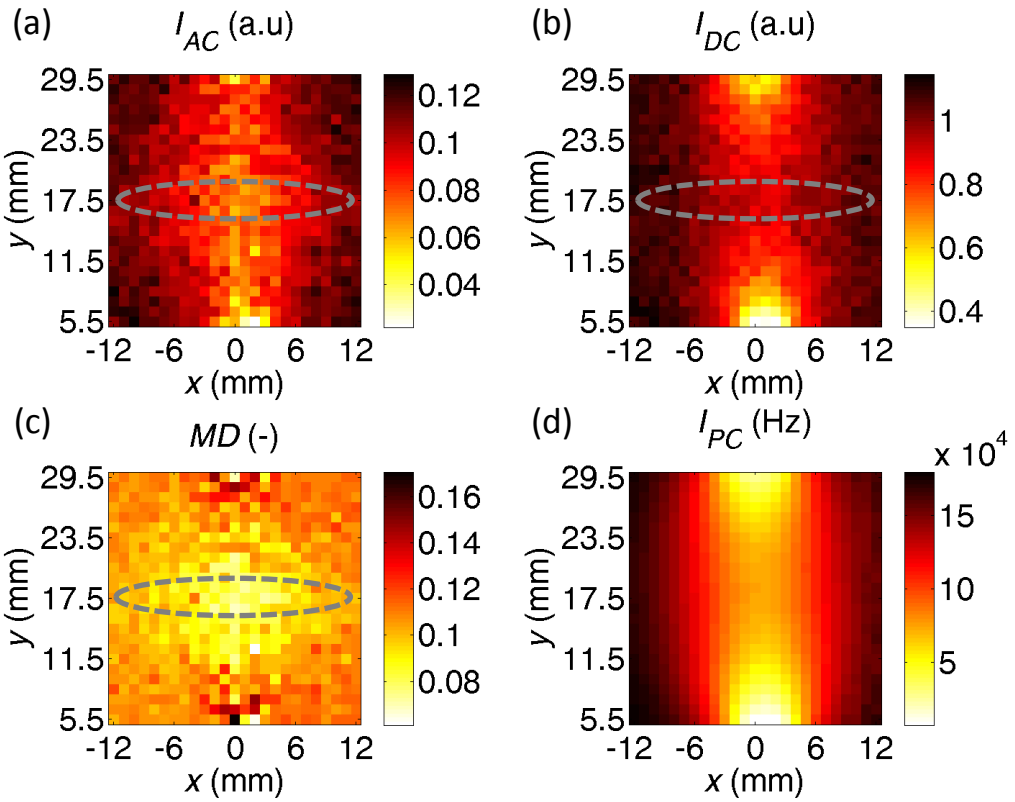

Figure 5-19 The measurement results of AO: (a) I_{AC}; (b) I_{DC}; (c) MD; and. (d) I_{PC} for transmission mode when the background μ_a = 0.1 cm^{-1}. (dashed line: FUR)

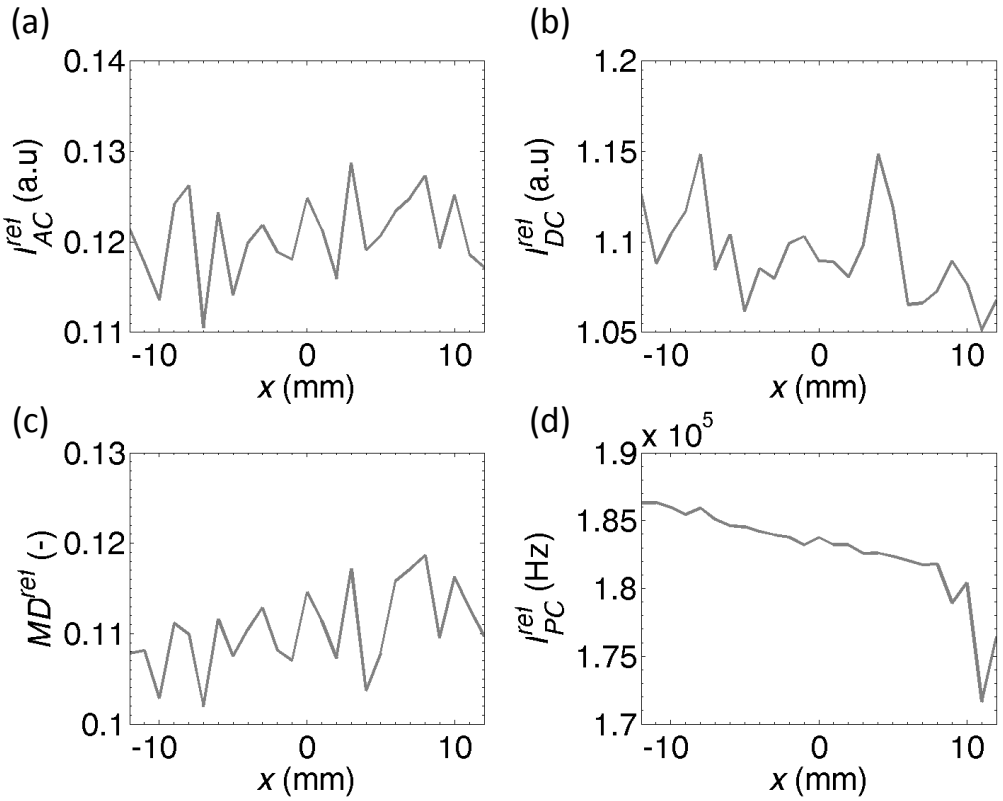

Figure 5-20 The reference measurement results of: AO (a) I_{AC}, (b) I_{DC}, (c) MD; and (d) I_{PC} for transmission mode when the background μ_a = 0.1 cm^{-1}.

The sensitivity maps are shown in Figure 5-21. The observations in the measurement results are also reflected in the sensitivity maps. Higher absorption causes greater difference in the sensitivity maps when the local absorber is close to the optodes and in the FUR. The AO sensitivity map shows that the highest sensitivity is observed in the FUR, which is close to 40%. This is higher than the value of approximately 35% when less background absorption is present (Figure 5-16a). There is also greater change in J_{PC} because of the added background absorption. However, the J_{AO} is noisier because of the difficulty in detecting the I_{AC} in a low light condition.

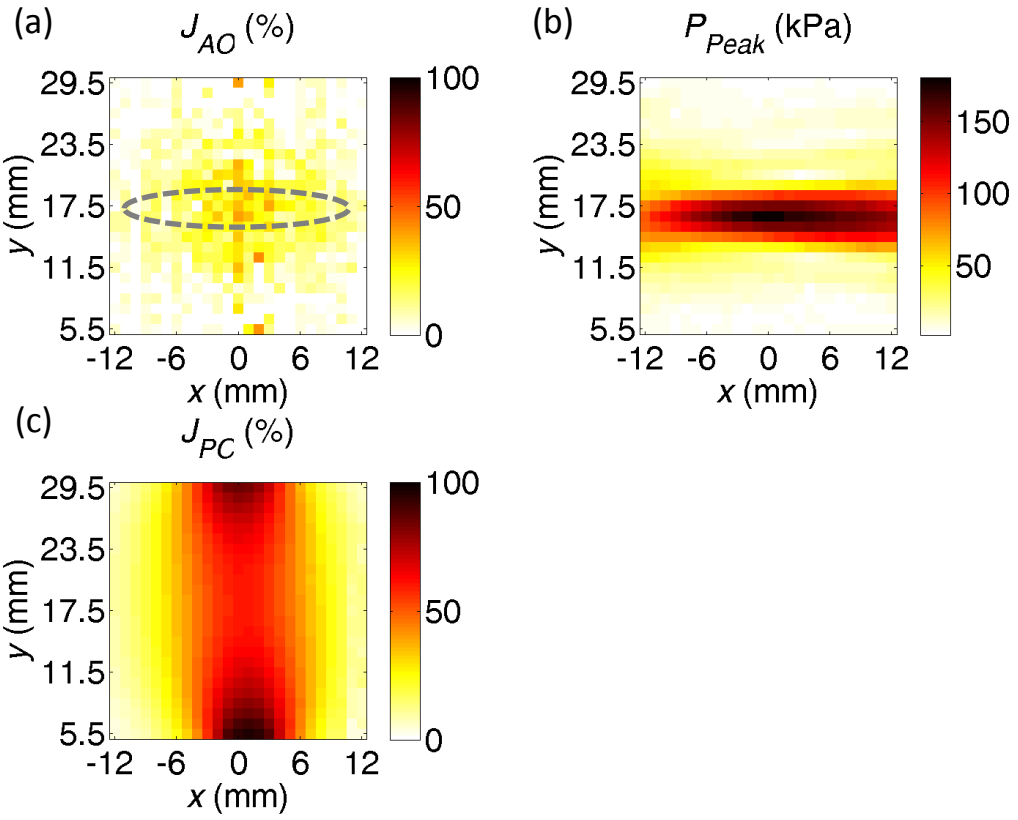

Figure 5-21 The spatial sensitivity maps of (a) AO and (c) I_{PC} with (b) the FUR for transmission mode when the background μ_a = 0.1 cm^{-1}. (dashed line: FUR)

5.2.4.3 Mean and Midway Sensitivity in the Superficial Region and the Region of Interest

The mean sensitivity profiles of AO and I_{PC} methods are shown in Figure 5-22 and the comparison of the mean sensitivities in the SFR and the ROI is summarised in Table 5-5. By comparing the results here to those depicted in Figure 5-17 and Table 5-1; there is a general drop in sensitivity here due to the local absorber for both AO and I_{PC} methods because of the increased background absorption.

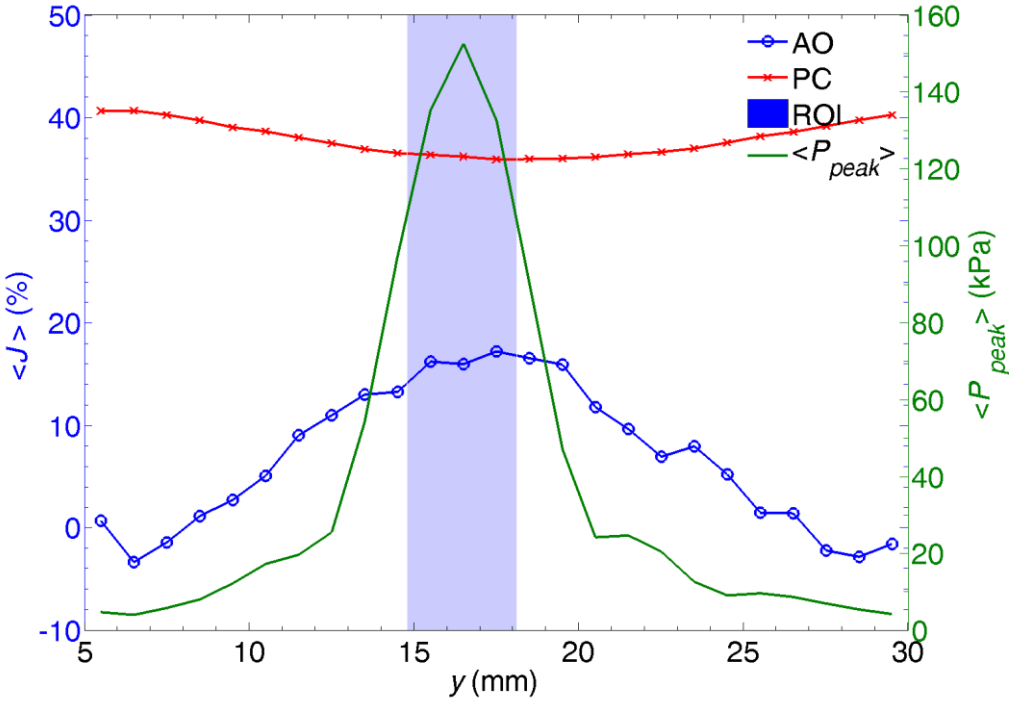

Figure 5-22 The mean sensitivity of AO and I_{PC} at different depth y for transmission mode when the background μ_a = 0.1 cm^{-1}: the AO method is more sensitive in the ROI than the SFR while $<J_{PC}>$ depicts the higher mean sensitivity in the SFR than in the ROI.

Detection Method	<J(SFR)> (%)	<J(ROI)> (%)	Is <J(ROI)> higher than <J(SFR)>?
I_{PC}	40.6	36.2	No
AO	0.71	16.0	Yes

Table 5-5 Comparison of the mean sensitivity of AO and I_{PC} in the SFR and the ROI for transmission mode when the background μ_a = 0.1 cm^{-1}: it shows the higher AO mean sensitivity in the ROI than the SFR.

Figure 5-22 also shows the increase in the MD when the absorber is near the optodes at y = 5 and 30 mm, which is not shown in Figure 5-17. The reason could

be the exponential absorption of light with increasing distance. The distance from the optical source to the optical detector is twice the distance from the FUR. Thus more I_{DC} is absorbed than I_{AC} because of the higher background absorption. This effect is further enhanced by the presence of the local absorber in close proximity to the optodes that absorbs more DC than AC. The net result is the observed increase in MD in these regions.

Only the AO method shows higher mean sensitivity in the ROI than the SFR in Table 5-5. The mean ROI and SFR sensitivities are lower than those that are tabulated in Table 5-3.

The midway AO and I_{PC} sensitivity profiles when x = 0 mm are shown in Figure 5-23 and the comparison of the SFR and ROI sensitivity is summarised in Table 5-6. In summary, the AO method is more sensitive in the ROI than SFR, and the PC method has the higher sensitivity in the SFR than the ROI.

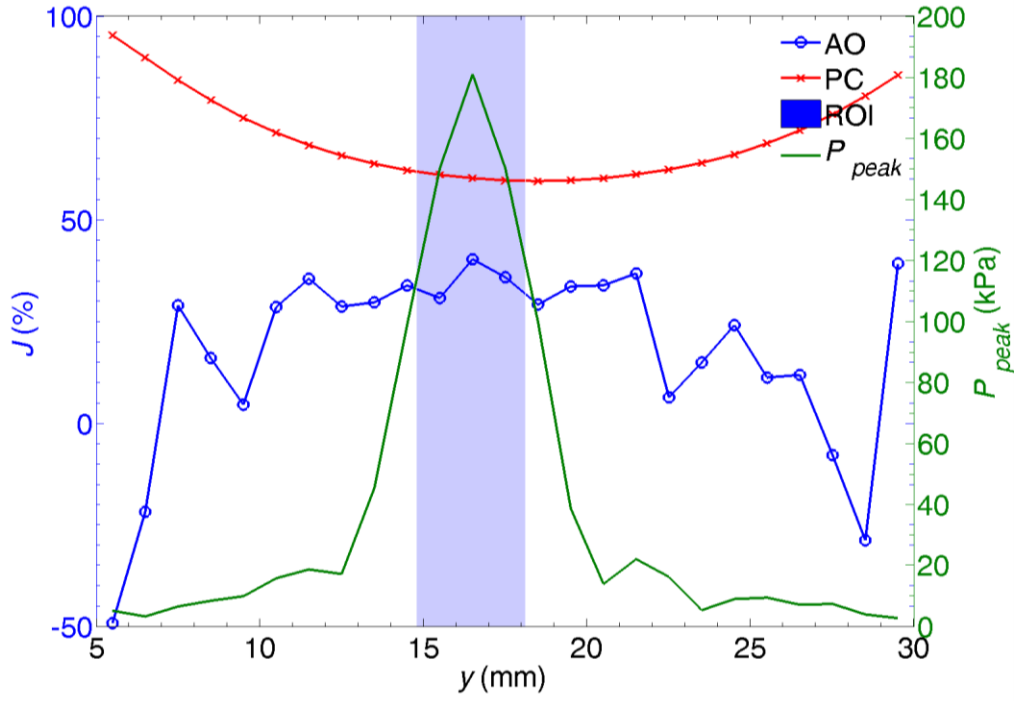

Figure 5-23 The midway sensitivity of AO and I_{PC} at different depth y for transmission mode when the background μ_a = 0.1 cm^{-1}.

Detection Method	*J*(SFR) (%)	*J*(ROI) (%)	Is *J*(ROI) higher than *J*(SFR)?
I_{PC}	95.2	60.1	No
AO	-49.0	40.2	Yes

Table 5-6 Comparison of the midway sensitivity of the AO and I_{PC} methods in the SFR and the ROI when the background μ_a = 0.1 cm^{-1}.

5.2.5 **Summary**

The implications of these transmission mode spatial sensitivity results are:

1. The presence of the local perturbation within the Intralipid solution appears to have no significant effect on the spatial sensitivity in the AO and the I_{PC} measurements. They are optically homogenous; however the slight mismatch between the acoustic properties seems to have produced a small localised increase in the AO signal in the FUR.
2. The optical measurements are shown to have higher absolute sensitivity to absorption changes in the transmission mode as compared to the AO method.
3. The AO method is sensitive to the localised absorption change in the ROI than in the SFR. On the contrary, any absorption change in the SFR has a greater effect on the optical measurement than in the ROI.
4. The overlap between the FUR and high AO sensitivity verifies the ability of AO method to localise or tag diffused light in a transmission mode absorption measurement.
5. With increased background absorption, the sensitivity of the AO and optical measurements becomes lower. The spatial sensitivity of the AO measurement becomes noisier but still shows good localisation in the FUR whereby the maximum AO sensitivity overlaps with the FUR.

5.3 Reflection Mode

This section details the experimental results of the reflection mode spatial sensitivity mapping. Additional results are presented for the spatially resolved system.

5.3.1 Sensitivity Maps

For the reflection mode experiments conducted for this section, the ROI was placed 20 mm away from the phantom surface. The AO and optical measurements' results are presented in Figure 5-24, whereby the classical 'banana' shape of the light propagation from an optical source to detector in a reflection mode is evident. The reference measurements for each method are shown in Figure 5-25.

The largest signal change in all of the detection schemes was found near to both the optical source and detector, except for the I_{CCD}. The largest change in the I_{CCD} was found near to the optical source in Figure 5-24 (e). This is because the width of the local absorber (5 mm) is smaller than the width of the CCD image area (8.67 mm). This means that the view of the CCD image area is never wholly obstructed by the local absorber, which in turn softens the drop of the mean intensity as compared to the I_{PC}.

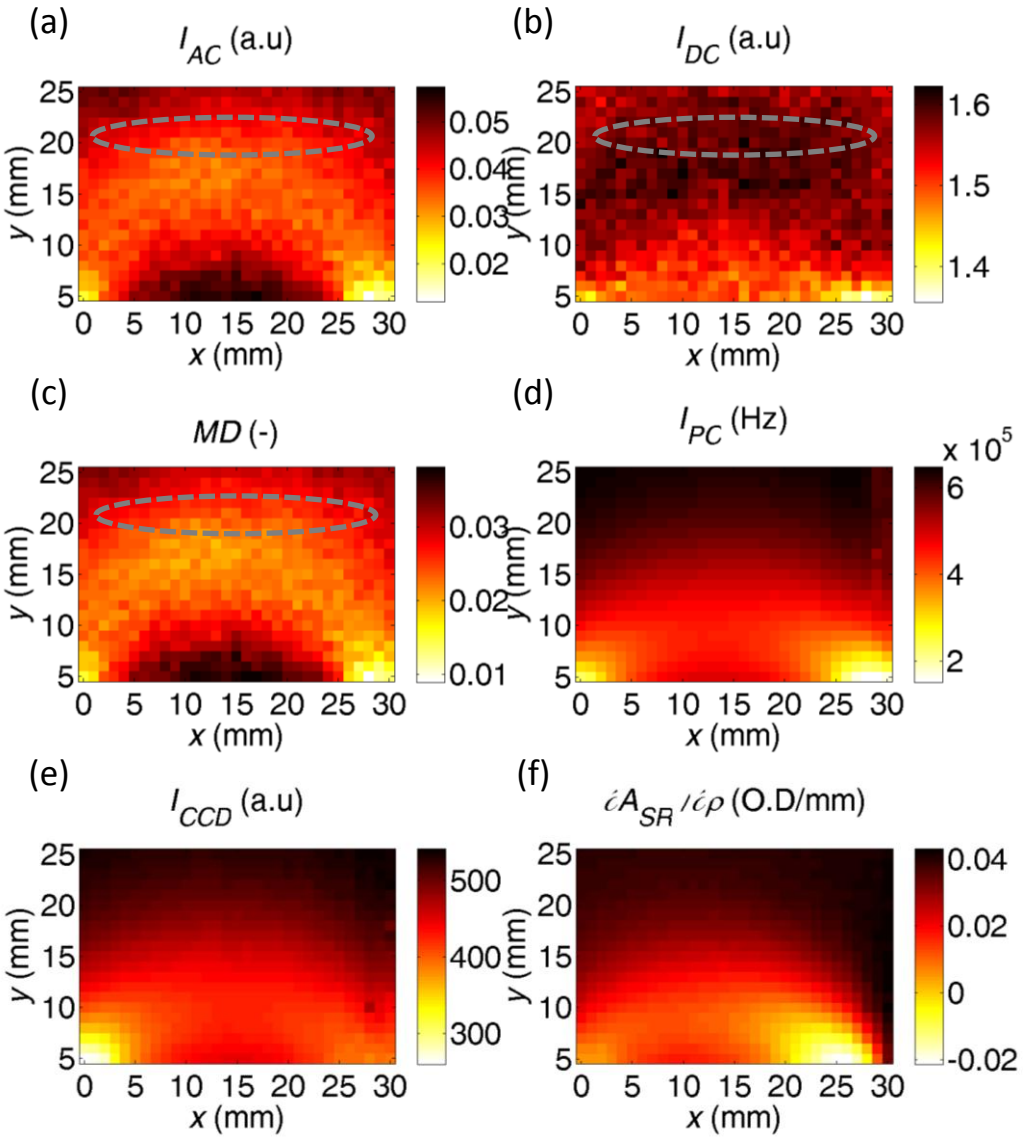

Figure 5-24 The measurement results of AO: (a) I_{AC}, (b) I_{DC}, (c) MD; (d) I_{PC}; (e) I_{CCD}; and (f) $\frac{\partial A_{SR}}{\partial \rho}$ for reflection mode when the background μ_a = 0.0235 cm^{-1}. (dashed line: FUR)

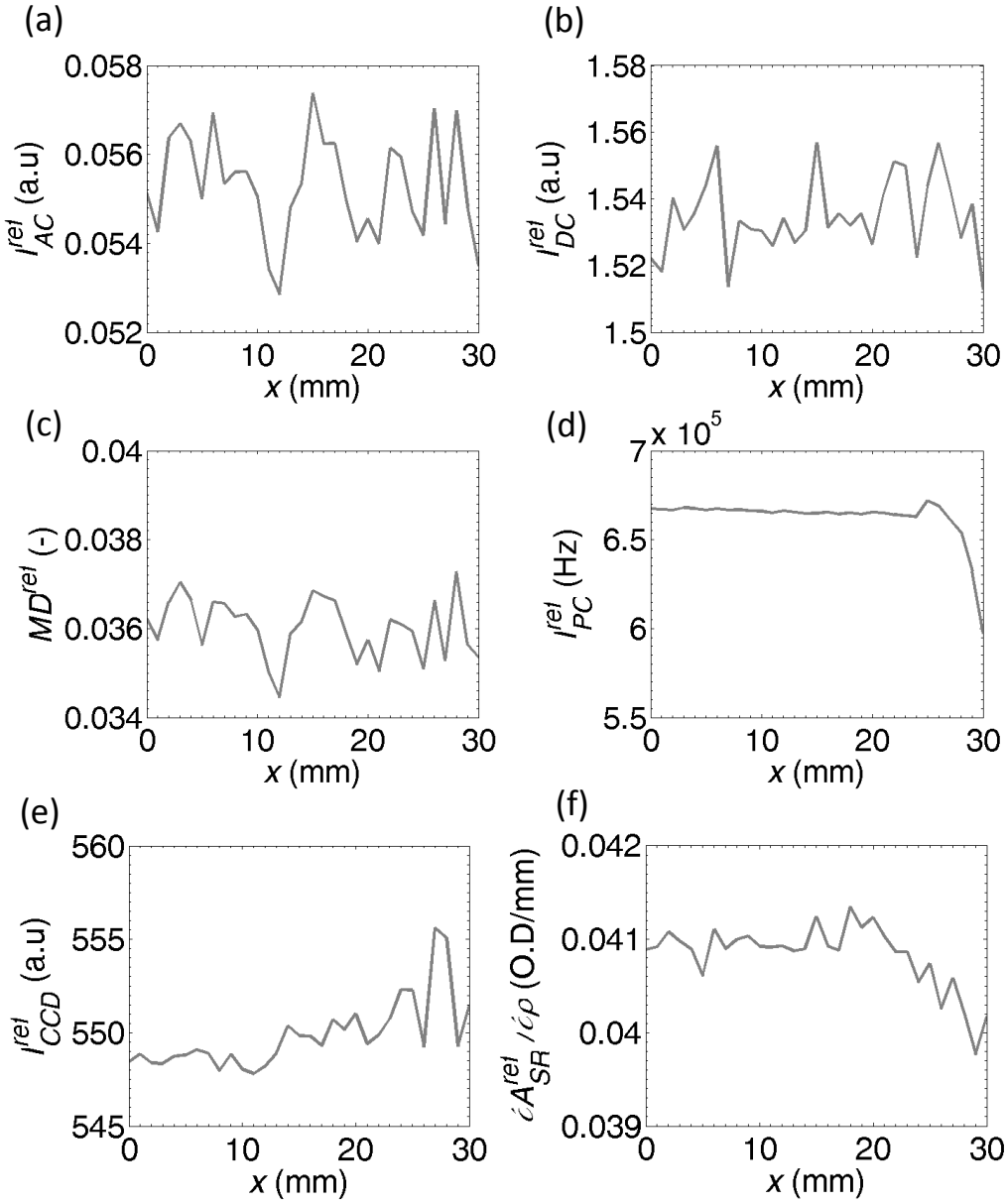

Figure 5-25 The reference measurement results of AO: (a) I_{AC}, (b) I_{DC}, and (c) MD; (d) I_{PC}; (e) I_{CCD} and (f) $\frac{\partial A_{SR}}{\partial \rho}$ for reflection mode when the background μ_a = 0.0235 cm^{-1}.

It is noted that, a negative signal change is observed in the $\frac{\partial A_{SR}}{\partial \rho}$ that is shown in Figure 5-24 (f). When the local absorber is near the 1st segment that is shown in

Figure 5-7, the A_1 is significantly higher than A_2 and A_3. This causes the reversal of the $\frac{\partial A_{SR}}{\partial \rho}$ to negative.

Similar to the results of the transmission mode, Figure 5-24a shows that the I_{AC} is strongly attenuated by the presence of the local absorber in the proximity of the FUR. On the contrary, there is less reduction of the I_{DC} in the same region (Figure 5-24b), which results in the decrease in the MD (Figure 5-24c). Another interesting observation is that the midway region between the optical source and detector (y = 5-10 mm) in the SFR exhibits low I_{AC} drop and high I_{DC} drop. The combined effect results in a minimal change in the MD in this region. This phenomenon is not observed in the optical measurement methods, which are very sensitive to absorption change in the SFR.

The spatial sensitivity maps of each detection method are shown in Figure 5-26. The spatial sensitivity of the AO measurement has three interesting observations. Firstly, the sensitive AO region does not overlap wholly with the FUR in the reflection mode measurement unlike in the transmission measurement. The magnitude of the AO signal depends on the overlap region of the FUR and the optical path length distribution. This phenomenon is also observed in the literature [Bratchenia 2011, Gunadi 2011]. Secondly, even though the region of the high AO sensitivity does not coincide with the FUR, it is deeper when compared to that of the optical measurements. Finally, the region that is close to the SFR and located between the optical source and detector, exhibits negative sensitivity. This means that the MD is increased because the local absorber blocks mostly DC intensity.

The most sensitive detection method is the spatially resolved system; however it is also the most sensitive method to the absorption changes in the SFR. The least sensitive system is the I_{CCD} method. The I_{CCD} measurement is less susceptible to changes near the viewing region of the camera. This is because the size of the local absorber is smaller than the camera's image area. Thus when the local absorber is very close to the position (30,5), only part of the CCD image area,

which is overshadowed by the local absorber, has large reduction in intensity. The drop in the mean intensity of the whole image is softened by other brighter pixels.

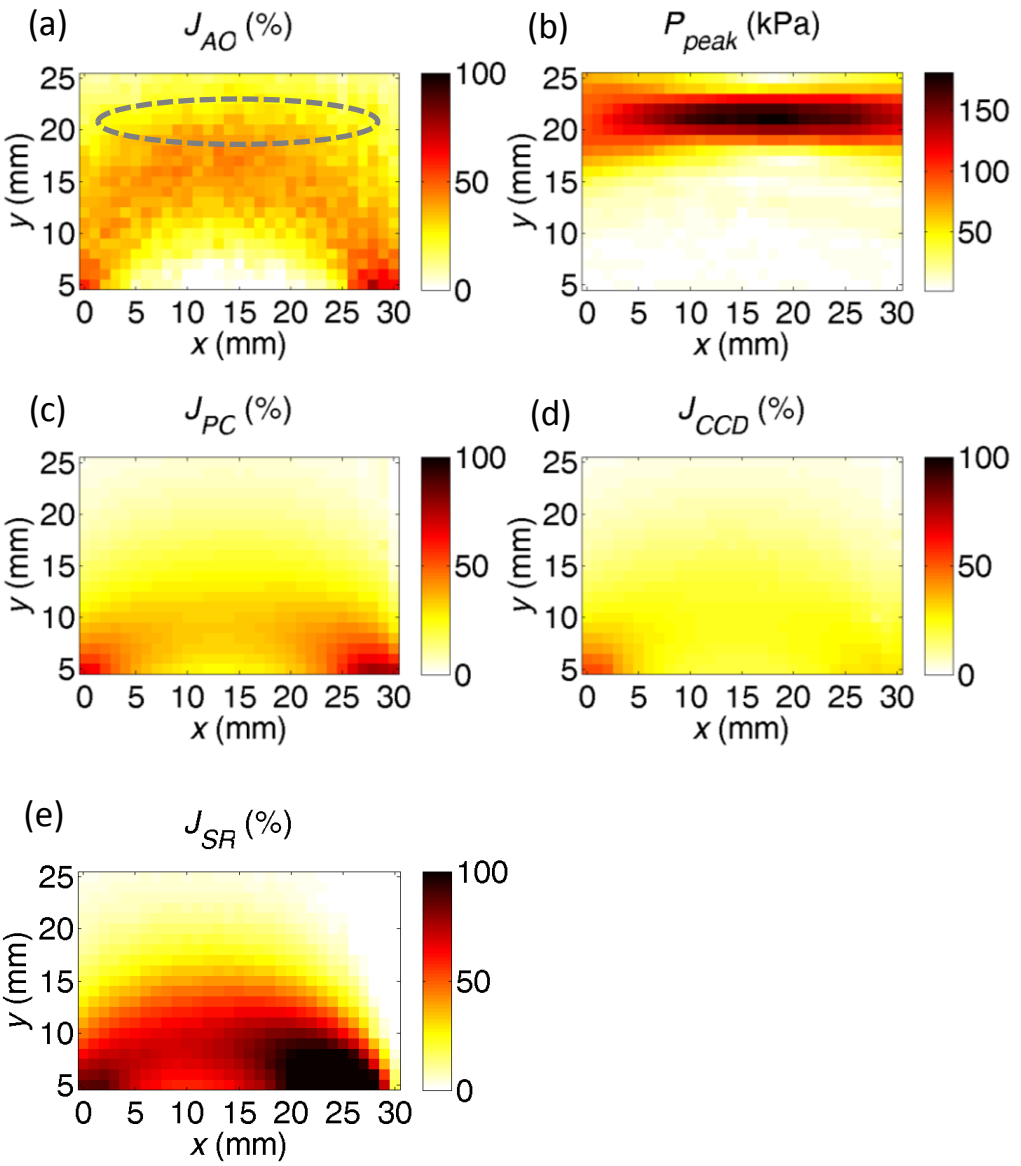

Figure 5-26 The spatial sensitivity maps of (a) AO, (c) I_{PC}, (d) I_{CCD} and (e) $\frac{\partial A_{SR}}{\partial \rho}$ for reflection mode when the background μ_a = 0.0235 cm^{-1}: the sensitive AO region does not overlap wholly with theFUR and negative AO sensitivity is observed near the SFR. The $\frac{\partial A_{SR}}{\partial \rho}$ method is the most sensitive method and the I_{CCD} is the least sensitive method. (dashed line: FUR)

When the local absorber is very close to the CCD detection place (30,5), the $\frac{\partial A_{SR}}{\partial \rho}$ sensitivities are actually higher than 100%. The $\frac{\partial A_{SR}}{\partial \rho}$ sensitivity map in Figure 5-26 (f) is clipped to the range of 0 to 100% for comparison. As mentioned earlier, the local absorber blocks more light in the 1st segment of the image area than the subsequent segments resulting in a negative $\frac{\partial A_{SR}}{\partial \rho}$, which is shown in Figure 5-24 (f). Therefore the $\frac{\partial A_{SR}}{\partial \rho}$ sensitivity calculated from equation (5-7) becomes higher than 100%.

The observations based on the results presented in this section generally agree with the computer simulation results by Powell [Powell 2011], which are shown in Figure 5-27 (a) and (b) for the optical and the AO spatial sensitivity maps respectively. A negative sensitivity here denotes there is a reduction in the measurement. The orientation of the FUR is different from the orientation, which is shown in Figure 5-4 (a). The photons (10^6) are injected at position (x = 0, y = 4 mm) denoted by Δ and the backscattered photons are captured at the blue plane, by reciprocity in the post processing, Δ and the blue plane can be considered as the point detector and a plane optical source respectively. The properties of the background medium are: μ_s' = 2 cm^{-1} and μ_a = 0.1 cm^{-1}. The peak pressure in the FUR is 143 kPa and the optical properties of the local absorber (5 x 5 x 20 mm) are μ_s' = 2 cm^{-1} and μ_a = 10 cm^{-1}.

Figure 5-27 shows that the AO measurement can probe deeper than the optical measurement and the increase in the MD in the region between the optodes in the SFR, which is shown in Figure 5-26 (a), is also evident in the simulated AO spatial sensitivity. The most sensitive AO measurements is not located very close to the optical source and detector in Figure 5-27 (b) because the placement of the FUR is different from the experimental study, which is shown in Figure 5-26 (b).

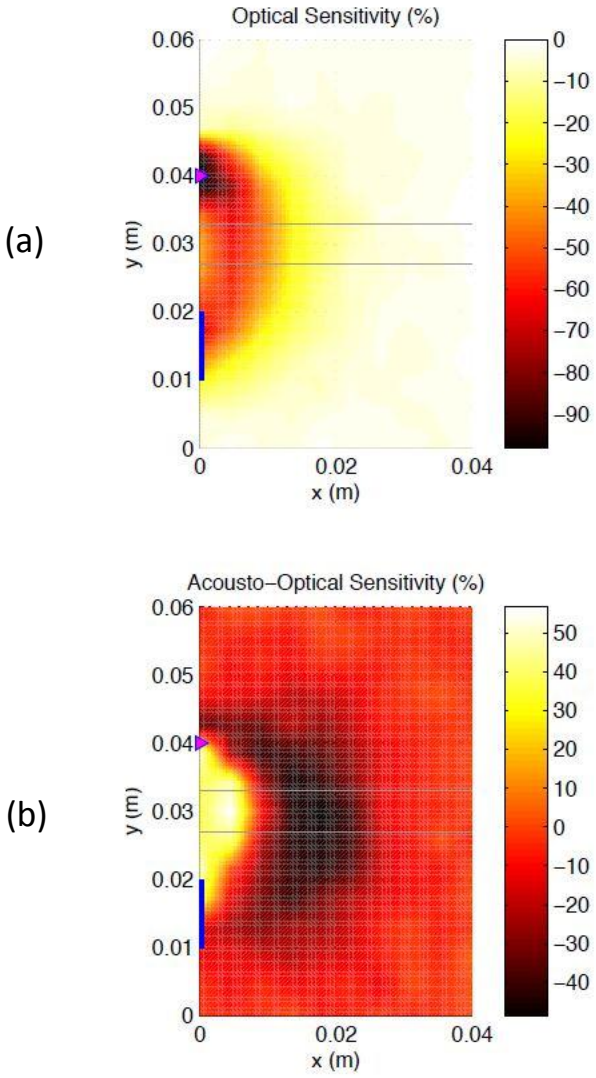

Figure 5-27 Monte Carlo simulation results by Powell [Powell 2011]: (a) the optical and (b) the AO sensitivity maps in reflection mode (a negative sensitivity here denotes a reduction in measurement) [FUR: area between the two grey lines].

5.3.2 Mean and Midway Sensitivity in the Superficial Region and the Region of Interest

The mean sensitivities of the measurement <*J*> are depicted in Figure 5-28. The comparison of the values in the SFR and the ROI and the mean penetration depths of each method are summarised in Table 5-7. They show that the AO method is the least sensitive in the SFR and most sensitive in the ROI. All optical

measurements are sensitive to changes near the SFR than the ROI. The maximum $<J_{AO}>$ does not occur in the ROI that is 22 mm deep, but at 16 mm deep. At this depth, $<J_{AO}>$ is higher than $<J_{PC}>$, $<J_{CCD}>$ and $<J_{SR}>$. The $<J_{AO}>$ in the ROI is also the highest when compared to $<J_{PC}>$, $<J_{CCD}>$ and $<J_{SR}>$ in the ROI. All optical methods are most sensitive in the SFR, especially the $\frac{\partial A_{SR}}{\partial \rho}$ method. The mean penetration depths of $\langle y_{AO} \rangle$ is the deepest at 14.8 mm according to Table 5-7. But it is not located in the ROI where the FUR is. The $\frac{\partial A_{SR}}{\partial \rho}$ method probes the shallowest at 10.2 mm and it is also the most sensitive method in the SFR (86.6 %).

Similar observations can be made about the midway sensitivities, which is shown in Figure 5-29 and summarised in Table 5-8. These results also verify the earlier observation of the increase in the MD when the local absorber is in the SFR. At this location, the local absorber absorbs more I_{DC} than I_{AC} resulting in the increase of the MD.

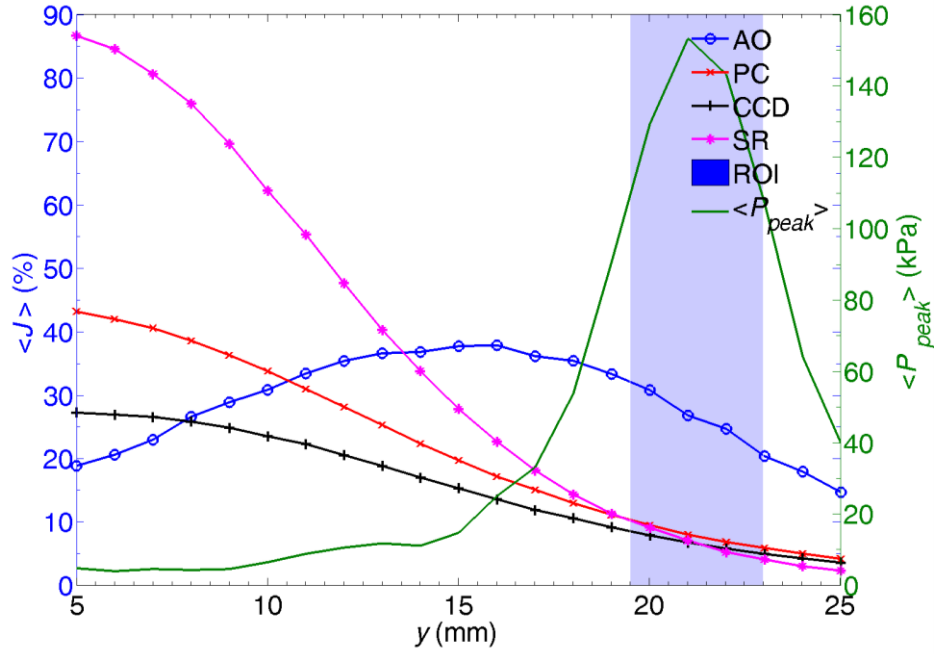

Figure 5-28 The mean sensitivity of AO, I_{PC}, I_{CCD} and $\frac{\partial A_{SR}}{\partial \rho}$ at different depth y for reflection mode when the background μ_a = 0.0235 cm^{-1}: the maximum <J_{AO}> does not reside in the FUR and the most sensitive method is the $\frac{\partial A_{SR}}{\partial \rho}$ method, but only <J_{AO}(ROI)> is higher thatn <J_{AO}(SFR)>.

Detection Method	<J(SFR)> (%)	<J(ROI)> (%)	Is <J(ROI)> higher than <J(SFR)>?	Mean Penetration Depth <y> (mm)
I_{CCD}	27.2	6.8	No	11.8
I_{PC}	43.16	8.0	No	11.4
AO	18.9	26.8	Yes	14.8
$\frac{\partial A_{SR}}{\partial \rho}$	86.6	7.1	No	10.2

Table 5-7 Comparison of the mean sensitivity of AO, I_{PC}, I_{CCD} and $\frac{\partial A_{SR}}{\partial \rho}$ in the SFR and the ROI and their mean penetration depths for reflection mode when the background μ_a = 0.0235 cm^{-1}: the AO method probes the deepest and is the least sensitive to localised absorption change in the SFR.

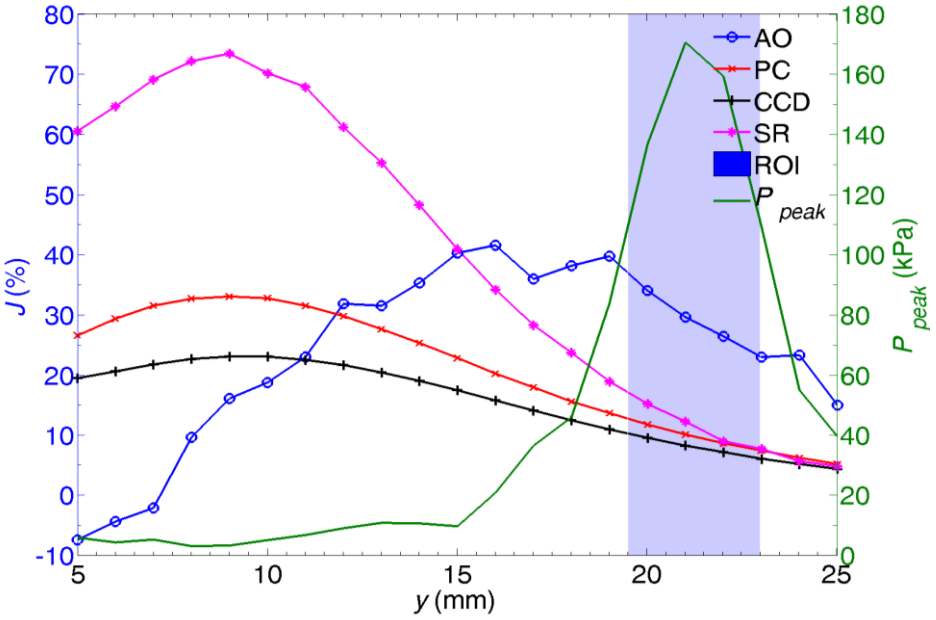

Figure 5-29 The midway sensitivity of AO, I_{PC}, I_{CCD} and $\frac{\partial A_{SR}}{\partial \rho}$ at different depth y for reflection mode when the background μ_a = 0.0235 cm^{-1}: they depict the similar sensitivity behaviour to the <J>. However the increase in MD (negative sensitivity) in the SFR is more evident.

Detection Method	J(SFR) (%)	J(ROI) (%)	Is J(ROI) higher than J(SFR)?
I_{CCD}	19.5	8.27	No
I_{PC}	26.6	10.1	No
AO	-7.36	29.6	Yes
$\frac{\partial A_{SR}}{\partial \rho}$	60.5	12.3	No

Table 5-8 Comparison of the midway sensitivity of AO, I_{PC}, I_{CCD} and $\frac{\partial A_{SR}}{\partial \rho}$ in the SFR and the ROI for reflection mode when the background μ_a = 0.0235 cm^{-1}.

5.3.3 Effects of the Location of the Focused Ultrasound Region on the Spatial Sensitivity

It has been shown in section 5.3.1 that the sensitive region of the AO measurement can be relocated by the FUR. But the most sensitive AO region does not overlap the FUR. It is concluded that the most sensitive region of the AO measurement depends on the proximity of the FUR and regions of high photon path distribution within the turbid medium. In order to investigate this phenomenon further, the spatial sensitivity maps of the AO measurements were repeated by systematically relocating the FUR to different depths. This was carried out so that the effect of the depth of the FUR on the mean penetration depth and regional sensitivity can be studied.

5.3.3.1 Methods

The experiment detailed in section 5.3.1 and 5.3.2 has demonstrated the J_{AO} when the FUR was located at y = 21 mm from the plane of optical source-detector. In this section, the FUR was re-located to y = 10, 15 and 25 mm systematically. For each FUR location, the spatial sensitivity was mapped using the same experimental setup and procedures for only the AO method. The optical measurements are not affected by the location of FUR.

5.3.3.2 Sensitivity Maps

The spatial sensitivity maps for the different FUR locations are shown in Figure 5-30. Figure 5-30 (a) and (b) show that when the FUR is located in the region of high J_{PC}, the most sensitive AO region and the FUR are nearly overlapped. When the FUR relocates deeper, the most sensitive AO region and the FUR are increasingly detached from each other. This result reaffirms the previous assertion that the proximity of the FUR and the region of high J_{PC} is influencing the location of the most sensitive AO region. When the FUR is relocated to the regions of lower J_{PC}; there are more fluctuations in the J_{AO}. This suggests that there is a limit when the signal to noise ratio of the AO signal is so poor that it is no longer detectable for the current AO detection setup.

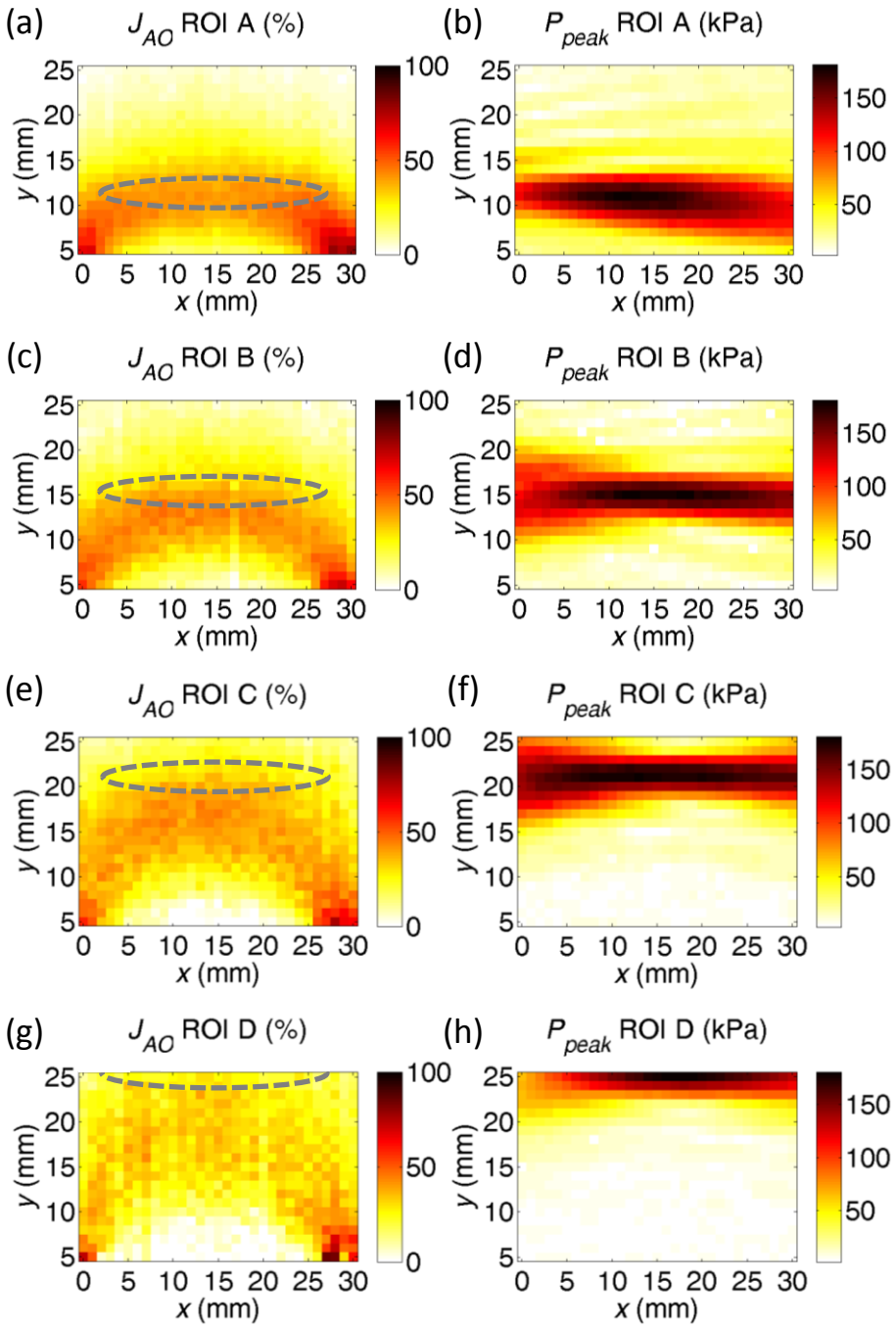

Figure 5-30 The spatial sensitivity maps of the AO method (a), (c), (e) and (g) when the FUR is located at: (b) ROI A (y = 10 mm); (d) ROI B (y = 15 mm); (f) ROI C (y = 20 mm); and (h) ROI D (y = 25 mm) respectively for reflection mode when the background μ_a = 0.0235 cm^{-1}: the location of sensitivie AO measurement can be relocated by positioning of the ultrasound transducer. (dashed line: FUR)

5.3.3.3 Mean and Midway Sensitivity in the Superficial Region and the Region of Interest

Similar observations can be drawn from the mean sensitivity of the AO measurement at different depths, which is shown in Figure 5-31. Table 5-9 demonstrate that the mean penetration depth of the AO method can be relocated from 11.8 mm to 15.8 mm. When the FUR is relocated to the deeper regions, the maximum $<J_{AO}>$ are also relocated to the deeper region. However when the FUR is relocated to the deeper regions, the $<J_{AO}(\text{SFR})>$ and $<J_{AO}(\text{ROI})>$ are becoming lower.

The differences between $<J_{AO}(\text{SFR})>$ and $<J_{AO}(\text{ROI})>$ for different FUR location are similar. The highest $<J_{AO}>$ is located within the ROI when the FUR is located at y = 11 mm. When FUR is relocated deeper, the location of the highest $<J_{AO}>$ is getting further away from its respective ROI.

Figure 5-32 shows the maximum penetration depth, which is the maximum midway sensitivity for different FUR location. The maximum midway AO sensitivities of the different FUR location (irrespective of the ROI) are similar at about 40% up to y = 25 mm; but they are increasingly noisier due to the inadequate detection of the I_{AC}.

Both Figure 5-32 and Table 5-10 shows that an increase in the MD in the SFR when the FUR is located at y > 15 mm, i.e. ROI C (y = 22 mm) and ROI D (y = 25 mm). When the FUR is located in the ROI C or the ROI D and the local absorber is located in the SFR, more I_{DC} is absorbed than I_{AC}.

Figure 5-32 shows that $<J_{AO}(\text{SFR})>$ is getting smaller when the FUR is relocated deeper. Thus, potential the AO method can adjusted to be insensitive ($J_{AO}(\text{SFR}) = 0$) to absorption changes in the SFR (excluding the regions very close to optical source and detector) by careful positioning of the FUR.

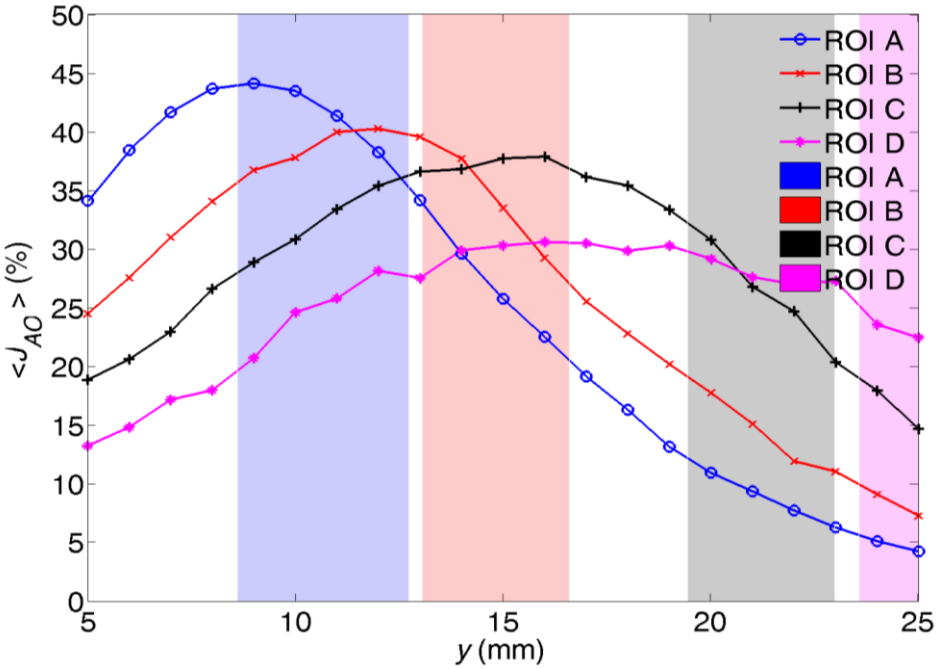

Figure 5-31 The mean sensitivity of the AO method for different FUR locations at different depth y for reflection mode when the background μ_a = 0.0235 cm^{-1}: the most sensitive region never overlap with its ROI but the maximum $<J_{AO}>$ can be relocated with different FUR location.

Location	$<J_{AO}$(SFR)> (%)	$<J_{AO}$(ROI)> (%)	Is $<J_{AO}$ (ROI)> higher than $<J_{AO}$ (SFR)>?	Mean Penetration Depth (mm)
ROI A	34.1	41.3	Yes	11.8
ROI B	24.5	33.5	Yes	13.1
ROI C	18.9	26.8	Yes	14.8
ROI D	13.3	22.5	Yes	15.8

Table 5-9 Comparison of the mean sensitivity of the AO method for different FUR locations in the SFR and the ROI and their mean penetration depths for reflection mode when the background μ_a = 0.0235 cm^{-1}.

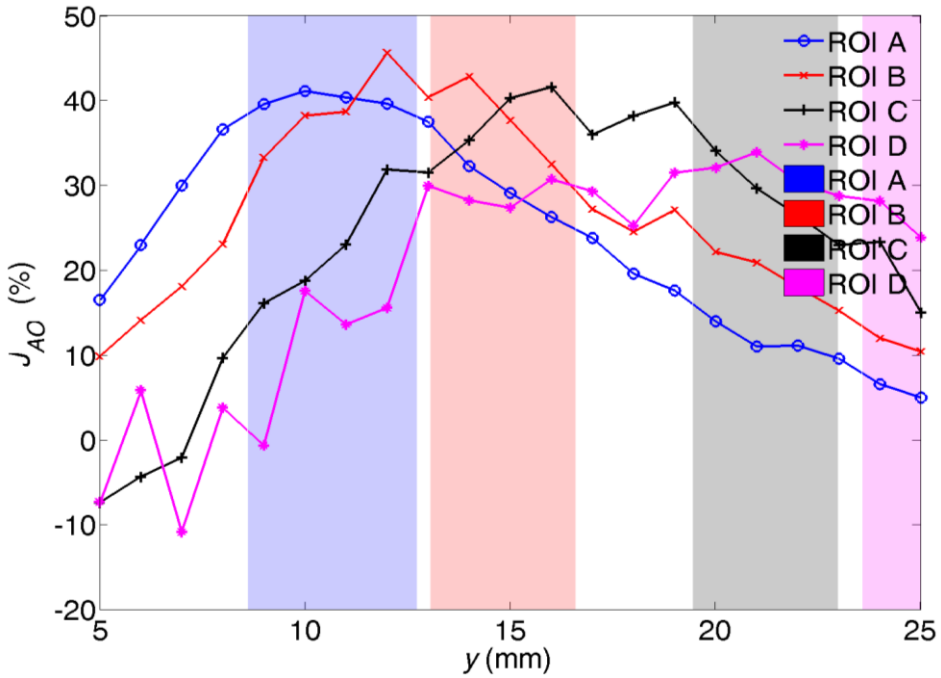

Figure 5-32 The midway sensitivity of the AO method for different FUR locations at different depth y for reflection mode when the background μ_a = 0.0235 cm^{-1}: they show the increasingly noisy midway sensitivity curves when the FUR is relocated deeper. The increase of the midway sensitivity in the SFR can only be observed when the FUR is located at y = 22 and 25 mm.

Location	J_{AO}(SFR) (%)	J_{AO}(ROI) (%)	Is J_{AO}(ROI) higher than J_{AO}(SFR)?	Maximum Penetration Depth at maximum J_{AO} (mm)
ROI A	16.5	40.3	Yes	10
ROI B	9.82	37.6	Yes	12
ROI C	-7.36	29.6	Yes	16
ROI D	-7.29	23.8	Yes	21

Table 5-10 The comparison of the midway sensitivity of the AO method for different FUR locations in the SFR and the ROI for reflection mode when the background μ_a = 0.0235 cm^{-1}: the AO method can probe up to 21 mm deep and the increase in MD in the SFR is only observable when the FUR is located at y > 15 mm.

5.3.4 Effects of Background Absorption on the Spatial Sensitivity

This section describes the results of the experiment, which is a repeat of the study described in section 5.2.4 for reflection mode. The background μ_a was increased from 0.0235 cm^{-1} to 0.1 cm^{-1}.

5.3.4.1 Materials and Methods

The NIR dye was added to the phantom to achieve μ_a = 0.1 cm^{-1} and the sensitivity mapping was repeated using the same setup and protocol. However, the detected AO signal was very noisy because the detected mean intensity was very low. To improve the signal-noise-ratio of the AO signal, the ultrasound transducer's excitation voltage was raised from 20 V to 25 V peak-peak and the integration time of the digital correlator was increased to 30 seconds from 20 seconds. Because of the increase in the integration time, the maximum depth *y* of the SA for this study was reduced from 25 mm to 20 mm. The FUR was placed in the ROI, which was 15 mm deep. The rest of the experimental parameters remained unchanged.

5.3.4.2 Sensitivity Maps

The AO and the I_{PC} measurements are shown in Figure 5-33 and the reference measurements are shown in Figure 5-34. Because of the higher background absorption, all measurements are lower. The I_{AC} and I_{DC} are noisier which in turn lead to noisier MD. The resulting sensitivity maps are shown in Figure 5-35. Only the normalised ultrasound field is shown in Figure 5-35 (c) to show the location of the FUR.

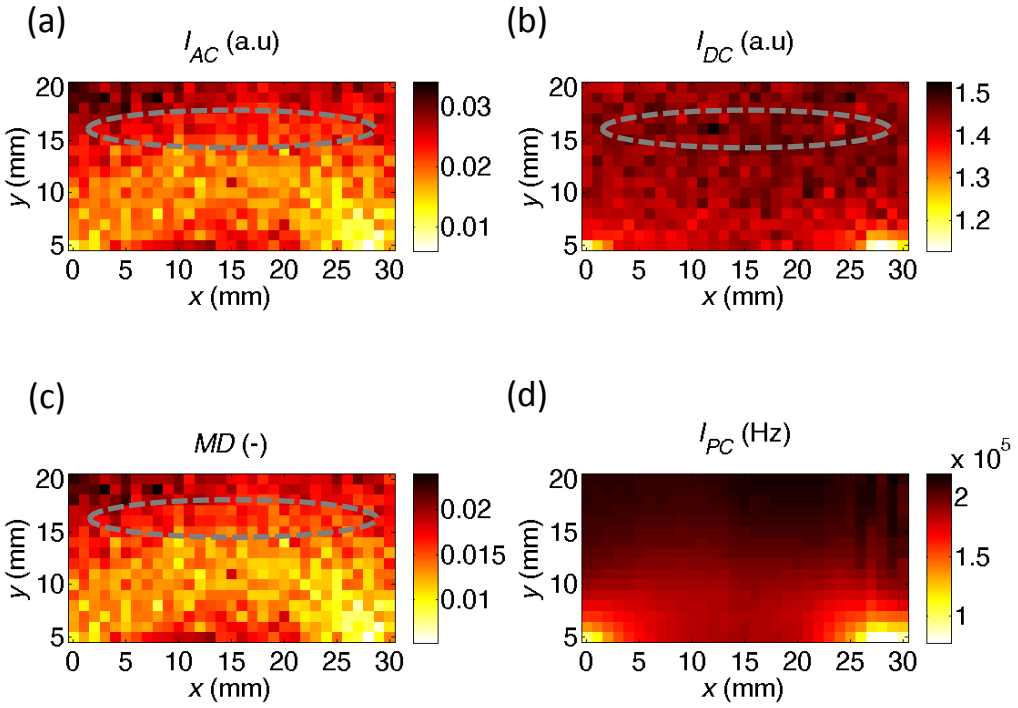

Figure 5-33 The measurement results of AO: (a) I_{AC}; (b) I_{DC}; (c) MD; and. (d) I_{PC} for reflection mode when the background μ_a = 0.1 cm^{-1}. (dashed line: FUR)

Based on the sensitivity maps, the AO method can probe deeper than I_{PC} method. Similarly, the location of high AO sensitivity does not overlap with the FUR. When compared to the AO sensitivity map in Figure 5-30 (c) with minimal background absorption, the higher absorption causes higher fluctuations in the spatial sensitivity. The region of high AO sensitivity is less defined than the one that is shown in Figure 5-30 (c). At x = 15 mm, the midway sensitive AO region is located at about y = 10-11 mm compared to y = 12-13 mm in Figure 5-30 (c). Thus because of the higher background absorption, the maximum penetration depth of the AO method becomes shallower. The I_{PC} sensitivity map also has similar behaviour, when compared to Figure 5-26 (c).

The region of the lower AO sensitivity in the SFR is smaller in this study when compared to that is depicted in Figure 5-30 (c) because the maximum penetration

depth is decreased. Thus, the AO method becomes more sensitive to any absorption changes in the SFR in a more absorbing medium.

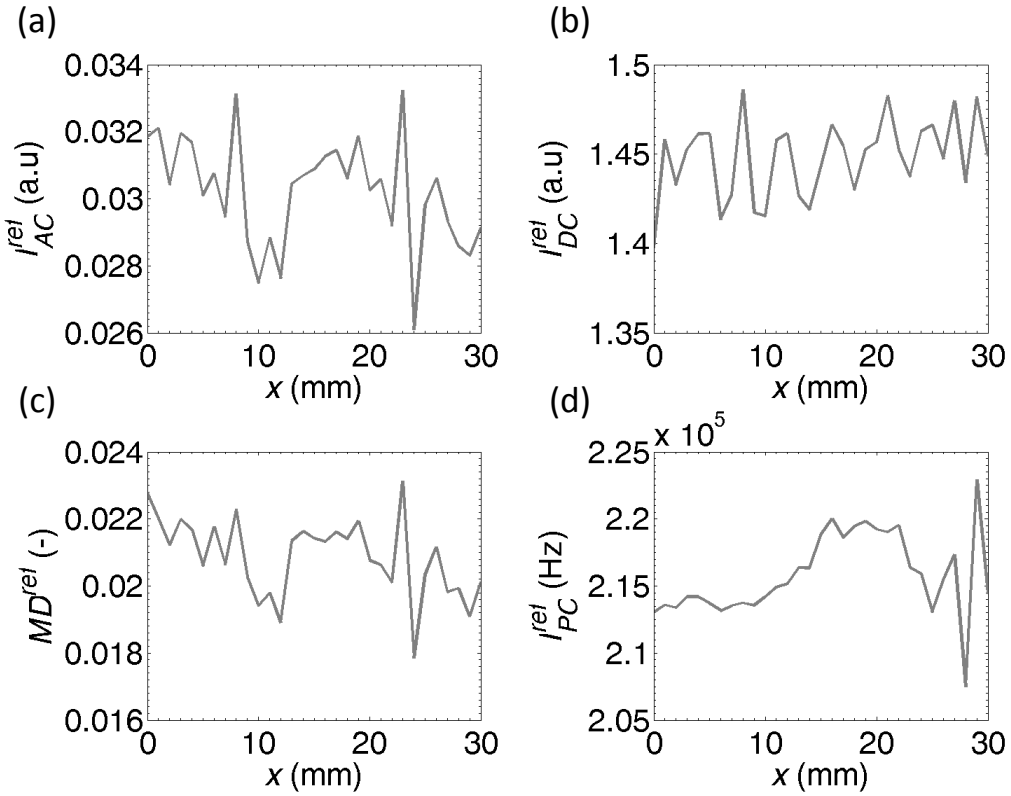

Figure 5-34 The reference measurement results of AO:(a) I_{AC}; (b) I_{DC}; (c) MD; and. (d) I_{PC} for reflection mode when the background μ_a = 0.1 cm^{-1}.

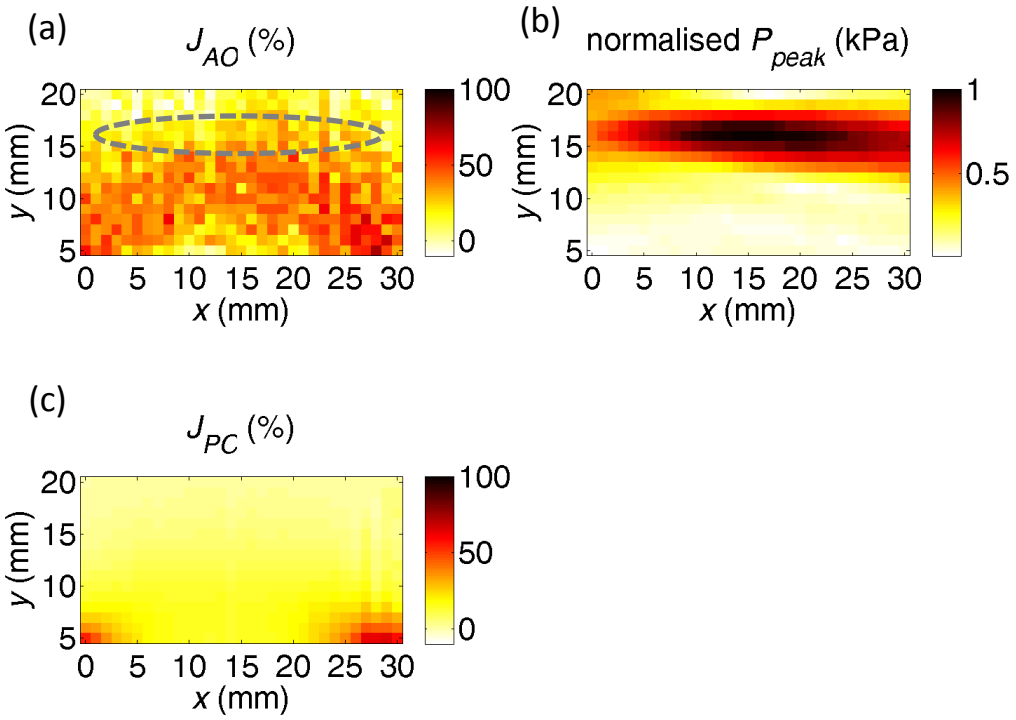

Figure 5-35 The spatial sensitivity maps of (a) AO and (c) I_{PC} with (b) the FUR for reflection mode when the background μ_a = 0.1 cm^{-1}. (dashed line: FUR)

5.3.4.3 Mean and Midway Sensitivity in the Superficial Region and the Region of Interest

The mean sensitivity profiles are presented in Figure 5-36 and the comparison of the mean sensitivity in the SFR and the ROI and the mean penetration depths are summarised in Table 5-11. The <J_{AO}(SFR)> is higher than <J_{AO}(ROI)>, which is opposite when there is only minimal absorption. But the highest <J_{AO}>, which is located at 8 mm, is higher than <J_{AO}(SFR)> and the highest <J_{PC}>. The mean penetration depth is now 11 mm, which less than 13.1 mm (Table 5-9) when there is minimal background absorption. But the AO method can still probe deeper than the I_{PC} method.

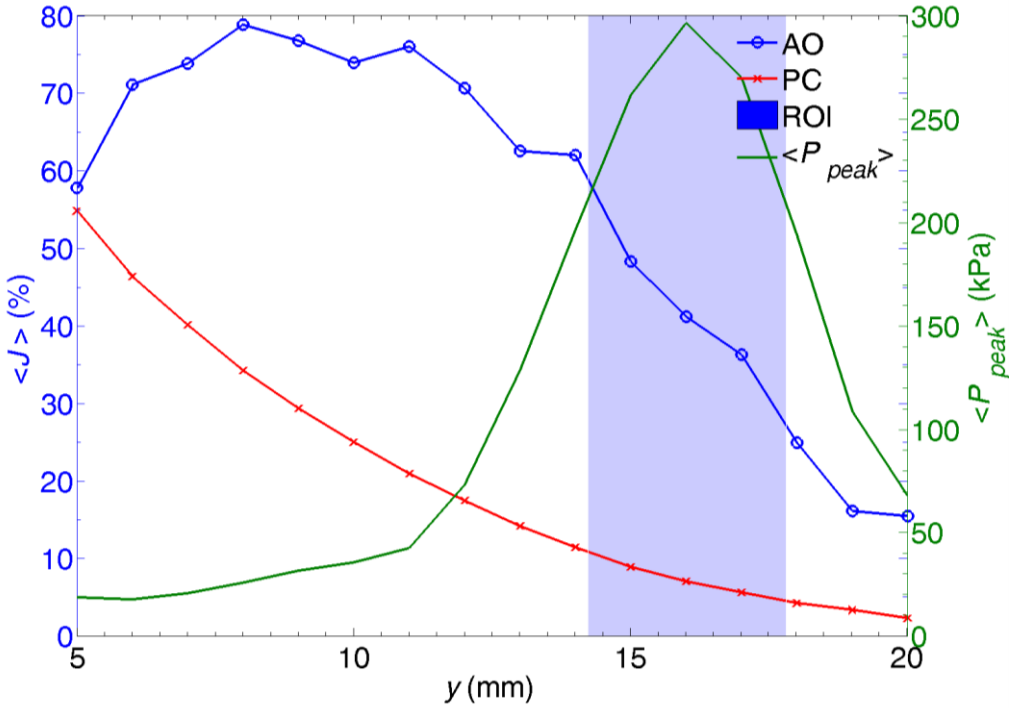

Figure 5-36 The mean sensitivity of AO and I_{PC} at different depth y for reflection mode when the background μ_a = 0.1 cm^{-1}.

Detection Method	<J(SFR)> (%)	<J(ROI)> (%)	Is <J(ROI)> higher than <J(SFR)>?	Mean Penetration Depth <y> (mm)
I_{PC}	54.8	7.1	No	9.0
AO	57.8	41.2	No	11.0

Table 5-11 Comparison of the mean sensitivity of AO and I_{PC} in the SFR and the ROI and their mean penetration depths for reflection mode when the background μ_a = 0.1 cm^{-1}.

The $\langle J_{AO}(SFR)\rangle$ is slightly higher than $\langle J_{PC}(SFR)\rangle$, which implies that the AO method is more sensitive in the SFR than the I_{PC} method. This suggests that to minimise the sensitivity in the SFR, the FUR has to be relocated deeper according to Figure 5-31. But doing so would require a higher ultrasound amplitude and a

longer integration time in order to compensate the higher noise level. Alternatively, a better AO detection method can be used. However, $<J_{AO}(\text{ROI})>$ is still higher than $<J_{PC}(\text{ROI})>$. The mean penetration depth of I_{PC} method is also shallower, a reduction from 11.4 mm (Table 5-7) to 9 mm.

The midway AO and I_{PC} sensitivity profiles are plotted in Figure 5-37 and the comparison between the midway sensitivities $J_{AO}(15, y)$ and $J_{PC}(15, y)$ is summarised in Table 5-12. $J_{AO}(\text{SFR})$ is higher than $J_{PC}(\text{SFR})$ but $J_{AO}(\text{ROI})$ is slightly higher than $J_{AO}(\text{SFR})$. On the other hand, $J_{PC}(\text{SFR})$ is greater than $J_{PC}(\text{ROI})$. The performance of the AO method is still better in the ROI because $J_{AO}(\text{ROI})$ is considerable higher than $J_{PC}(\text{ROI})$.

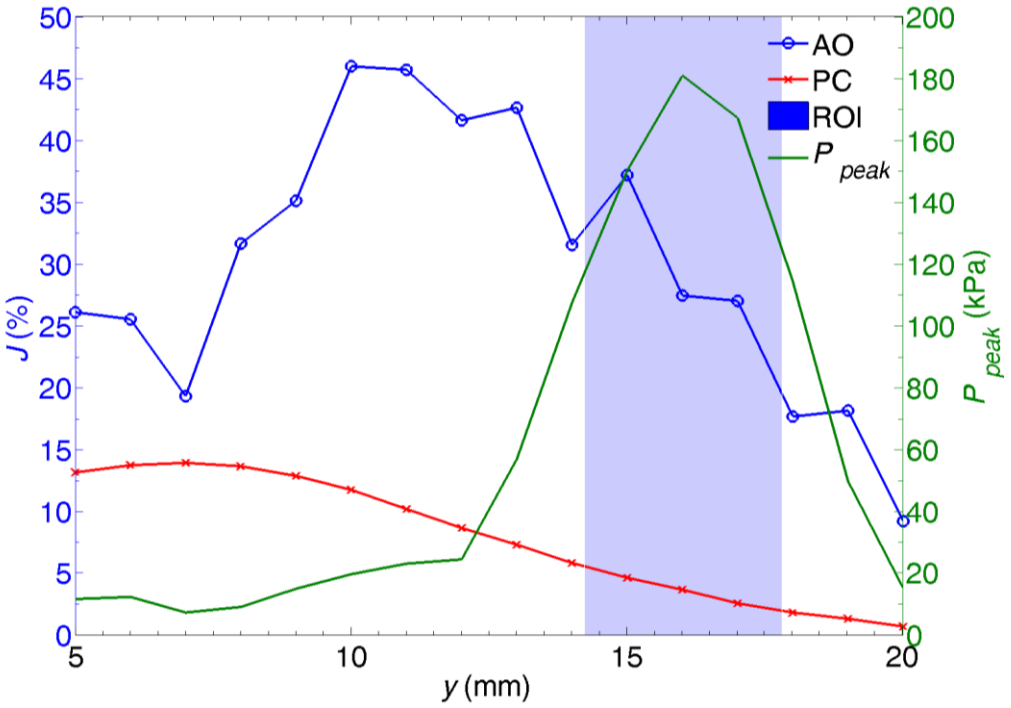

Figure 5-37 The midway sensitivity of AO and I_{PC} at different depth y for reflection mode when the background μ_a = 0.1 cm^{-1}.

Detection Method	J(SFR) (%)	J(ROI) (%)	Is J(ROI) higher than J(SFR)?
I_{PC}	13.2	3.7	No
AO	26.1	27.4	Yes

Table 5-12 Comparison of the midway sensitivity of AO and I_{PC} in the SFR and the ROI for reflection mode when the background μ_a = 0.1 cm^{-1}.

5.3.5 **Summary**

In summary, the reflection mode experiments show that:

1. For a reflection mode measurement, the most sensitive region of AO measurement does not coincide with the FUR. It depends of the overlap region of the FUR and the fluence distribution in the FUR.
2. The sensitive region of the AO measurement can be relocated deeper into tissue as compared to the most sensitive optical measurement methods i.e. the $\frac{\partial A_{SR}}{\partial \rho}$ method. However this is carried out at the expense of increasing noise level due to poor detection of the ultrasound modulated intensity, which remains a key challenge in AO detection.
3. The AO and optical measurements are most sensitive to absorption changes, which occur in regions very close to the optical probes. The AO measurement can have minimal to even reduce the effect of localised absorption changes in the region between optical source-detection in the SFR depending on the location of the FUR.
4. In a more absorbing medium, the mean and maximum penetration depths of the AO and optical methods are reduced. The AO method is still more sensitive in the ROI than the optical measurement. The AO sensitivity in the SFR can be reduced by relocating the FUR deeper into the phantom.

However this approach requires high ultrasound amplitude or/and longer integration time. Alternatively, a more efficient AO method can be used.

5.4 Conclusions

This section summarises the key conclusions from the study described in this chapter.

1. The most sensitive region of the AO measurement coincides with the FUR in transmission mode measurement. In reflection mode measurement, the most sensitive AO region does not always occur in the FUR because it depends on the overlap between the FUR and the region of high optical path distribution e.g. J_{PC}.
2. The most sensitive AO region is the regions very close to the optical source and detector; which are also the locations of most sensitive optical measurements.
3. The highest mean sensitivity of the optical measurements is always located in the SFR. The highest mean sensitivity of the AO method, which is located in the deeper region, is always higher than its mean sensitivity in the SFR. Therefore, the AO method can probe deeper than the optical measurements.
4. The region of high AO sensitivity can be relocated by controlling the location of the FUR.
5. In a diffusing medium whose μ_a is similar to that of tissue, the mean and maximum penetration depths of the AO and the optical measurements become shallower than when the background absorption is minimal. But the AO method can probe deeper and achieve higher sensitivity in the ROI than the optical measurements.

6 Spatial Sensitivity to a Localised Change in Scattering

HIFU therapy uses highly intense focused ultrasound beam to ablate cancerous soft tissue non-invasively [Hill 1995, Kennedy 2003, ter Haar 2007]. However, conventional diagnostic ultrasound imaging has difficulty in monitoring HIFU lesions in real time. This is because these lesions may form before the formation of hyper-echoic region (where significant change in the local acoustic property can scatter/reflect ultrasound waves) as a result of cavitation [Rabkin 2005]. During cavitation, the dimension of lesion becomes unpredictable and the gas bubbles may be formed due to the rapid increase in the local temperature. Therefore, there is a clinical need to monitor the lesion formation before the formation of hyper-echoic region.

It has been shown that typical HIFU lesions have significant higher μ_a and μ_s' due to the thermal necrosis [Lai 2011]. The AO method can monitor both absorption and scattering changes, thus it has been considered as a potential real-time monitoring technique of HIFU lesions [Draudt 2009, Lai 2011]. Furthermore, acoustic radiation force can also be used to monitor these lesions [Lizzi 2003] and potentially can be used to amplify the AO signal [Kim 2006, Zemp 2007, Li 2011].

Unlike the spatial absorption sensitivity maps, the interpretation of the change in sensitivity due to a highly scattering perturbation cannot be interpreted as the photon path distribution. The introduction of a highly scattering perturbation (a local scatterer) in a diffusing medium causes the distribution of the fluence rate within the medium to change due to the mismatch of the μ_s' of the local scatterer and the background medium. The dominant factor is the surface-induced backscatter [Ostermeyer 1997], which is shown in Figure 6-1. The mismatch in the μ_s' causes photons to be reflected in the regions near the boundary of the local scatterer. Thus, a local scatterer *alters* the path length of photons instead of

depletion, which in turn results in a change in the detected signal [Feng 1995]. Feng et al [Feng 1995] also demonstrated the overall spatial sensitivity profile in a reflection geometry due to a local scatterer is similar to the absorption sensitivity, which is the 'banana' shaped profile shown in section 5.3.1.

Figure 6-1 The change in the total fluence ϕ^{Pert} (solid line) from the steady state due to a highly scattering (μ_s' is twice of the background) sphere is the sum of the effect of the surface (dotted line) and volume (dashed) with the same μ_a.The total change depicts the effects of the surface-induced backscattering and volume-induced scattering-enhanced absorption. Adapted from Ostermeyer et al. [Ostermeyer 1997]

The effect of a localised change in absorption in the spatial sensitivity of the AO method is discussed in chapter 5. Thus, the aim of this chapter is to verify the feasibility of using the AO method in the monitoring of the HIFU lesions by spatially mapping its sensitivity in response to a localised change in μ_s'.

6.1 Materials and Methods

The materials, the experimental setup and procedures with the exception of the local scatterer are identical to the previous study of the spatial sensitivity due to local absorption, which is described in section 5.1. The local scatterer for this study is shown in Figure 6-2, which has a higher μ_s' of 20 cm^{-1} that is nearly twice

of the background Intralipid solution μ_s' of 12 cm^{-1}. Its μ_a is the same as the Intralipid solution, which is 0.00235 cm^{-1}.

Figure 6-2 An image of the local scatterer, which has the μ_s' of 20 cm^{-1} and the μ_a of 0.0235 cm^{-1}. The local scatterer is held by a thin metallic rod, whose dimension is shown in Figure 5-5 (b).

Multiple experiments were conducted to map the spatial sensitivity of the AO and the optical measurements in response to a localised change in μ_s' for both transmission and reflection modes.

6.2 Transmission Mode

This section describes the results of the study to map the scattering spatial sensitivity maps for transmission mode measurements.

6.2.1 Sensitivity Maps

The experimental results are presented in Figure 6-3, Figure 6-4 and Figure 6-5 respectively for the measurement results, the reference measurements and the spatial sensitivity maps.

In the AO measurement shown in Figure 6-3 (a)-(c), there is no visible change in the AO signal as the result of the local scatterer. There is only a slight change in the I_{DC}; however the I_{AC} and MD do not show any localised change in the FUR.

The drift of the measurements can be explained by examining the reference measurements whereby the similar drift due to the settling of the diluted Intralipid solution can be observed.

On the other hand, the expected change of the optical measurements due to the introduction of the local scatterers can be readily observed and they are verified by the result from the literature [Fantini 1995], which is shown in Figure 6-3 (f). The I_{PC} measurement depicts a higher drop in intensity when compared to the I_{CCD}'s measurement, which are shown in Figure 6-3 (d) and (e) respectively. This is caused by the photon counter's superior quantum efficiency at 808 nm wavelength. The distribution of the I_{PC} and I_{CCD} are not symmetrical is the regions of x = 5-12 mm can be attributed to the settling of the Intralipid globules, which can be observed in the reference measurements in Figure 6-4.

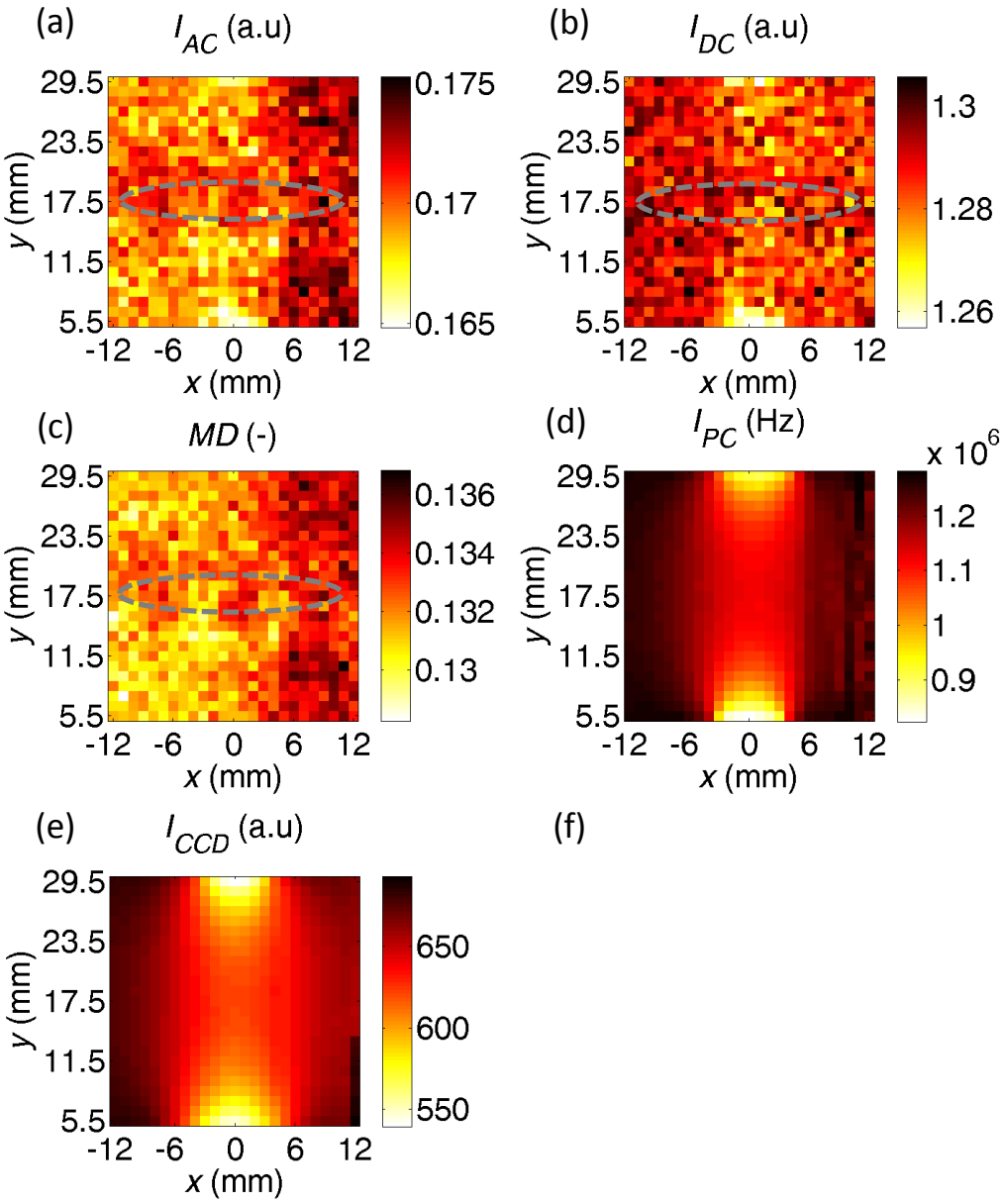

Figure 6-3 The measurement results of AO: (a) I_{AC}, (b) I_{DC}, (c) MD ; (d) I_{PC}; (e) I_{CCD}; and (f) the literature [Fantini 1995] for transmission mode when the background μ_a = 0.0235 cm^{-1}: there is no localised MD reduction in the FUR and there is good agreement between the optical results and the literature. (dashed line: FUR)

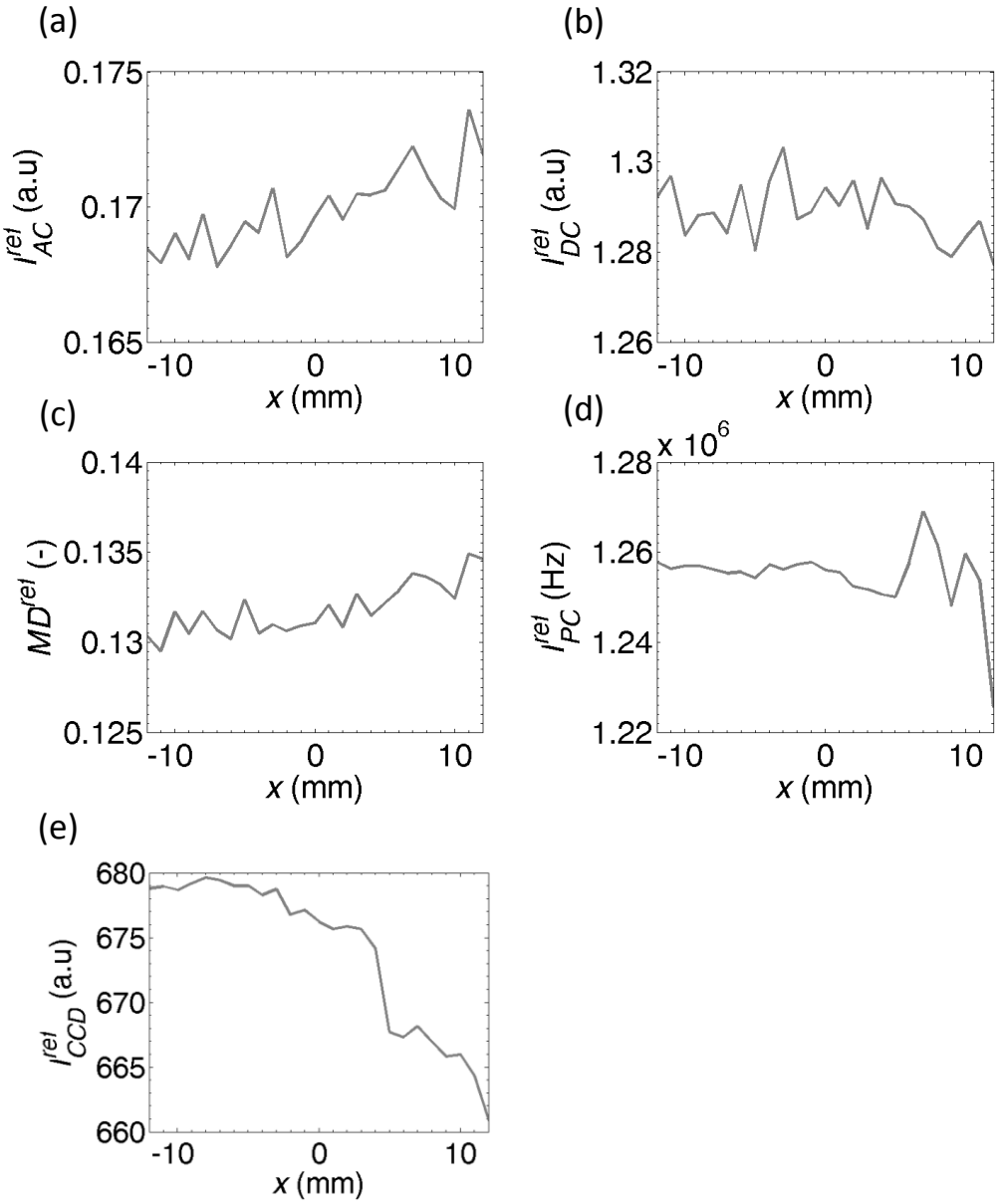

Figure 6-4 The reference measurement results of: AO (a) I_{AC}, (b) I_{DC}, (c) MD; (d) I_{PC}; and I_{CCD} for transmission mode when the background μ_a = 0.0235 cm^{-1}: the drift is caused by the slow percipitation of the Intralipid solution.

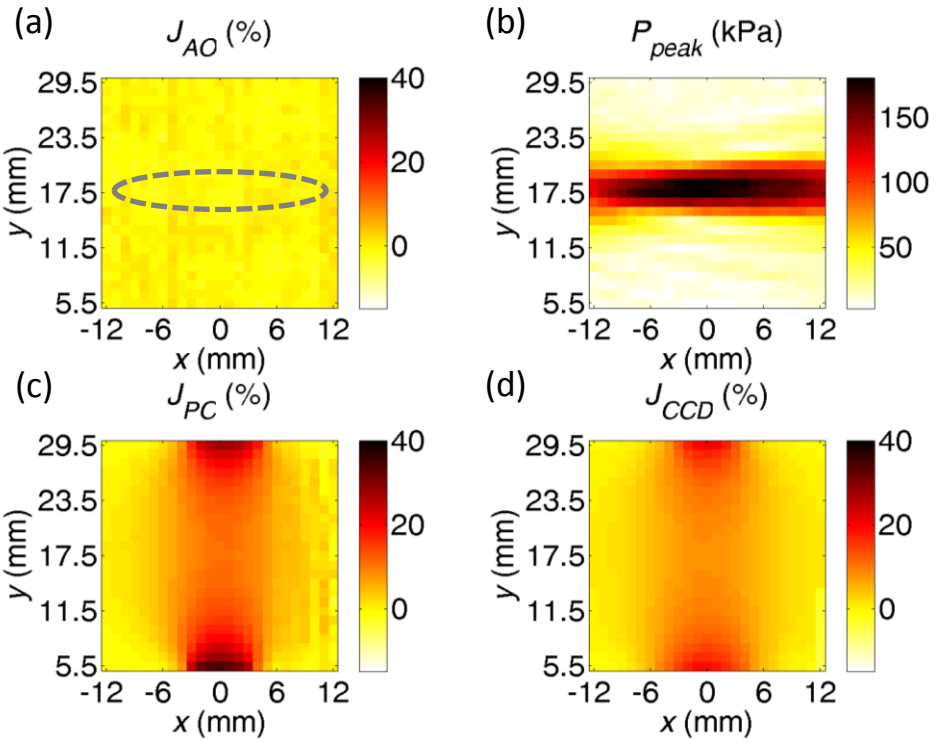

Figure 6-5 The spatial sensititivity maps of: (a) AO; (b); (c) I_{PC} and (d) I_{CCD} for transmission mode when the background μ_a = 0.0235 cm^{-1}: the AO sensitivity is fairly homogenous throughout the SA without any localisation. The optical measurement sensitivities agree with the published results by Fantini et al. [Fantini 1995]. (dashed line: FUR)

The AO sensitivity map in Figure 6-5 (a) shows that AO measurement is insensitive to the presence of the local scatterer within the phantom. This is rather puzzling because there have been previous UOT studies [Devi 2006, Kothapalli 2007] that demonstrated the AO measurement in transmission mode to image highly scattering targets within a diffuse medium. But there are distinctions between the experiment described here and the literature.

Devi et al. [Devi 2006] detected the AO signal by using a similar setup of a photo-multiplier tube and a digital correlator but they increased the number of freeze-thaw cycles on the PVA gel phantom, which resulted in the increase of μ_s' and

also changes in the mechanical properties of the phantoms [Devi 2005]. Thus the change in detected signal is a combined effect of the increase in μ_s' and the storage moduli of the PVA gels. Kothapalli et al. [Kothapalli 2007] imaged scattering inclusions whose μ_s' are 30 and 100 cm^{-1}, which is considerably higher than the μ_s' of the local scatterer (20 cm^{-1}) used here. Furthermore they used the parallel detection of the AO speckle contrast, which has much greater signal-to-noise in the AO detection by a factor of square-root of the total number of CCD pixels when compared to the single detection method. They also showed that the higher μ_s' of the inclusions resulted in reductions of the MD.

These suggest that the reduction in the AO signal due to the surface-induced scattering in this study may be very small and it is cancelled out by the change because of the mismatch in the acoustic properties of the local scatterer and the background medium; which is described in section 5.2.1. The control measurement shows that there is a small increase in the MD whereby the optical property of the local scatterer is the same as the background medium. This increment may counteract any reduction in the MD, which results in no localisation in the spatial sensitivity map.

The spatial scattering sensitivity maps of the optical measurements in Figure 6-5 (c) and (d) are similar to the absorption spatial sensitivity maps that are shown in section 5.2.2; but the change in sensitivity is lower. The optical measurements are most sensitive to any scattering changes in the regions near to the optical source and detector. For example, the maximum absorption sensitivity (Figure 5-16 (c)) of the I_{PC} measurement is close to 100% whereas the maximum scattering sensitivity in Figure 6-5 (c) is 40%. This suggests that generally both the AO and optical measurements are more sensitive to absorption changes than to μ_s' changes.

6.2.2 Mean and Midway Sensitivity in the Superficial Region and the Region of Interest

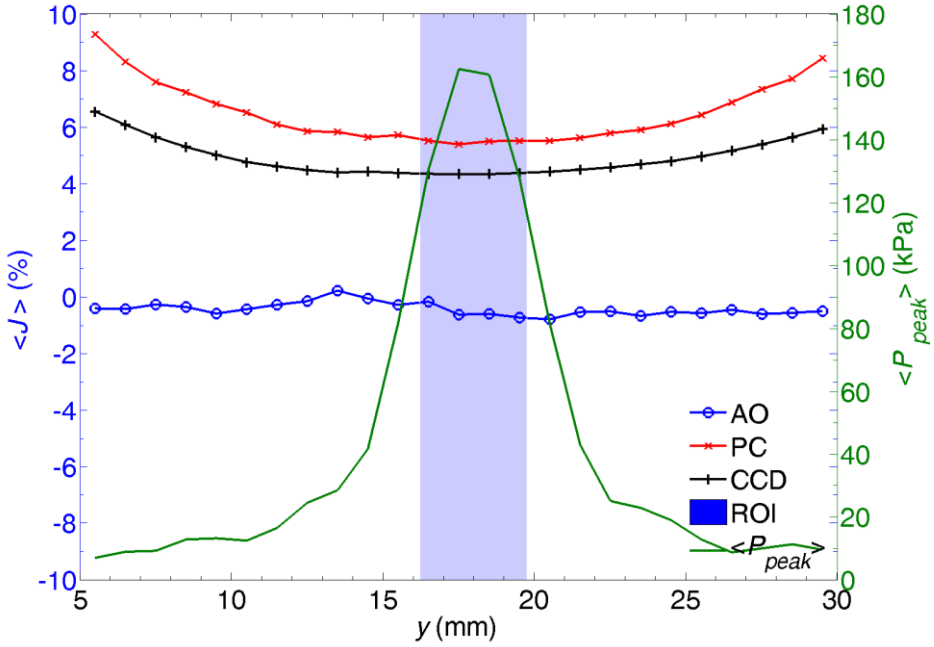

Figure 6-6 The mean sensitivity of AO, I_{PC} and I_{CCD} at different depth y for transmission mode when the background μ_a = 0.0235 cm^{-1}: $<J_{AO}>$ shows that the AO method is insensitive to μ_s' changes in a transmission geometry. The optical measurements are similar to their absorption counterparts but at a much lower level of sensitivity.

By employing the same method used in the absorption sensitivity study, the mean sensitivity at different depths is investigated and the results are summarised in Figure 6-6 and Table 6-1. The mean scattering sensitivities of the AO, I_{CCD} and I_{PC} measurements in the ROI are -0.6, 4.3 and 5.4 %, which are shown in Figure 6-6 and Table 6-1; and their mean absorption sensitivities are 22, 31 and 50 % (Figure 5-17 and Table 5-3) respectively. In first impression, this may imply that AO and optical systems are generally less sensitivity to changes in the μ_s'. However, it is worth noting that the μ_s' of the local scatterer is twice the μ_s' of the background medium whereas the μ_a of the local absorber used in the previous chapter is 1715 times higher than the μ_a of the background medium. The reduction

in sensitivity is small, thus it is entirely plausible that the change in the AO signal due to the local scatterer is so minute that the current AO detection method is not capable of detecting this change.

Detection Method	<J(SFR)> (%)	<J(ROI)> (%)	Is <J(ROI)> higher than <J(SFR)>?
I_{CCD}	6.54	4.32	No
I_{PC}	9.26	5.38	No
AO	-0.41	-0.63	No

Table 6-1 Comparison of the mean sensitivity of AO, I_{PC} and I_{CCD} in the SFR and the ROI for transmission mode when the background μ_a = 0.0235 cm^{-1}: there is little change in the AO measurement and the optical measurements exhibit higher mean sensitivity in the regions close to the optodes than in the ROI.

The behaviour of the midway sensitivities at x = 13 mm at different depths y (mm) are similar to the mean sensitivities, which are shown in Figure 6-7 and summarised in Table 6-2. The FUR has no effect on the AO measurement and the optical sensitivities exhibit similar trends to their absorption counterparts, which are shown in Figure 5-18 and Table 5-4. There are no distinction between the AO sensitivity in the SFR and the ROI. The optical measurements are more sensitive to the μ_s' changes in the SFR than the ROI.

Multiple experiments were repeated in order to verify that the loss of the AO localisation in the spatial sensitivity was not due to experimental error. The results of these studies showed the same findings. They also show that the studies have good repeatability.

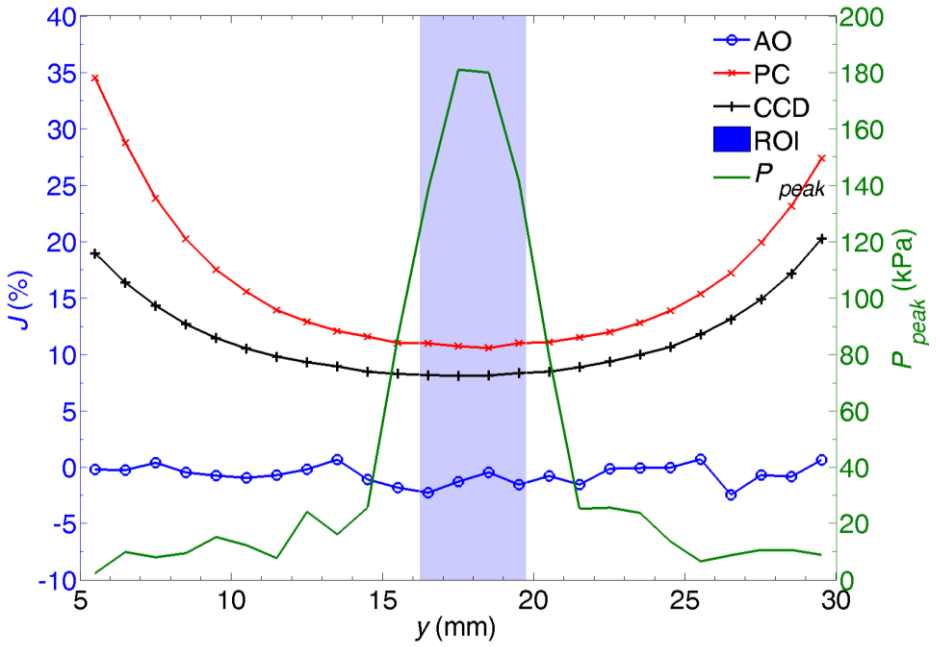

Figure 6-7 The midway sensitivities of AO, I_{PC} and I_{CCD} at different depth y for transmission mode when the background μ_a = 0.0235 cm^{-1}: the AO method is incapable of detecting a higher scattering change in a transmission mode measurement.

Detection Method	J(SFR) (%)	J(ROI) (%)	Is J(ROI) higher than J(SFR)?
I_{CCD}	18.96.0	8.10	No
I_{PC}	34.46	10.72	No
AO	-0.18	-1.25	No

Table 6-2 Comparison of the midway sensitivity of AO, I_{PC} and I_{CCD} in the SFR and the ROI for transmission mode when the background μ_a = 0.0235 cm^{-1}: the location of FUR has little effect on the AO measurement. The optical results demonstrate the expected changes in the superficial layer, which are similar to the absorption sensitivity.

6.2.3 Effect of Background Absorption on the Spatial Sensitivity

This section describes the experiment and the results of mapping the spatial scattering sensitivity of the AO and I_{PC} measurements with the biological tissue level of μ_a in both the local scatterer and background medium.

6.2.3.1 Material and Methods

The same study was repeated in this section, but the μ_a of the background and the local scatterer is set to the typical of level of tissue level, which is 0.1 cm^{-1}. The absorption is achieved by adding appropriate amount of near-infrared dye (ICI S109564). This dye was not used in the previous studies because it diffuses out of the PVA gel over time. However, it was not of importance in this study because both the background solution of Intralipid and the PVA local scatterer contained the same concentration of the dye.

6.2.3.2 Sensitivity Maps

The measurement results are presented in Figure 6-8 and the reference measurements are shown in Figure 6-9.

Contrary to the results presented in section 6.2.1, the effect of the higher background absorption has profound effect on the AO measurements, which are shown in Figure 6-8 (a)-(c). The I_{AC} demonstrates that there is a localised drop in intensity in the FUR and there is smaller drop in the I_{DC}, which results in the noticeable drop in the MD in the FUR. The I_{PC} shows the similar general pattern of reduction in intensity, whereby the amount of decrease is more profound due to the higher background absorption.

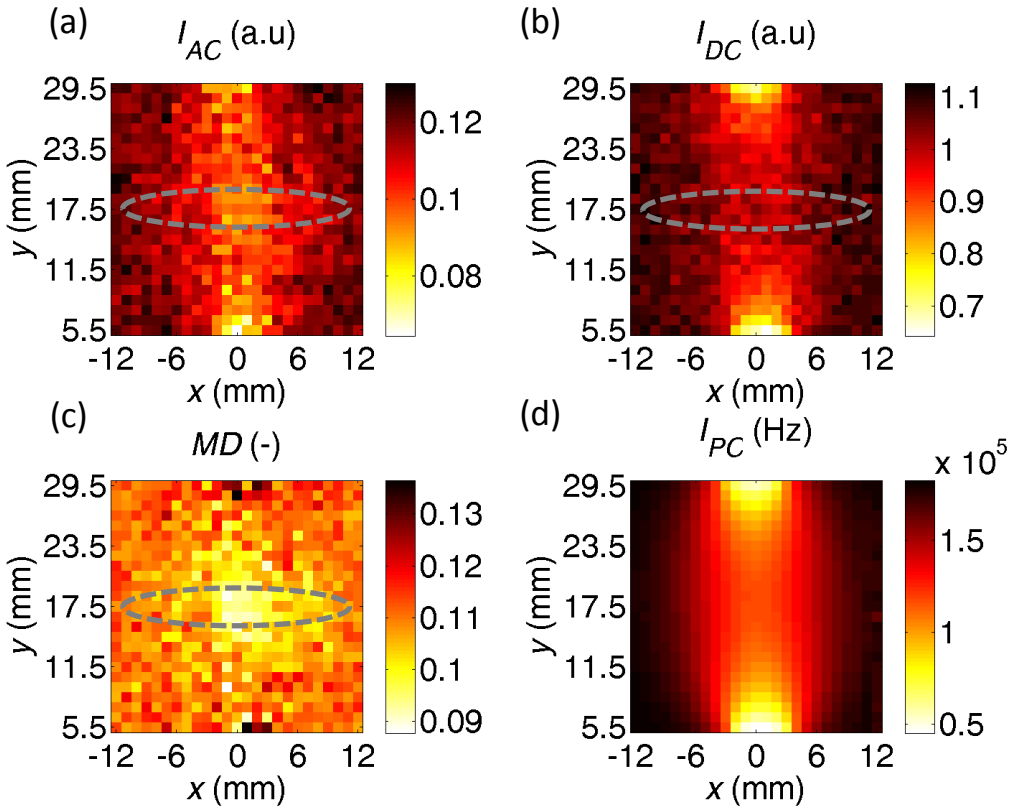

Figure 6-8 The measurement results of AO: (a) I_{AC}; (b) I_{DC}; (c) MD; and. (d) I_{PC} for transmission mode when the background μ_a = 0.1 cm^{-1}: the MD result shows that there is AO localisation in the FUR and the optical measurements show a greater reduction in intensity. (dashed line: FUR)

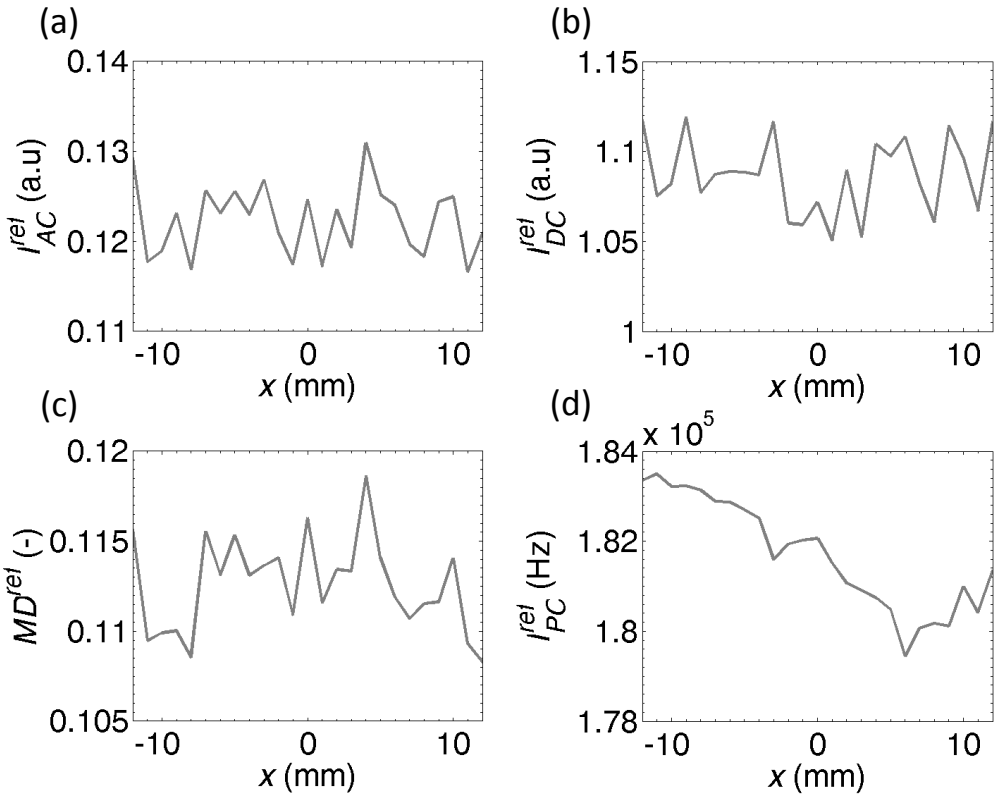

Figure 6-9 The reference measurement results of: AO (a) I_{AC}, (b) I_{DC}, (c) MD; and (d) I_{PC} for transmission mode when the background μ_a = 0.1 cm^{-1}.

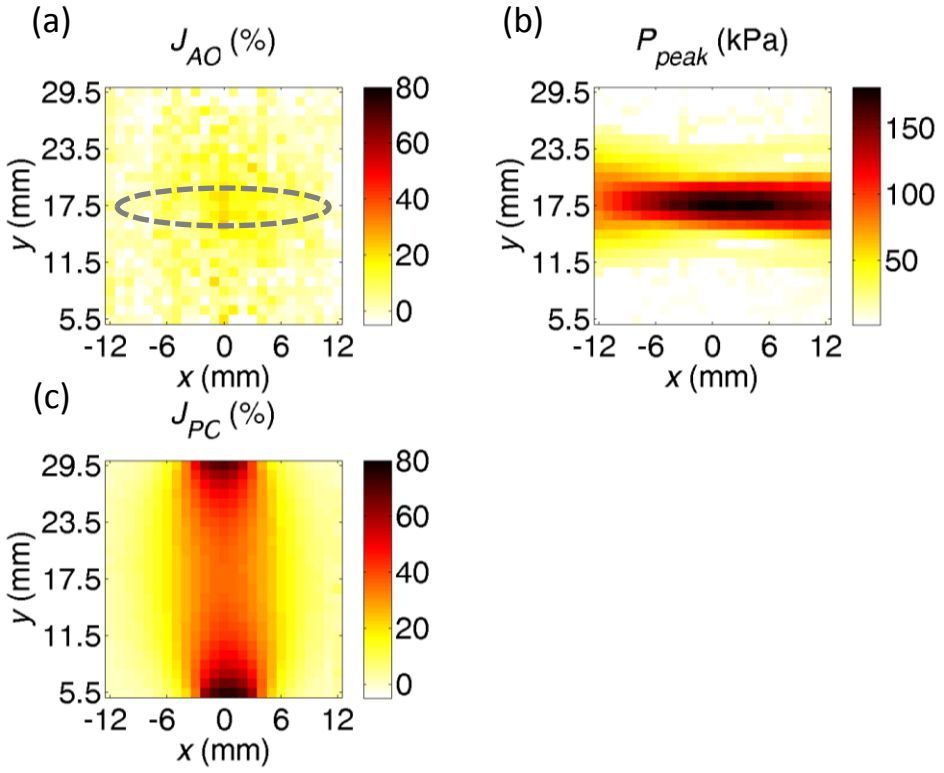

Figure 6-10 The spatial sensitivity maps of (a) AO and (c) I_{PC} with (b) the FUR for transmission mode when the background μ_a = 0.1 cm^{-1}: the J_{AO} shows that there is localisation in the FUR and the J_{PC} demonstrates a greater reduction in the detected intensity. (dashed line: FUR)

The AO spatial sensitivity map J_{AO} is depicted in Figure 6-10 (a) and it shows the higher sensitivity in the FUR, which is shown in Figure 6-10 (b). The reason of this phenomenon can be explained by the idea of volume-induced scattering-enhanced absorption, which is depicted in Figure 6-1. According to the Beer-Lambert equation (6-1), the attenuated intensity is a function of exponential decay with an increasing optical path length z. The increase in μ_s' increases the mean path length of the light within the local scatterer, which results in more photons being absorbed by the dye according to equation (6-1).

$$I = I_0 \mathrm{e}^{-(\mu_a + \mu_s')z} \tag{6-1}$$

where I: the attenuated intensity, I_0: the initial intensity and the mean path length z.

When the local scatterer is in the FUR, more ultrasound modulated photons are absorbed due to the scattering enhanced absorption. This is the reason why the AO measurement is now showing the localised change in the FUR. Similar phenomena can be observed in the sensitivity of the I_{PC} measurement in Figure 6-10 (c). The maximum J_{PC} of 80% is twice of the observed level (40%) in the study when the background absorption is minimal. The most sensitive J_{PC} regions remain very close to the optodes.

6.2.3.3 Mean and Midway Sensitivity in the Superficial Region and the Region of Interest

Further confirmation of the effect of higher background absorption on the AO measurement can be observed in Figure 6-11 and Table 6-3. The mean sensitivity profile of the AO measurement shows its maximum value in the ROI, which is 16 %. The slight increase in MD (negative $<J_{AO}>$) observed in the regions close to the optical source and detector is because the local scatter reflects and scatters the ballistic beam, which reduces the amount of I_{DC}. The mean sensitivity of the I_{PC} measurement is higher in the regions close to the optodes than in the ROI. But the absolute value of the mean sensitivity of the I_{PC} measurement remains higher in both the SFR and the ROI when compared to $<J_{AO}>$. This implies that I_{PC} measurement is more sensitive to any scattering changes in the ROI than the AO measurement but it is also highly susceptible to changes in the SFR.

The midway sensitivities as a function of depth y (mm) at x = 13 mm are shown in Figure 6-12 and the comparison between the AO and I_{PC} midway sensitivities in the SFR and the ROI is summarised in Table 6-4. The difference of the AO midway sensitivity in the SFR and ROI is small on average, which can be attributed to the poorer signal-to-noise as a result of the reduction in the detected

photons. The midway J_{PC} shows that the I_{PC} remains the most sensitive measurement in both SFR and the ROI.

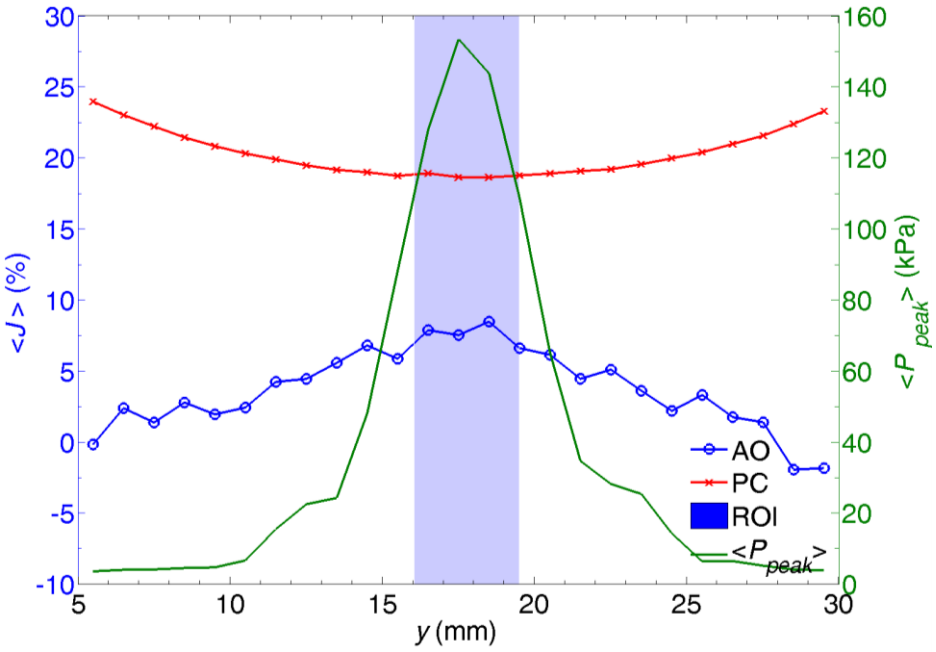

Figure 6-11 The mean sensitivity of AO and I_{PC} at different depth y for transmission mode when the background μ_a = 0.1 cm^{-1}: the maximum $<J_{AO}>$ overlaps with the FUR.

Detection Method	$<J$(SFR)$>$ (%)	$<J$(ROI)$>$ (%)	Is $<J$(ROI)$>$ higher than $<J$(SFR)$>$?
I_{PC}	23.93	18.63	No
AO	-0.15	7.53	Yes

Table 6-3 Comparison of the mean sensitivity of AO and I_{PC} in the SFR and the ROI for transmission mode when the background μ_a = 0.1 cm^{-1}: the AO measurement has higher $<J_{AO}$(ROI)$>$ than $<J_{AO}$(SFR)$>$ and $<J_{PC}$(ROI)$>$ while $<J_{PC}$(SFR) is higher than $<J_{PC}$(ROI)$>$.

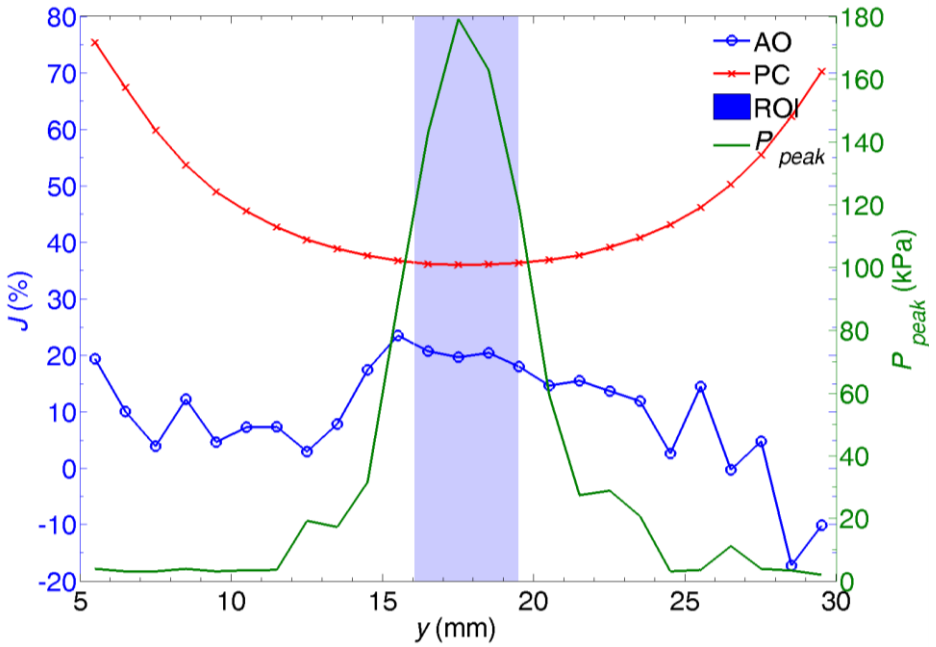

Figure 6-12 The midway sensitivity of AO and I_{PC} at different depth y for transmission mode when the background μ_a = 0.1 cm^{-1}.

Detection Method	J(SFR) (%)	J(ROI) (%)	Is J(ROI) higher than J(SFR)?
I_{PC}	75.28	35.99	No
AO	19.36	19.66	Yes

Table 6-4 Comparison of the midway sensitivity of the AO and I_{PC} methods in the SFR and the ROI for transmission mode when the background μ_a = 0.1 cm^{-1}: the AO measurement is only slightly more sensitive in the ROI.

6.2.4 **Summary**

In summary, the transmission mode spatial sensitivity map of the AO and optical measurements show that:

1. The single detector AO system cannot detect the change of AO signal that is caused by the local scatterer in the absence of significant background absorption.
2. The AO system only shows localisation when the volume-induced scattering-enhanced absorption of the local scatterer amplifies the change in MD.
3. The scattering sensitive region of the AO method overlaps with the FUR, which is similar to the AO absorption spatial sensitivity.
4. The AO measurement is more sensitive in the ROI than in the SFR, even though its absolute sensitivity values in these regions are lower than the optical measurements' sensitivity values.

6.3 Reflection Mode

This section details the experimental results of the reflection mode spatial sensitivity mapping in response to a localised change in the μ_s'. Additional results are presented for the spatially resolved measurement and also when the background absorption is higher.

6.3.1 Sensitivity Maps

The results of both the AO and the optical measurements are presented in Figure 6-13 and their reference measurements are shown in Figure 6-14 when the FUR is located at y = 20 mm. Contrary to the transmission mode measurement, the effects of the local scatterer on the AO signal are obvious in Figure 6-13 (a)-(c). In region near y = 15 mm, the I_{AC} shows a 'banana' pattern of decrease in intensity, which is similar to the change in I_{AC} due to a localised absorption change in Figure 5-14 (a). In the same region, there is only slight decrease in the DC intensity. The resulting effect is the reduction in the MD, which is close to the FUR but they do not wholly overlapped.

There are interesting observations about the change in the MD that is shown in Figure 6-13 (c). The region between the optical source-detector in the SFR and the

deepest regions (deeper than the location of the FUR), higher MD also can be observed. To further investigate this phenomena, the I_{AC}, I_{AC}^{ref}, I_{DC}, I_{DC}^{ref}, MD, MD^{ref} and J_{AO} are averaged from x = 10 to 20 mm for each depth y and are shown in Figure 6-15 (a) and (b).

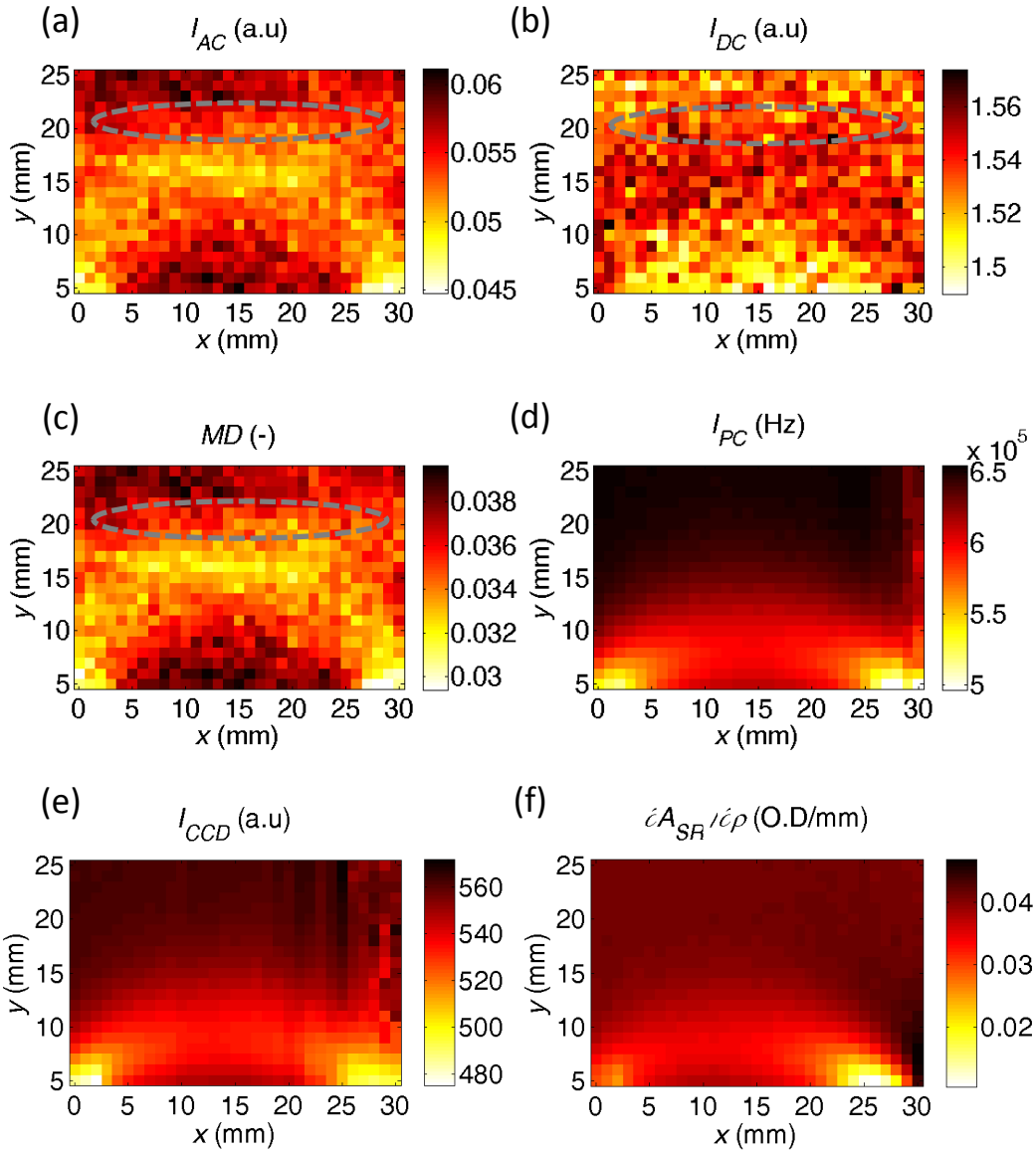

Figure 6-13 The measurement results of AO: (a) I_{AC}, (b) I_{DC}, (c) MD; (d) I_{PC}; (e) I_{CCD}; and (f) $\frac{\partial A_{SR}}{\partial \rho}$ for reflection mode when the background μ_a = 0.0235 cm^{-1}. (dashed line: FUR)

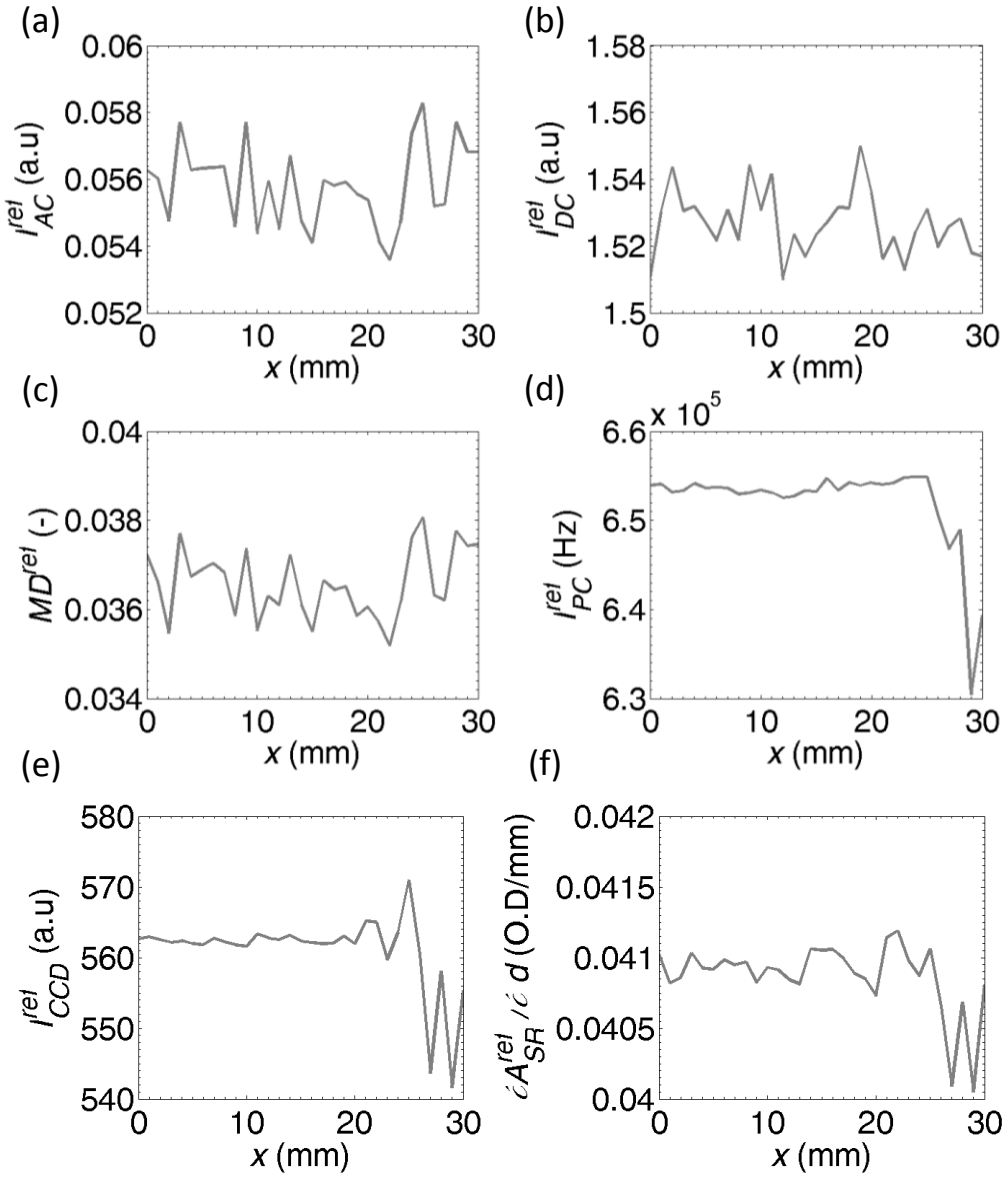

Figure 6-14 The reference measurement results of AO: (a) I_{AC}, (b) I_{DC}, and (c) MD; (d) I_{PC}; (e) I_{CCD} and (f) $\frac{\partial A_{SR}}{\partial \rho}$ for reflection mode when the background μ_a = 0.0235 cm^{-1}.

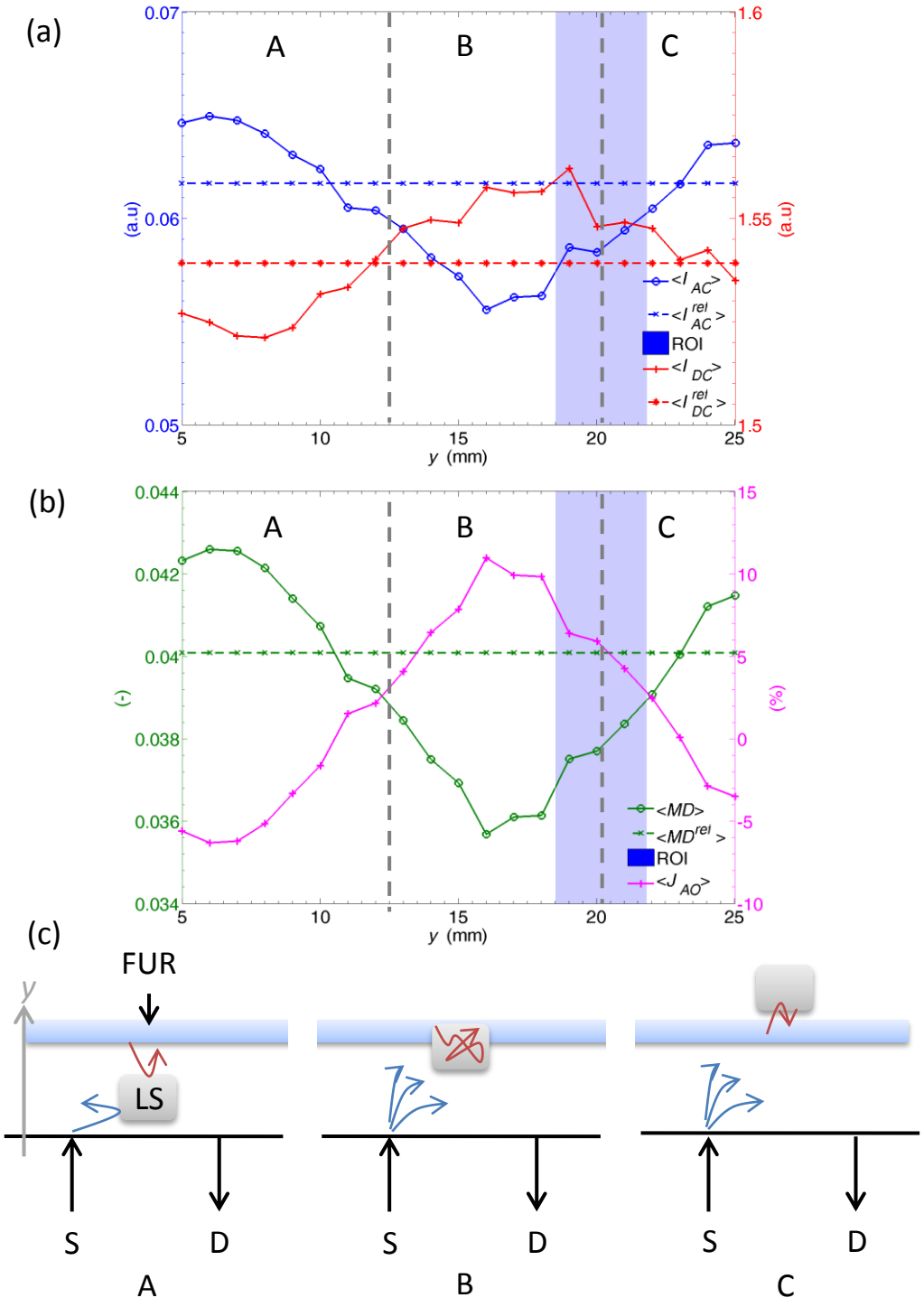

Figure 6-15 (a) The mean I_{AC}, I_{AC}^{ref}, I_{DC} and I_{DC}^{ref} of the AO measurement and (b) the corresponding mean MD, MD^{ref} and J_{AO} in x = 10-20 mm at each depth y when the background μ_a = 0.0235 cm^{-1}; (c) the locations of the local scatterers: segments A, B and C.

In segment A depicted Figure 6-15 (c), the increase in the MD in Figure 6-15 (b) is the result of concurrent increase in the I_{AC} and decrease in the I_{DC} in Figure 6-15 (a). It is hypothesised that when the local scatterer (LS) is in this region, it strongly scatters the light bundle away from the detector resulting in the higher drop in the I_{DC} due to the surface induced scattering [Ostermeyer 1997]. At the same time, some I_{AC} may be reflected back into the FUR, which results in more ultrasound modulation and higher $<I_{AC}>$ than the $\langle I_{AC}^{ref} \rangle$.The combined effect is the observed increase in the $<MD>$ and the negative $<J_{AO}>$.

In segment B, the local scatterer is within the FUR and it would reflect more I_{DC} towards the optical detector thus resulting in the higher $<I_{DC}>$ than the $\langle I_{DC}^{ref} \rangle$. On the other hand, there is a decrease in the detected I_{AC}, whereby $<I_{AC}>$ is higher than $\langle I_{AC}^{ref} \rangle$. It is expected for the I_{AC} to increase in this region [Sakadzic 2002] for a homogenous medium wholly irradiated by planar ultrasound waves. This is because a higher μ_s' will increase I_{AC} due to the increase in the ultrasound modulated scattering events, which is shown in Figure 3-17. However, a decrease in the MD is observed in this study and it is also reported by Kothapalli et al. [Kothapalli 2007]. There are two reasons for the decrease in the MD.

Firstly, it has been suggested that the observed drop in the MD is caused by the increase in anti-correlation factor [Sakadzic 2005] between the particle-displacement and the variation of refractive index mechanisms, which is discusssed in greater detail in section 3.3.2.3. Secondly, a significant amount of the light are prevented from entering the local scatterer because of the surfaced-induced backscattering, which is shown in Figure 6-1. This results in a reduction in the amount of photons being modulated by the focused ultrasound waves in the FUR. Hence, a decrease in MD is observed.

In segment C, the $<I_{DC}>$ fluctuates around its reference measurement because the presence of the local scatterer in this region has little effect on the optical field detected by the photon counter, which is shown in Figure 6-13 (d). However, the local scatterer here increases the possibility of the ultrasound modulated photon

being reflected back to the FUR because of the surface-induced backscattering, thus the $<I_{AC}>$ is higher than $\langle I_{AC}^{ref} \rangle$ and the MD rises.

These observations can also be observed in the AO spatial sensitivity map J_{AO}, which is depicted in Figure 6-16 (a), and the location of the FUR is shown in Figure 6-16 (b). The J_{PC}, J_{CCD} and J_{SR} are shown in Figure 6-16 (c), (d) and (e) respectively.

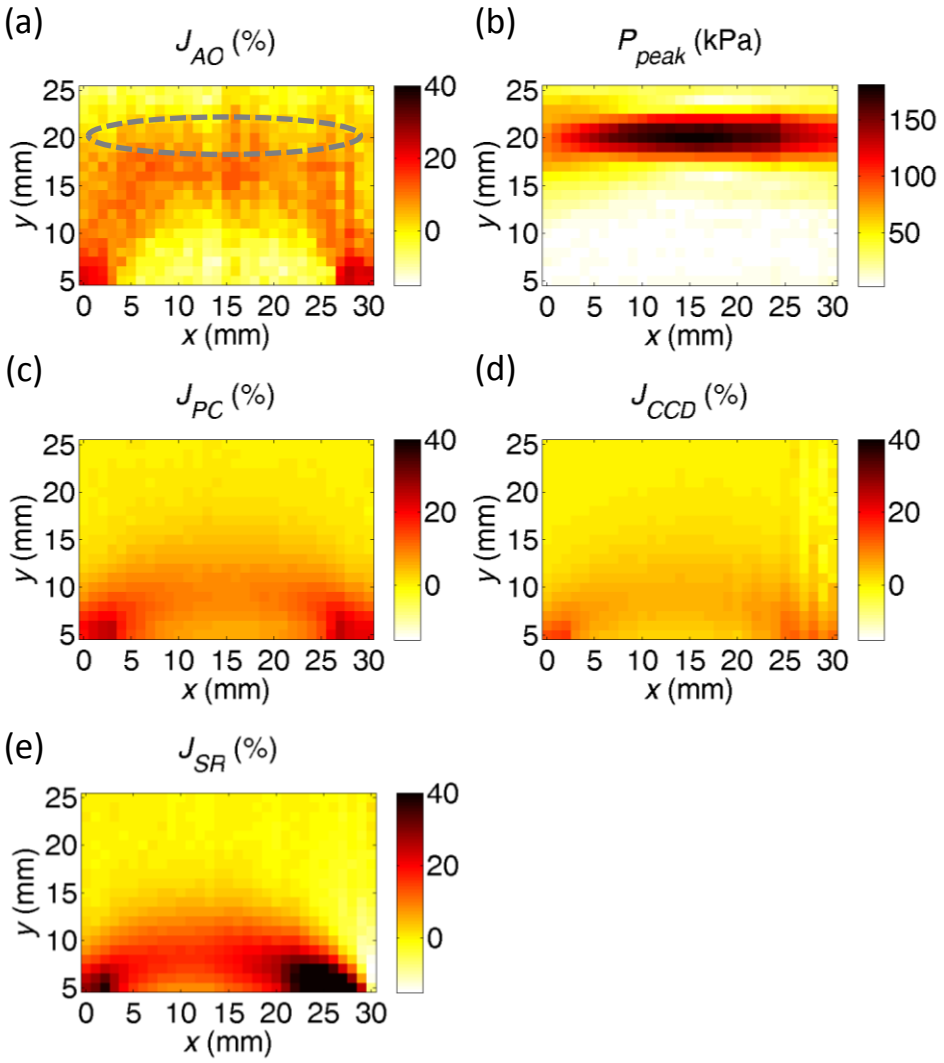

Figure 6-16 The spatial sensitivity maps of (a) AO, (c) I_{PC}, (d) I_{CCD} and (e) $\frac{\partial A_{SR}}{\partial \rho}$ for reflection mode when the background μ_a = 0.0235 cm^{-1}. (dashed line: FUR)

Unlike the transmission mode result, there is a strong AO localisation near the FUR in Figure 6-16 (a). But similar to the absorption sensitivity, the sensitive region of AO measurement does not overlap with the FUR. Based on the results, AO can detect scattering changes the deepest but the most sensitive measurement method is the spatially resolved. All optical measurements are highly sensitive in the superficial layer.

The optical measurements show there is generally a decrease in intensity due to the local scatterer. However, the largest drop for each method is not in regions closest to the optical source or detector. The highest sensitivity are in regions, which are located 'next' to the closest spot to the source and detector. When the local scatterer is directly in line with the optical source or detector at x = 0 and 30 mm (note that there is the gap in the y-direction between SA and wall of phantom is 5 mm), it is not as obstructive to the 'banana' shaped light bundle as when it is located at x = 3 and 27 mm.

Unlike the local absorber study in Figure 5-24 (f), the $\frac{\partial A_{SR}}{\partial \rho}$, which is shown in Figure 6-13 (f), is consistently positive because the change in light intensity due to the local scatterer is significantly smaller than when the local absorber is present. Therefore there is no reversal in the polarity of the $\frac{\partial A_{SR}}{\partial \rho}$ and the J_{SR} never exceeds 100%.

6.3.2 Mean and Midway Sensitivity in the Superficial Region and the Region of Interest

The mean sensitivity of the AO and the optical measurements for two repeated studies are shown in Figure 6-17. Table 6-5 summarises the comparison of the mean sensitivities in the SFR and the ROI and the mean penetration depths of each method.

The mean sensitivities show that only AO achieve higher mean sensitivity in the ROI than in the SFR. Furthermore, AO also probes the deepest because its mean

penetration depth is on average 13.9 mm when the FUR is 20 mm away from the optical source-detector plane. The mean penetration depths of the optical measurements range from 7.4 to 9.7 mm. The negative AO sensitivity in the deepest region in the SA is because of the increase in modulation to the backscattered I_{AC} back into the FUR, which has been discussed earlier. Furthermore, the most sensitive measurement technique in the ROI is the AO at 4.45 %, which considerably smaller than the absorption sensitivity in the previous chapter at 26.8 %. The AO mean sensitivity in the SFR is nearly zero while the optical measurements have their highest mean sensitivities here.

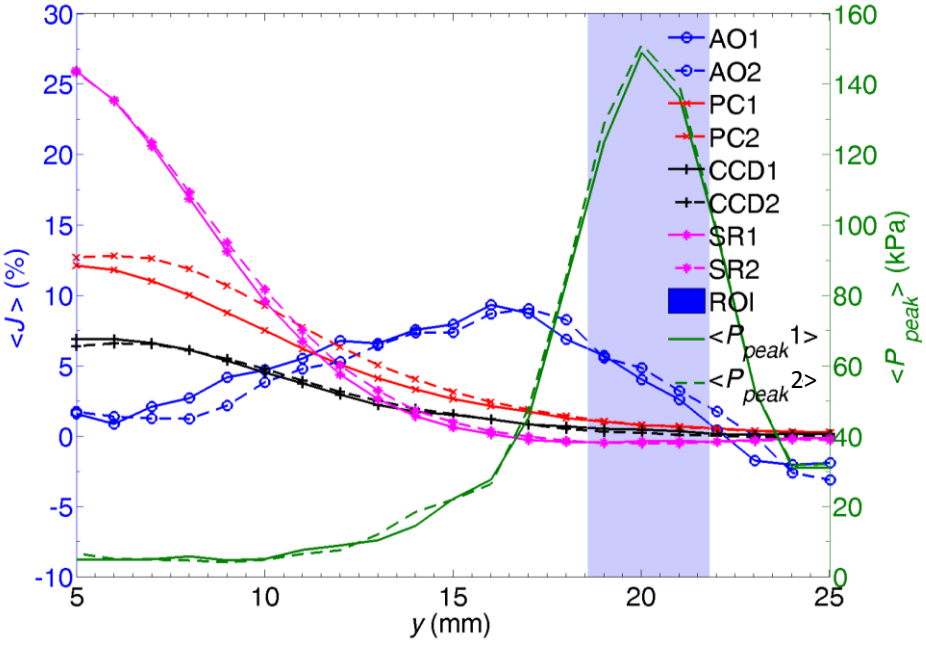

Figure 6-17 The mean sensitivity of AO, I_{PC}, I_{CCD} and $\frac{\partial A_{SR}}{\partial \rho}$ at different depth y for reflection mode when the background μ_a = 0.0235 cm^{-1}: two repeated studies show that the most sensitive AO regions do not coincide with the FUR. The most sensitive method in the ROI is AO while the optical methods are most sensitive in the SFR.

Detection Method	<J(SFR)> (%)		<J(ROI)> (%)		Is <J(ROI)> higher than <J(SFR)>?	Mean Penetration Depth <y> (mm)	
	Study 1	Study 2	Study 1	Study 2		Study 1	Study 2
I_{CCD}	6.90	6.40	0.48	0.25	No	9.47	9.26
I_{PC}	12.10	12.69	0.78	0.82	No	9.64	9.65
AO	1.60	1.74	4.02	4.85	Yes	13.63	14.23
$\frac{\partial A_{SR}}{\partial \rho}$	25.91	25.81	-0.35	-0.49	No	7.33	7.44

Table 6-5 Comparison of the mean sensitivity of AO, I_{PC}, I_{CCD} and $\frac{\partial A_{SR}}{\partial \rho}$ in the SFR and the ROI and their mean penetration depths for reflection mode when the background μ_a = 0.0235 cm^{-1}: two repeated studies show that only AO method is more sensitive in the ROI than in the SFR and it can probe a scattering change deeper than optical methods.

Similar observations can be made from the plots of midway sensitivities at different y depths when x = 15 mm, which are displayed in Figure 6-18 and summarised in Table 6-6. The increase of the MD, which can be observed in the regions of negative midway J_{AO} when y = 5-11.5 and y > 22 mm, is more prominent here than the mean sensitivity analysis. The negative midway J_{AO} is caused by the same phenomenon, which is discussed earlier in Figure 6-15.

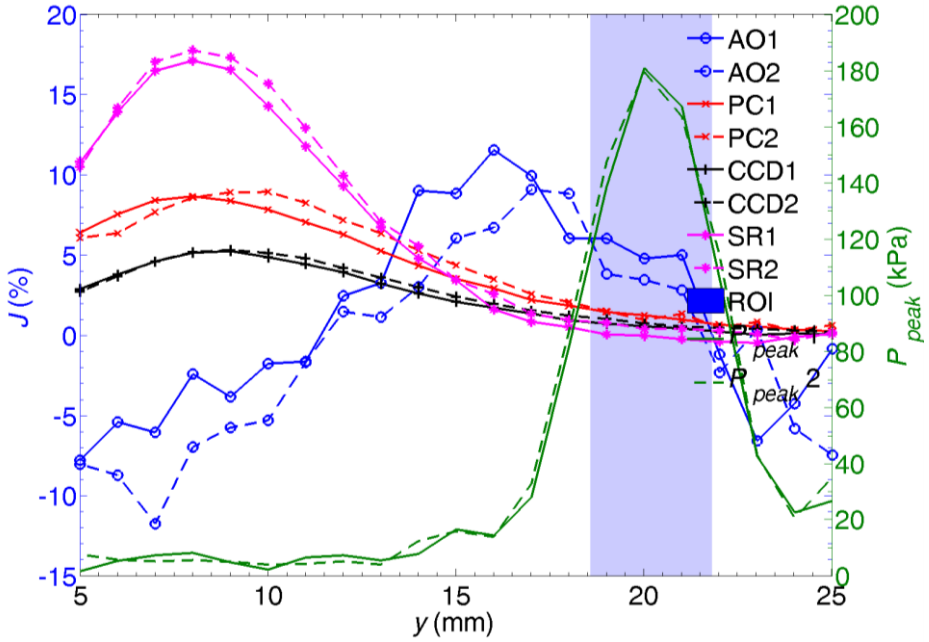

Figure 6-18 The midway sensitivity of AO, I_{PC}, I_{CCD} and $\frac{\partial A_{SR}}{\partial \rho}$ at different depth y for reflection mode when the background μ_a = 0.0235 cm^{-1}: two repeated studies show that the negative J(AO) in the SFR and when y > 22 mm are caused by the combined effect of the surface-induced scattering of the local scatterer on the I_{AC} and I_{DC}.

Detection Method	J(SFR) (%)		J(ROI) (%)		Is J(ROI) higher than J(SFR)?
	Study 1	Study 2	Study 1	Study 2	
I_{CCD}	2.88	2.72	0.56	0.74	No
I_{PC}	6.38	6.06	1.25	0.95	No
AO	-7.77	-8.02	4.77	3.45	Yes
$\frac{\partial A_{SR}}{\partial \rho}$	10.82	10.47	-0.02	0.4	No

Table 6-6 Comparison of the midway sensitivity of AO, I_{PC}, I_{CCD} and $\frac{\partial A_{SR}}{\partial \rho}$ in the SFR and the ROI for reflection mode: two repeated studies show that only the AO measurement has a higher J(ROI) than J(SFR).

6.3.3 Effects of the Location of the Focused Ultrasound Region on the Spatial Sensitivity

It has been shown that the most sensitive AO region in response to a localised change in absorption can be relocated by positioning the FUR in section 5.3.3. The same experiment was repeated to investigate the effect of the location of the FUR on the scattering spatial sensitivity. In this experiment, the spatial sensitivity map is obtained when the FUR is relocated to four pre-set ROIs: A, B, C and D, which are located at y = 10, 15, 20 and 25 mm respectively.

6.3.3.1 Sensitivity Maps

The comparison the AO spatial sensitivity maps for the different ROI is presented in Figure 6-19. The most sensitive AO region can be re-located by positioning the FUR. However, similar to the AO absorption spatial sensitivity maps, the most sensitive region of the AO measurement does not always overlap with the FUR. The maximum AO sensitivity is only located within the FUR in Figure 6-19 (a), the FUR depicted in Figure 6-19 (b) is located in region of high optical sensitivity, such high J_{PC}, which is shown in Figure 6-16 (c).

When the FUR is relocated to the regions of lower J_{PC}, the region of high AO sensitivity grows larger and noisier, which are shown in Figure 6-19 (c), (e) and (g). These results reaffirm the same observation of the absorption spatial sensitivity maps in Figure 5-30, whereby the overlap region between the FUR and the high J_{PC} plays a crucial role in the location of the high AO sensitivity.

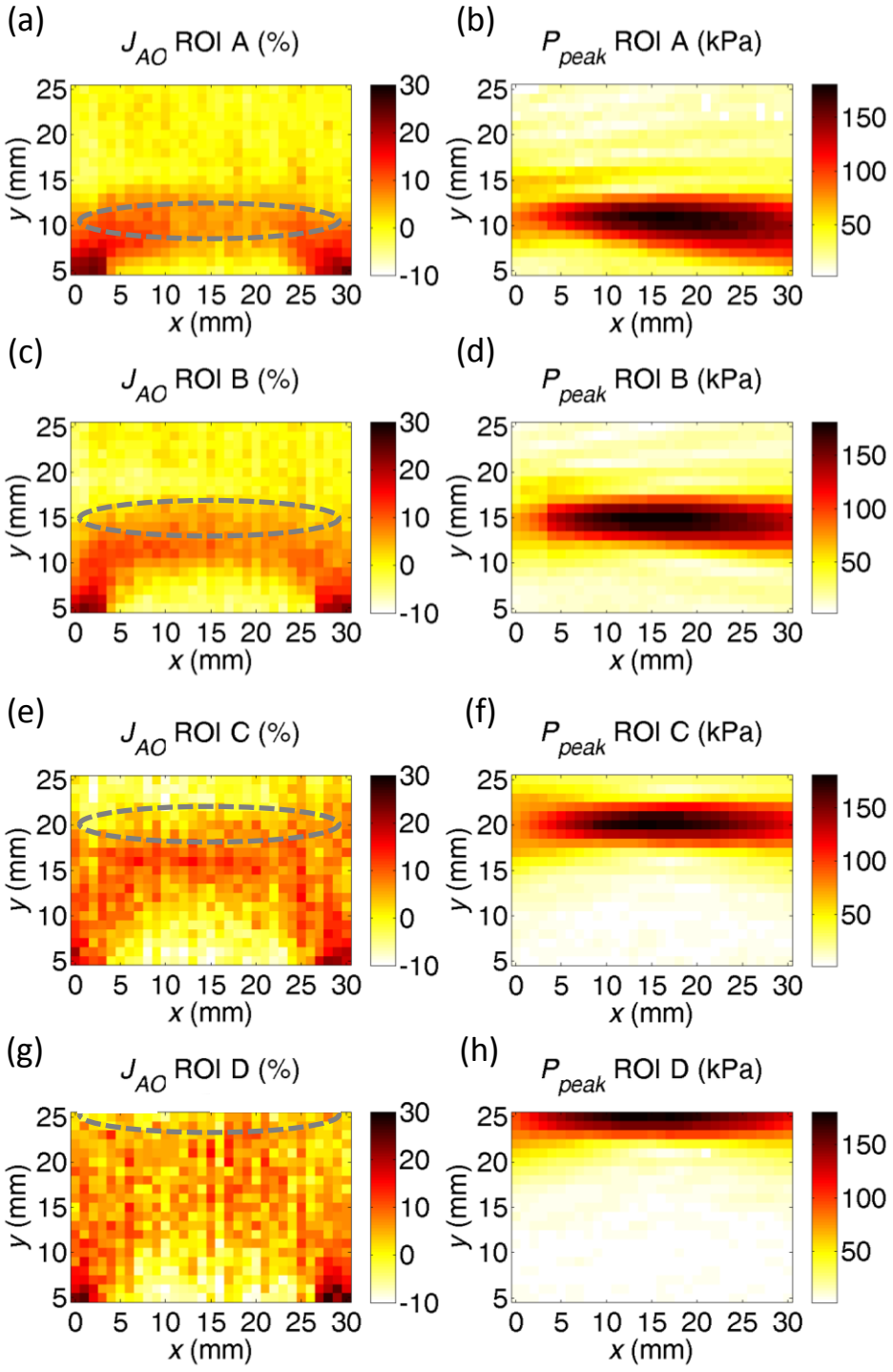

Figure 6-19 The spatial sensitivity maps of the AO method (a), (c), (e) and (g) when the FUR is located at: (b) ROI A (y = 10 mm); (d) ROI B (y = 15 mm); (f) ROI C (y = 20 mm); and (h) ROI D (y = 25 mm) respectively for reflection mode when the background μ_a = 0.0235 cm^{-1}. (dashed line: FUR)

6.3.3.2 Mean and Midway Sensitivity in the Superficial Region and the Region of Interest

The mean sensitivities at different depth *y* are plotted in Figure 6-20 for the AO measurements of different FUR location. The maximum mean sensitivities are never located within their corresponding ROIs. One puzzling observation is that the maximum value of the $<J_{AO}>$ of ROI C is higher than that of maximum value of the $<J_{AO}>$ ROI B. The same experiment was repeated and their results were similar.

Table 6-7 shows the tabulation of the AO mean sensitivities in the SFR and ROI, the mean penetration depths and the maximum mean sensitivities with their corresponding FUR locations. The AO measurements are more sensitive in the ROI than in the SFR, except when the FUR is relocated to the ROI D, which is located at y = 25 mm. The maximum $<J_{AO}>$ of ROI D is still higher than the $<J_{AO}(\text{SFR})>$ of ROI D, which is located at y = 5.9 mm. But this depth is less than the mean penetration depths of the I_{PC}, I_{CCD} and $\frac{\partial A_{SR}}{\partial \rho}$ measurements that is shown in Table 6-5.

The AO midway sensitivities at x = 15 mm are plotted in Figure 6-21 and the comparison of the midway sensitivity in the SFR and the ROI is tabulated in Table 6-6. They show that the AO method has the highest midway sensitivity when the FUR is located at y = 20 mm (ROI C), which is much deeper than the depth of the maximum midway optical measurement sensitivities at approximately 8-9 mm, which is shown in Figure 6-18.

The midway AO sensitivity in the SFR in Table 6-8 is generally negative except when the FUR is at 10 mm deep (ROI A), which is quite close to zero. In comparison to Figure 5-32 and Table 5-10 whereby the midway J_{AO}(SFR) due to absorption change is only negative when the FUR is located in the ROI C and the ROI D. This suggests that the AO method requires prior knowledge of the behaviours of the J_{AO}(SFR) and the J_{AO}(ROI) for both absorption and scattering changes. For example, when the FUR is located in the ROI B, an increase of μ_a in

the SFR would result in a 10% drop in the MD while an increase of μ_s' in the SFR would result in a 10% increase in the MD. This implies that depending on the location of the FUR, the AO measurement may be susceptible to absorption and scattering changes that occurs in close proximity or/and simultaneously.

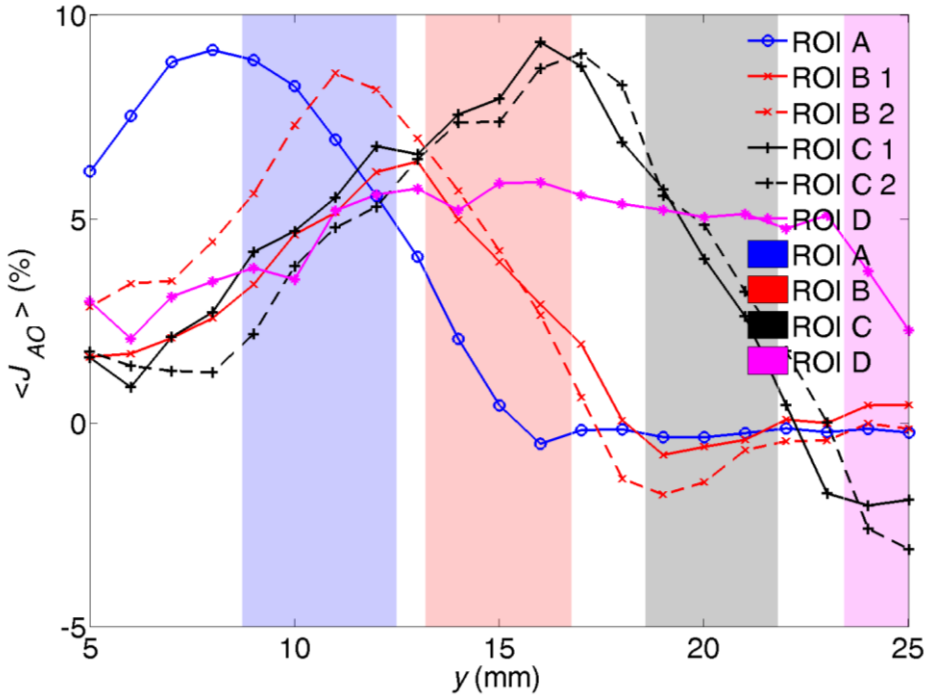

Figure 6-20 The mean sensitivity of the AO method for different FUR locations at different depth y for reflection mode when the background μ_a = 0.0235 cm^{-1}.

Location	$<J_{AO}$ (SFR)> (%)		$<J_{AO}$ (ROI)> (%)		Is $<J_{AO}$ (ROI)> higher than $<J_{AO}$ (SFR)>?	Mean Penetration Depth (mm)		*y* position of Maximum $<J_{AO}>$ (mm)		Maximum $<J_{AO}>$ (%)	
	Study 1	Study 2	Study 1	Study 2		Study 1	Study 2	Study 1	Study 2	Study 1	Study 2
ROI A	6.16	-	6.93	-	Yes	8.48	-	8	-	9.12	-
ROI B	1.62	2.84	3.95	4.21	Yes	11.59	9.91	13	11	6.40	8.56
ROI C	1.60	1.74	4.02	4.85	Yes	13.63	14.23	16	17	9.32	9.03
ROI D	2.97	-	2.26	-	No	15.5	-	16	-	5.89	-

Table 6-7 Comparison of the mean sensitivity of the AO method for different FUR location in the SFR and the ROI and their mean penetration depths for reflection mode when the background μ_a = 0.0235 cm^{-1}.

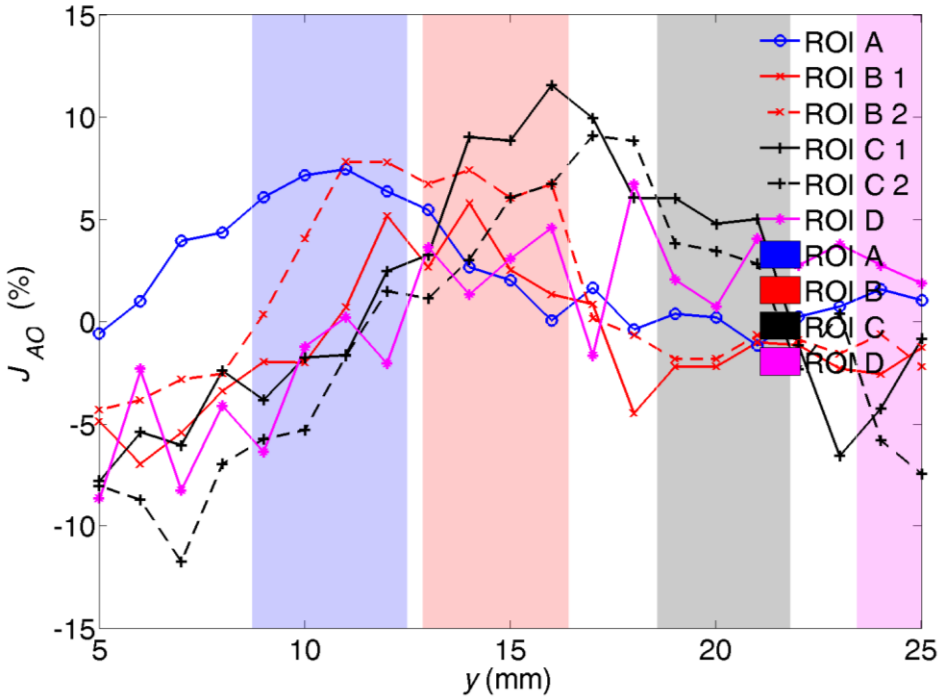

Figure 6-21 The midway sensitivity of the AO method for different FUR locations at different depth y for reflection mode when the background μ_a = 0.0235 cm^{-1}: the AO measurement is most sensitive when the FUR is located 20 mm from the surface.

Location	J_{AO} (SFR) (%)		J_{AO} (ROI) (%)		Is J_{AO} (ROI) higher than J_{AO} (SFR)?	y position of Maximum J_{AO} (mm)		Maximum J_{AO} (%)	
	Study 1	Study 2	Study 1	Study 2		Study 1	Study 2	Study 1	Study 2
ROI A	-0.59	-	7.43	-	Yes	11	-	7.43	-
ROI B	-4.88	-4.31	2.52	6.03	Yes	14	11	5.77	7.80
ROI C	-7.77	-8.02	4.77	3.45	Yes	16	17	11.53	9.07
ROI D	-8.63	-	1.85	-	Yes	18	-	6.70	-

Table 6-8 Comparison of the midway sensitivity of AO, I_{PC}, I_{CCD} and $\frac{\partial A_{SR}}{\partial \rho}$ in the SFR and the ROI for reflection mode when the background μ_a = 0.0235 cm^{-1}.

6.3.4 Effects of Background Absorption on the Spatial Sensitivity

In the section, the results of mapping the AO and the I_{PC} spatial sensitivity to localised μ_s' change when a higher background absorption (μ_a = 0.1 cm^{-1}) was used are presented. The same experimental setup and procedures except the local absorber, which are described in section 5.3.4.1, were used. The local scatterer, which is described in section 6.1, was used.

6.3.4.1 Sensitivity Maps

The experimental results of the AO and I_{PC} measurements are shown in Figure 6-22 (a)-(c) and (d) respectively. Their reference measurements are presented in Figure 6-23. The AO measurement results of I_{AC} and MD are similar to the results of using the local absorber, which are showed in Figure 5-33 (a) and (c). In comparison, the I_{DC} results in Figure 5-33 (b) and Figure 6-22 (b) shows that a localised change in μ_s' has a greater influence on the I_{DC} than a localised change in absorption. The local scatterer causes a higher I_{DC} change in regions near the FUR and in the SFR.

The fluctuations observed in region at x = 22- 28 mm of the I_{PC} measurement in Figure 5-33 (d) are caused by the slow precipitation of the Intralipid solution, which can be observed in Figure 6-23 (d). The highest I_{PC} changes (due to the local absorber) are observed in regions closest to the optical source and detector. In Figure 5-33 (d), the largest I_{PC} change are located at x = 3 and 26 mm and y = 5 mm. This result echoes the observation that is discussed section 6.3.1. This phenomenon is more evident in the scattering spatial sensitivity of the I_{PC} measurement, which is shown in Figure 6-24 (c) (in comparison the absorption case that is shown in Figure 5-35 (c)).

The spatial sensitivity maps of the AO measurement is shown in Figure 6-24 (a) and (b) shows the location of the FUR. Once again, the sensitive AO region does not overlap with the FUR. Figure 6-19 (c) shows the AO spatial sensitivity map

when the background absorption is minimal (μ_a = 0.0235 cm^{-1}) for the same FUR location at ROI B. It is very obvious that the higher background absorption causes the J_{AO} to become noisier because of the lower level of the detected I_{AC}. The AO measurement is also more sensitive to scattering changes than the I_{PC} measurements. And it can also be observed that the AO method can probe deeper than the I_{PC} method.

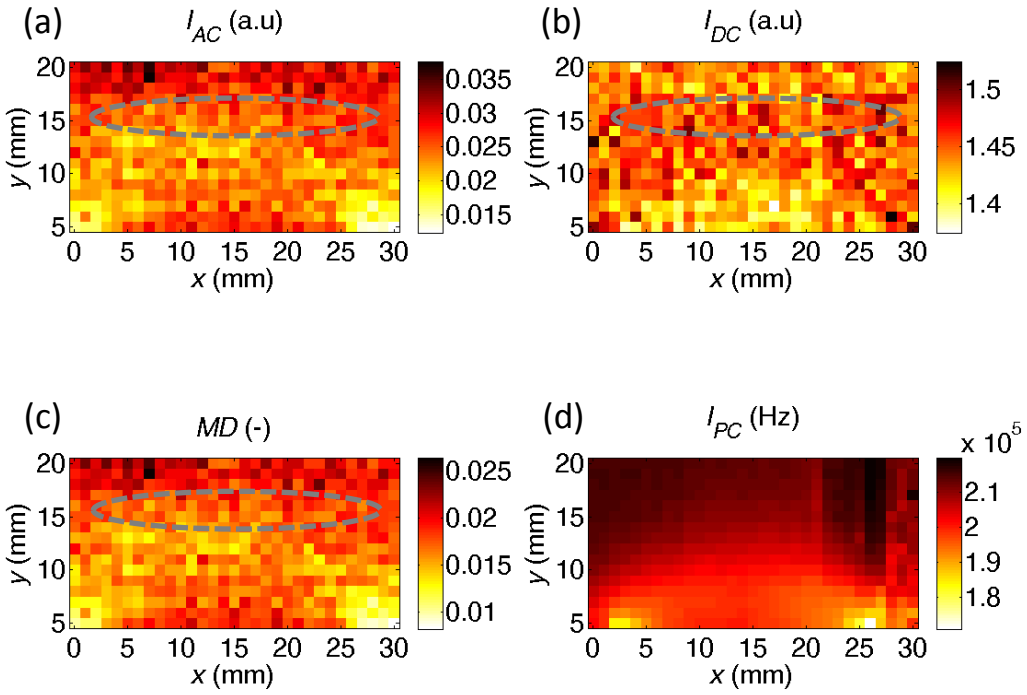

Figure 6-22 The measurement results of AO: (a) I_{AC}; (b) I_{DC}; (c) MD; and. (d) I_{PC} for reflection mode when the background μ_a = 0.1 cm^{-1}. (dashed line: FUR)

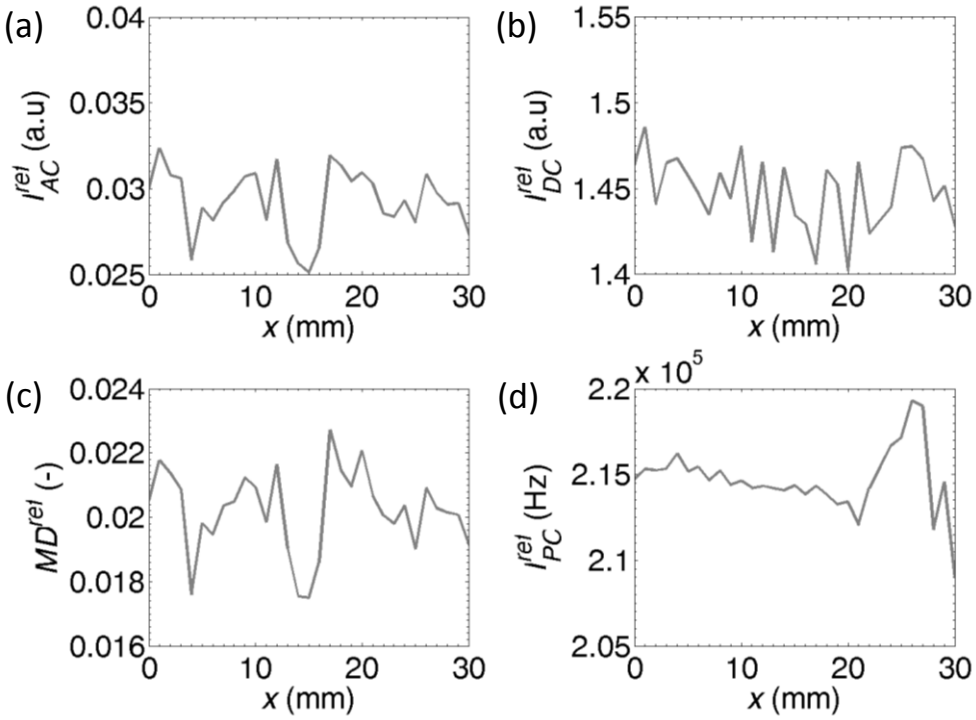

Figure 6-23 The reference measurement results of AO:(a) I_{AC}; (b) I_{DC}; (c) MD; and. (d) I_{PC} for reflection mode when the background μ_a = 0.1 cm^{-1}.

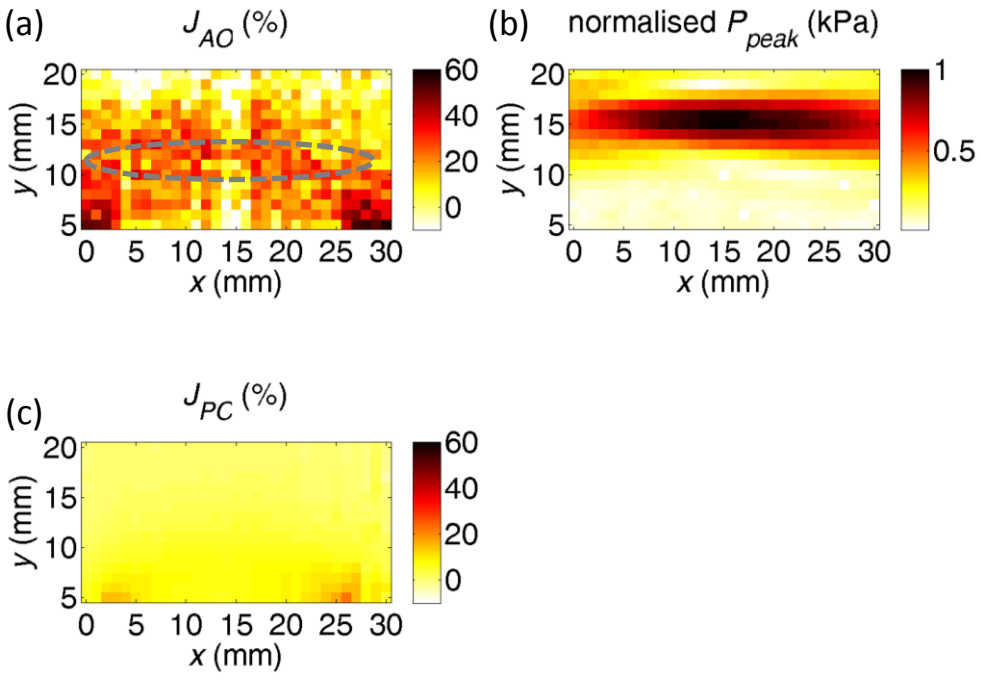

Figure 6-24 The spatial sensitivity maps of (a) AO and (c) I_{PC} with (b) the FUR for reflection mode when the background μ_a = 0.1 cm^{-1}. (dashed line: FUR)

6.3.4.2 Mean and Midway Sensitivity in the Superficial Region and the Region of Interest

The mean sensitivity of the AO and the I_{PC} measurements at different depth y are shown in Figure 6-25. The comparison of the mean sensitivity in the SFR and the ROI and the mean penetration depth are summarised in Table 6-9. Similar to the mean sensitivity due to absorption change in Figure 5-36, $<J_{AO}(\text{SFR})>$ is higher than $<J_{AO}(\text{ROI})>$ and the $<J_{AO}(\text{SFR})>$ is also higher $<J_{PC}(\text{SFR})>$. However $<J_{AO}(\text{ROI})>$ is much higher than $<J_{PC}(\text{ROI})>$. The mean penetration depth of the AO measurement is 10.3 mm, which is higher than the I_{PC}'s of 8.5 mm but shallower than the AO mean penetration depth due to absorption change of 11 mm (Table 5-11).

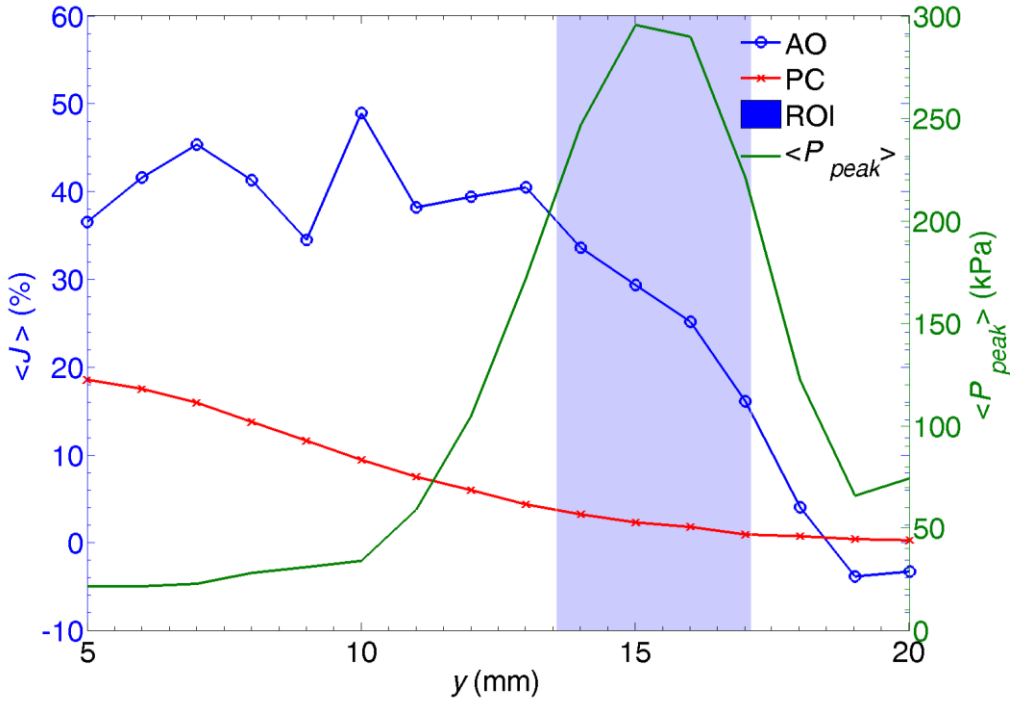

Figure 6-25 The mean sensitivity of AO and I_{PC} at different depth y for reflection mode when the background μ_a = 0.1 cm^{-1}.

Detection Method	<J(SFR)> (%)	<J(ROI)> (%)	Is <J(ROI)> higher than <J(SFR)>?	Mean Penetration Depth <y> (mm)
I_{PC}	18.2	2.3	No	8.5
AO	36.5	29.3	No	10.3

Table 6-9 Comparison of the mean sensitivity of AO and I_{PC} in the SFR and the ROI and their mean penetration depths for reflection mode when the background μ_a = 0.1 cm^{-1}.

The midway AO and I_{PC} sensitivity profiles are shown in Figure 6-26 and the comparison of their midway sensitivities in the SFR and the ROI are summarised in Table 6-10. The midway AO sensitivity in the ROI is higher than in the SFR while the midway J_{PC} is higher in the SFR than in the ROI. Furthermore, the midway J_{AO} in the ROI is considerably higher than the midway J_{PC} in the ROI.

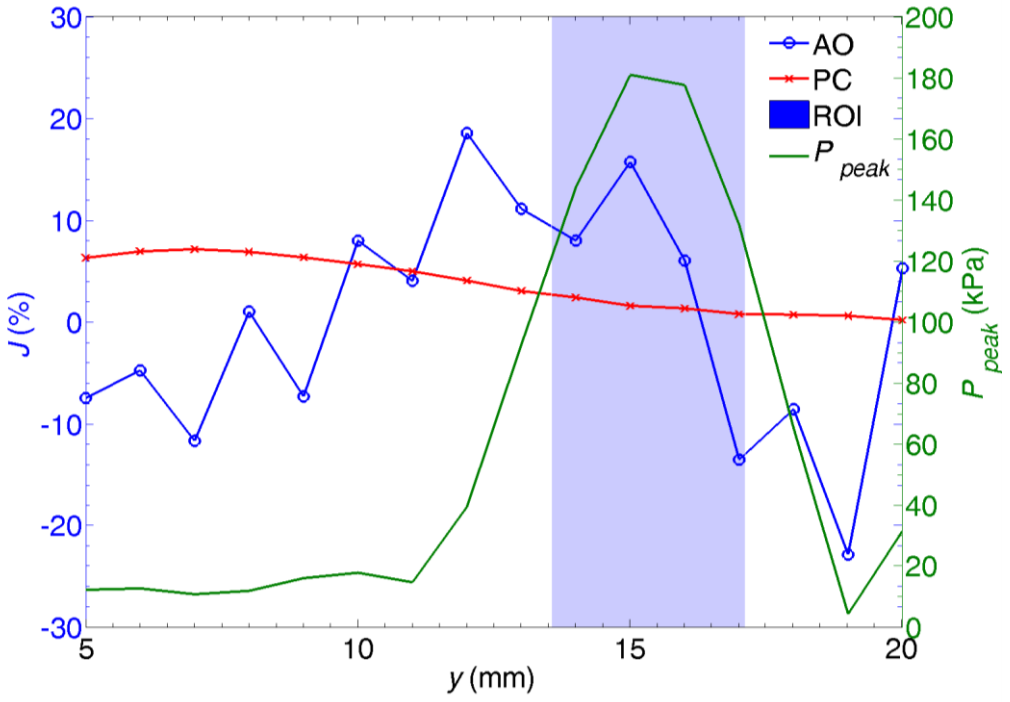

Figure 6-26 The midway sensitivity of AO and I_{PC} at different depth y for reflection mode when the background μ_a = 0.1 cm^{-1}.

Detection Method	J(SFR) (%)	J(ROI) (%)	Is J(ROI) higher than J(SFR)?
I_{PC}	6.4	1.7	No
AO	-7.5	15.7	Yes

Table 6-10 Comparison of the midway sensitivity of AO and I_{PC} in the SFR and the ROI for reflection mode when the background μ_a = 0.1 cm^{-1}.

6.3.5 **Summary**

This section summarises the study of the scattering special sensitivity maps comparison between the AO and the optical measurements in reflection mode.

1. The most sensitive region of the AO measurement does not overlap with the FUR and their relationship is not the same as that of the absorption sensitivity. The highest mean and midway J_{AO} are achieved when the FUR is located in the ROI C (Figure 6-20 and Figure 6-21), which requires further investigation to identify the cause of this phenomenon.
2. The AO method can detect scattering changes in regions that are located up to 18 mm (maximum penetration depth) deep by relocating the location of the FUR to 25 mm deep. This is considerably higher than the maximum penetration depth of the optical measurements, which is approximately 8-9 mm. On the other hand, the AO method can detect absorption changes in regions that are located up to 21 mm deep.
3. The AO measurement has negative scattering sensitivity in the SFR and the regions located deeper than the FUR because of the surface-induced backscattering effect of the local scatterer.

6.4 Conclusions

Key conclusions that can be drawn from this chapter are:

1. The AO measurement in transmission mode shows no change to μ_s' changes when the background medium has minimal absorption. This is because the change is very small and it is overshadowed by the increase in the MD due to mismatch of the mechanical properties between the local scatterer and the background medium. The AO spatial sensitivity map shows highly localised change in the FUR when the background absorption is increased to the level of healthy soft tissue due to the volume-induced scattering-enhanced absorption. The change in the MD is magnified by the volume induced scattering enhanced absorption when the background absorption is raised.
2. The optical measurements are most sensitive to scattering changes in the SFR in reflection mode. When the background absorption is minimal, the AO measurement is always more sensitive in the ROI than in the SFR. When the background absorption is higher, whether the sensitivity in the ROI would be higher than in the SFR depends on the location of the FUR in the spatial sensitivity of the optical measurements.
3. In reflection mode, the most sensitive region of the AO measurement is not located in the FUR. Similar to the previous chapter, the location of this region depends on the overlap between the FUR and the sensitivity level of the optical measurement e.g. J_{PC}.
4. The AO method can relocate the region it probes for a localised μ_s' changes by repositioning the FUR in reflection mode.
5. In a more absorbing medium, the mean and maximum penetration depths of the AO and the optical measurement in reflection mode become shallower.

7 Optimisation of Acousto-Optic Detection in Cylindrical Tissue Mimicking Phantom

The studies presented in chapter 5 and 6 were conducted for simple geometries, i.e. transmission and reflection slab geometries, which are anatomically unrealistic. Typical AO studies in the literature were also conducted in similar geometry. Therefore there is a need to investigate the feasibility of the AO measurement in a geometry, which is not slab-based. In this chapter, we investigate the AO measurement in the cylindrical geometry, which can be considered as the neonatal neck [Gunadi 2010].

Secondly, a continuous-wave focused ultrasound and laser were used chapters 5 and 6, which are potentially unsafe when higher output level is used to amplify the AO signal. Increasing the peak pressure of the focused ultrasound produces greater particle displacement and variation of refractive index of the tissue. Higher output power of the laser source will ensure an adequate amount of light that would propagate through the FUR. Chapters 5 and 6 have shown that the human tissue level of μ_a causes the sensitivity of the AO measurement to drop. Pulsed [Marks 1993, Lev 2003, Sakadzic 2004] or pulsed-wave [Kim 2006, Zemp 2006, Li 2011] excitation of the ultrasound transducer can be used to achieve a higher output power, which can be synchronised to the output of the laser source and the optical detector.

The single detector AO system, based on the digital correlator [Leutz 1995, Devi 2006], which is described in section 4.3.1, is not popular in the UOT community because of its poorer signal to noise ratio when it is compared to the parallel detection method. However, for sensing purposes, the fibre coupled setup is more convenient and practical. This setup has not been shown to operate with pulsed-wave excitation of the focused ultrasound; therefore, we aim to verify its feasibility in the detection of pulsed-wave induced AO signal.

The work presented in this chapter aims to address two issues. Firstly, the optimisation of the AO measurement for a cylindrical geometry is studied, which involves the investigation of the optimal configuration of the optical source and detector for a given location of the FUR and the parameters of the single detector AO system. Secondly, the feasibility of using pulsed-wave ultrasound with the AO method, which is based on the measurement of temporal intensity autocorrelation function, is investigated.

This chapter is based on our published work [Gunadi 2010] and additional phantom development and experimental work, which was assisted by Nadir R. Chowdhury (development and measurements of two phantoms).

7.1 Materials and Methods

7.1.1 Experimental Setup and Protocol

The experimental setup is shown in Figure 7-1 and Figure 7-2.

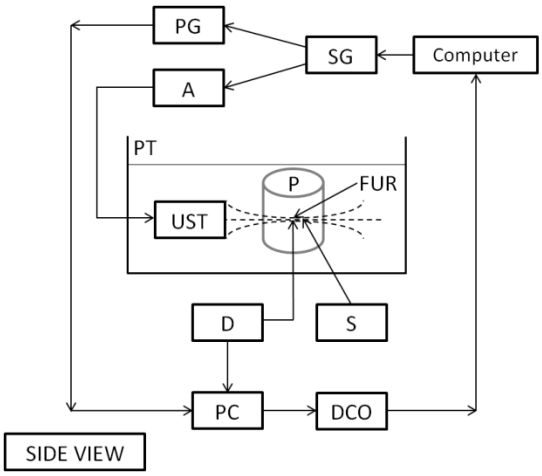

Figure 7-1 The basic setup of the AO measurement with pulsed-wave ultrasound in a cylindrical geometry; [SG: signal generator; A: RF amplifier; PG: pulse generator; PT: plastic water tank, which is filled with deionised water; UST: ultrasound transducer; P: cylindrical PVA gel phantom; D: optical detector; S: optical source; PC: the single photon counter unit; DCO: the digital correlator.

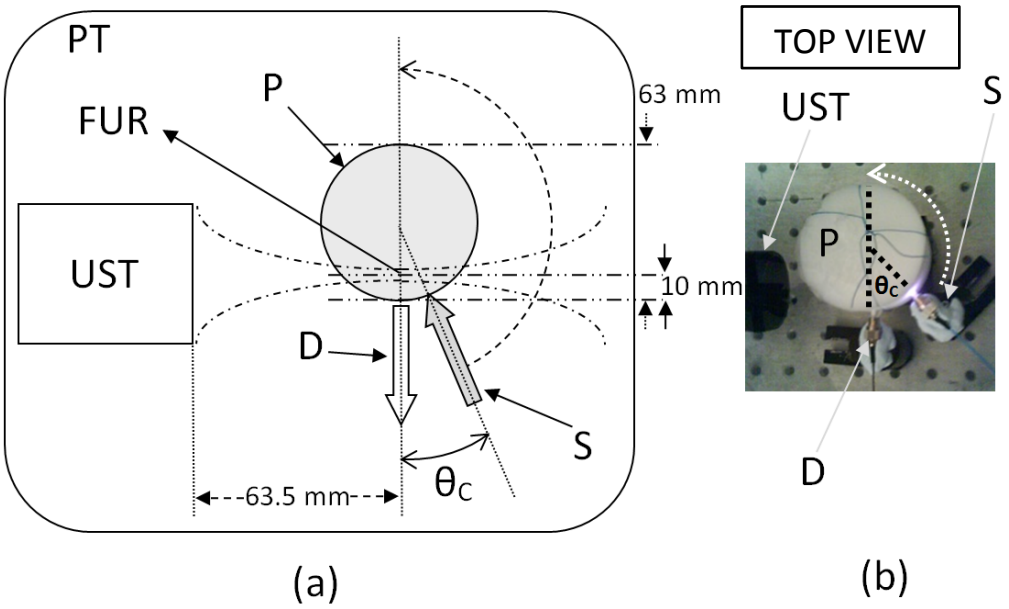

Figure 7-2 (a) The schematic diagram of the experimental setup (top view); where θ_C is the angle between the optical source and detector (°). (b) An image of the phantom with the S-D and UST.

The optical detector and the ultrasound transducer were fixed at positions as shown in Figure 7-1 (b), where at θ_C = 0° the optical detector is perpendicular to the direction of the ultrasound propagation. The angle θ_C between the optical source and detector was gradually increased from 22.5° to 45°, 67.5°, 90°, 135° and 180° in every AO measurement by re-positioning the optical source along the surface of the phantom. The relocation of the optical source was carried out manually, which might induce experimental inconsistency.

The integration time $t_{\int}$ of the digital correlator was also varied from 10 to 600 seconds in order to identify the optimal measurement time for the digital correlator. The pulsed-wave ultrasound excitation parameters are calculated using (7-4): *NC* = 20 cycles, *RR* = 1.5 kHz and V_{pp} = 47 V, which results in peak pressure of 88 kPa in the FUR (measured in water). Five measurements were conducted for each protocol so that the variability of the detected AO signal can be analysed.

7.1.2 **Phantoms**

Six 10% polyvinyl alcohol (PVA) cylindrical gel phantoms of 63 mm diameter and 60 mm height were constructed to have μ_s' of 6, 7.5, 10, 12, 15 and 17 cm^{-1}. The phantom development is discussed in section 4.2.2. It had been shown that their mechanical properties are similar to that of healthy soft tissue [Price 2010]. The geometry and image of one of the phantoms is shown in Figure 7-2 (b).

7.1.3 **Pulsed-Wave Focused Ultrasound**

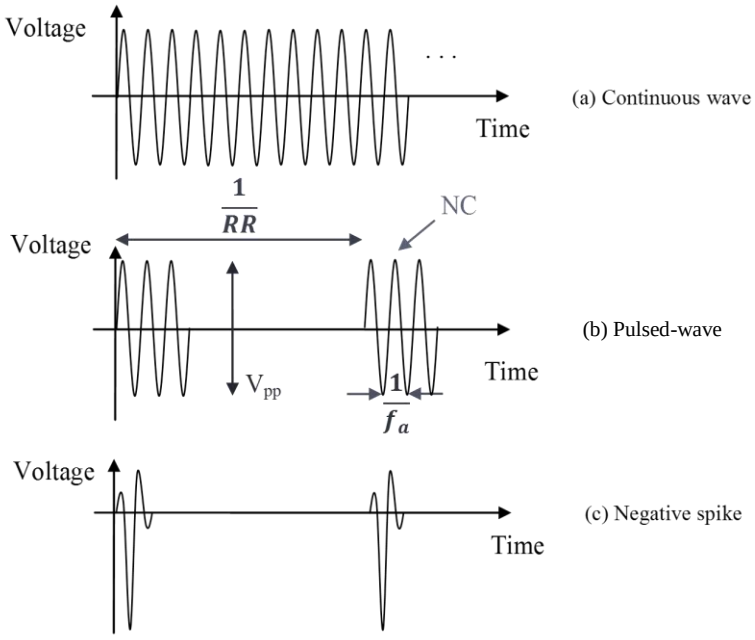

Figure 7-3 Ultrasound transducer excitation signal for: (a) continuous wave, (b) pulsed-wave (b) and (c) pulse. [*RR*: repetition rate, *NC*: number of cycles, *Vpp*: peak-to-peak excitation voltage, f_a: acoustic frequency]

The ultrasound transducer (Olympus Panametrics, V392SU) used in this study is the immersion type with centre frequency 1 MHz with a focal distance of 63.5 mm and a focal region of 2.56 mm (focal zone width) by 29.36 mm (focal zone length). The transducer was driven by a combination of a signal generator (Agilent 33210A) and a 75 W RF amplifier (Electronics & Innovation A075) as

shown in Figure 7-1. The amplifier has a gain of 50 dB and its input signal must be less than 1 volt root-mean-square. The FUR of this transducer is located 10 mm deep from the surface of the phantom, instead of the deeper region that can be achieved by the AO method, which is discussed in chapter 5 and 6. This is to ensure that AO signal can be readily detected due to the weaker output power of this transducer.

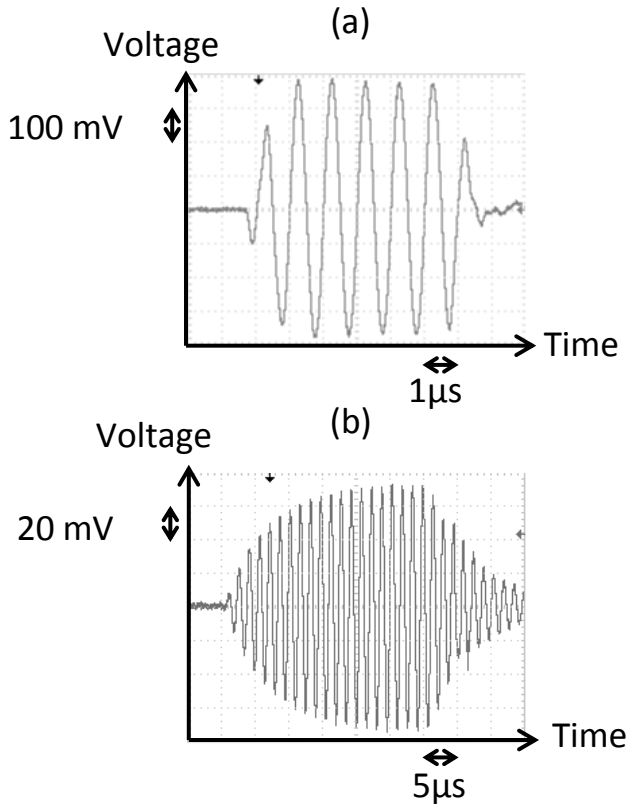

Figure 7-4 (a) 1 MHz pulsed-wave of 6 cycles and (b) 0.66 MHz pulsed-wave of 20 cycles. The 1 MHz UST stabilises after one cycle while the 0.66 MHz takes more than 15 cycles. The waveforms were recorded using the needle hydrophone setup, which is described in 4.1.5, at their respective focal distances.

This transducer is designed for negative spike excitation according to its excitation guidelines. The average power dissipated by the transducer must not exceed 125 mW in pulsed-wave mode to avoid overheating and *depoling* damage.

An example of pulsed-wave excitation is shown in Figure 7-3. This ultrasound transducer is used instead of the one that is used in chapters 5 and 6 because of its wider bandwidth (0.71 MHz compared to 0.12 MHz) that minimises damping when the excitation voltage is applied shown in Figure 7-4.

In order to calculate the parameters for the pulsed-wave excitation (repetition rate, number of excitation cycles and input voltage) to meet the excitation guidelines, the following equations (7-1)-(7-4) are used.

$$V_{rms} = \frac{V_{pp}}{2\sqrt{2}} \tag{7-1}$$

$$P_{max} > \frac{DCy \cdot {V_{rms}}^2 \cdot \cos\theta}{Z} \tag{7-2}$$

$$NC = \frac{f_a \cdot DCy}{RR} \tag{7-3}$$

By combining (7-1), (7-2) and (7-3),

$$V_{pp} < \sqrt{\frac{8 \cdot Z \cdot P_{max} \cdot f_a}{NC \cdot RR \cdot \cos\theta}} \tag{7-4}$$

where V_{pp}: peak-to-peak voltage (V) of excitation signal; V_{rms}: root-mean-square voltage (V) of excitation signal; P_{max}: maximum power dissipation (0.125 W); *DCy*: duty cycle of pulsed-wave (fraction); *RR*: repetition rate of pulsed-wave (Hz); *NC*: number of acoustic cycles; f_a: fundamental acoustic frequency of transducer (Hz); θ: phase angle (typically -45°); and *Z*: nominal impedance of transducer (typically 50 Ω)

A Labview program was developed to control the instruments according to the excitation and the operation guidelines. Besides the above equations, the gain and input voltage requirements of the RF amplifier were also incorporated in the Labview program as well. The user controls the number of cycles (*NC*), repetition rate (*RR*) and output voltage of amplifier (V_{pp}). The program automatically adjusts the RF output voltage to the allowed maximum allowed magnitude when user's inputs exceed the limits.

7.1.4 Time-Gated Acousto-Optic Signal Detection

7.1.4.1 Time-Gated Acousto-Optic Detection

The single detector scheme used in this study is the fibre-coupled optical system described in sections 4.1.1-4.1.3, which consists of an 808nm 100 mW laser source (CrystaLaser, IRCL-100-808-S), a single photon counter (Perkin Elmer, SPCM-AQR-14) and a digital correlator (Correlator.com, Flex02-01D). The basic setup is shown in Figure 7-1.The laser output at the end of optic fibre was 45 mW due to the poor coupling of the fibre.

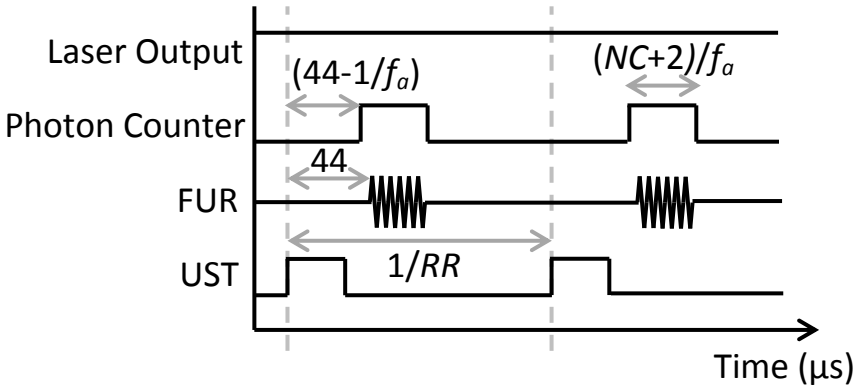

Figure 7-5 The synchronisation of the time-gated AO detection.

It is essential to synchronize the laser output and/or photon detection to the ultrasonic pulsed-waves at the FUR. The synchronisation is shown in Figure 7-5. Due to hardware limitations, the laser output cannot be switched off when the

ultrasonic pulsed-wave is off. Thus, the photon counter is switched off during the off period of the pulsed-wave. This is to ensure the detection of the I_{AC} (ultrasound modulated intensity) and minimizing the detection of the I_{DC} (un-modulated intensity) when the pulsed-wave ultrasound is off; which in turn will improve the MD.

The photon counter can be activated and de-activated by an appropriate TTL (transistor-transistor logic) high and low signal respectively. However the switching pulse must be delayed to allow the ultrasonic pulsed-wave to reach the transducer's FUR, which is shown in Figure 7-6. The delay of 44 μs can be easily measured or computed based on the speed of sound in water.

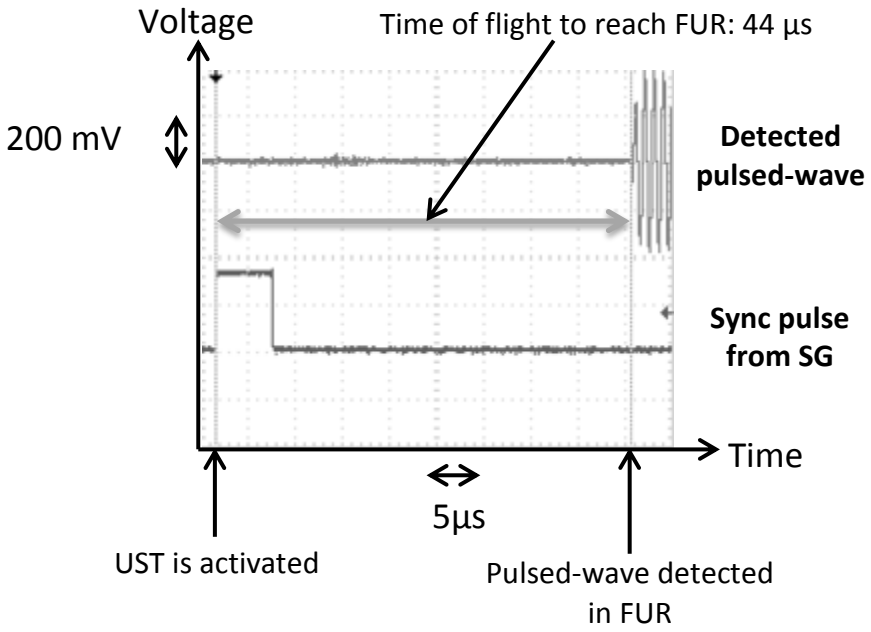

Figure 7-6 The time of flight of the ultrasonic pulsed-wave to propagate to the FUR when the ultrasound transducer is activated.

When the ultrasound is activated, the signal generator will produce a sync pulse, which will be delayed by 44 μs by a pulse generator. The frequency of the switching pulse is the same as the *RR*. The on period is determined from

(NC+2)/f_a, which can be set by the pulse generator. The additional two cycles to compensate the slight error in the estimation of delay time because the speed of sound in the phantom is not the same in water.

7.1.4.2 Analysis of Time-Gated Acousto-Optic Signal

The difference between the continuous and time-gated detections using the pulsed-wave ultrasound waves is demonstrated in Figure 7-7 (a) and (b) respectively. The continuous detection using the continuous ultrasound wave is shown Figure 7-7 (c).

Figure 7-7 (a) does not show the exponential decay that is caused by the Brownian motion of the scatterers within the phantom because the decorrelation time of the PVA gel phantom is very long, which is 3.4 ms (section 4.3.2.2). The effect of using the pulsed-wave ultrasound is evident in Figure 7-7 (b) whereby the amplitude of the sinusoidal modulation is decreasing as the lag time increases. This is because of the decreasing number of cycles within the pulsed-wave being integrated by the digital correlator at larger lag time. When compared to the continuous wave excitation, the autocorrelation of pulsed-wave excitation exhibits slight distortion near the zero lag time. It is possible that this is caused by the damped initial cycle, which is shown in Figure 7-4 (a).

The time-gated autocorrelation function shows large distortion of the linear decay due to the off period of photon counting, which transforms the intensity series into a square-wave–like function. The autocorrelation function of a square-wave has the form of a triangular function, which is depicted in Figure 7-7 (c). The distortion is also influenced by the amount of photon detected. This is because the actual photon ‘counting’ is carried out by the digital correlator, which uses symmetric normalisation [Schätzel 1990] scheme to improve the statistical accuracy at large lag time. Thus zero-photon period causes the digital correlator to normalise incorrectly, which is demonstrated in Figure 7-8.

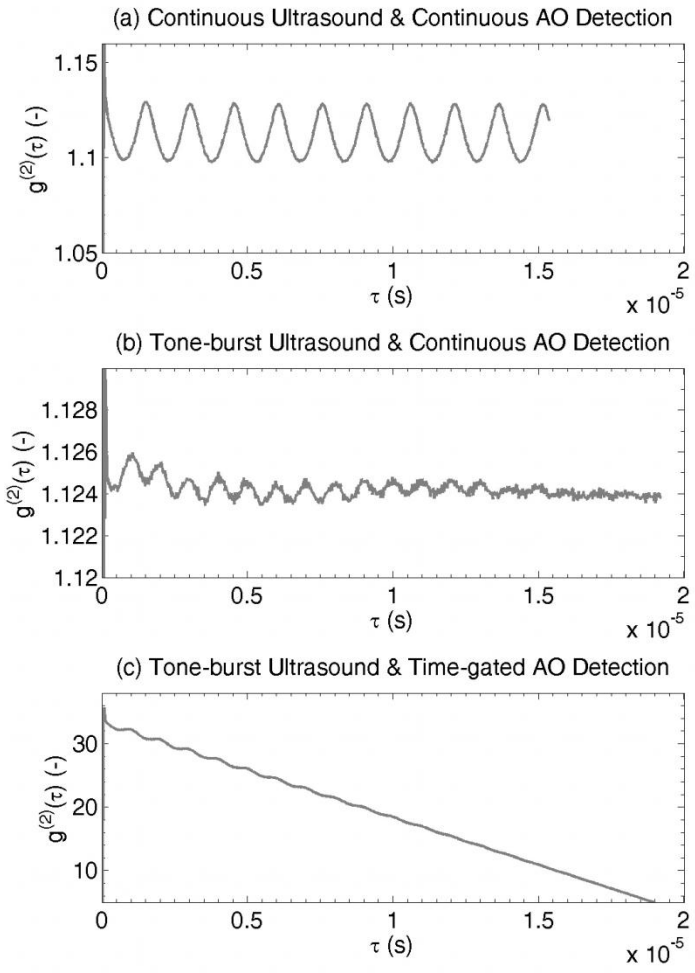

Figure 7-7 (c) The temporal intensity autocorrelation functions of: (a) the continuous AO detection using the continuous ultrasound; (b) the continuous AO detection using the pulsed-wave ultrasound; and (c) the time-gated AO detection using the pulsed-wave ultrasound.

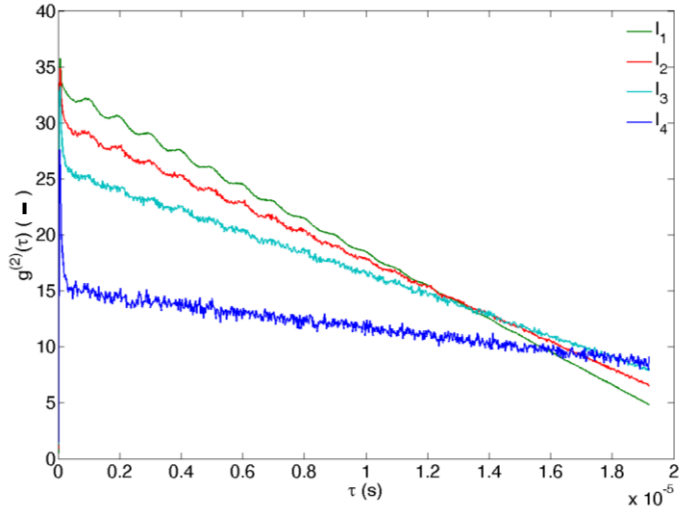

Figure 7-8 The effect of incorrect normalisation by the digital correlator, which is caused by the photon-counting off period in the intensity time-series. The average detected intensities are such that $I_1 > I_2 > I_3 > I_4$ when the θ_C was set to 45°, 67.5°, 90° and 135° respectively. These measurements were recorded using the same setup, which is shown in Figure 7-1; and the μ_s' of phantom is 12 cm^{-1}.

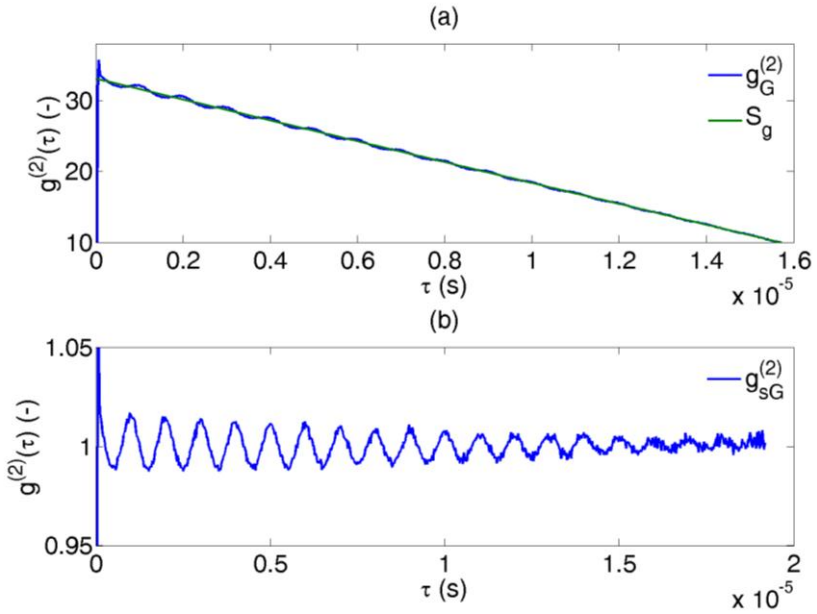

Figure 7-9 (a) The time-gated autocorrelation function $g_G^{(2)}$ with the linear decay S_g and (b) the scaled time-gated autocorrelation function $g_{sG}^{(2)}$.

This means that the method of computing the MD as described in section 5.1.5.1 cannot be used here. The following describes a modified method to calculated the MD from the time-gated autocorrelation function $g_G^{(2)}(\tau)$:

1. A linear function S_g is estimated by using linear regression on the $g_G^{(2)}(\tau)$, which is shown in Figure 7-9 (a).
2. The $g_G^{(2)}(\tau)$ is then divided by S_g in order to remove the linear decay of the $g_G^{(2)}(\tau)$ to produce a scaled $g_G^{(2)}(\tau)$, $g_{sG}^{(2)}(\tau)$, which is shown in Figure 7-9 (b).
3. In section 5.1.5.1, the value of $g_{sG}^{(2)}(\tau \to 0)$ is used to estimate β by using equation (4-16) so that $g^{(1)}(\tau)$ can be computed. However, the time-gated AO detection and the normalisation using S_g aggravated the distortion at $\tau \to 0$. Therefore $g_{sG}^{(2)}(\tau = 1\mu s)$ is used instead.
4. The $g_G^{(1)}$ can be calculated by using equation (4-15).
5. The *MD* is calculated by using equation (5-3).

For comparison, the $g^{(2)}(\tau = 1\mu s)$ is also used to compute the *MD* for the autocorrelation function of the continuous AO detection.

7.2 Results & Discussion

7.2.1 Effects of Location of Optodes and Integration Time on Noise Measure

A noise measure (N_M) is used to characterise the level of noise (frequency > 5 MHz) for a configuration of the ultrasound and the optodes. This noise measure is the ratio of the area of the Fourier spectrum of $g_G^{(1)}(\tau)$ when the frequency > 5 MHz and the total area under the spectrum. The comparison of the noise measure between the continuous and time-gated AO signal at different θ_C and $t_\int$ is shown in Figure 7-10. At every θ_C, the time-gated AO detection outperforms the

continuous AO detection in term of the noise measure. This is because of the overall reduction of un-modulated photon detection.

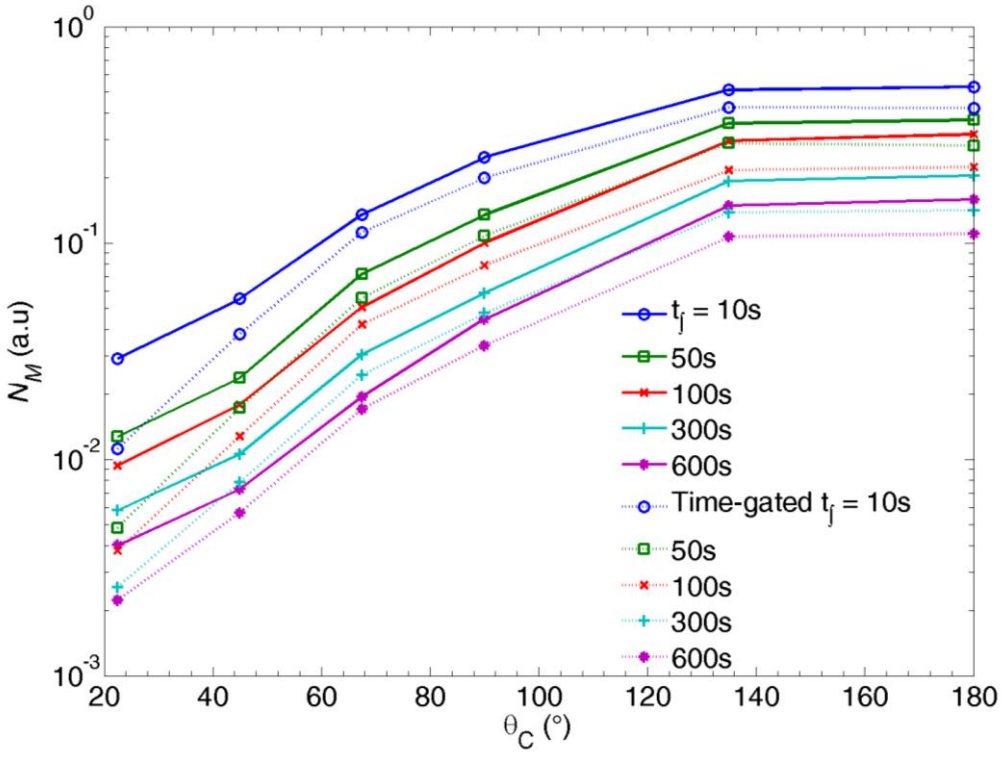

Figure 7-10 Comparison of the noise measure N_M of the continuous and the time-gated AO detection for pulsed-wave ultrasound: the time-gated AO measurement has better N_M because there are less I_{DC} detected.

The time-gated AO measurement is the least noisy when the laser source was located at θ_C = 22.5°. As the source was systematically relocated further away from the detector, the noise measure of both time-gated and continuous AO measurements increased. The reason is because when the θ_C increases, the detected photon count rate decreases as the separation distance between the optical source-detector. When θ_C > 135°, the noise measure stabilises because the amount of light detected is similar.

Increasing the integration time of the digital correlator (which is also the measurement time) generally improves the AO signal measured by both methods.

The least noisy configuration in this study is to use time-gated detection and integration time $t_{\int}$ of 600 s. Each time-gated AO measurement was repeated five times in order to assess the variability of the detected signal. By time-gating, the measurement time can be reduced while maintaining similar noise measure to the normal method.

7.2.2 Effects of Transport Scattering and Integration Time on Time-Gated Acousto-Optic Measurement

When θ_C is set to 45°, the plots of the MD when the μ_s', and the $t_{\int}$ vary are presented in Figure 7-11. Similar to the observations discussed in section 7.2.1, increasing the $t_{\int}$ reduces the variability of the time-gated AO measurement. The variability of the MD stabilises when $t_{\int}$ > 100 s when $\mu_s' \leq 12$ cm^{-1}. When $\mu_s' > 12$ cm^{-1}, $t_{\int} > 300s$ is required to minimise the variability in the time-gated AO measurement. The MD tends to increase with increasing μ_s' till $\mu_s' = 12$ cm^{-1}. When $\mu_s' > 12$ cm^{-1}, the MD seems to plateau or even drop.

A closer look at the MD is by examining the I_{AC} (ultrasound modulated intensity) and I_{DC} (un-modulated intensity) shown in Figure 7-12 for all phantoms. The variability in the MD tends to increase with increasing μ_s'. This is because increasing the μ_s' reduces the amount of photon detected by the photon counter. The I_{AC} increases with increasing μ_s'. But it stabilises when $\mu_s' > 12$ cm^{-1}, which explains the behaviour of the MD plots. However, the I_{DC} is generally comparable for the varying μ_s'.

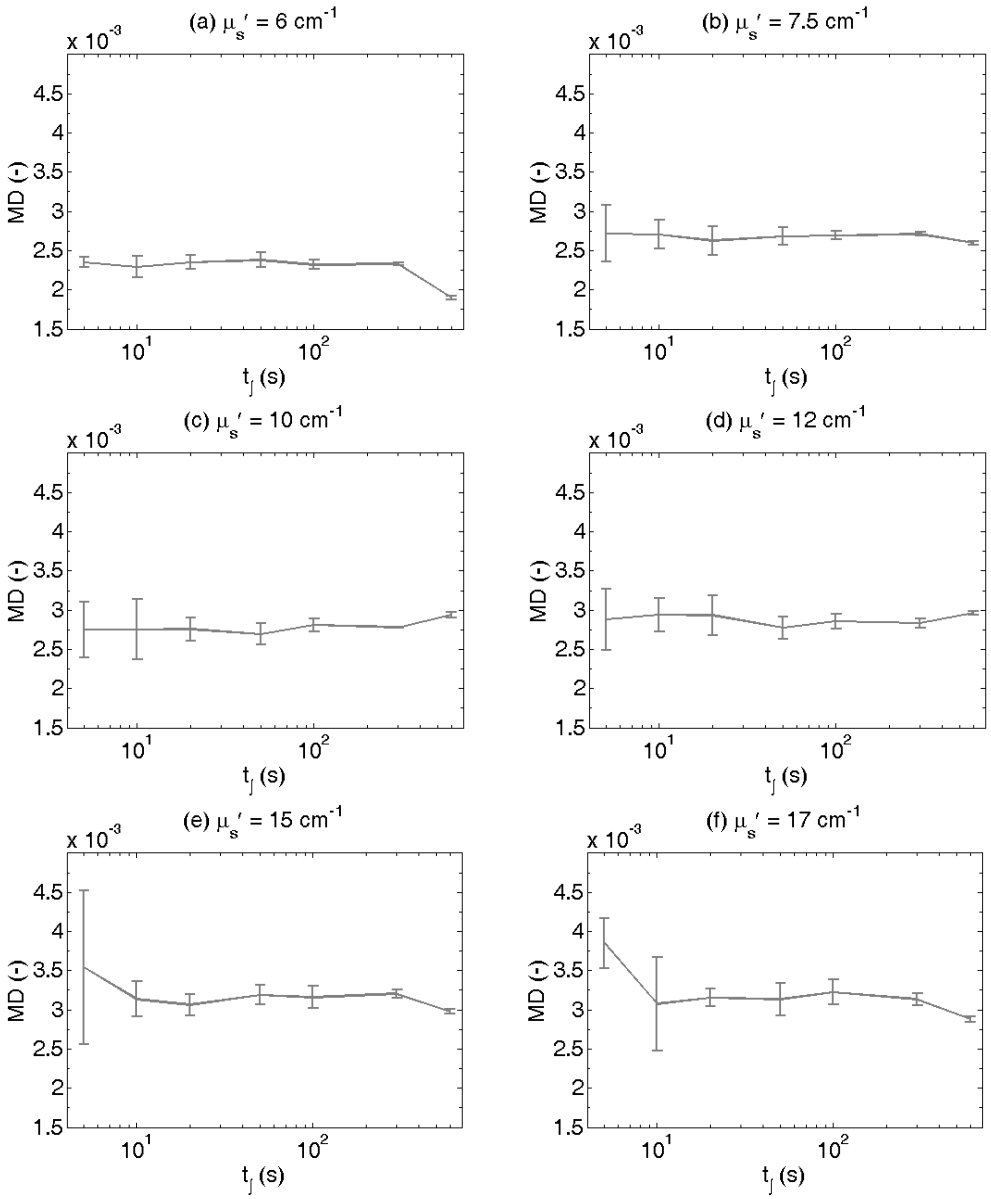

Figure 7-11 Comparison of the MD and the $t_{\int}$ for the phantoms of μ_s': (a) 6 cm^{-1}, (b) 7.5 cm^{-1}, 10 cm^{-1}, 12 cm^{-1}, 15 cm^{-1} and 17 cm^{-1}. Each measurement was repeated five times and the angle between the optical source-detector is 45°.

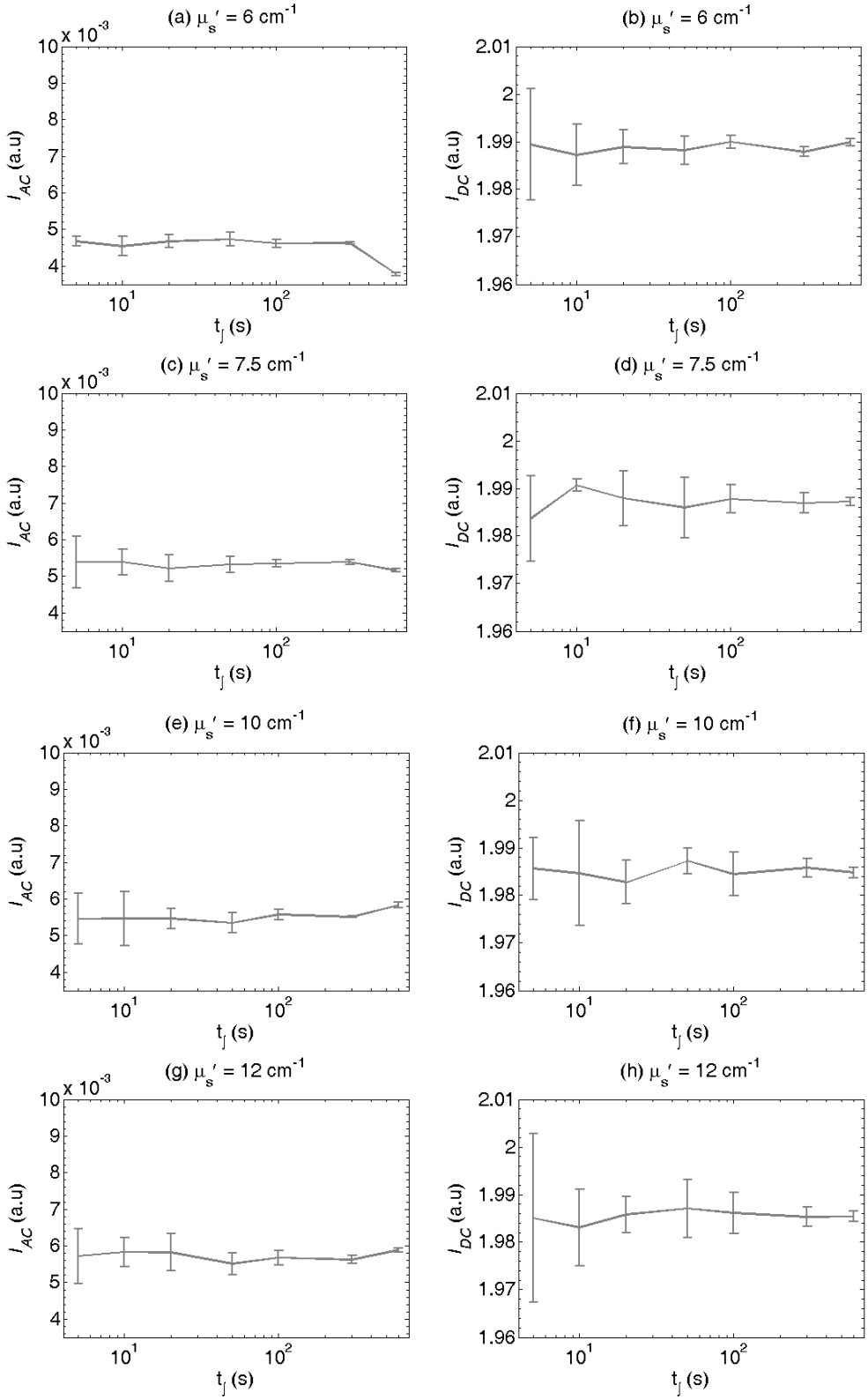
(a) μs′ = 6 cm-1
x 10-3
10
9
8
7
6
5
4
IAC (a.u)
10¹
10²
tJ (s)
(b) μs′ = 6 cm-1
2.01
2
1.99
1.98
1.97
1.96
IDC (a.u)
10¹
10²
tJ (s)
(c) μs′ = 7.5 cm-1
x 10-3
10
9
8
7
6
5
4
IAC (a.u)
10¹
10²
tJ (s)
(d) μs′ = 7.5 cm-1
2.01
2
1.99
1.98
1.97
1.96
IDC (a.u)
10¹
10²
tJ (s)
(e) μs′ = 10 cm-1
x 10-3
10
9
8
7
6
5
4
IAC (a.u)
10¹
10²
tJ (s)
(f) μs′ = 10 cm-1
2.01
2
1.99
1.98
1.97
1.96
IDC (a.u)
10¹
10²
tJ (s)
(g) μs′ = 12 cm-1
x 10-3
10
9
8
7
6
5
4
IAC (a.u)
10¹
10²
tJ (s)
(h) μs′ = 12 cm-1
2.01
2
1.99
1.98
1.97
1.96
IDC (a.u)
10¹
10²
tJ (s)

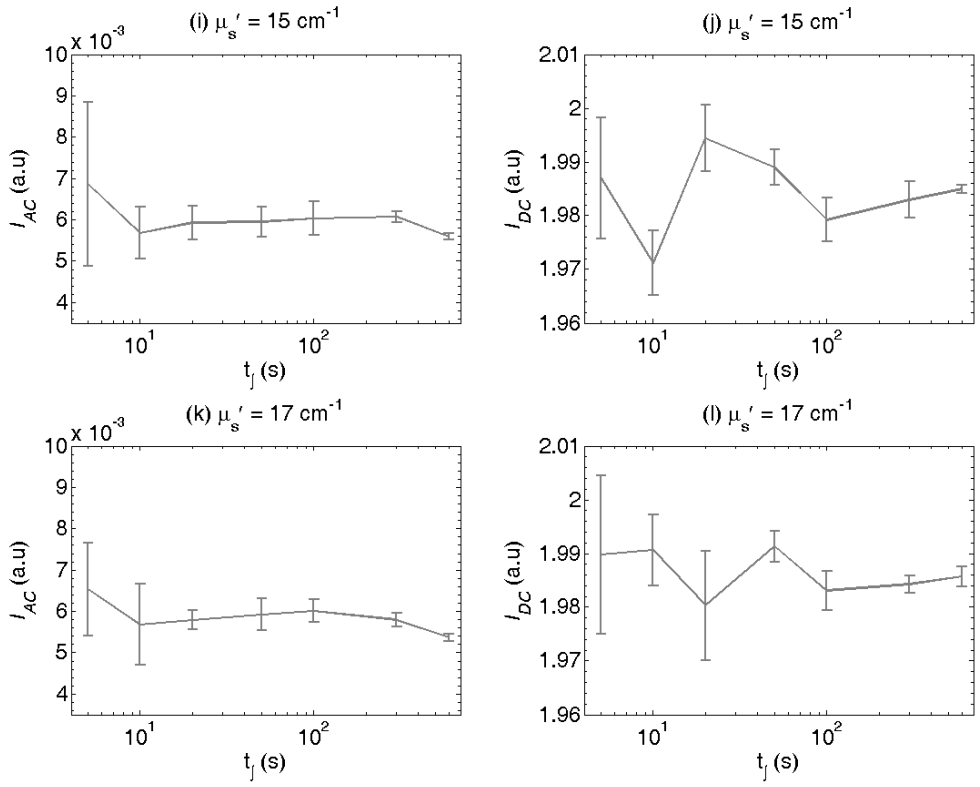

Figure 7-12 The I_{AC} and I_{DC} of the time-gated AO measurement when θ_C = 45° and the μ_s' are: (a)-(b) 6 cm^{-1}, (c)-(d) 7.5 cm^{-1}, (e)-(f) 10 cm^{-1}, (g)-(h) 12 cm^{-1}, (i)-(j) 15cm^{-1} and (k)-(l) 17 cm^{-1} respectively.

Alternatively, the plots are re-arranged so that the time-gated AO measurement is plotted for $t_{\int}$ = 600 s, which are shown in Figure 7-13. The trend of MD in Figure 7-13 (c) when the μ_s' varies is fairly obvious now. The MD increases when the μ_s' rises, however it peaks at μ_s' = 12 cm^{-1}. This observation is very similar to the I_{AC} that is shown in Figure 7-13 (a). The I_{DC} Figure 7-13 (b) is fairly stable, but when the μ_s' increases, the light is more scattered resulting in the less detected intensity. As μ_s' continues to rise, the MD will decrease instead. Such behaviour is caused by the anti-correlation effect [Sakadzic 2005] between the ultrasound modulated particle displacement and refractive index variation, which is discussed in section 3.3.2.3. The effect of increasing the μ_s' increases the number of scattering events within the FUR, which causes stronger correlation between the two coherent mechanisms. As a result, the contribution of the anti-correlation

factor starts to dominate and the MD decreases. Depending on the acoustic frequency, the MD tends to increase from low μ_s'. The MD will then peak at certain μ_s' and starts to descend, which is shown in Figure 3-19.

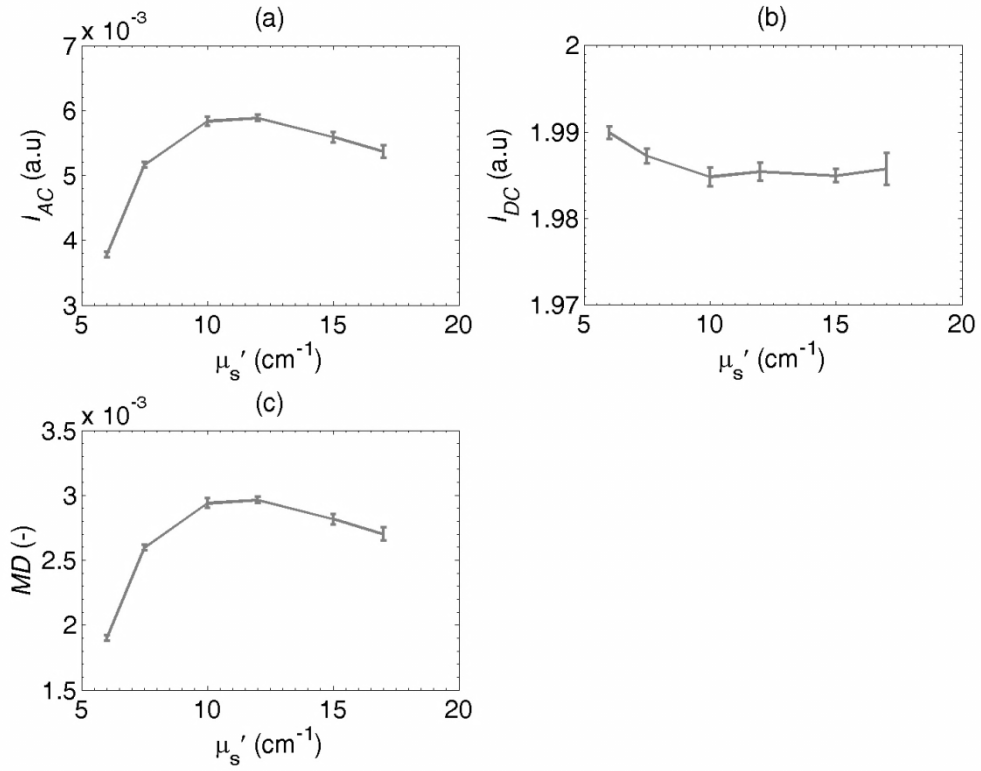

Figure 7-13 The time-gated AO measurements of varying μ_s' when θ_C = 45° and $t_\int$ = 600 s: (a) I_{AC}, (b) I_{DC} and (c) MD: the MD peaks at μ_s' = 12 cm^{-1}.

7.2.3 Effects of Location of Optodes and Transport Scattering on the Time-Gated Acousto-Optic Measurement

The time-gated AO measurements for different θ_C and different μ_s' are summarised in Figure 7-14. The general trend is that the variability of the time-gated AO measurement increases with increasing θ_C. At higher θ_C, the separation between the optical source and detector is further, which result in less light detected.

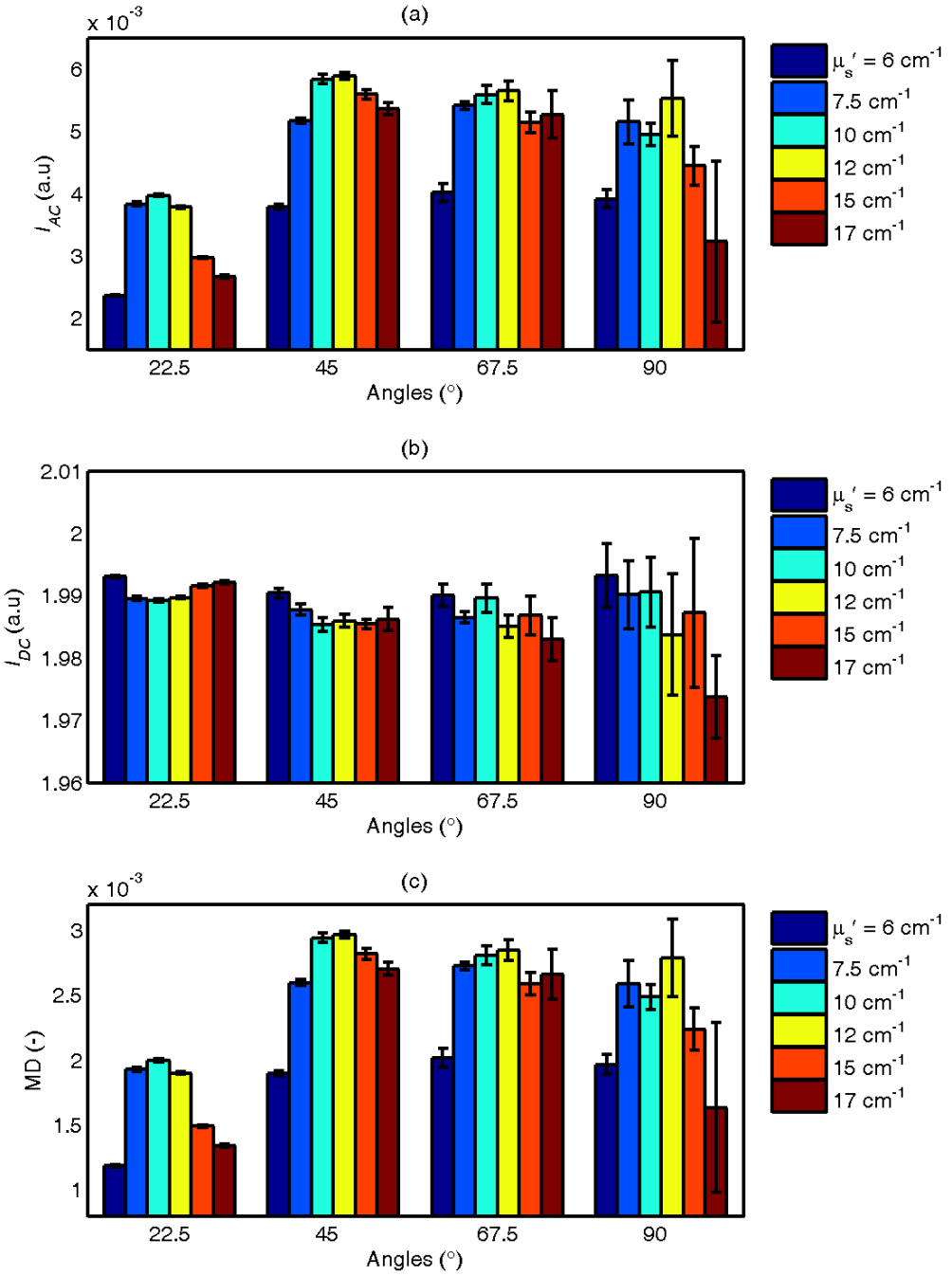

Figure 7-14 (a) I_{AC}, (b) I_{DC} and (c) MD of different μ_s' for different θ_C that shows that there is an optimal configuration for the optodes for the time-gated AO measurement.

Figure 7-14 (a) shows the I_{AC} and the lowest I_{AC} occurs when θ_C = 22.5°. At this θ_C, the distance between the source and detector is the closest, so most detected light is I_{DC}. In this optodes' arrangement, the light penetration depth is the shallowest thus there is less light that propagates to the FUR resulting in a reduction of I_{AC}. As θ_C increases, the separation between the optodes becomes greater and the light penetrates deeper into the phantom. The I_{AC} increases because of more light that propagates into the FUR. But as θ_C increases and the I_{AC} becomes also more variable due to decreasing amount of detected intensity. The highest I_{AC} is observed when θ_C = 45° when $\mu_s' \geq 10$ cm^{-1} and θ_C = 67.5° when $\mu_s' < 10$ cm^{-1}.

The I_{DC} that is depicted in Figure 7-14 (b) shows a decrease with increasing μ_s' and θ_C. Higher μ_s' scatters more light away from the detector and increasing θ_C causes the region of high photon path distribution to be re-located closer to the FUR, which increases the I_{AC}.

The net effect is shown in the trend of the MD, which is shown Figure 7-14 (c). The MD is the lowest at θ_C = 22.5° due to the high I_{DC}. At higher θ_C, the MD grows higher but is becoming more variable due to the worsening of the noise measure. The MD tends to peak when μ_s' is at 10 or 12 cm^{-1}. The highest observable MD can be detected when the θ_C = 45° when μ_s' = 12 cm^{-1}. This is because the magnitude of MD is heavily influenced by the overlap region between regions of high photon path distribution and the FUR; which is also shown in chapter 5 and 6. This implies that for a given geometry and configuration of the FUR and the optical source, there is an optimal location for the optical detector to capture the highest MD. This observation agrees with the computer simulation result in Gunadi et al. [Gunadi 2010], which is shown in Figure 7-15. Therefore, the optimal positioning of the probes can be predicted experimentally or through computer simulator for future studies.

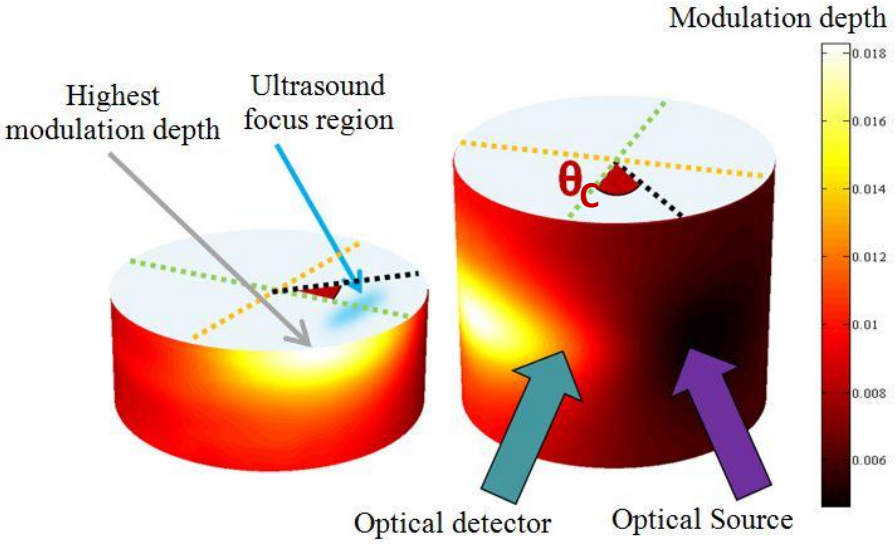

Figure 7-15 Monte Carlo simulation result shows an optimal location where the highest MD can be detected for a cylindrical phantom of $\mu_s' = 7.5\ cm^{-1}$,.$\theta_C = 45°$ and the peak pressure of 88 kPa in the FUR [Gunadi 2010].

7.3 Conclusions

In summary, the key findings in this chapter are:

1. Time-gated detection method can shorten the measurement time while maintaining a low noise measure.
2. Time-gated detection induces distortion to the autocorrelation function due to zero-photon period that results in the incorrect normalisation of the autocorrelation function.
3. The overlap between the optical path length distribution and the FUR affects the magnitude of the MD.
4. For a given geometry, there is an optimised configuration of the optical probes and ultrasound transducer for optimal AO measurement, which can be estimated experimentally.

8 Conclusions

An optical method such as NIRS, which uses non-ionising light to measure tissue oxygenation and blood flow non-invasively, is affordable. It can provide valuable information about the oxygenation and haemodynamics of the probed tissue. The thesis began as an investigation into the applications of the Diffuse Correlation Spectroscopy method, which is a variant of the NIRS family that can provide a measure of change in total blood volume and relative blood flow in the tissue capillary network. However, it is well described in the literature that the NIR light cannot penetrate very deep because of the highly scattering nature of tissue. Furthermore, it is also susceptible to haemodynamic and metabolic changes in the superficial layer of tissue. This is because this method measures changes that occur in the region where light propagates from the optical source to the detector.

To mitigate the limitations, we propose to use focused ultrasound waves to "label" the light that propagates through a ROI, a technique which is commonly known as the Acousto-Optic (AO) technique. The region of measurement can be controlled by positioning of FUR. Therefore, this method can probe deeper into tissue by relocating the FUR to deeper region of tissue. Furthermore, only light, which is modulated in the FUR, is tagged. The AO measurement should indicate the optical property of that region thus providing better specificity.

In order to demonstrate the feasibility of the AO method in improving the conventional optical measurement for potential oxygenation measurement, its spatial sensitivity in response to a localised change in absorption was mapped and scrutinised. Besides absorption, the AO method can also monitor changes in μ_s', which implies that it can also be used in other clinical applications such as monitoring of HIFU lesions. Therefore the AO spatial sensitivity in response to μ_s' changes was also investigated.

The majority of the AO studies in the literature use simple slab geometry, which is not anatomically realistic. Studies were carried out to investigate the feasibility

of the AO method in a cylindrical geometry, which mimics the shape of human limbs or the neck. In order to minimise the exposure of the target to the laser light and the ultrasound waves, the use of pulsed-wave ultrasound in the AO method was investigated. Furthermore optimisation strategy for the configuration of the ultrasound and optical probes and the detection of the AO signal were also studied.

8.1 Major Findings

8.1.1 Acousto-Optic Signal Detection

The MD can be increased by simply increasing the output power of the ultrasound transducer. However, the acoustic waves at higher power will be highly non-linear and cavitation also produces air bubbles that may impede the propagation of both acoustic waves and light. It is shown in Figure 4-24 and Figure 4-25 in section 4.3 that at high acoustic amplitude, the AO temporal intensity autocorrelation function saturates leading to a MD that is no longer sensitive to optical property changes in the FUR.

8.1.2 Absorption Spatial Sensitivity

In transmission mode measurement, the optical measurement is found to be more sensitive to the absorption change than the AO method. However, the maximum detected changes are observed in the regions close to the optical probes. On the contrary, the AO measurement possesses high localisation ability; which overlaps with the location of the FUR.

When an absorber is introduced in the medium that is probed by the AO method, the MD is expected to decrease because the absorber will reduce the amount of light that will interact with the focused ultrasound and light that is already modulated by the focused ultrasound. An interesting observation is that the MD is actually increased when the absorber is introduced in regions between the optical probes in the superficial layer. The reason is because the MD is the proportional to the ratio of the ultrasound modulated intensity to the un-modulated intensity.

When the absorber is in these regions, it absorbs a larger amount of the un-modulated light compared to the modulated light; thus resulting in an increase in the MD, which is evident in Figure 5-22 and Figure 5-23.

In reflection mode measurement, the conclusions are similar to those in the transmission mode. All optical measurements have the highest sensitivity in the regions close to the surface of phantom; which is shown in Figure 5-26 and Figure 5-29. On the other hand, the highest AO sensitivity is located in the deeper region. Further investigation by relocating the location of the FUR confirms that the most sensitive region of AO measurement can be relocated. However, the location of this region is not always the same as the location of the FUR. It depends on the overlap of the acoustic field and photon path length distribution.

In summary, the AO method can probe absorption changes in regions that are located deeper (up to 20 mm) than that of the optical methods. The sensitive AO region can be relocated by re-positioning of the FUR. This shows that AO method can provide a localised measurement of a ROI within tissue and the location of the ROI can be relocated. The effect of absorption changes in the SFR can be minimised, except when the changes occur in the regions very close to the optical source and detector. This is achieved by placing the FUR at least 15 mm away from the surface. This is an advantage of AO over NIRS, which is highly susceptible to the SFR. But the deeper the location of FUR is, the noisier the AO measurement becomes. This suggests that there is a trade-off between the maximum penetration depth and signal to noise ratio of the AO measurements.

8.1.3 **Scattering Spatial Sensitivity**

In transmission mode, the single source and detector AO system cannot detect any significant change in the spatial sensitivity when the background μ_a is nearly zero (0.0235 cm^{-1}) as shown in Figure 6-5. This is because the change caused by the local scatterer is very small and it is masked by the effect of the acoustic property mismatch between the local scatterer and the background medium as shown in Figure 5-13. But, when the background absorption is raised to that of the healthy

soft tissue, the scattering spatial sensitivity of the AO method is very similar to that of the absorption case; which demonstrates high sensitivity in the location of the FUR. The optical path length of light in the local scatterer is longer because of the higher μ_s'. When the local scatter is located in the FUR, more ultrasound modulated light is absorbed when the background absorption is higher according to equation (6-1). Generally, the sensitivity of the AO measurement is much higher in the ROI than in the SFR. On the other hand, the optical measurements are most sensitive to regions close to the surface of the phantom.

The behaviour of the scattering spatial sensitivity in reflection mode is similar to that of the absorption spatial sensitivity. However the regions in between the optical probe, which are located close to the surface and deeper than the FUR, show increase in the MD as shown in Figure 6-18. This is because of the surface-induced scattering effect from the mismatch of the refractive indices of the local scatterer and the background medium. The optical measurements are most sensitive to scattering changes that occur in the SFR. Similar to the absorption study, the most sensitive AO measurement is not located in the FUR but it can also be relocated by repositioning the FUR as demonstrated in Figure 6-19 and Figure 6-20.

These observations have implications in the application of HIFU lesion monitoring. HIFU lesions have higher μ_a and μ_s'. It has been shown that an increment in both μ_a and the μ_s' may result in either an increase or a reduction in the MD depending on the location of the FUR. Thus, the FUR should be set so that the trend of change is the same when these changes occur. For example: negative sensitivity in the SFR for both absorption and scattering change.

Concurrent monitoring of HIFU lesion using the digital correlator based AO detection is not possible. The intense ultrasound intensity used in HIFU therapy causes the ultrasound modulated autocorrelation function to become non-linear and saturate as shown in Figure 4-24 and Figure 4-25. Thus, the current theory of extracting MD from the autocorrelation function may no longer be valid and

requires further investigation. But there is a possible solution to this problem. Instead of real time monitoring, the AO measurement using a weaker focused ultrasound beam (< 250 kPa) can interleave the HIFU therapy to prevent the nonlinearity and saturation of the autocorrelation function.

It has also been shown that when the optical properties of the medium are similar to those of realistic tissue, the AO method can only improve the penetration depth of conventional optical methods marginally and the AO signal also suffers from poorer signal to noise ratio. This means that the AO method may only monitor lesions that are located near to the SFR.

8.1.4 Acousto-Optic Detection in Cylindrical Tissue Mimicking Phantom

It has been shown that pulsed-wave ultrasound can be used with the digital correlator setup to detect the AO signal as shown in Figure 7-9. Pulsed-wave ultrasound and time-gated detection allow higher ultrasound power to be used while still complying with safety regulations. Similarly, higher optical source power can potentially be used by time-gated illumination. Furthermore, for a given geometry of a medium and a location of FUR, there is an optimal position for the optical probes so that the optimal AO signal can be readily detected as is shown in Figure 7-13. This is influenced by the overlap region between the photon path length distribution and the FUR, which is verified by the spatial sensitivity maps in chapters 5 and 6.

However, the measurement of the digital correlator requires additional post processing so that the detection of pulsed-wave AO signal is feasible. This is because the time-gating detection creates distortion to the autocorrelation function.

8.2 Future Work

8.2.1 Verification of the Sensitivity Maps by Computer Simulations

The spatial sensitivity maps were mapped experimentally and should be verified by computer simulation, which is currently under development within our group. Therefore in the future, the sensitivity maps can be fully validated.

8.2.2 Acousto-Optic Spatial Sensitivity Mapping in a Multi-Layered Geometry

The spatial sensitivity maps are generated using homogeneous single layer phantom as background medium. However, the human tissue has complex heterogeneous structure that consists of multiple layers of different mechanical and optical properties. It has been shown that the skin and the subcutaneous fat layer [Niwayama 2000, Van Beekvelt 2001, Ferrari 2004] can affect the NIRS measurement in muscle study that requires correction. In brain measurement, the light penetration is severely affected the skull and the layer of cerebral spinal fluid as depicted in Figure 2-5. Therefore it will be helpful to repeat the AO studies described in this thesis for a more complex geometry.

The phantoms described in Figure 5-4 can be easily modified to incorporate more layers. One layer of clear silicone can be used to simulate the layer of the cerebral spinal fluid. Additional layers for the skull and skin can be substituted by resin and PVA gel phantoms respectively, whose optical properties can be readily matched. The AO measurement described in chapter 5 and 6 can be repeated to demonstrate whether the AO method can still probe a ROI beyond the additional layers using the modified phantom design, which is depicted in Figure 8-1.

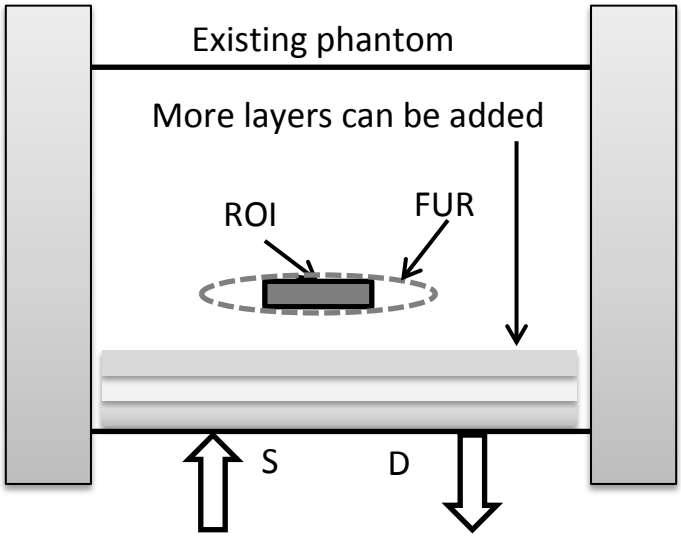

Figure 8-1 Existing phantoms can be readily modified to simulate multi-layers model

It has been shown that the pressure contrast AO imaging technique [Lai 2009] can provide a localised measurement of the local optical property within a turbid medium. The performance of this method can be further investigated by mapping its spatial sensitivity. The same experimental setup and procedures used in chapter 5 and 6 can be utilised with some minor modifications.

8.2.3 **Acousto-Optic Sensing**

It has been shown that the AO method can improve the conventional optical measurement based on the spatial sensitivity maps that are shown in chapter 5. The next step will be to use the AO method for a sensing application whereby the absorption changes occurs within and/or outside the predefined ROI; which is shown in Figure 8-2. The geometry of the phantom and the placement of the optical probes are shown in Figure 5-4 (a) in 5.1.2.1.This is carried out to investigate the variation of the AO measurement in response to the variation of the μ_a in the ROI in comparison to the I_{PC} measurement.

The ROI is placed slightly outside of the FUR, which is the AO optimal spot based on the AO spatial sensitivity map. The μ_a of the ROI can be varied from 0

to the level that is typically recorded in the muscle and the functional activation NIRS studies. The MD and I_{PC} measurement can then be plotted against the value of the μ_a.

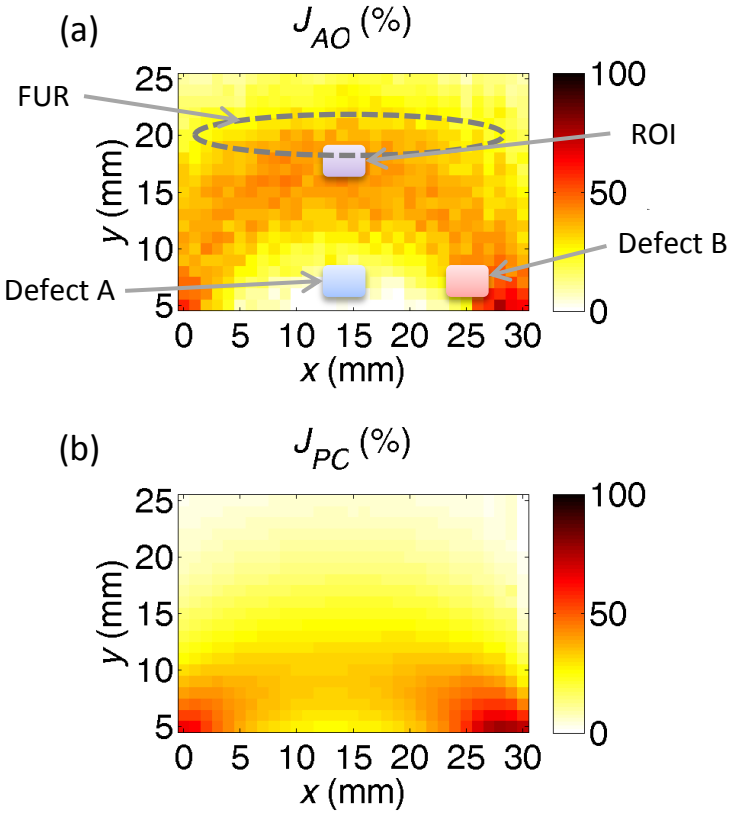

Figure 8-2 The reflection mode AO Sensing with a background μ_a = 0.0235 cm^{-1}: to study the effect of varying absorption in the ROI on: (a) AO and (b) I_{PC} measurements that are based on the absorption spatial sensitivity maps, which are shown in Figure 5-16.

The pattern of change observable by the AO and the I_{PC} measurements can be hypothesised to have the behaviours that are depicted in Figure 8-3. The initial baseline of the AO measurement shows the threshold of the minimum absorption coefficient μ_a^{AO} that the AO detection method can detect. Based on the spatial sensitivity map in Figure 8-2 (b), the threshold of the minimum absorption coefficient μ_a^{PC} of the I_{PC} measurement is expected to be significantly higher than μ_a^{AO}. The slope of the measurements is assumed to be linear in Figure 8-3, the

relationship of the change in μ_a and the AO measurement can be verified by this study.

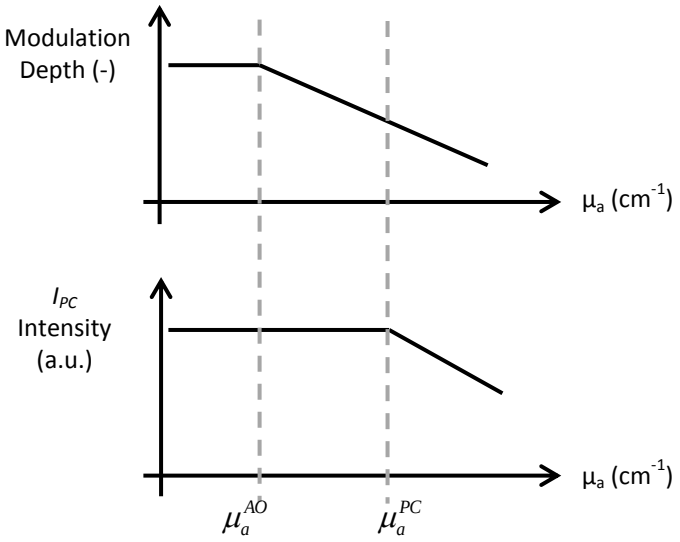

Figure 8-3 Hypothesised behaviour of the MD and I_{PC} measurement when the μ_a in the ROI varies whereby μ_a^{AO} and μ_a^{PC} are the minimum threshold of absorption coefficients of the AO and I_{PC} measurements respectively.

The same experiment can be repeated for optical defects that occur in regions near the SFR, which are the depicted Defect A and the Defect B in Figure 8-2 (a). According to the results in chapter 5, the Defect A should have small effect on the AO measurement while very significant changes can be expected from the I_{PC} measurement. The Defect B is located very close to the optical detector therefore its presence should have severe effects on both AO and I_{PC} measurement. However, the performance of the different schemes can be further assessed by analysing the rate of change in the detected signal in contrast to the change in absorption. The results of this study will then clearly demonstrate the strength of the AO measurement in comparison to the I_{PC} measurement.

The phantom design for this sensing study is relatively straightforward. The background medium can be built using the silicone rubber that is doped with appropriate amount of the NIR dye and titanium dioxide for the desired optical

property. The hollow parts, which are to contain the inclusions for the ROI and the defects, can be easily achieved by incorporating metal rods in the mould for the silicone rubber. Mixture of diluted Intralipid solution and the NIR dye can be used to achieve the varying μ_a in the ROI and in the defects.

8.2.4 Spatial Sensitivity of Acousto-Optic Detection by Parallel Detection Methods

The AO detection method used in this project is the single detector method, which is less robust in comparison to the multiple detector methods that are becoming the norm in the UOT studies. Therefore, it is useful to compare the performance of different AO detection methods in order to identify the best detection scheme for AO sensing. The performance parameter should not be just the signal to noise ratio of the AO signal but also the localisation capability, which can be informed by the spatial sensitivity maps.

However, in order to map the spatial sensitivity of the other parallel AO detection methods, which are sensitive to the decorrelation time of phantom, a more suitable phantom is required. The photon counter and digital correlator setup has very high sampling rate so it is insensitive to even the fastest decorrelation time in tissue (in micro-seconds). However, the phantoms described in this thesis are not suitable for the multi-phase [Leveque 1999] and the speckle contrast [Li 2002] detection methods because the decorrelation time of these phantoms is shorter than the optimal exposure time [Boas 2010] of the CCD camera. The result of an experiment to demonstrate the loss of AO localisation is shown in Figure 8-4.

The experimental setup is discussed in section 5.1 for the transmission mode measurement. However, the AO detection method used was the detection of the ultrasound modulated speckle contrast using a CCD camera. The exposure time of the CCD camera was 5 ms to ensure adequate light detection, but it was considerably longer than the decorrelation time of the phantom, which was 8 μs (Figure 4-21). The CCD images were taken when the ultrasound was off and on (same ultrasound excitation parameter described in section 5.1). The MD is

proportional to the difference in the image speckle contrast when the ultrasound is on and off [Li 2002, Kothapalli 2007]. The sensitivity was computed by the method discussed in section 5.1.5.1.

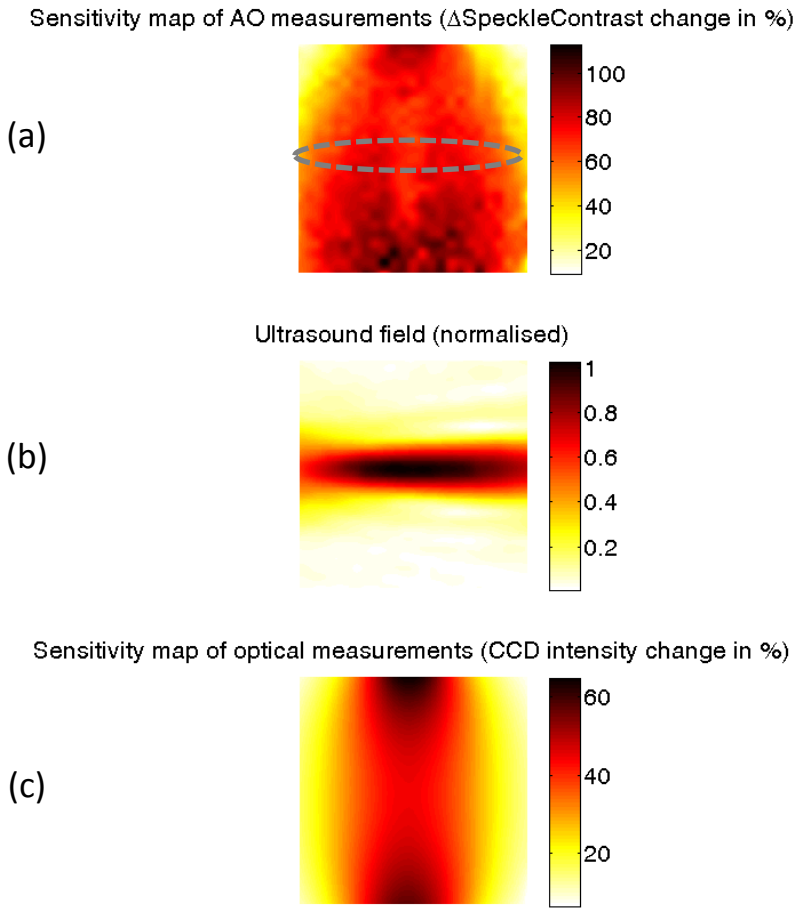

Figure 8-4 The loss of AO localisation because the decorrelation time of phantom is faster than the detector's sampling rate. The absorption spatial sensitivity map of: (a) the AO measurement by the CCD speckle contrast and (c).I_{CCD} measurement in a transmission mode with minimal background absorption (μ_a = 0.0235 cm^{-1}); (c) shows the location of the FUR. (dashed line: FUR)

The phantoms used in this thesis are suitable for other parallel detection methods that are insensitive to speckle decorrelation, such as the photo-refractive crystal [Murray 2004] or the spectral hole burning [Li 2008] methods. Therefore, by using the spatial sensitivity approach, the best detection scheme for AO sensing

can be identified. Furthermore, the strengths and limitations of each detection methods can be investigated.

8.2.5 Spatially-resolved Acousto-Optic Measurement

The spatially resolved measurement discussed in section 2.2.3 has been shown to be able to minimise the effect of a global optical change in the SFR [Wolf 2007]. This is because this global change in the SFR will affect all detectors similarly, thus it will not substantially affect the $\frac{\partial A_{SR}}{\partial \rho}$ measurement. It is hypothesised that the same method may be able to improve the performance of the current single detector AO system, which can further incorporate additional optical sources of different wavelength for sensing.

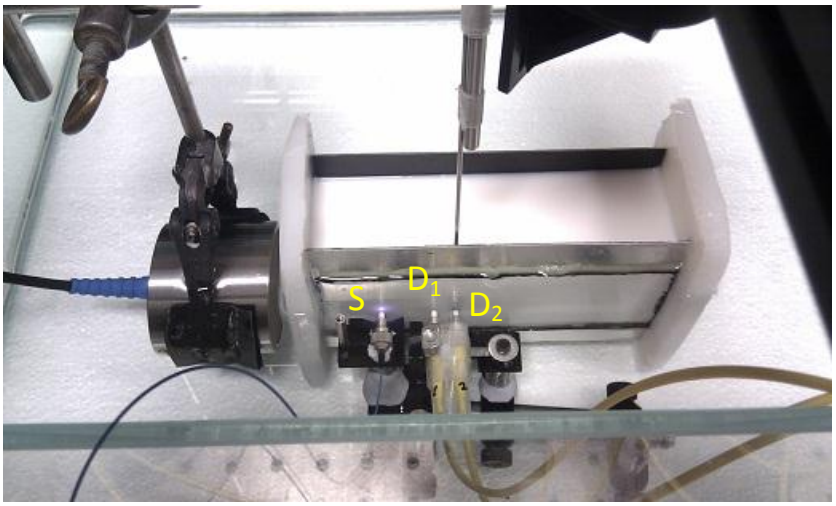

Figure 8-5 Spatially resolved AO measurement by using two optical detectors, the separations between S to D1 and D2 are 25 and 35 mm respectively.

In order to investigate this hypothesis, a preliminary study was conducted to map the absorption spatial sensitivity of the spatially resolved AO measurement. The experimental setup and procedures described in chapter 5 remained unchanged except an additional optical detector was added to channel B of the digital correlator (Figure 4-5), which is shown in Figure 8-5. The new single-mode fibres have a core diameter of 5 µm. The Labview program was modified to operate the

digital correlator in dual-autocorrelation mode and the spatial sensitivity of the AO and the I_{PC} measurements were mapped and are shown in Figure 8-6. The result shows that the attenuation gradient of the MD detected across two detectors is very noisy.

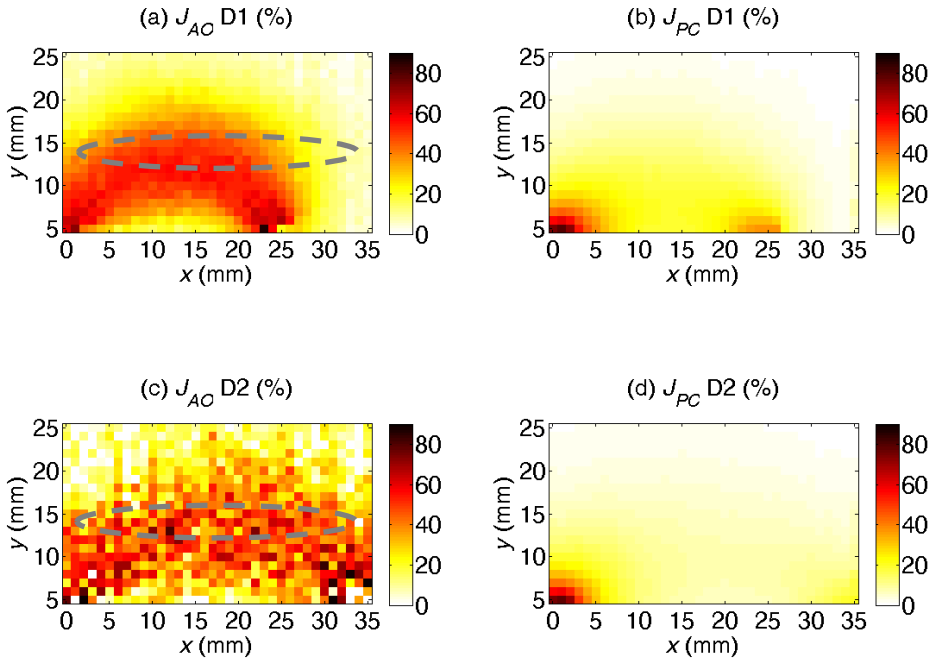

Figure 8-6 The absorption spatial sensitivity maps of the AO and I_{PC} measurements: (a)-(b) detector 1 (D1) and (c)-(d) detector 2 (D2) respectively when the background μ_a = 0.0235 cm^{-1} in reflection mode. (dashed line: FUR)

For example, the averaged J_{AO} of D1 and D2 is presented in Figure 8-7 (a). The $<J_{AO}>$ shows that the sensitivity in the regions close to the optical detectors in the SFR (x = 20-35 mm and y = 5 mm) is smaller in comparison to the same regions in Figure 8-6 (a) and (c) for a single detector configuration. The main limitation of this setup is the inadequate number of optical detectors and the large separation between the D1 and D2 (10 mm), which resulted in a very noisy J_{AO} for D2. The detectors spacing of 1-2 mm should be used. These results suggest that the use of multiple-detectors may allow more options in post processing so that AO signal detection can be optimised for AO sensing.

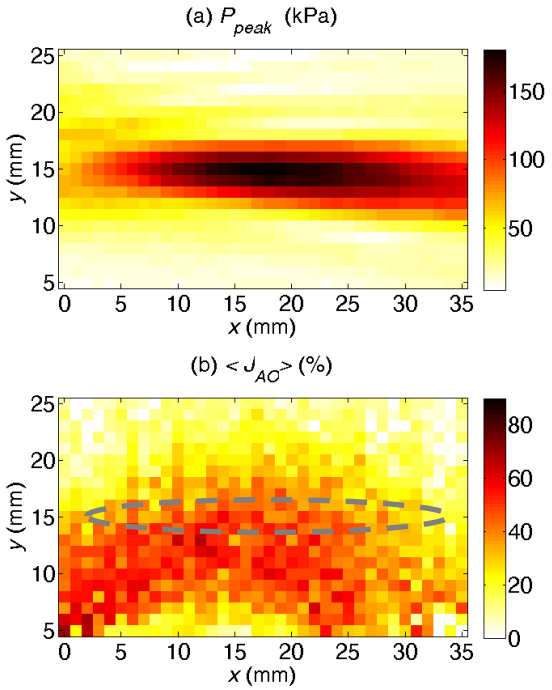

Figure 8-7 (a) The FUR (dashed line) and the averaged spatial sensitivity map $<J_{AO}>$.

8.3 Summary

An optical sensing method such as NIRS is widely used to measure muscle and cerebral oxygenation. However, the maximum penetration depth of this method is approximately 15 mm beneath the skin because light is strongly scattered in tissue. Optical measurements are also susceptible to the optical properties of the superficial layers of tissue such as the skin and fat. Furthermore, conventional optical measurement cannot probe a specific region of interest within tissue. It has been suggested that the AO method, which can "tag" diffused light in tissue by using focused ultrasound, can potentially improve the regional sensitivity of optical measurement. This thesis aims to verify this claim by mapping and comparing the AO and optical spatial sensitivity.

The phantom development and detection methods used in the mapping of the AO and optical spatial sensitivity are described in this thesis. The main limitation of

the digital correlator based AO detection scheme is that the peak pressure of continuous-wave ultrasound must not exceed 250 kPa for water-based and PVA gel phantoms in order to prevent the AO signal from becoming non-linear and saturated.

This thesis has demonstrated for the first time that the regional absorption and scattering sensitivity of the AO measurement is better than that of the optical measurement in a pre-defined region of interest, which is located deeper than 15 mm, and can be relocated by repositioning the focused ultrasound. This has been observed in both the experimental and preliminary simulation results. However, the location of high regional sensitivity (besides regions that are located near to the optical source and detector) depends on the optical sensitivity in the focused ultrasound beam. It has been shown that there is an improvement of approximately 10 mm in the maximum penetration depth of the AO method for an optical source and detector separation of 30 mm (reflection mode). The penetration depth of optical sensitivity can be improved by increasing the optical source and detector separation, and therefore the penetration depth of AO method as well, but at the expense of higher noise level.

The spatial sensitivity maps show that the AO method can minimise the effects of optical properties (absorption and scattering) changes in the superficial layer, which has been shown to strongly affect the optical measurements. This means that over the course of a continuous measurement, a localised optical property change in the superficial region (besides optical properties changes in the region of interest) has a smaller effect on the AO signal than the optical signal. However, localised changes in the superficial layer may slightly increase or decrease the AO signal depending on the location of the focused ultrasound. The proximity of the localised change to the focused ultrasound affects the magnitude of change to the ultrasound modulated intensity and un-modulated intensity differently.

For tissue oxygenation measurement, it is generally acceptable to assume only absorption changes to occur. In HIFU therapy monitoring, the HIFU lesions have

been shown to have considerably higher absorption and scattering. The results in this thesis show that, depending on the location of focused ultrasound, an increase in localised absorption may result in a reduction in the AO signal while an increase in localised scattering may increase the AO signal. Therefore, for potential HIFU lesions monitoring, careful positioning of the focused ultrasound and optical probes is required to ensure that an increase in both absorption and scattering would result in a reduction in the AO signal.

The thesis also demonstrated that there is an optimal position for a specific ultrasound and optical setup whereby the maximum AO signal can be measured for a cylindrical geometry, which mimics anatomical geometry. This optimal location is influenced by the overlap region between region of high optical sensitivity and focused ultrasound, which is also shown by the described spatial sensitivity maps. A new detection method has also been proposed based on the digital correlator for time-gated AO measurement so that higher output power of ultrasound and laser can be used without exceeding the safety limits.

A more comprehensive validation by computer simulation is required to provide a better understanding of the effect of localised optical property change in the AO spatial sensitivity. The thesis has only described a single source and detector AO detection scheme. The spatial sensitivity approach can be used in future investigation to identify the most suitable detection scheme for AO sensing, that can also incorporate multiple optical sources of different wavelength and detectors. The spatial sensitivity maps shown are the result of a localised optical property change in a single layer medium, which is not realistic. Future AO sensing study should include multiple localised changes in “key” regions in a multi-layered medium, which has been identified in this thesis, such as the superficial region, region of interest and regions near the optical source and detectors.

9 Appendix: Summary of Acousto-Optic Experimental Studies

9.1 Methods

The different experimental setups (setups A-E) are shown in section 9.3.

Reference	Purpose	Set-up	Optical Detector	Ultrasound	Conclusion	Suggestions/Extra Notes
[Leutz 1995]	Proof of basic AO concept	A	PMT	2.17 (autocorrelation measurement) & 27.3 MHz (Interferometric measurement) continuous wave	Ultrasound-modulated G_1 (analytical model & experimental result). Interferometric measurement did not fit analytical model well	Use of the Raman-Nath to calibrate ultrasound parameters
[Wang 1995]	Tomography	A	PMT	1MHz (continuous-wave)	2D image of absorbing cube, ac different between black & blue sphere, claim rubber works too	
[Kempe 1997]	Tomography	A	Photo-diode	3.4MHz (50us pulse)	In the case of breast cancer imaging, not good enough S/N noise, importance of coherence area	coating sample with light reflecting material to increase intensity in tissue to improve signal to noise ratio
[Wang 1997]	Tomography	A	PMT	1MHz (continuous-wave)	Use of incoherent light source was not detected. The scatterer displacement dominated but must include modulation of refractive index to path length modulation (phase) --> coherent mechanism dominates	3 mechanism: light intensity modulation - optical properties modulation [incoherent modulation] (density, compressibility changes), particle displacement due to US modulation, Doppler shift.

[Wang 1998]	Tomography	A	PMT	chirp frequency sweep 7-10MHz (rate: 297MHz)	fast scanning compared to single acoustic frequency	wide-bandwidth = poor signal to noise ratio
[Leveque 1999, Leveque-Fort 2001]	Tomography	B	CCD & PMT	2.2MHz (Pressure <101.3kPa) & 2.3MHz	parallel processing of multiple speckle grains	simulation detection of more coherence area (speckle grains) better signal, ccd frame rate: 200Hz, average of multiple frames
[Lev 2000]	AO detection in reflection mode	C	fibre-coupled PMT	1.25MHz	Demonstration of AO detection in reflection mode	distance between optical probes : 19mm
[Lev 2002]	Tomography	C	fibre-coupled PMT	1MHz	AO in reflection mode and estimation of the of mean transport length by using 2 different optical sources	absorption is estimated provided that the scattering length is known
[Selb 2002]	Tomography	A	CCD	3MHz (pulses of 2x acoustic wavelength)	demonstration of 2nd acoustic harmonics modulation of multiple scattered light	claim to yield better contrast due to smaller ultrasound modulation zone
[Li 2002]	Tomography by Speckle Contrast	D	CCD	1MHz (peak pressure 0.1MPa)	Demonstration of AO tomography by speckle-contrast and it is superior to optically only speckle-contrast technique as it can detect buried strongly-absorbing objects	
[Forget 2003]	Tomography	A	CCD	1-3MHz chirp (peak pressure at FUR - 1MPa)	more refinement required to acquire depths information	detection with an additional zoom lens
[Lev 2003]	Tomographic photon density in turbid medium	C	fibre-coupled PMT	pulsed-wave of fundamental freq. 1.25MHz, 4 cycles and reprate:19kHz - peak pressure 0.25MPa	use of phase-synchronized ultrasound pulses to demonstrate AO signal in reflection mode	pulsed-wave parameters used is similar to US Doppler

[Lev 2003]	Tomography	C	fibre-coupled PMT	1.08MHz	Speckle noise is the main contribution of poor SNR in static phantom experiments, can be improved by increasing integration time or increasing number of optical detectors	distance between fibre:25mm, experiment also involves different fibre core sizes
	In vivo imaging	REFLECTION		1.25MHz (64us pulse length, rep-rate:39kHz)	in vivo demonstration of acousto-optic (1-D mapping of ultrasound modulated light signal)	
[Li 2003]	Tomography	D,E	CCD	1MHz, peak pressure - 0.1MPa	AO tomography for biological tissue of thickness up to 5cm demonstrated	side-by-side detection scheme
[Li 2004]	Tomography	D	rotational-CCD	1MHz	the rotational CCD is behaving like CT scanners	
[Murray 2004]	AO signal detection using photorefractive-crystal	A	APD & photorefractive-crystal	1MHz (20cycle - pulsed-wave) at peak pressure 0.4MPa	Photorefractive-based detection scheme is insensitive to speckle decorrelation (if crystal response time is faster) and provides high optical *entendue* (as compared to CCD-based parallel detection	Relatively simpler electronics compared to CCD-based systems
[Sakadzic 2004]	Tomography	B	APD	pulsed 15MHz - 3.9MPa	demonstration of high resolution AO tomography (depth few millimetres)	interferometry method
[Bossy 2005]	Combined photorefractive-crystal AO & Ultrasound imaging	A	APD & Ultrasound scanner	pulsed 5MHz medical scanner	AO detection using photorefractive-crystal can differentiate optically different but mechanically similar structures in turbid medium.	Potential of co-registration of images using both AO and medical ultrasound scanner
[Lev 2005]	Physiological Measurement	C	PMT-photon-counter & Dual-x-ray	pulsed 1.24MHz (4cycles, repetition rate: 40kHz)	Demonstration of the use of Acousto-optic in physiological measurement	There are correlation between AO data and dual-x-ray-absorption data

			absorption scanner			
[Kim 2006]	Tomography	D	CCD	intense ultrasound burst 1MHz (1.5MPa) 8ms bursts	Intense burst of ultrasound provided better SNR compared to weak continuous-wave ultrasound, which in turn could reduce scanning time as well.	comparison to continuous and quasi- continuous wave ultrasound
[Devi 2006]	Effects of elasticity on AO signal	A	fibre-coupled PMT and digital correlator	plane 1MHz (80.6kPa)	MD is affected by both optical and mechanical properties (elasticity) of medium. Use of absorption map for tomographic application must be corrected by a corresponding map of storage modulus	use of pmt with digital correlator
[Zemp 2006]	AO Speckle-contrast Tomography	D	CCD	1MHz & 3.5MHz (2ms of burst at 1Hz repetition rate)	The speckle intensity changes is predicted by a stochastic model	Peak acoustic pressure above 0.1MPa may bend the light path (phase-based AO mechanisms assume straight path)
[Kim 2007]	Multi-wavelength AO tomography	D	CCD	1MHz (<1.9MPa) 1Hz of 2ms pulsed-wave	demonstrated the feasibility of functional AO tomography by estimating dye concentrations and ratios	potentially can be improved to measure oxygenation and total haemoglobin concentration
[Kothapalli 2007]	AO Tomography of optically scattering objects	D	CCD	1MHz (peak pressure 1.5MPa) of 2ms bursts	Demonstration of AO tomography of objects with different absorption and scattering coefficients	Contrast changes due to ultrasound is higher when the scattering coefficient is higher
[Xu 2007]	AO Tomography using photorefractive-crystal	D	PMT & photorefractive-crystal	1MHz (peak pressure 1.5MPa) of 1ms bursts at 100 Hz burst rate	The acoustic radiation force effect can be detected on top of the optical properties	Use of vibration block enclosure

[Zemp 2007]	AO Tomography using different intense ultrasound bursts	D	CCD	1MHz of 0.2-20 ms of bursts	Higher acoustic pressure causes higher localised displacement resulting in better AO signal, however it requires camera exposure to be synchronised	Poor spatial resolution at higher acoustic peak pressure (≥2MPa). Time-gating of light capture to avoid the destructive shear waves front
[Bratchenia 2008]	AO Spectroscopic measurement of local absorbance	A	CCD	5MHz (focal zone 1mm) of 1μs intense burst (7MPa) at 25kHz repetition rate	The amount of local absorbance correlates to the AO signal, further verified by Monte Carlo simulation. Use of the Beer-Lambert law to the MDs (as a function of μ_a). Use of multi-wavelength approach can further improve the detection	The use of very short pulse of ultrasound results in few mm of penetration depth.
[Rousseau 2008]	AO Tomography with powerful long laser pulse	A	Photorefractive interferometer	4.35MHz pulsed-wave (10 cycles)	A powerful laser source increases the amount of light propagating through the ultrasound focal region resulting in increase of modulated photons.	Such approach also reduces the negative effects of speckle decorrelation of turbid medium
[Li 2008]	AO Tomography with spectral hole burning	D	Si Photodetector	5 MHz pulsed-wave (2 cycles) of peak pressure 4.3 MPa	Both theoretical model and experimental results are presented. Spectral hole burning suppresses the un-modulated photon (also speckle decorrelation) so the AO signal detection is greatly improved	Complex instrumentation i.e. Spectral-hole-burn crystal requires cooling to 4 K and the optical filters has a lifetime of 4 ms.
[Devi 2008]	AO detection (using 2 different alignment between optical source and ultrasound beam)	A & REFER TO PAPER	Photon-counting PMT	1MHz continuous-wave (peak pressure 0.2MPa)	Comparison of AO signal detection when the optical source propagating direction is the same as ultrasound wave direction and (a).	It shows potential to map both the mechanical and optical properties of medium

[Bratchenia 2009]	AO multi-wavelength quantitative measurement	A	CCD	2.25 MHz (1µs bursts at 30 kHz repetition rate), peak pressure 1.5MPa	Demonstration of quantitative measurement of total absorbers concentration using AO technique. The change in local absorption is estimated from a model, which is based on exponential Beer-Lambert law. The model also proposes the use of *normalised MD*, where a measured MD is normalised to the modulation of depth where there are no absorbers.	The model assumes homogeneous scattering throughout the turbid medium and relies on Monte Carlo simulation to estimate the mean light path within the ultrasound focal region. Also [Bratchenia 2011] and use of sensitivity functions to reconstruct absorption maps [Bratchenia 2011]
[Lai 2009]	Pressure Contrast AO imaging	A	Photorefractive crystal	Pulsed ultrasound 1.1 MHz (2 mm by 9 mm) at 0.3 and 1.5 MPa	The pressure contrast signal (ratio of the AO signal using two different acoustic pressure) is found to be only depended on the pressures and the local optical property	The PCS is nearly the same for localised scattering change and homogeneous phantom.
[Draudt 2009]	AO imaging of HIFU lesions	A	Photorefractive crystal	HIFU: 1.1MHz (peak pressure: +6MPa, -4.32MPa) AO: 5MHz pulsed	AO imaging of HIFU lesions, which is not visible on standard ultrasound scanner.	Potential of using HIFU as the AO ultrasound source to for combined ablation therapy and AO tracking of HIFU lesion.
[Li 2010]	Use of Amplitude Modulated Ultrasound and AO	A	CCD speckle contrast	Amplitude-modulated ultrasound at 5 MHz of peak pressure: 0.318-1.27 MPa	Low frequency amplitude modulated ultrasound can improve the AO signal but require higher CCD exposure time	Effect of shear waves can be observed and minimised [Li 2011]
[Yuan 2010]	Ultrasound modulated fluorescence	A	PMT	CW 1MHz	Use of ultrasound modulated fluorescence is demonstrated.	Potential improvement by use of microbubbles

[Lai 2011]	Real-time monitoring of HIFU lesion using AO method	A	Photorefractive crystal	Pulsed-wave (50% duty cycle) of peak pressure 9.5 MPa	Real time monitoring of the formation of HIFU lesions is shown and the intense acoustic pressure amplified the AO signal substantially. AO signal showed reduction and correlated to the size of lesions. Passive HIFU monitoring and B-mode imaging did not detect any changes	However, sample used is degassed to prevent formation of bubbles.

Table 9-1 Summary of the AO studies in the literature

9.2 Phantom

Reference	Wavelength (nm)	Phantom					
		Medium & Target					Additional Target/Notes
		Material	μ_s` (cm^{-1})	μ_s (cm^{-1})	g	μ_a (cm^{-1})	
[Leutz 1995]	514	0.25um polystyrene beads, DI water in a glass cell (5x20mm)	autocorrelation: 13-4 interferometer: 90-588				
[Wang 1995]	632.8	(579±21)nm polystyrene spheres, Trypan blue dye & DI water in a cuvette (150x100x150mm)		2	0.853	0.01	black/blue cube/sphere glass bead (8.8*8.8*7.9mm) + rubber cube
[Kempe 1997]	514.5 (collimated to 6mm)	single block of latex colloid in water tank (0.48µm latex spheres)	1.2-7.87				5mm black teflon sphere
[Wang 1997]	632.8	5 cm thick gel tissue phantom: Trypan blue dye, Intralipid 5% (tomography)	intensity study: 10 depth study: 6.2		0.8	0.1	5mm gel cube, μ_a=1.1cm^{-1}, μ_s'=10cm^{-1}
[Wang 1998]	633nm (collimated to 15 mm)	clear water and 2 turbid media		0.16	0.73		8.4×1.6mm (rubber in clear water and turbid1),
				0.21	0.73		
[Leveque 1999, Leveque-Fort 2001]	780	10 & 20 mm thick of turkey breast between 2 glass plates (10x40x40mm)					buried in turkey: cylindrical modelling clay d:3mm, l:6mm) & 10mm-cube of black paint, turkey breast

							tissue pressed between 2 cylindrical disk (25mm)
[Lev 2000]	690	80mm cube of agar gel (98% water & Intralipid)	17.5			0.05	cylindrical target(d:9mm, l:10mm) of agar and carbon black
[Lev 2002]	690	diffusive gel & Pelican 4001 dye	17.5			0.05	
	690 & 820	gel: 2% unclear agar, 1% Intralipid, 0.5% human blood					
[Selb 2002]	840	water gel phantom: 10% gelatin, 4% agar, 0.16% latex spheres (220nm) by weight	2				
[Li 2002]	690	15-25mm thick skinless chicken breast with buried soft rubbers (1.9 & 2.1 x3.1x10mm) & chicken gizzards (2x3x8 & 10 mm)					
[Forget 2003]	835nm	200ml phantom [rectangular parallelepipeds : 30mm wide face, thickness 10-30mm] of gelatin(20g), agar(6g), 220nm latex spheres(6ml)	2				same material (20mm thickness) with added black ink (4x2mm)
[Lev 2003]	690	clear silicon elastomer & 193nm Titanium Dioxide	15				
[Lev 2003]	785	ethylene glycol (index-matching gel) for contact & 80mm cube of agar gel of 98% H2O + Intralipid 1% + dye	17			0.05	agar gel under mouse, water spacer between ultrasound transducer and arm for coupling
[Li 2003]	786	chicken breast of 40-50mm thickness					soft rubber buried within chicken breast
[Li 2004]	690	14mm-thick chicken breast					8x3x3mm chicken blood

	(collimated to 20 mm)						buried & turkey muscle
[Murray 2004]	(1064)(frequency-doubled)	43x43x29mm transparent poly-acrylamide gel & 0.4µm polystyrene microspheres	6				10x10x8mm of the background medium with added ink (μ_a=4.6cm^{-1})
[Sakadzic 2004]	532 (100mW - pulsed)	3-3.2mm (radius) chicken breast					100 µm thick black latex
[Bossy 2005]	(1064)(frequency-doubled)	40x40x27mm transparent poly-acrylamide gel & 0.4µm polystyrene microspheres	10				2x2x8mm & 3x3x8mm targets of the background medium with added ink (μ_a=4.6cm^{-1})
[Lev 2005]	830	healthy (higher attenuation) & osteoporotic (lower attenuation) wrists (bone)					ultrasound 20x90mm gel pad (Aquaflex Parker) for contact,
[Kim 2006]	532	10% gelatin & 10% cornstarch	9				Trypan blue coated object (2.1*2.6*17 & 2.3*2.5*17mm)
[Devi 2006]	632.8	30x10x30mm poly-vinyl alcohol (PVA) gel phantom with ink in water tank	14.41-45			0.0025-0.5	
[Zemp 2006]	532	20mm-thick slab phantom of 10% gelatin & 10% cornstarch	9.2				
[Kim 2007]	633	20 mm thick : 10% gelatin, 10% cornstarch phantom with red & blue inks targets (of 2.2 x 2.2 x 11 mm made of 10% gelatin) of different concentrations	9			red: 2.2 blue: 11.9	
	657					red: 1 blue: 5.2	

[Kothapalli 2007]	532	20x20x100mm slab of gelatin, water & Intralipid with buried multiple scattering objects (2x2x20mm)	background: 10 objects: 0.5-30			0.1	additional highly absorbing object (2x2x20mm) (same as background μ_s'=10cm^{-1} & blue ink μ_a=100cm^{-1})
[Xu 2007]	532	100x40x100 phantom of 10% porcine gelatin & 1% Intralipid and chicken breasts with buried chicken gizzards	10 (background)				10% cornstarch & segments of nude mouse tails
[Zemp 2007]	532	10% gelatin & 10% corn starch and use of absorbing (Trypan blue) targets	9.2				
[Bratchenia 2008]	633	15x45x40mm Perspex container filled with Intralipid in an agar matrix	15				3mm (inner diameter) silicone tubing with solid Intralipid (mix of Intralipid and ink of μ_a=0.5-16cm^{-1})
[Rousseau 2008]	1064 (200mW) 530 µs pulse at 25 Hz repetition rate	liquid phantom of thickness 30-60 mm: sunflower oil & TiO_2 (0.41 µm) target: thin polyester (Mylar) tube (d:4.3 & 5.3mm & wall thickness: 12.7µm) of the same background solution and carbon black				0.032	30-60mm thick of chicken breasts & black rubber
[Li 2008]	793 (20µs pulse of 500mW)	50x50x10mm phantom of 10 porcine gelatin and 1% Intralipid & 2.8x1.3x0.8 mm absorbing object dyed with black ink	7				0.85mm cube absorbers. Xu et al. [Xu 2010] used thicker sample and improved filtering
[Devi 2008]	632.8	50x50x20mm PVA phantom (storage modulus G'=11kPa) 6mm cube of object 1 (G'=51kPa)	1.8 5		0.89	0.0025 0.0025	6mm cube object 3 of combined (μ_s'=5cm^{-1}) & (u_a=0.06cm^{-1}) objects;

		6mm cube of object 2 (G'=11kPa)	1.8			0.44	6mm cube object 4 of combined object 1 & 2
[Bratcheni a 2009]	514 & 633 (1µs pulses)	Intralipid solution and agar matrix in a 15x45x40 mm / 20x45x40 mm Perspex tank with 3 mm internal diameter tubing(s) with the same solution and ink	both: 15			tubing: 0-15	The depth (position) of tubing(s) is varied.
[Lai 2009]	1064	Polyacrylamide gel phantom with 0.75 µm polystyrene microspheres (7 phantoms 40x25x40mm)	4-10			water	Inclusions μ_s': 5 & 7 and background μ_s': 6
[Draudt 2009]	1064	40x40x20mm of chicken breast degassed (40min) in phosphate buffered saline					
[Li 2010]	532 (100 mW)	93.5x43x20mm of 1% agar matrix (young's modulus: 25 kPa) and 0.4% Intralipid solution	5			water	[Li 2011] included black inclusions of different stiffness (Young's moduli of 25 kPa and 42.3 Pa)
[Yuan 2010]	532	40x115x115mm of Intralipid solution	7.8				Fluorescent tubing contained rhodamine B aqueous solution (0.1 mg/ml)
[Lai 2011]	1064	50x50x15-30 mm chicken breast sample, which was degassed in 1% phosphate buffered saline solution for 3 hours					Background water was also degassed.

Table 9-2 Summary of the phantoms used in the AO studies in the literature.

9.3 Experimental Setup

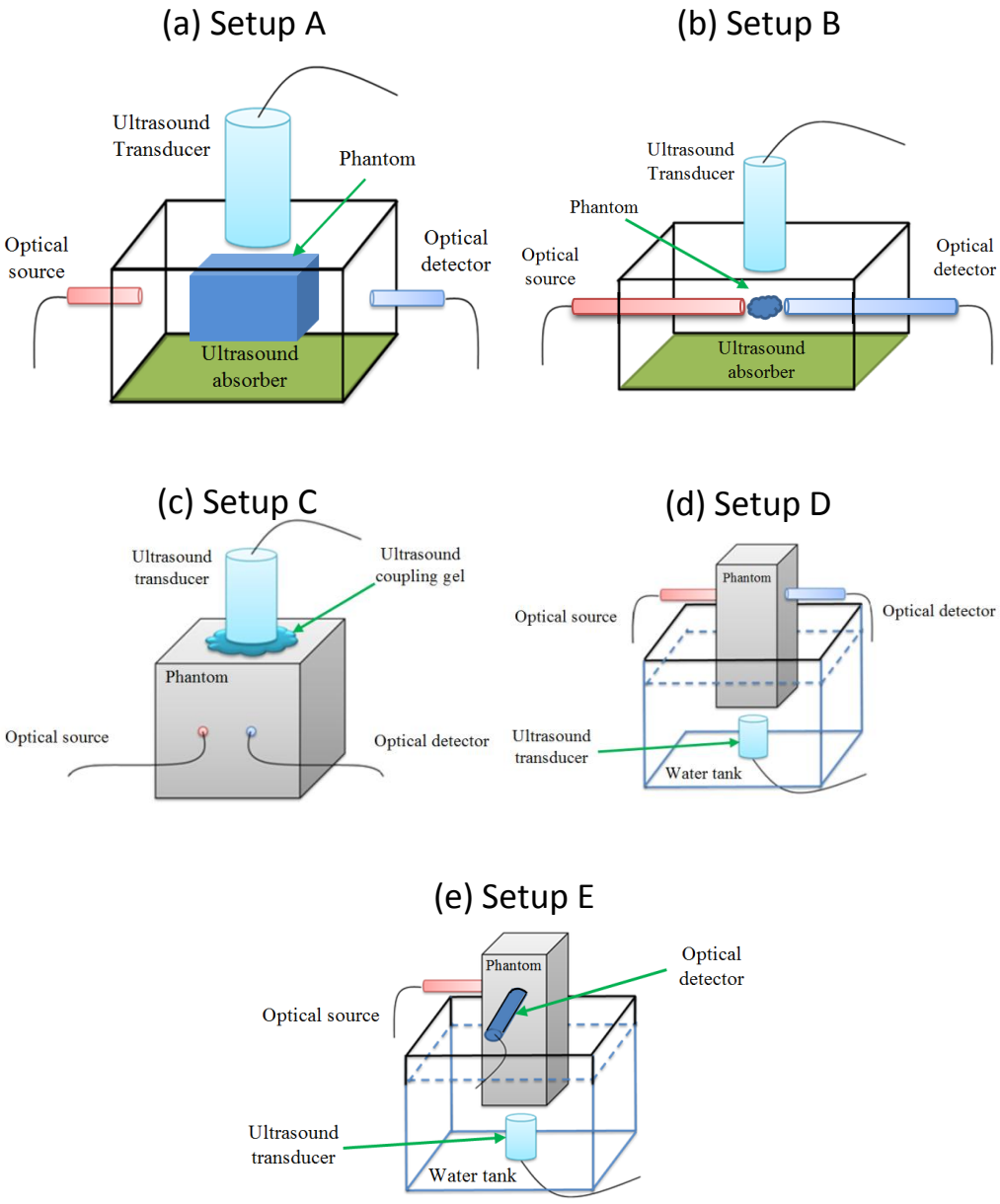

Figure 9-1 Summary of the different experimental setups in the AO studies in the literature

10 References

Alerstam, E., Svensson, T. and Andersson-Engels, S. (2008). "Parallel computing with graphics processing units for high-speed Monte Carlo simulation of photon migration." Journal of Biomedical Optics **13**(6): 060504.

Arridge, S. R., Schweiger, M., Hiraoka, M. and Delpy, D. T. (1993). "A finite element approach for modeling photon transport in tissue." Medical Physics **20**(2 I): 299-310.

Arridge, S. R. (1995). "Photon-measurement density functions. Part I: Analytical forms." Appl. Opt. **34**(31): 7395-7409.

Arridge, S. R. and Schweiger, M. (1995). "Photon-measurement density functions. Part 2: Finite-element-method calculations." Appl. Opt. **34**(34): 8026-8037.

Arridge, S. R. (1999). "Optical tomography in medical imaging." Inverse Problems **15**(2).

Bal, G. and Schotland, J. C. (2010). "Inverse scattering and acousto-optic imaging." Physical Review Letters **104**(4).

Barbour, R. L., Graber, H. L., Xu, Y., Pei, Y., Ansari, R., Levin, M. B. and Farber, M. (2006). Diffuse optical tissue simulator (DOTS): an experimental calibrating system for functional DOT imaging. Fifth Inter-Institute Workshop on OpticalDiagnostic Imaging fromBench to Bedside at the National Institutes of Health.

Barnett, S. B., Ter Haar, G. R., Ziskin, M. C., Rott, H. D., Duck, F. A. and Maeda, K. (2000). "International recommendations and guidelines for the safe use of diagnostic ultrasound in medicine." Ultrasound in Medicine and Biology **26**(3): 355-366.

Beard, P. (2011). "Biomedical photoacoustic imaging." Interface Focus **1**(4): 602-631.

Blonigen, F. J., Nieva, A., DiMarzio, C. A., Manneville, S., Sui, L., Maguluri, G., Murray, T. W. and Roy, R. A. (2005). "Computations of the acoustically induced phase shifts of optical paths in acoustophotonic imaging with photorefractive-based detection." Applied Optics **44**(18): 3735-3746.

Boas, D. A. and Yodh, A. G. (1997). "Spatially varying dynamical properties of turbid media probed with diffusing temporal light correlation." Journal of the Optical Society of America A: Optics and Image Science, and Vision **14**(1): 192-215.

Boas, D. A. and Dale, A. M. (2005). "Simulation study of magnetic resonance imaging-guided cortically constrained diffuse optical tomography of human brain function." Applied Optics **44**(10): 1957-1968.

Boas, D. A. and Dunn, A. K. (2010). "Laser speckle contrast imaging in biomedical optics." Journal of Biomedical Optics **15**(1): 011109.

Bonner, R. and Nossal, R. (1981). "MODEL FOR LASER DOPPLER MEASUREMENTS OF BLOOD FLOW IN TISSUE." Applied Optics **20**(12): 2097-2107.

Bossy, E., Sui, L., Murray, T. W. and Roy, R. A. (2005). "Fusion of conventional ultrasound imaging and acousto-optic sensing by use of a standard pulsed-ultrasound scanner." Opt.Lett. **30**(7): 744-746.

Bratchenia, A., Molenaar, R. and Kooyman, R. P. H. (2008). "Feasibility of quantitative determination of local optical absorbances in tissue-mimicking phantoms using acousto-optic sensing." Applied Physics Letters **92**(11).

Bratchenia, A., Molenaar, R., van Leeuwen, T. and Kooyman, R. P. (2009). "Millimeter-resolution acousto-optic quantitative imaging in a tissue model system." Journal of Biomedical Optics **14**(3): 034031.

Bratchenia, A., Molenaar, R. and Kooyman, R. P. H. (2011). "Towards quantitative acousto-optic imaging in tissue." Laser Physics: 1-7.

Bratchenia, A., Molenaar, R., Van Leeuwen, T. G. and Kooyman, R. P. H. (2011). "Acousto-optic-assisted diffuse optical tomography." Optics Letters **36**(9): 1539-1541.

Briers, J. D. (1996). "Laser Doppler and time-varying speckle: A reconciliation." Journal of the Optical Society of America A: Optics and Image Science, and Vision **13**(2): 345-350.

Briers, J. D. (2001). "Laser Doppler, speckle and related techniques for blood perfusion mapping and imaging." Physiological Measurement **22**(4).

Bruce, N. C. (1994). "Experimental study of the effect of absorbing and transmitting inclusions in highly scattering media." Applied Optics **33**(28): 6692-6698.

Buchheit, M., Laursen, P. B. and Ahmaidi, S. (2009). "Effect of prior exercise on pulmonary O2 uptake and estimated muscle capillary blood flow kinetics during moderate-intensity field running in men." Journal of Applied Physiology **107**(2): 460-470.

Buckley, E. M., Cook, N. M., Durduran, T., Kim, M. N., Zhou, C., Choe, R., Yu, G., Shultz, S., Sehgal, C. M., Licht, D. J., Arger, P. H., Putt, M. E., Hurt, H. and Yodh, A. G. (2009). "Cerebral hemodynamics in preterm infants during positional intervention measured with diffuse correlation spectroscopy and transcranial Doppler ultrasound." Optics Express **17**(15): 12571-12581.

Calderon-Arnulphi, M., Alaraj, A., Amin-Hanjani, S., Mantulin, W. W., Polzonetti, C. M., Gratton, E. and Charbel, F. T. (2007). "Detection of cerebral ischemia in neurovascular surgery using quantitative frequency-domain near-infrared spectroscopy." Journal of Neurosurgery **106**(2): 283-290.

Calle, S., Remenieras, J. P., Matar, O. B., Hachemi, M. E. and Patat, F. (2005). "Temporal analysis of tissue displacement induced by a transient ultrasound radiation force." Journal of the Acoustical Society of America **118**(5): 2829-2840.

Carp, S. A., Dai, G. P., Boas, D. A., Franceschini, M. A. and Kim, Y. R. (2010). "Validation of diffuse correlation spectroscopy measurements of rodent cerebral blood flow with simultaneous arterial spin labeling MRI; towards MRI-optical continuous cerebral metabolic monitoring." Biomed Opt Express **1**(2): 553-565.

Carp, S. A., Roche-Labarbe, N., Franceschini, M. A., Srinivasan, V. J., Sakadži , S. and Boas, D. A. (2011). "Due to intravascular multiple sequential scattering,

Diffuse Correlation Spectroscopy of tissue primarily measures relative red blood cell motion within vessels." Biomedical Optics Express **2**(7): 2047-2054.

Carraresi, S., Mohamed Shatir, T. S., Martelli, F. and Zaccanti, G. (2001). "Accuracy of a perturbation model to predict the effect of scattering and absorbing inhomogeneities on photon migration." Applied Optics **40**(25): 4622-4632.

Chartier, G. (2005). Introduction to optics, Springer.

Cheong, W. F., Prahl, S. A. and Welch, A. J. (1990). "A review of the optical properties of biological tissues." Ieee Journal of Quantum Electronics **26**(12): 2166-2185.

Cheung, C., Culver, J. P., Takahashi, K., Greenberg, J. H. and Yodh, A. G. (2001). "In vivo cerebrovascular measurement combining diffuse near-infrared absorption and correlation spectroscopies." Physics in Medicine and Biology **46**(8): 2053-2065.

Chu, K. and George, N. (2007). "Correlation function for speckle size in the right-half-space." Optics Communications **276**(1): 1-7.

Chu, K. C. and Rutt, B. K. (1997). "Polyvinyl alcohol cryogel: An ideal phantom material for MR studies of arterial flow and elasticity." Magnetic Resonance in Medicine **37**(2): 314-319.

Correia, T., Banga, A., Everdell, N. L., Gibson, A. P. and Hebden, J. C. (2009). "A quantitative assessment of the depth sensitivity of an optical topography system using a solid dynamic tissue-phantom." Physics in Medicine and Biology **54**(20): 6277-6286.

Correia, T., Gibson, A. and Hebden, J. (2010). "Identification of the optimal wavelengths for optical topography: a photon measurement density function analysis." Journal of Biomedical Optics **15**(5): 056002.

Cubeddu, R., Pifferi, A., Taroni, P., Torricelli, A. and Valentini, G. (1997). "A solid tissue phantom for photon migration studies." Phys Med Biol **42**(10): 1971-1979.

Cui, W., Kumar, C. and Chance, B. (1991). Experimental study of migration depth for the photons measured at sample surface. Proc. SPIE, 1431:180-191, Publ by Int Soc for Optical Engineering.

Dainty, J. C. (1975). Laser Speckle and Related Phenomena, Springer-Verlag.

Dehghani, H. and Delpy, D. T. (2000). "Near-infrared spectroscopy of the adult head: Effect of scattering and absorbing obstructions in the cerebrospinal fluid layer on light distribution in the tissue." Applied Optics **39**(25): 4721-4729.

Del Bianco, S., Martelli, F. and Zaccanti, G. (2002). "Penetration depth of light re-emitted by a diffusive medium: Theoretical and experimental investigation." Physics in Medicine and Biology **47**(23): 4131-4144.

Delpy, D. T., Cope, M., Van Der Zee, P., Arridge, S., Wray, S. and Wyatt, J. (1988). "Estimation of optical pathlength through tissue from direct time of flight measurement." Physics in Medicine and Biology **33**(12): 1433-1442.

Delpy, D. T. and Cope, M. (1997). "Quantification in tissue near-infrared spectroscopy." Philosophical Transactions of the Royal Society B: Biological Sciences **352**(1354): 649-659.

Devi, C. U., Vasu, R. M. and Sood, A. K. (2005). "Design, fabrication, and characterization of a tissue-equivalent phantom for optical elastography." Journal of Biomedical Optics **10**(4).

Devi, C. U., Vasu, R. M. and Sood, A. K. (2006). "Application of ultrasound-tagged photons for measurement of amplitude of vibration of tissue caused by ultrasound: theory, simulation, and experiments." J.Biomed.Opt. **11**(3): 34019.

Devi, C. U., Chandran, R. S., Vasu, R. M. and Sood, A. K. (2008). "Detection of optical and mechanical property inhomogeneities in tissue mimicking phantoms using an ultrasound assisted optical probe." J.Biomed.Opt. **13**(6): 064025.

DiMarzio, C. A. and Murray, T. W. (2003). "Medical Imaging Techniques Combining Lightand Ultrasound." Subsurface Sensing Technologies and Applications **4**(4).

Draudt, A., Lai, P., Roy, R. A., Murray, T. W. and Cleveland, R. O. (2009). Detection of hifu lesions in excised tissue using acousto-optic imaging. 8th International Symposium on Therapeutic Ultrasound, 1113:270-274.

Duck, F. A. (1987). "The measurement of exposure to ultrasound and its application to estimates of ultrasound 'dose'." Physics in Medicine and Biology **32**(3): 303-325.

Durduran, T., Yu, G., Burnett, M. G., Detre, J. A., Greenberg, J. H., Wang, J., Zhou, C. and Yodh, A. G. (2004). "Diffuse optical measurement of blood flow, blood oxygenation, and metabolism in a human brain during sensorimotor cortex activation." Opt.Lett. **29**(15): 1766-1768.

Durduran, T., Zhou, C., Edlow, B. L., Yu, G., Choe, R., Kim, M. N., Cucchiara, B. L., Putt, M. E., Shah, Q., Kasner, S. E., Greenberg, J. H., Yodh, A. G. and Detre, J. A. (2009). "Transcranial optical monitoring of cerebrovascular hemodynamics in acute stroke patients." Opt.Express **17**(5): 3884-3902.

Durduran, T., Choe, R., Baker, W. B. and Yodh, A. G. (2010). "Diffuse optics for tissue monitoring and tomography." Reports on Progress in Physics **73**(7).

Durduran, T., Zhou, C., Buckley, E., Kim, M., Yu, G., Choe, R., Gaynor, J., Spray, T., Durning, S. and Mason, S. (2010). "Optical measurement of cerebral hemodynamics and oxygen metabolism in neonates with congenital heart defects." Journal of Biomedical Optics **15**: 037004.

Edlow, B. L., Kim, M. N., Durduran, T., Zhou, C., Putt, M. E., Yodh, A. G., Greenberg, J. H. and Detre, J. A. (2010). "The effects of healthy aging on cerebral hemodynamic responses to posture change." Physiological Measurement **31**(4): 477-495.

Elazar, J. M. and Steshenko, O. (2008). "Doppler effect's contribution to ultrasonic modulation of multiply scattered coherent light: Monte Carlo modeling." Opt.Lett. **33**(2): 131-133.

Elson, D. S., Li, R., Dunsby, C., Eckersley, R. and Tang, M. X. (2011). "Ultrasound-mediated optical tomography: a review of current methods." Interface Focus **1**(4): 632.

Elwell, C. E. (1995). A Practical Users Guide to Near Infrared Spectroscopy, Hamamatsu Photonics KK.

Fantini, S., Franceschini, M. A., Walker, S. A., Maier, J. S. and Gratton, E. (1995). Photon path distributions in turbid media: applications for imaging. Proc. SPIE, 2389:340–349, Proc. SPIE.

Feng, S., Zeng, F. A. and Chance, B. (1995). "Photon migration in the presence of a single defect: A perturbation analysis." Applied Optics **34**(19): 3826-3837.

Ferrari, M., Mottola, L. and Quaresima, V. (2004). "Principles, techniques, and limitations of near infrared spectroscopy." Canadian Journal of Applied Physiology **29**(4): 463-487.

Firbank, M., Oda, M. and Delpy, D. T. (1995). "An improved design for a stable and reproducible phantom material for use in near-infrared spectroscopy and imaging." Physics in Medicine and Biology **40**(5): 955-961.

Firbank, M., Arridge, S. R., Schweiger, M. and Delpy, D. T. (1996). "An investigation of light transport through scattering bodies with non-scattering regions." Physics in Medicine and Biology **41**(4): 767-783.

Firbank, M., Okada, E. and Delpy, D. T. (1998). "A theoretical study of the signal contribution of regions of the adult head to near-infrared spectroscopy studies of visual evoked responses." NeuroImage **8**(1): 69-78.

Flock, S. T., Jacques, S. L., Wilson, B. C., Star, W. M. and Van Gemert, M. J. C. (1992). "Optical properties of intralipid: A phantom medium for light propagation studies." Lasers in Surgery and Medicine **12**(5): 510-519.

Forget, B. C., Ramez, F., Atlan, M., Selb, J. and Boccara, A. C. (2003). "High-contrast fast Fourier transform acousto-optical tomography of phantom tissues with a frequency-chirp modulation of the ultrasound." Applied Optics **42**(7): 1379-1383.

Gatti, A., Magatti, D. and Ferri, F. (2008). "Three-dimensional coherence of light speckles: Theory." Physical Review A - Atomic, Molecular, and Optical Physics **78**(6).

Gibson, A. P., Hebden, J. C. and Arridge, S. R. (2005). "Recent advances in diffuse optical imaging." Physics in Medicine and Biology **50**(4).

Giglio, M., Carpineti, M., Vailati, A. and Brogioli, D. (2001). "Near-field intensity correlations of scattered light." Applied Optics **40**(24): 4036-4040.

Goodman, J. W. (2005). Introduction to Fourier Optics, Roberts & Co.

Granot, E., Lev, A., Kotler, Z., Sfez, B. G. and Taitelbaum, H. (2001). "Detection of inhomogeneities with ultrasound tagging of light." J.Opt.Soc.Am.A Opt.Image Sci.Vis. **18**(8): 1962-1967.

Gunadi, S., Powell, S., Elwell, C. E. and Leung, T. S. (2010). Optimization of the acousto-optic signal detection in cylindrical geometry. Proc. SPIE, 7564:756431.

Gunadi, S. and Leung, T. S. (2011). Regional sensitivity comparison between optical and acousto-optic sensing. Proc. SPIE, 7899:78992Q.

Hebden, J. C., Price, B. D., Gibson, A. P. and Royle, G. (2006). "A soft deformable tissue-equivalent phantom for diffuse optical tomography." Physics in Medicine and Biology **51**(21): 5581-5590.

Hebden, J. C., Brunker, J., Correia, T., Price, B. D., Gibson, A. P. and Everdell, N. L. (2008). "An electrically-activated dynamic tissue-equivalent phantom for assessment of diffuse optical imaging systems." Physics in Medicine and Biology **53**(2): 329-337.

Hecht, E. (2002). Optics, Addison Wesley.

Hedrick, W. R., Hykes, D. L. and Starchman, D. E. (2005). Ultrasound Physics and Instrumentation, Elsevier Mosby.

Hill, C. R. and Ter Haar, G. R. (1995). "High intensity focused ultrasound - Potential for cancer treatment." British Journal of Radiology **68**(816): 1296-1303.

Huang, D., Swanson, E. A., Lin, C. P., Schuman, J. S., Stinson, W. G., Chang, W., Hee, M. R., Flotte, T., Gregory, K., Puliafito, C. A. and Fujimoto, J. G. (1991). "Optical coherence tomography." Science **254**(5035): 1178-1181.

Humphrey, V. F. (2007). "Ultrasound and matter-Physical interactions." Progress in Biophysics and Molecular Biology **93**(1-3): 195-211.

Jobsis, F. F. (1977). "Noninvasive, infrared monitoring of cerebral and myocardial oxygen sufficiency and circulatory parameters." Science **198**(4323): 1264-1267.

Kempe, M., Larionov, M., Zaslavsky, D. and Genack, A. Z. (1997). "Acousto-optic tomography with multiply scattered light." Journal of the Optical Society of America A-Optics Image Science and Vision **14**(5): 1151-1158.

Kennedy, J. E., Ter Haar, G. R. and Cranston, D. (2003). "High intensity focused ultrasound: surgery of the future?" The British journal of radiology **76**(909): 590-599.

Kim, C., Zemp, R. J. and Wang, L. V. (2006). "Intense acoustic bursts as a signal-enhancement mechanism in ultrasound-modulated optical tomography." Opt.Lett. **31**(16): 2423-2425.

Kim, C. and Wang, L. V. (2007). "Multi-optical-wavelength ultrasound-modulated optical tomography: a phantom study." Opt.Lett. **32**(16): 2285-2287.

Kim, M. N., Durduran, T., Frangos, S., Edlow, B. L., Buckley, E. M., Moss, H. E., Zhou, C., Yu, G., Choe, R., Maloney-Wilensky, E., Wolf, R. L., Grady, M. S., Greenberg, J. H., Levine, J. M., Yodh, A. G., Detre, J. A. and Kofke, W. A. (2009). "Noninvasive Measurement of Cerebral Blood Flow and Blood Oxygenation Using Near-Infrared and Diffuse Correlation Spectroscopies in Critically Brain-Injured Adults." Neurocritical Care: 1-8.

Kim, M. N., Durduran, T., Frangos, S., Edlow, B. L., Buckley, E. M., Moss, H. E., Zhou, C., Yu, G., Choe, R., Maloney-Wilensky, E., Wolf, R. L., Grady, M. S., Greenberg, J. H., Levine, J. M., Yodh, A. G., Detre, J. A. and Kofke, W. A. (2010). "Noninvasive measurement of cerebral blood flow and blood oxygenation using near-infrared and diffuse correlation spectroscopies in critically brain-injured adults." Neurocritical Care **12**(2): 173-180.

Kinnunen, M. and Myllylä, R. (2005). "Effect of glucose on photoacoustic signals at the wavelengths of 1064 and 532 nm in pig blood and intralipid." Journal of Physics D: Applied Physics **38**(15): 2654-2661.

Kinsler, L. E., Frey, A. R., Coppens, A. B. and Sanders, J. V. (1982). Fundamentals of Acoustics, John Wiley & Sons.

Klein, W. R. and Cook, B. D. (1967). "Unified approach to ultrasonic light diffraction." IEEE Trans. Sonics Ultrason. **SU-14**(3): 123-134.

Kothapalli, S. R., Sakadzic, S., Kim, C. and Wang, L. V. (2007). "Imaging optically scattering objects with ultrasound-modulated optical tomography." Opt.Lett. **32**(16): 2351-2353.

Kwiek, P., Molkenstruck, W. and Reibold, R. (1996). "Determination of the Klein-Cook parameter in ultrasound light diffraction." Ultrasonics **34**(8): 801-805.

Lai, P., Roy, R. A. and Murray, T. W. (2009). "Quantitative characterization of turbid media using pressure contrast acousto-optic imaging." Optics Letters **34**(18): 2850-2852.

Lai, P., McLaughlan, J. R., Draudt, A. B., Murray, T. W., Cleveland, R. O. and Roy, R. A. (2011). "Real-Time Monitoring of High-Intensity Focused Ultrasound Lesion Formation Using Acousto-Optic Sensing." Ultrasound in Medicine and Biology **37**(2): 239-252.

Laufer, J., Zhang, E. and Beard, P. (2010). "Evaluation of absorbing chromophores used in tissue phantoms for quantitative photoacoustic spectroscopy and imaging." IEEE Journal on Selected Topics in Quantum Electronics **16**(3): 600-607.

Lesaffre, M., Farahi, S., Boccara, A. C., Ramaz, F. and Gross, M. (2011). "Theoretical study of acousto-optical coherence tomography using random phase jumps on ultrasound and light." Journal of the Optical Society of America A: Optics and Image Science, and Vision **28**(7): 1436-1444.

Leutz, W. and Maret, G. (1995). "Ultrasonic Modulation of Multiply Scattered-Light." Physica B **204**(1-4): 14-19.

Lev, A., Kotler, Z. and Sfez, B. G. (2000). "Ultrasound tagged light imaging in turbid media in a reflectance geometry." Optics Letters **25**(6): 378-380.

Lev, A. and Sfez, B. G. (2002). "Direct, noninvasive detection of photon density in turbid media." Optics Letters **27**(7): 473-475.

Lev, A. and Sfez, B. (2003). "In vivo demonstration of the ultrasound-modulated light technique." Journal of the Optical Society of America A-Optics Image Science and Vision **20**(12): 2347-2354.

Lev, A. and Sfez, B. G. (2003). "Pulsed ultrasound-modulated light tomography." Optics Letters **28**(17): 1549-1551.

Lev, A., Rubanov, E., Sfez, B., Shany, S. and Foldes, A. J. (2005). "Ultrasound-modulated light tomography assessment of osteoporosis." Optics Letters **30**(13): 1692-1694.

Leveque-Fort, S. (2001). "Three-dimensional acousto-optic imaging in biological tissues with parallel signal processing." Appl.Opt. **40**(7): 1029-1036.

Leveque, S., Boccara, A. C., Lebec, M. and Saint-Jalmes, H. (1999). "Ultrasonic tagging of photon paths in scattering media: parallel speckle modulation processing." Opt.Lett. **24**(3): 181-183.

Li, J., Ku, G. and Wang, L. V. (2002). "Ultrasound-modulated optical tomography of biological tissue by use of contrast of laser speckles." Applied Optics **41**(28): 6030-6035.

Li, J. and Wang, L. H. V. (2002). "Ultrasound-modulated laser speckle imaging of biological tissues." Second Joint Embs-Bmes Conference 2002, Vols 1-3, Conference Proceedings: 2319-2320

2682.

Li, J., Sakadzic, S., Ku, G. and Wang, L. V. (2003). "Transmission- and side-detection configurations in ultrasound-modulated optical tomography of thick biological tissues." Appl.Opt. **42**(19): 4088-4094.

Li, J. and Wang, L. H. V. (2004). "Ultrasound-modulated optical computed tomography of biological tissues." Applied Physics Letters **84**(9): 1597-1599.

Li, J., Dietsche, G., Iftime, D., Skipetrov, S. E., Maret, G., Elbert, T., Rockstroh, B. and Gisler, T. (2005). "Noninvasive detection of functional brain activity with near-infrared diffusing-wave spectroscopy." Journal of Biomedical Optics **10**(4).

Li, J., Ninck, M., Koban, L., Elbert, T., Kissler, J. and Gisler, T. (2008). "Transient functional blood flow change in the human brain measured noninvasively by diffusing-wave spectroscopy." Optics Letters **33**(19): 2233-2235.

Li, Q. B. and Chiang, F. P. (1992). "3-Dimensional Dimension of Laser Speckle." Applied Optics **31**(29): 6287-6291.

Li, R., Song, L., Elson, D. S. and Tang, M. X. (2010). "Parallel detection of amplitude-modulated, ultrasound-modulated optical signals." Optics Letters **35**(15): 2633-2635.

Li, R., Elson, D. S., Dunsby, C., Eckersley, R. and Tang, M. X. (2011). "Effects of acoustic radiation force and shear waves for absorption and stiffness sensing in ultrasound modulated optical tomography." Optics Express **19**(8): 7299-7311.

Li, Y., Hemmer, P., Kim, C., Zhang, H. and Wang, L. V. (2008). "Detection of ultrasound-modulated diffuse photons using spectral-hole burning." Optics Express **16**(19): 14862-14874.

Liu, Q., Norton, S. and Vo-Dinh, T. (2008). "Modeling of nonphase mechanisms in ultrasonic modulation of light propagation." Applied Optics **47**(20): 3619-3630.

Lizzi, F. L., Muratore, R., Deng, C. X., Ketterling, J. A., Alam, S. K., Mikaelian, S. and Kalisz, A. (2003). "Radiation-force technique to monitor lesions during ultrasonic therapy." Ultrasound in Medicine and Biology **29**(11): 1593-1605.

MacLeod, D., Ikeda, K., Keifer, J., Moretti, E. and Ames, W. (2006). "Validation of the CAS adult cerebral oximeter during hypoxia in healthy volunteers." Anesth Analg **102**(IARS 80th Clinical and Scientific Congress): S162.

Magatti, D., Gatti, A. and Ferri, F. (2009). "Three-dimensional coherence of light speckles: Experiment." Physical Review A - Atomic, Molecular, and Optical Physics **79**(5).

Mahan, G. D., Engler, W. E., Tiemann, J. J. and Uzgiris, E. (1998). "Ultrasonic tagging of light: theory." Proc.Natl.Acad.Sci.U.S.A **95**(24): 14015-14019.

Maret, G. and Wolf, P. E. (1987). "Multiple light scattering from disordered media. The effect of brownian motion of scatterers." Zeitschrift f++r Physik B Condensed Matter **65**(4): 409-413.

Marks, F. A., Tomlinson, H. W. and Brooksby, G. W. (1993). Comprehensive approach to breast cancer detection using light: photon localization by ultrasound modulation and tissue characterization by spectral discrimination, 1888:500-510, Publ by Society of Photo-Optical Instrumentation Engineers.

Matcher, S. J., Kirkpatrick, P. J., Nahid, K., Cope, M. and Delpy, D. T. (1995). Absolute quantification methods in tissue near-infrared spectroscopy, 2389:486.

Matcher, S. J., Cope, M. and Delpy, D. T. (1997). "In vivo measurements of the wavelength dependence of tissue-scattering coefficients between 760 and 900 nm measured with time-resolved spectroscopy." Applied Optics **36**(1): 386-396.

Mesquita, R. C., Skuli, N., Kim, M. N., Liang, J., Schenkel, S., Majmundar, A. J., Simon, M. C. and Yodh, A. G. (2010). "Hemodynamic and metabolic diffuse optical monitoring in a mouse model of hindlimb ischemia." Biomed Opt Express **1**(4): 1173-1187.

Michels, R., Foschum, F. and Kienle, A. (2008). "Optical properties of fat emulsions." Optics Express **16**(8): 5907-5925.

Moharam, M. G. and Young, L. (1978). "CRITERION FOR BRAGG AND RAMAN-NATH DIFFRACTION REGIMES." Applied Optics **17**(11): 1757-1759.

Murray, T. W., Sui, L., Maguluri, G., Roy, R. A., Nieva, A., Blonigen, F. and DiMarzio, C. A. (2004). "Detection of ultrasound-modulated photons in diffuse media using the photorefractive effect." Opt.Lett. **29**(21): 2509-2511.

Murray, T. W. and Roy, R. A. (2007). "Illuminating Sound: Imaging Tissue Optical Properties with Ultrasound." Acoustics Today **3**(3): 17-24.

Niemz, M. H. (2004). Laser-tissue interactions : fundamentals and applications, Springer.

Ninck, M., Untenberger, M. and Gisler, T. (2010). "Diffusing-wave spectroscopy with dynamic contrast variation: disentangling the effects of blood flow and extravascular tissue shearing on signals from deep tissue." Biomed Opt Express **1**(5): 1502-1513.

Niwayama, M., Lin, L., Shao, J., Kudo, N. and Yamamoto, K. (2000). "Quantitative measurement of muscle hemoglobin oxygenation using near-infrared spectroscopy with correction for the influence of a subcutaneous fat layer." Review of Scientific Instruments **71**(12): 4571-4575.

Obrig, H. and Villringer, A. (2003). "Beyond the visible - Imaging the human brain with light." Journal of Cerebral Blood Flow and Metabolism **23**(1): 1-18.

Ohmae, E., Ouchi, Y., Oda, M., Suzuki, T., Nobesawa, S., Kanno, T., Yoshikawa, E., Futatsubashi, M., Ueda, Y., Okada, H. and Yamashita, Y. (2006). "Cerebral hemodynamics evaluation by near-infrared time-resolved spectroscopy: Correlation with simultaneous positron emission tomography measurements." NeuroImage **29**(3): 697-705.

Okada, E. and Delpy, D. T. (2003). "Near-infrared light propagation in an adult head model. II. Effect of superficial tissue thickness on the sensitivity of the near-infrared spectroscopy signal." Applied Optics **42**(16): 2915-2922.

Ono, M., Kashio, Y., Schweiger, M., Dehghani, H., Arridge, S. R., Firbank, M. and Okada, E. (2000). "Topographic distribution of photon measurement density functions on the brain surface by hybrid radiosity-diffusion method." Optical Review **7**(5): 426-431.

Ostermeyer, M. R. and Jacques, S. L. (1997). "Perturbation theory for diffuse light transport in complex biological tissues." Journal of the Optical Society of America A: Optics and Image Science, and Vision **14**(1): 255-261.

Page, A. J., Coyle, S., Keane, T. M., Naughton, T. J., Markham, C. and Ward, T. (2006). Distributed Monte Carlo simulation of light transportation in tissue. 20th International Parallel and Distributed Processing Symposium, IPDPS 2006 2006, art. no. 1639511, 2006.

Patil, A. V., Safaie, J., Moghaddam, H. A., Wallois, F. and Grebe, R. (2011). "Experimental investigation of NIRS spatial sensitivity." Biomedical Optics Express **2**(6): 1478-1493.

Patterson, M. S., Chance, B. and Wilson, B. C. (1989). "Time resolved reflectance and transmittance for the non-invasive measurement of tissue optical properties." Applied Optics **28**(12): 2331-2336.

Pine, D. J., Weitz, D. A., Chaikin, P. M. and Herbolzheimer, E. (1988). "Diffusing wave spectroscopy." Physical Review Letters **60**(12): 1134-1137.

Pogue, B. W. and Patterson, M. S. (2006). "Review of tissue simulating phantoms for optical spectroscopy, imaging and dosimetry." Journal of Biomedical Optics **11**(4).

Powell, S. (2011). Parallel Simulation of Ultrasound Modulated Light in Meshed Heterogenous Media with Arbitrary Acoustic Fields. Medical Physics & Bioengineering. London, University College London. **MPhil**.

Price, B., Gibson, A. and Royle, G. (2010). Dual-modality imaging of a compressible breast phantom with realistic optical and x-ray properties. Medical Imaging 2010: Physics of Medical Imaging, 7622:762207(762201-762208), Proc. of SPIE.

Price, B. D. (2010). Towards combined x-ray and optical mammography. Medical Physics & Bioengineering. London, UK, University College London. **Ph.D**.

Rabal, H. J. and Braga Jr., R. A. (2009). Dynamic Laser Speckle and Applications, CRC Press.

Rabkin, B. A., Zderic, V. and Vaezy, S. (2005). "Hyperecho in ultrasound images of HIFU therapy: Involvement of cavitation." Ultrasound in Medicine and Biology **31**(7): 947-956.

Rajan, V., Varghese, B., van Leeuwen, T. G. and Steenbergen, W. (2008). "Speckle size and decorrelation time; space-time correlation analysis of coherent light dynamically scattered from turbid media." Optics Communications **281**(6): 1755-1760.

Raman, C. V. and Nagendra Nath, N. S. (1935). "The diffraction of light by sound waves of high frequency: Part II." Proceedings of the Indian Academy of Sciences - Section A **2**(4): 413-420.

Raman, C. V. and Nath, N. S. N. (1935). "The diffraction of light by high frequency sound waves: Part I." Proc. Indian Acad. Sci. **2**: 406-412.

Raman, V. and Venkataraman, K. (1939). "Determination of the adiabatic piezo-optic coefficient of liquids." Proceedings of the Royal Society of London. Series A. Mathematical and Physical Sciences **171**(945): 137.

Rickey, D. W., Picot, P. A., Christopher, D. A. and Fenster, A. (1995). "A wall-less vessel phantom for Doppler ultrasound studies." Ultrasound in Medicine and Biology **21**(9): 1163-1176.

Roche-Labarbe, N., Carp, S. A., Surova, A., Patel, M., Boas, D. A., Grant, P. E. and Franceschini, M. A. (2010). "Noninvasive optical measures of CBV, StO2, CBF index, and rCMRO2 in human premature neonates' brains in the first six weeks of life." Human Brain Mapping **31**(3): 341-352.

Rousseau, G., Blouin, A. and Monchalin, J. P. (2008). "Ultrasound-modulated optical imaging using a powerful long pulse laser." Optics Express **16**(17): 12577-12590.

Sakadzic, S. and Wang, L. V. (2002). "Ultrasonic modulation of multiply scattered coherent light: An analytical model for anisotropically scattering media." Physical Review E - Statistical, Nonlinear, and Soft Matter Physics **66**(2): 026603.

Sakadzic, S. and Wang, L. V. (2004). "High-resolution ultrasound-modulated optical tomography in biological tissues." Opt.Lett. **29**(23): 2770-2772.

Sakadzic, S. and Wang, L. V. (2005). "Modulation of multiply scattered coherent light by ultrasonic pulses: an analytical model." Phys.Rev.E.Stat.Nonlin.Soft.Matter Phys. **72**(3 Pt 2): 036620.

Sakadzic, S. and Wang, L. V. (2006). "Correlation transfer equation for ultrasound-modulated multiply scattered light." Phys.Rev.E.Stat.Nonlin.Soft.Matter Phys. **74**(3 Pt 2): 036618.

Sakadzic, S. and Wang, L. V. (2007). "Correlation transfer equation for multiply scattered light modulated by an ultrasonic pulse." J.Opt.Soc.Am.A Opt.Image Sci.Vis. **24**(9): 2797-2806.

Schätzel, K., Drewel, M. and Stimac, S. (1988). "PHOTON CORRELATION MEASUREMENTS AT LARGE LAG TIMES: IMPROVING STATISTICAL ACCURACY." Journal of Modern Optics **35**(4): 711-718.

Schätzel, K. (1990). "Noise on photon correlation data. I. Autocorrelation functions." Quantum Optics: Journal of the European Optical Society Part B **2**(4): 287-305.

Selb, J., Pottier, L. and Boccara, A. C. (2002). "Nonlinear effects in acousto-optic imaging." Opt.Lett. **27**(11): 918-920.

Shang, Y., Zhao, Y., Cheng, R., Dong, L., Irwin, D. and Yu, G. (2009). "Portable optical tissue flow oximeter based on diffuse correlation spectroscopy." Opt Lett **34**(22): 3556-3558.

Sterling, D. J., Pardoe, T. D. and Chartrand, L. (2003). Technician's Guide to Fiber Optics, Delmar Learning.

Suzuki, S., Takasaki, S., Ozaki, T. and Kobayashi, Y. (1999). Tissue oxygenation monitor using NIR spatially resolved spectroscopy, 3597:582-592, Society of Photo-Optical Instrumentation Engineers.

ter Haar, G. and Coussios, C. (2007). "High intensity focused ultrasound: Physical principles and devices." International Journal of Hyperthermia **23**(2): 89-104.

Tuchin, V. V. (2007). Tissue optics : light scattering methods and instruments for medical diagnosis, SPIE Press.

Ueda, Y., Ohta, K. and Yamashita, Y. (2005). "Diffuse optical tomography using time-resolved photon path distribution." Optical Review **12**(4): 334-337.

Vaithianathan, T., Tullis, I. D. C., Everdell, N., Leung, T., Gibson, A., Meek, J. and Delpy, D. T. (2004). "Design of a portable near infrared system for

topographic imaging of the brain in babies." Review of Scientific Instruments **75**(10 I): 3276-3283.

Van Beekvelt, M. C. P., Borghuis, M. S., Van Engelen, B. G. M., Wevers, R. A. and Colier, W. N. J. M. (2001). "Adipose tissue thickness affects in vivo quantitative near-IR spectroscopy in human skeletal muscle." Clinical Science **101**(1): 21-28.

Van der Zee, P., Cope, M., Arridge, S. R., Essenpreis, M., Potter, L. A., Edwards, A. D., Wyatt, J. S., McCormick, D. C., Roth, S. C., Reynolds, E. O. R. and Delpy, D. T. (1992). "Experimentally measured optical pathlengths for the adult head, calf and forearm and the head of the newborn infant as a function of inter optode spacing." Advances in experimental medicine and biology **316**: 143-153.

van Staveren, H. J., Moes, C. J. M., van Marie, J., Prahl, S. A. and van Gemert, M. J. C. (1991). "Light scattering in Intralipid-10% in the wavelength range of 400-1100 nm." Appl. Opt. **30**(31): 4507-4514.

Villringer, A., Planck, J., Hock, C., Schleinkofer, L. and Dirnagl, U. (1993). "Near infrared spectroscopy (NIRS): A new tool to study hemodynamic changes during activation of brain function in human adults." Neuroscience Letters **154**(1-2): 101-104.

Vo-Dinh, T. (2003). Biomedical photonics handbook, SPIE Society of Photo-Optical Instrumentation Engineers.

Wang, L., Jacques, S. L. and Zheng, L. (1995). "MCML - Monte Carlo modeling of light transport in multi-layered tissues." Computer Methods and Programs in Biomedicine **47**(2): 131-146.

Wang, L. H., Jacques, S. L. and Zhao, X. M. (1995). "Continuous-Wave Ultrasonic Modulation of Scattered Laser-Light to Image Objects in Turbid Media." Optics Letters **20**(6): 629-631.

Wang, L. H. and Zhao, X. M. (1997). "Ultrasound-modulated optical tomography of absorbing objects buried in dense tissue-simulating turbid media." Applied Optics **36**(28): 7277-7282.

Wang, L. V. (1998). "Ultrasonic modulation of scattered light in turbid media and a potential novel tomography in biomedicine." Photochem.Photobiol. **67**(1): 41-49.

Wang, L. V. and Ku, G. (1998). "Frequency-swept ultrasound-modulated optical tomography of scattering media." Opt.Lett. **23**(12): 975-977.

Wang, L. V. (2001). "Mechanisms of ultrasonic modulation of multiply scattered coherent light: an analytic model." Phys.Rev.Lett. **87**(4): 043903.

Wang, L. V. (2001). "Mechanisms of ultrasonic modulation of multiply scattered coherent light: a Monte Carlo model." Opt.Lett. **26**(15): 1191-1193.

Wang, L. V. (2004). "Ultrasound-mediated biophotonic imaging: A review of acousto-optical tomography and photo-acoustic tomography." Disease Markers **19**(2-3): 123-138.

Wang, L. V. and Wu, H. (2007). Biomedical optics : principles and imaging, Wiley-Interscience.

Wolf, M., Ferrari, M. and Quaresima, V. (2007). "Progress of near-infrared spectroscopy and topography for brain and muscle clinical applications." Journal of Biomedical Optics **12**(6): 062104.

Xu, X., Zhang, H., Hemmer, P., Qing, D. K., Kim, C. and Wang, L. V. (2007). "Photorefractive detection of tissue optical and mechanical properties by ultrasound modulated optical tomography." Opt.Lett. **32**(6): 656-658.

Xu, X., Kothapalli, S., Liu, H. and Wang, L. (2010). "Spectral hole burning for ultrasound-modulated optical tomography of thick tissue (Journal Paper)." Journal of Biomedical Optics **15**(06): 066018.

Xu, X., Liu, H. and Wang, L. V. (2011). "Time-reversed ultrasonically encoded optical focusing into scattering media." Nature Photonics.

Yodh, A. G., Pine, D. J., Kaplan, P. D., Kao, M. H. and Georgiades, N. (1992). "Speckle fluctuations and their use as probes of dense random media." Molecular Crystals and Liquid Crystals Science and Technology Section B: Nonlinear Optics **3**(1-2): 149-160.

Yoshitani, K., Kawaguchi, M., Tatsumi, K., Kitaguchi, K. and Furuya, H. (2002). "A comparison of the INVOS 4100 and the NIRO 300 near-infrared spectrophotometers." Anesthesia and Analgesia **94**(3): 586-590.

Yu, G., Floyd, T. F., Durduran, T., Zhou, C., Wang, J., Detre, J. A. and Yodh, A. G. (2007). "Validation of diffuse correlation spectroscopy for muscle blood flow with concurrent arterial spin labeled perfusion MRI." Optics Express **15**(3): 1064-1075.

Yuan, B. and Liu, Y. (2010). "Ultrasound-modulated fluorescence from rhodamine B aqueous solution." Journal of Biomedical Optics **15**(2).

Yuan, S., Devor, A., Boas, D. A. and Dunn, A. K. (2005). "Determination of optimal exposure time for imaging of blood flow changes with laser speckle contrast imaging." Applied Optics **44**(10): 1823-1830.

Zell, K., Sperl, J. I., Vogel, M. W., Niessner, R. and Haisch, C. (2007). "Acoustical properties of selected tissue phantom materials for ultrasound imaging." Physics in Medicine and Biology **52**(20): N475–N484.

Zemp, R., Sakadzic, S. and Wang, L. V. (2006). "Stochastic explanation of speckle contrast detection in ultrasound-modulated optical tomography." Phys.Rev.E.Stat.Nonlin.Soft.Matter Phys. **73**(6 Pt 1): 061920.

Zemp, R. J., Kim, C. and Wang, L. V. (2007). "Ultrasound-modulated optical tomography with intense acoustic bursts." Appl.Opt. **46**(10): 1615-1623.

Zhou, C., Choe, R., Shah, N., Durduran, T., Yu, G., Durkin, A., Hsiang, D., Mehta, R., Butler, J., Cerussi, A., Tromberg, B. J. and Yodh, A. G. (2007). "Diffuse optical monitoring of blood flow and oxygenation in human breast cancer during early stages of neoadjuvant chemotherapy." Journal of Biomedical Optics **12**(5).

Zhou, C., Eucker, S. A., Durduran, T., Yu, G., Ralston, J., Friess, S. H., Ichord, R. N., Margulies, S. S. and Yodh, A. G. (2009). "Diffuse optical monitoring of hemodynamic changes in piglet brain with closed head injury." J.Biomed.Opt. **14**(3): 034015.

Zhu, Q., Durduran, T. and Yodh, A. G. (1999). "Imaging using ultrasound and near infrared diffusive light." Bioengineering, Proceedings of the Northeast Conference: 104-105.

Ziskin, M. C. (1993). "Fundamental physics of ultrasound and its propagation in tissue." Radiographics **13**(3): 705.